COMPLEX COMPOSITIONAL ZONING IN CLINOPYROXENE IN LATE CRETACEOUS POTASSIC-ALKALINE VOLCANIC ROCKS FROM NORTHERN TURKEY: IMPLICATIONS FOR MAGMA MIXING

by

FRANK EARL WATERS III

(Under the Direction of MICHAEL F. RODEN)

ABSTRACT

Textural signatures and compositional variations in major, minor, and trace elements within individual phenocrysts are strong indicators of changing conditions in a crystallizing magma chamber, potentially caused by open system processes. The clinopyroxenes from a series of mafic potassic lava flows and dikes from north-central Turkey show exceptional examples of such textural and chemical zonation patterns. The lava flows and dikes come from a Late Cretaceous continental magmatic arc on the southern edge of Laurasia formed from the subduction of Neotethyan oceanic crust. Two main rock groups were observed in the mafic potassic rocks: leucitites and minettes. The leucitites display more complex intra-phenocryst textural features including repeating layers of differing compositions and have more varied clinopyroxene populations. The observed textural and compositional variations in the clinopyroxenes suggest the influence of magma mixing induced convection in the evolution of the mafic potassic rocks of the Pontide Arc.

INDEX WORDS: Pontide Arc, volcano, clinopyroxenes, complex zoning, Turkey, mafic potassic magmas, magma mixing

COMPLEX COMPOSITIONAL ZONING IN CLINOPYROXENE IN LATE CRETACEOUS POTASSIC-ALKALINE VOLCANIC ROCKS FROM NORTHERN TURKEY: IMPLICATIONS FOR MAGMA MIXING

by

FRANK EARL WATERS III

B.S., College of Charleston, 2011

A Thesis Submitted to the Graduate Faculty of The University of Georgia in Partial Fulfillment of the Requirements for the Degree

MASTER OF SCIENCE

ATHENS, GEORGIA

2016

COMPLEX COMPOSITIONAL ZONING IN CLINOPYROXENE IN LATE CRETACEOUS POTASSIC-ALKALINE VOLCANIC ROCKS FROM NORTHERN TURKEY: IMPLICATIONS FOR MAGMA MIXING

by

FRANK EARL WATERS III

Major Professor:	Mike Roden
Committee:	Doug Crowe Alberto Patiño Douce

Electronic Version Approved:

Suzanne Barbour
Dean of the Graduate School
The University of Georgia
August 2016

ACKNOWLEDGMENTS

Thank you to Dr. Roden for his nearly limitless supply of patience and most importantly his instruction over the years, my apologies for sticking around so long. Thank you to Chris Fleisher and his sage like teaching of the microprobe. Thank you to Dr. Crowe and Dr. Patiño Douce for their instruction and unique insights into the subject material surrounding hard rock geology. I want to thank the Department of Geology as a whole for allowing me this opportunity to better myself and our esteemed colleagues in Turkey without whom I would have had neither samples nor foundational knowledge of the Pontide Arc. Finally, I thank my family members, who have never failed at providing my life with a foundation.

TABLE OF CONTENTS

LIST OF TABLES

LIST OF FIGURES

1 INTRODUCTION

Mafic potassic rocks are igneous rocks that possess abnormally high K_2O wt% alongside primitive MgO and FeO wt% values. These volcanic rocks typically have very low SiO_2 resulting in the formation of feldspathoid minerals such as leucite as opposed to feldspars like plagioclase and sanidine. Despite this mafic affinity the clinopyroxenes found within these magmas commonly have green salite cores and bands, both rich in Fe, Al, and Ti compared to the coexisting diopside bands, which are rich in Mg and Cr (O'Brien et al., 1988). This juxtaposition of differing clinopyroxene compositions within the same crystal is referred to as zoning and is common in mafic potassic rocks. Zoning is discussed in Section 1.1. Mafic potassic rocks are found in many localities around the world from the Highwoods Mountains in Montana (O'Brien et al., 1988), to the magmatic provinces of Italy (Cioni et al., 1988; Peccerillo, A., 2005), to the Western Mexican Volcanic belt (Wallace and Carmichael 1989). This study will focus on the clinopyroxenes of the mafic potassic rocks of the Pontide Arc located in what is today north-central Turkey. The Pontide Arc was situated above an ocean-continent subduction zone that consumed the crust of the Neotethyan Ocean in the Late Cretaceous (Gülmez and Genç, 2015) and is discussed in more detail in Section 1.2 below.

1.1 Overview of mineral zoning

There are several types of zoning in igneous minerals and only ones common to clinopyroxene will be covered here; however, work on plagioclase zoning will be cited to

describe zoning patterns seen in clinopyroxene. Composition zoning arises when equilibrium is not maintained between the crystal and the melt, resulting in a layer of crystal material with a slightly different composition being added around the preexisting crystal (Winter, 2010). ***Sector zoning*** is characterized by neighboring pyramidal zones in the same clinopyroxene with slightly different compositions (e.g. Si and Al exchanging) and is indicative of rapid initial crystal growth (Wass, 1973). ***Low amplitude oscillatory zoning***, characterized by small (~1-10 micrometer) gradual variations in crystal composition, is interpreted to arise during crystallization by localized cation depletion in the melt at the crystal face followed by cyclical re-enrichment (Winter, 2010; Streck, 2008). This process is interpreted to correspond with high crystal growth rates and is evident as rolling oscillations on composition-distance plots with small amplitudes (~2% An for plagioclase) (Ginibre et al., 2002). Next is so-called ***saw-tooth resorption oscillatory zoning***, a pattern marked by ***normal*** (high temperature, Mg-rich layer followed by low temperature, Fe-rich layer) and ***reverse*** (Fe-rich layer followed by Mg-rich layer) zoned bands 10 to 20 microns across with medium sized amplitudes (~5 to 10 % An for plagioclase) (Ginibre et al., 2002). In saw-tooth oscillatory zoning bands are separated by dissolution surfaces potentially caused by the crystal passing through temperature gradients in a convecting magma (Ginibre et al., 2002). Substantially larger are the compositional incongruities that separate ***epitaxial bands*** found in ***complex zoning***. An epitaxial band is a relatively thick layer of material deposited on a preexisting crystal with a slightly different composition and indicates a unique crystallization environment (Streck, 2008). There are several names for complex zoning including 'concentric zoning,' 'step zoning,' 'recurrent zoning,' 'high amplitude discontinuities,' and others. Complex zoning

manifests as a set of normal and reverse zoned epitaxial bands inside a phenocryst (Streck, 2008). These epitaxial bands are separated by sharp boundaries or resorption surfaces and form nearly parallel to the exterior crystal faces of their host phenocryst (O'Brien et al. 1988). Complex zoning can be seen as large composition discontinuities on profiles with boxed or saw tooth patterns on core-rim transverses. The reverse zoning and resorption features associated with complex zoning are commonly interpreted as signs of open system processes (Streck, 2008). This interpretation is bolstered when magma-melt and crystal compositional data show a lack of equilibrium between phases, indicating magma recharge and/or contamination (Streck, 2008). An indication that there are different mechanisms behind saw-tooth oscillatory zoning and complex zoning is the observation that both types of oscillatory zoning (low amplitude and saw-tooth) can occur inside individual epitaxial bands. Occasionally complexly zoned clinopyroxenes possess Fe-rich salite cores that are often rounded, resorbed, or display embayments and have a jacket of a Mg-rich material surrounding them (O'Brien et al. 1988; Streck, 2008; Semiz et al., 2012). The origin of these cores will be examined in Section 4.3. All the above zoning patterns are represented in the clinopyroxenes from samples from the Pontide Arc.

1.2 Geologic Background of the Pontide Arc

The Pontide magmatic arc formed atop the southern margin of Eurasia during the Cretaceous at the closing of the northern branch of the Tethys Ocean (Gülmez et al., 2016). This led to a complicated collision between Eurasia and Africa involving several continental slivers; the middle portion of the suture belt that formed during these collisions is the Izmir-Anakara-Erzincan Suture Zone, a subsection of the Alpine Himalayan Mountain Belt

(Gülmez et al., 2016) [See Figure 1.1]. The nine Pontide Arc samples of this study were gathered from three different localities spanning 300 km along the Ankara-Erzincan suture belt north of the Kirschir continental sliver [See Figure 1.1]. These samples are part of a larger study (Gülmez et al., 2016) inquiring into the origin of leucite-bearing basaltic and mafic potassic volcanism that took place along the arc during the Late Cretaceous.

Today the trace of the southern margin of Eurasia in the Central Pontides is seen as a 100 km wide subduction-accretionary complex that started growing in either the Permian or Triassic (Gülmez et al., 2016). The Pontides represent a long-lived Eurasian active margin that formed atop this complex in response to the northward subduction of Tethyan oceanic crust starting in the Middle Jurassic (Gülmez et al., 2016). Interestingly there is an absence of volcanic products between the Middle Jurassic to the Upper Cretaceous, when volcanism re-initiated. This re-initiation is recorded as the Upper Cretaceous Volcano-sedimentary Succession (UCVS) (Gülmez et al., 2016) and it is from this sequence that the samples were collected.

The UCVS is comprised of units deposited in forearc basins along the Izmir-Ankara-Erzincan Suture Zone of the Central Pontides, these include Cenomanian and Maastrichtian aged turbidites and pelagic limestones interlaced with abundant calc-alkaline andesitic lava lenses and related clastic deposits; ultrapotassic magmatic products (mafic potassic magmas with molar K_2O / Na_2O > 3) also interlace with and cross cut these units (Gülmez et al., 2016). It is difficult to distinguish between continental arc units, forearc units, and mélange units in the UCVS, reflecting the simultaneous the growth of the accretionary prism and slab rollback during which the arc migrated approximately 450 km to the south over a span of ~14 million years from the Turonian to the Campanian (Gülmez et al., 2016).

The onset of ultrapotassic volcanism along the Pontide Arc occurs during the same time interval. Ultrapotassic products include leucitites, lamprophyres, and trachytes and occur as discrete dikes, domes, stocks, lava flows, breccias, and composite dikes (Gülmez et al., 2016). These ultrapotassic rocks display subduction-related signatures including significant enrichment in the LILE and LREE relative to the HFSE and HREE as well as depletions of Nb and Ta (Gülmez et al., 2016). Strontium, neodymium, and lead isotope signatures are interpreted to indicate that subduction from the Middle Triassic to the Late Cretaceous metasomatized a region of depleted mantle creating a potassium-rich, isotopically unique mantle source (Gülmez et al., 2016). Subsequent slab roll back followed by slab tear during the Late Cretaceous may have triggered the generation of ultrapotassic magmas (Gülmez et al., 2016).

1.3 Objectives of this study

Investigations of clinopyroxenes from the mafic potassic rocks of the Pontide Arc were conducted using the JEOL JXA-6800 microprobe at the University of Georgia. The goal of the project was to examine textural and chemical features present in the clinopyroxenes from these mafic potassic volcanic rocks to constrain the magmatic processes involved in the evolution of mafic potassic arc volcanism. Textural features of importance include fossil phenocryst resorption features and associated epitaxial bands. To supplement this approach, calculations on temperature and pressure conditions prior to eruption and magma water content, will be considered. The compositional and spatial data of these epitaxial bands indicate the importance of magma mixing events in the development of these mafic potassic magmas.

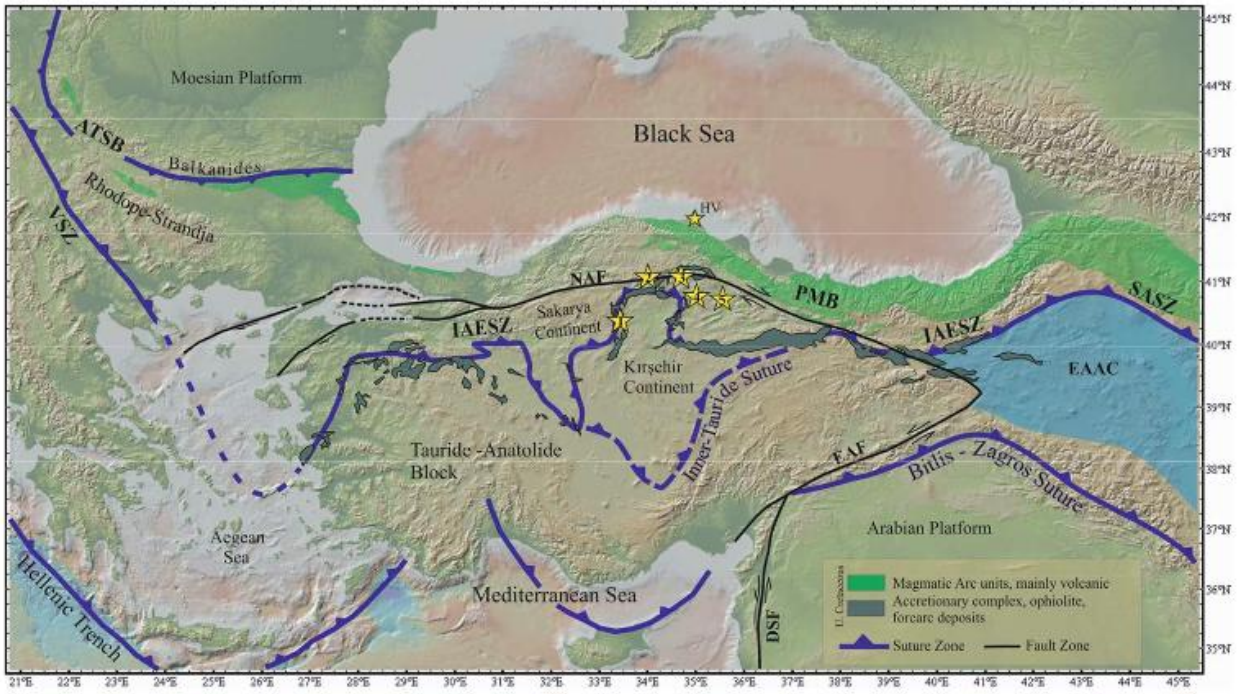

Figure 1.1) The location of the Izmir-Ankara-Erzincan Suture Zone (IAESZ). Ophiolites and accretionary complexes, and forearc deposits related to the IAESZ are shown in teal. Calc-alkaline volcanic rock deposits of the Pontide magmatic belt (PMB) related to Cretaceous subduction of the Neo-Tethys Ocean are shown in green. Yellow stars denote the location of Upper Cretaceous ultrapotassic rocks that were collected by F. Gülmez (Gülmez et al., 2016). Samples from Kalecik (star 1), Osmancik (star 3), and Amasya (star 5) were shared with this study. Source: Figure 1 of Gülmez et al. (2016).

2 ANALYTICAL METHODS

Samples of mafic potassic rocks were prepared as thin sections in Turkey and provided by Fatma Gülmez of Istanbul Technical University, Department of Geological Engineering. Mineralogical classification of each sample was performed using a standard petrographic microscope in conjunction with a camera mount. Rock thin sections were polished to produce a probe-amicable surface and coated in carbon so as to dissipate charge buildup on the surface during probing.

Clinopyroxene compositions were determined using the JEOL JXA-8600 electron microprobe at the University of Georgia Department of Geology in Athens, Georgia following previously established lab methodology. For quantitative elemental analysis the electron beam was focused to a diameter of 1 micrometer, beam current was held at either 15nA or 10nA, and a 15kV accelerating voltage was applied. Wavelength dispersive spectrometers automated with Advanced Microbeam Inc. electronics and Probe for EPMA software recorded X-ray emissions for 10 seconds at peak intensities and five seconds at background intensities above and below the peak. Recorded X-ray intensities were analyzed using Armstrong's (1988) Phi-Rho-Z matrix correction model to calculate element oxide weight percent. Elemental concentrations inferred from X-ray intensities in unknown samples were measured against known concentrations in a suite of natural and synthetic standards during calibration [See Table 2.1 for standards list]. Backscatter electron images were acquired using the ESPRIT Software for EDS software suite from Bruker Corporation.

To ensure instrument calibration was effective mineral standards were treated as unknowns and probed at the end of each calibration. Specifically the Cr-augite standard (Smithsonian Standard: NMNH 164905) was used at the end of each daily calibration of the microprobe prior to the analysis of unknown samples. The analytical precision and accuracy of the microprobe was monitored throughout the project resulting in 77 'unknown' analyses of the Cr augite standard. The average weight percent oxides and the corresponding 2-sigma values from those analyses are found in Table 2.2.

The repeated analysis of the Cr augite standard shows that the precision of the microprobe varies depending on the elemental oxide being measured. SiO_2 displayed a 2-sigma value of less than 1.5 wt%, while all other oxides displayed 2-sigma values less than 0.7 wt%. It is also worth noting that the majority of the fluctuation in the total weight of those analyses can be attributed to fluctuations in the measurements of SiO_2.

Published values for the Cr augite standard are displayed in Table 2.2 along with percent errors between the average 'unknown' analyses of this study and published values. Despite SiO_2 displaying the least precision of the oxides, it appears to be one of the more accurately measured elements, having only a 0.5% error when compared to Cr augite published values. Additionally Fe, Mg, and Na all had percent errors less than 0.7% compared to published values. Cr, Mn, and Ca displayed percent errors ranging between 1.5% and 3.7%. The least accurate elements were Al and Cr (percent errors of 7.3% and 6.4% respectively). That being said the UGA microprobe has consistently given low Al readings. Potassium was consistently below instrument detection levels.

Several computer programs were used in the processing of the data. Photoshop was used to place probe location data onto backscatter images obtained on the microprobe.

Visual examination of backscatter images was vital in determining clinopyroxene growth histories, particularly when looking for visual indicators such as epitaxial banding (complex zoning) and dissolution features. Microsoft Excel was used to generate graphs.

Table 2.1: Element standards used for calibration		
Element	Standard name	Standard ID
Al	Spinel CMT	Spinel C.M. Taylor
Mg	Olivine1 CMT	Olivine 1 C.M. Taylor
K	Orthoclase 10 CMT	MAD-10 C.M. Taylor
Si	Diopside 5A CMT	Diopside 4A C.M. Taylor
Ti	TiO2 CMT	Syn. TiO2 C.M. Taylor
Ca	Sphene CMT	Sphene 1A C.M. Taylor
Mn	Spessartine 4b CMT	Spessartine 4b C.M. Taylor
Fe	Fayalite UofOre	Synthetic Fayalite (U. of Ore OL-11)
Cr	Chromite CA	Caledonian Chromite (USNM 117075)
Na	Abox	Amelia Albite Oxygen Std 131705

Table 2.2) Cr Augite standard analysis results				
Wt% oxide	Average Analysis	2σ	Published Cr Augite oxide Wt%	% Error
SiO_2	50.23	1.49	50.48	0.49
Al_2O_3	7.44	0.34	8.03	7.29
MgO	17.28	0.68	17.32	0.25
FeO	4.70	0.29	4.71	0.22
MnO	0.12	0.15	0.12	3.68
CaO	17.82	0.65	17.3	3.03
K_2O	n.d.	n.d.	0.01	NA
Na_2O	0.83	0.10	0.84	0.67
TiO_2	0.48	0.10	0.51	6.36
Cr_2O_3	0.86	0.27	0.85	1.54
total	99.77	1.59	100.17	

3. RESULTS

This section will present the available field descriptions, petrographic descriptions, and the results of electron microprobe analysis and backscatter image reconnaissance of the samples used in this study.

3.1 Field and Thin Section Descriptions

The purpose of this study is to uncover petrologic relationships and evidence for the style of magmatism in the Late Cretaceous mafic potassic and leucite-bearing igneous rocks found in Turkey's Ankara-Erzincan suture zone. In order to accomplish these goals nine samples from three locations along the suture belt were studied [Figure 3.1]. Photomicrographs of the thin sections accompany each of the following petrographic description. Sample names, field description, and location of each sample are listed in Table 3.1. An overview of the phenocrysts, groundmass minerals, and textures in each sample is in Table 3.2.

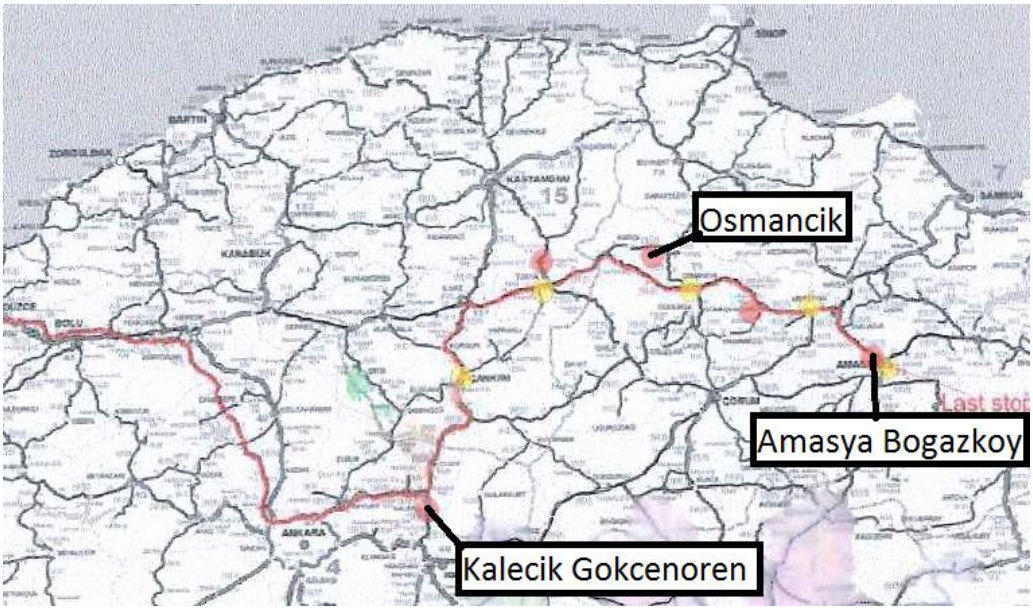

B

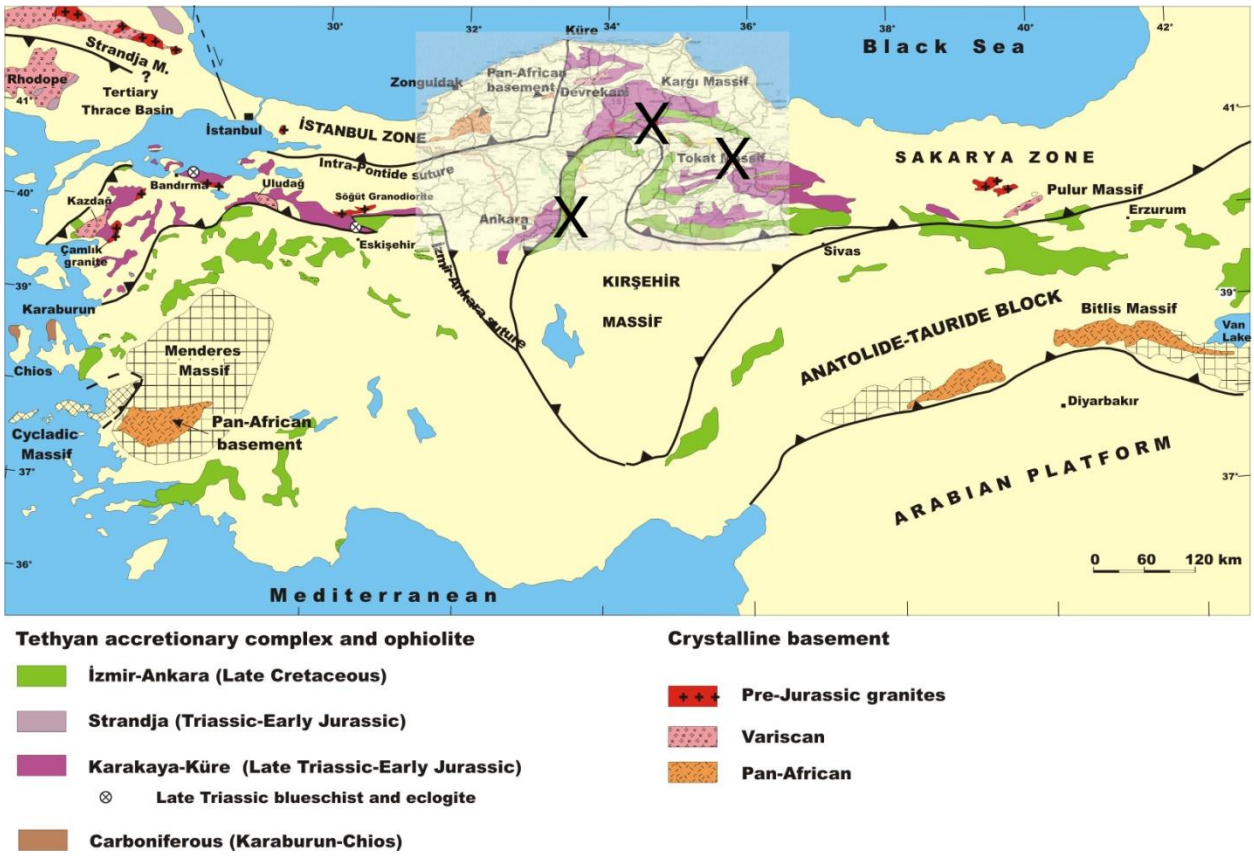

Figure 3.1) Maps showing the general locations of the sample collection sites. A) is a map showing the 3 field areas sampled by F. Gülmez (written communication, Gülmez, 2015) B) an overlay of the first map on a map showing major tectonic features of Anatolia (Okay, 2015)

Table 3.1) Sample Information					
Sample Name		Region	Field Description**	X*	Y*
11-AMS-06		Amasya Bogazkoy	Boulder in epiclastic	733854	4511494
11-KT-34B		Amasya Bogazkoy	Boulder in epiclastic	733097	4512069
11-KT-36D		Amasya Bogazkoy	Dyke	732805	4512295
11-OS-12		Osmancik	Lava flow	636781	4550773
11-OS-33		Osmancik	Stock	637445	4551210
11-OS-42		Osmancik	Stock	635462	4551004
11-KT-02		Kalecik Gokcenoren	Lava flow	540491	4452139
11-KT-03A		Kalecik Gokcenoren	Boulder in epiclastic	542127	4452873
11-KT-04D		Kalecik Gokcenoren	Lava flow	542127	4452873
	*	Geographic Coordinate System: GCS_European_1950 Datum: D_European_1950 ED_1950_UTM_Zone_36N			
	**	Locations and field descriptions provided by F. Gülmez (personal communication, 2015)			

Table 3.2) Sample petrologic information			
Sample Name	Phenocrysts	Groundmass	Texture
11-AMS-06	Cpx, Ol, Mag	Pl, Sa, Bt, Cpx, Mag	glomeropyhric, medium grained
11-KT-34B	Lct, Cpx, Pl, Mag	Cpx, Mag, Lct	glomeropyhric, medium grained
11-KT-36D	Bt, Cpx, Ol, Mag, Ap, Pl	Sa, Bt, Mag, Cpx	glomeropyhric, fine grained
11-OS-12	Cpx, Lct, Ol, Mag	Sa/Pl, Mag, Lct, Cpx	glomeropyhric, medium grained
11-OS-33	Cpx, Lct, Mag	Sa/Pl, Mag, Lct, Cpx	glomeropyhric, medium grained
11-OS-42	Cpx, Lct, Ol, Mag	Cpx, Ol, Mag, Lct	glomeropyhric, medium grained
11-KT-02	Cpx, Bt, Mag, Ol, Ap	Sa, Mag, Cpx	glomeropyhric, fine grained
11-KT-03A	Lct, Cpx, Mag, Ap, Ol, Sa	Cpx, Mag, Lct	glomeropyhric, medium grained
11-KT-04D	Cpx, Bt, Mag, Ap	Mag, Bt, Cpx	glomeropyhric, coarse grained

*Mineral abbreviations are taken from recommendations by the IUGS Subcommission on the Systematics of Metamorphic Rocks: Web version 01.02.07

3.1.1 Amasya Bogazkoy Region

The Amasya Bogazkoy region hosts lamprophyric dikes and leucite-bearing lava flows in relation with volcanoclastic and sedimentary rocks of the Lokman Formation, an Upper Cretaceous sedimentary sequence (2011 study Field Excursion Guide by Genç et al., written communication, 2012, Fatma Gülmez). These units are in close proximity to an ophiolitic mélange and Cretaceous pelagic carbonates (2011 study Field Excursion Guide by Genç et al.). In addition to leucite-bearing basalts and lamprophyres, this region also hosts trachytes (written communication, 2012, Fatma Gülmez).

3.1.1.1 Sample 11-AMS-06

Sample 11-AMS-06 was collected from a boulder in an epiclastic unit in the Lokman Formation. 11-AMS-06 is a melanocratic medium-grained porphyritic rock with a phenocryst assemblage consisting of clinopyroxene (~90%), olivine (~5%), magnetite (~5%), and a groundmass of biotite, albite, sanidine, clinopyroxene, and magnetite. Clinopyroxene phenocrysts are up to 4mm in length, euhedral, frequently twinned, slightly pleochroic, and strongly zoned, containing green cores with alternating clear and green epitaxial bands [See Figure 3.2]. Olivine phenocrysts in this sample have been completely altered to phyosilicates and were up to 2mm in diameter. Magnetite phenocrysts are up to 0.25 mm in diameter. 11-AMS-06 also displays glomeroporphyritic texture with glomerocrysts of clinopyroxene, magnetite, and sometimes olivine.

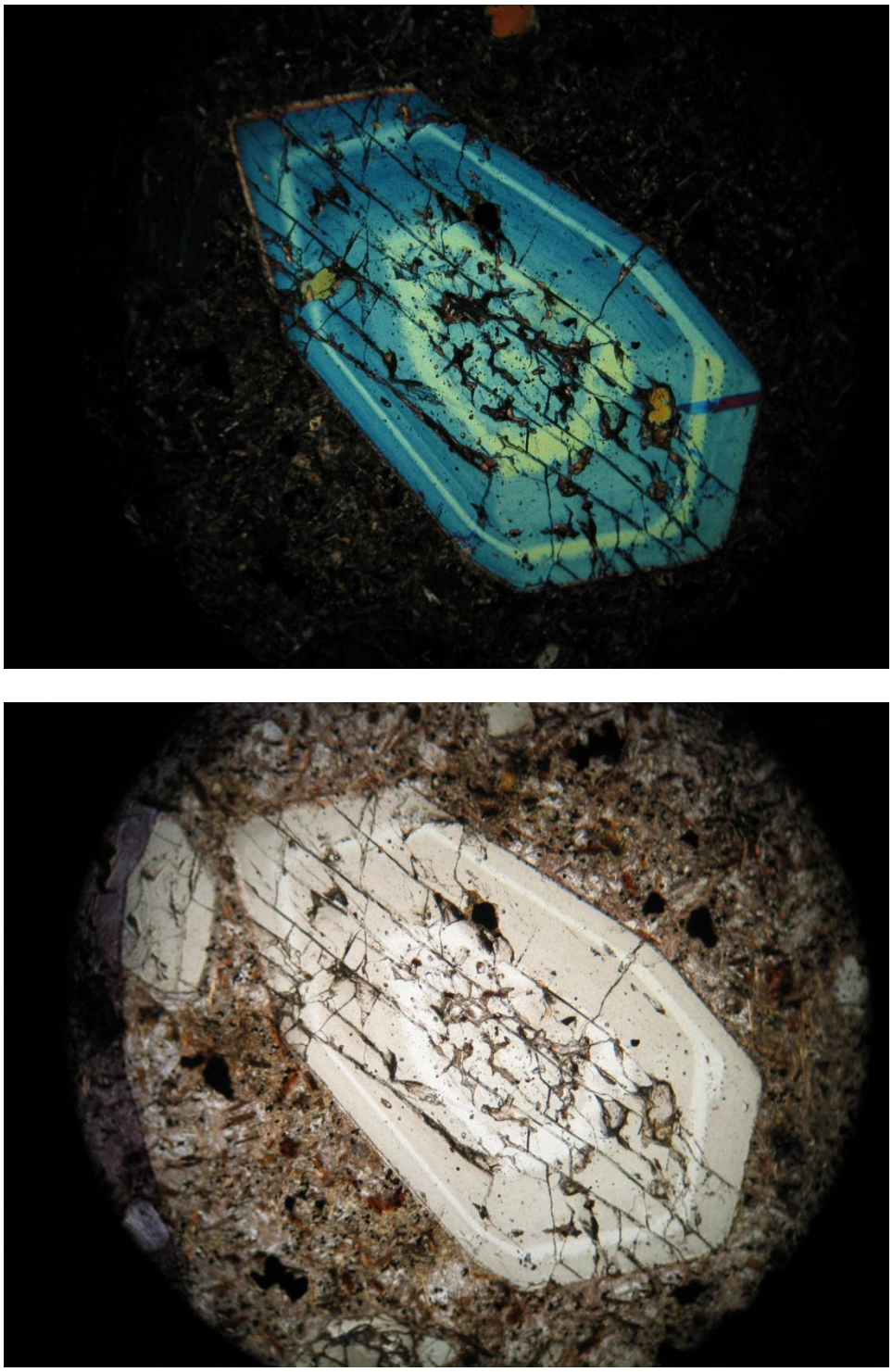

Figure 3.2) Light photomicrographs of 11-AMS-06 Cpx 9. Cross polarized and plane polarized light, field of view is ~5 mm in diameter.

3.1.1.2 Sample 11-KT-34B

11-KT-34B was collected from a boulder in an epiclastic unit and is medium-grained porphyritic. Petrographic analysis reveals a phenocryst assemblage of clinopyroxene (~45%), leucite (~45%), sanidine (~5%), and magnetite (~5%) and a groundmass of magnetite, leucite, and clinopyroxene. Clinopyroxene phenocrysts in 11-KT-34B are up to 3mm in length, euhedral, pleochroic, frequently twinned, and complexly zoned [See Figure 3.3]. The leucite phenocrysts in 11-KT-34B are euhedral and have been completely replaced by analcime. There are infrequent first order gray feldspar laths believed to be sanidine. Magnetite phenocrysts are up to 0.3 mm in diameter. 11-KT-34B contains several vugs filled with analcime or calcite. 11-KT-34B also displays glomerophyric texture with clusters of smaller clinopyroxene and magnetite.

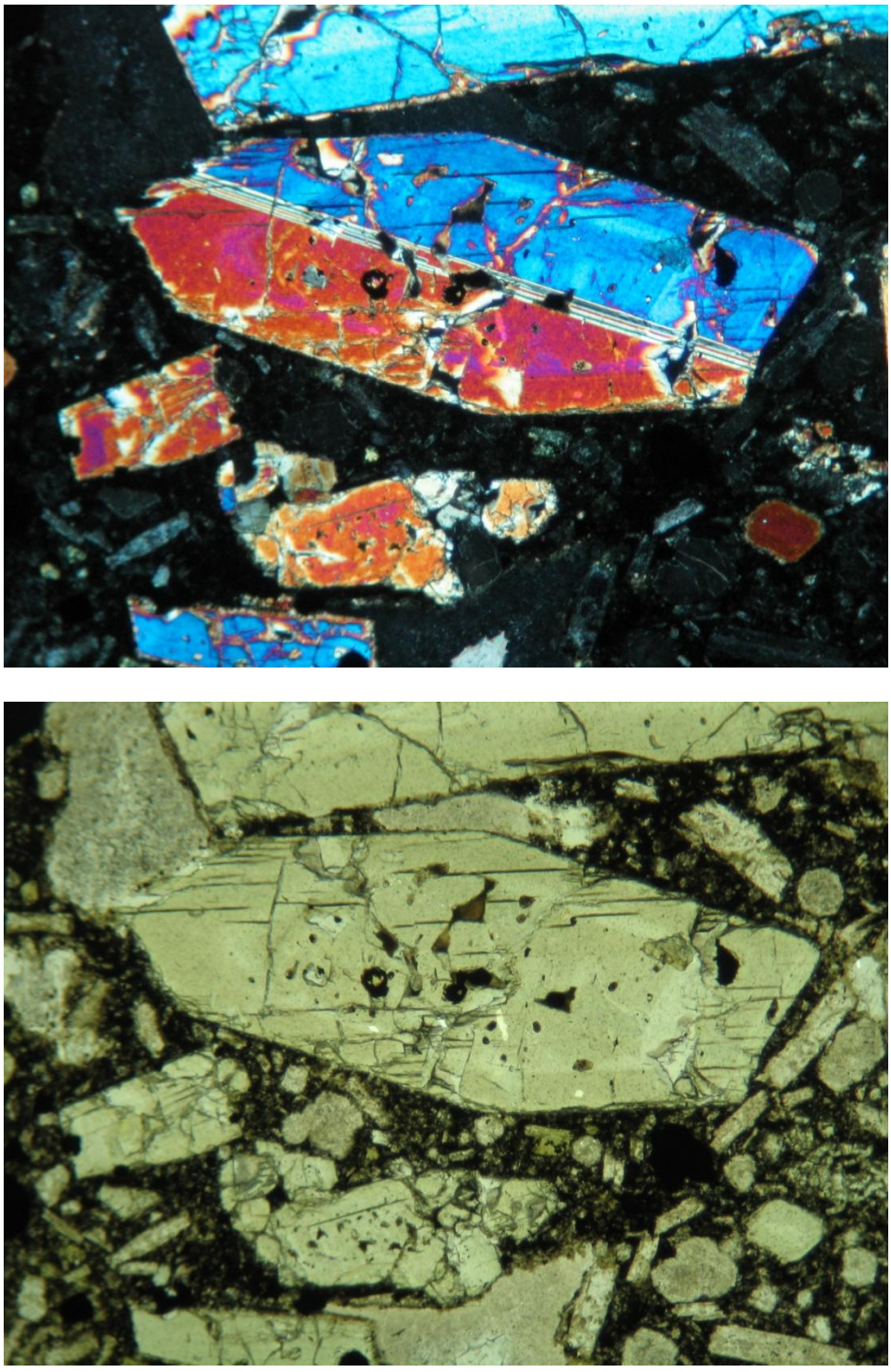

Figure 3.3) Light photomicrographs of 11-KT-34B Cpx 11. Cross-polarized and plane polarized light photomicrographs of a complexly zoned and twined clinopyroxene. Field of view is 2.1 mm in diameter.

3.1.1.3 Sample 11-KT-36D

Sample 11-KT-36D was collected from a dike in the Amasy-Bogazkoy region. It is a melanocratic medium to fine-grained porphyritic rock. Petrographic analysis reveals a phenocryst assemblage of biotite (~45%), clinopyroxene (~40%), magnetite (~10%), olivine (~5%), apatite, minor plagioclase, and possible evidence for minor leucite [See Figure 3.4]. Groundmass minerals include plagioclase and sanidine laths, biotite, magnetite and clinopyroxene. Biotite phenocrysts are highly pleochroic (from clear/light-yellow to dark red brown) and up to 3mm in length. Clinopyroxenes are up to 1mm in length, euhedral, and some have clear cores surrounded by light green mantles. Magnetite phenocrysts are up to 1mm in diameter. Olivine phenocrysts are completely altered to iddingsite. Apatite is frequently included in or adjacent to magnetite. Vugs are filled with clay minerals and calcite. Sample 11-KT-34D displays glomerophyric texture with glomerocrysts of clinopyroxene, magnetite, biotite, and apatite.

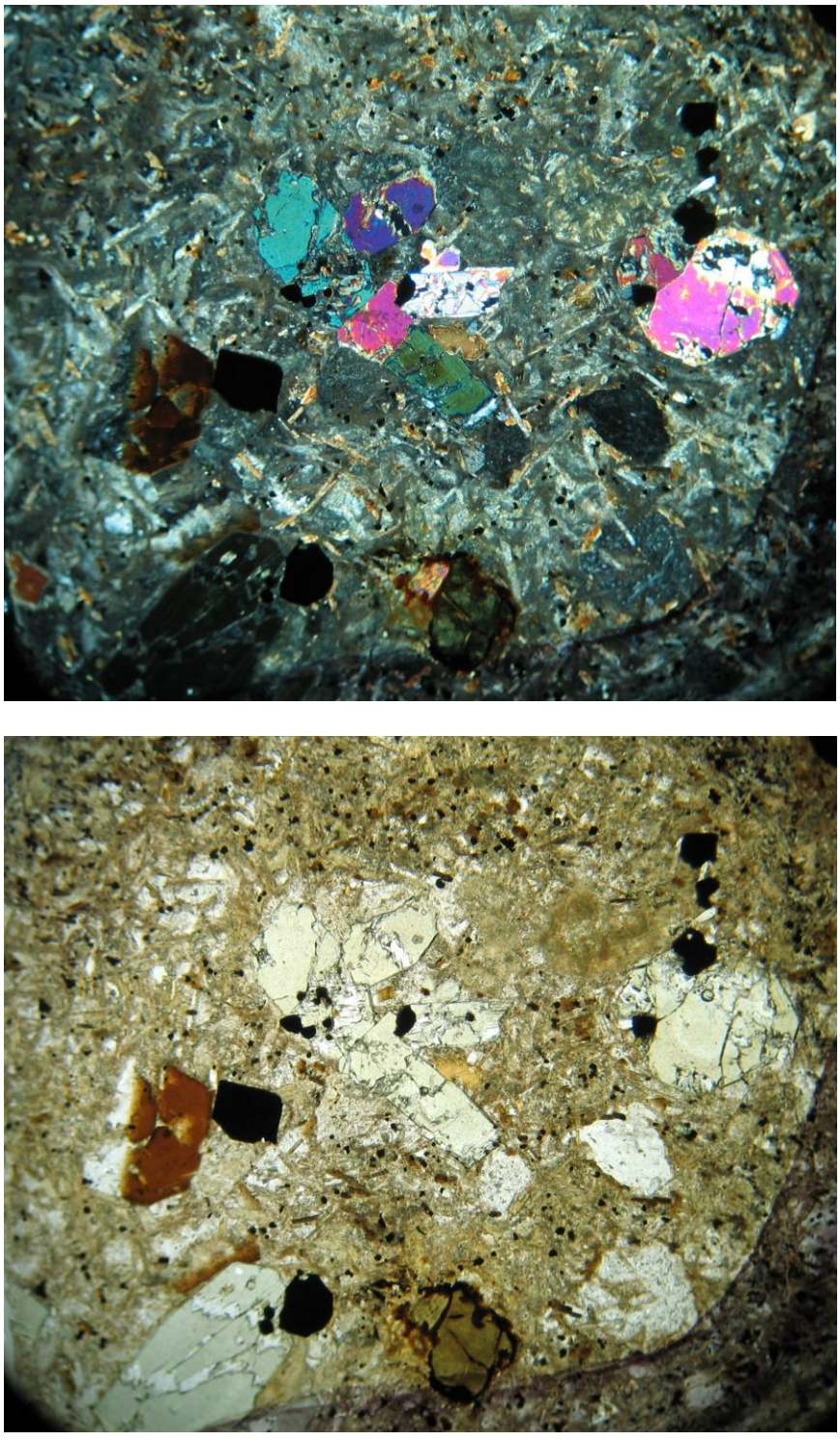

Figure 3.4) Light photomicrographs of phenocrysts from 11-KT-36D. Cross-polarized and plane-polarized light photomicrographs of clinopyroxene, biotite, and magnetite. Note the brown-red biotite phenocryst, the green-brown altered olivine phenocryst near the bottom of the picture, and the feldspar laths restricted to groundmass. Cpx 20 is far right. Field of view is 3.8 mm in diameter.

3.1.2 Osmancik Region

In the Osmancik region the sampled leucite bearing stocks and lava flows are in close spatial and temporal relation to flysch sedimentary sequences and volcanoclastic units (2011 study Field Excursion Guide by Genç et al.). Additionally the field location hosts metamorphic rock units (2011 study Field Excursion Guide by Genç et al.).

3.1.2.1 Sample 11-OS-12

Sample 11-OS-12 was collected from lava flow in the Osmancik region. 11-OS-12 is a melanocratic medium-grained porphyritic rock. Petrographic analysis reveals a phenocryst assemblage of clinopyroxene (~50%), leucite (~30%), olivine (~15%), and magnetite (~5%) with a groundmass assemblage of first order gray laths (sanidine), magnetite, leucite, and clinopyroxene. Clinopyroxene phenocrysts are light green in color, up to 3 mm in diameter, display oscillatory zoning and epitaxial banding (complex zoning), are frequently twinned, and possess common magnetite inclusions. Leucite phenocrysts are up to 2 mm in diameter and are completely replaced by analcime. Olivine phenocrysts are up to 2 mm in diameter and are completely replaced by hematite and calcite. Vugs are filled by analcime and calcite. The sample displays glomerophyric texture with glomerocrysts of clinopyroxene. In one instance a clinopyroxene was mantled by leucite.

3.1.2.2 Sample 11-OS-33

Sample 11-OS-33 is a sample of a stock in the Osmancik region. 11-OS-33 is a melanocratic medium-grained porphyritic rock. Petrographic analysis reveals a phenocryst assemblage of clinopyroxene (~55%), leucite (~40%), and magnetite (~15%) with a

groundmass assemblage magnetite, clinopyroxene, and leucite. Clinopyroxene phenocrysts are up to 2mm in length, occasionally twinned, pleochroic (light yellow to light green), several have light green cores followed by a clear epitaxial band followed by a final green band; green sections display oscillatory zoning. Leucite phenocrysts are up to 1.5 mm in diameter and have been completely replaced by analcime. Clinopyroxene phenocrysts form fairly large glomerocrysts of small phenocrysts; some clusters are over 5mm across and include magnetite.

3.1.2.3 Sample 11-OS-42

Sample 11-OS-42 is from a stock in the Osmancik region. 11-OS-42 is a medium to coarse-grained porphyritic rock. Petrographic analysis reveals a phenocryst assemblage of clinopyroxene (~50%), leucite (~40%), olivine (~5%), and magnetite (~5%) with a groundmass assemblage, clinopyroxene, olivine, leucite, and magnetite. Three clinopyroxene megacrysts were observed in 11-OS-42, the largest being 7mm in diameter, all displayed oscillatory zoning and two had a slight tabular structure. Clinopyroxene phenocrysts are light green, slightly pleochroic (yellow-green to blue-green), occasionally twinned, and occasionally display clear epitaxial bands surrounded by a light green band. Leucite phenocrysts are up to 1.5 mm across and have been completely replaced by analcime. Olivine phenocrysts are at largest 1 mm in diameter and have been completely replaced by iron oxides and clays. 11-OS-42 displays glomerophyric texture with glomerocrysts of medium sized clinopyroxene and small magnetite.

3.1.3 Kalecik Gokcenoren Region

There are two main rock units in the Kalecik study area, an ophiolitic mélange and an Upper Cretaceous volcanic sequence. The Upper Cretaceous sequence includes volcanic rocks interlayered with submarine flysch-like sedimentary rocks, in the Amasya region this sequence also contains marly sediments (Gülmez and Genç, 2015). These rocks are cross cut by hypabyssal dikes that are related to the aforementioned volcanic rocks. The stratigraphic relationship between volcanic and the sedimentary rocks shows that the volcanism occurred in a marine environment (written communication, 2012, Fatma Gülmez). The majority of these volcanic rocks are of andesitic composition with minor amounts of leucite-bearing lavas, usually in the form of lava flows and autobreccia lava flows (written communication, 2012, Fatma Gülmez). Hypabyssal rocks are mainly lamprophyres.

3.1.3.1 Sample 11-KT-02

Sample 11-KT-02 was collected from a lava flow in the Kalecik Gokcenoren Region. 11-KT-02 is a melanocratic fine-grained porphyritic rock. Petrographic analysis reveals a phenocryst assemblage of clinopyroxene (~45%), biotite (~30%), magnetite (~20%), and olivine (5%) and a groundmass assemblage of plagioclase and sanidine laths, magnetite, clinopyroxene, and apatite. Clinopyroxene phenocrysts are light green, display slight pleochroism (green yellow to green blue), occasionally twinned, euhedral, elongate, at most 1 mm in length, most are under 0.2 mm, and display little complex zoning. Biotite phenocrysts are strongly pleochroic from golden yellow to dark red brown and are at most 0.75 mm in diameter. Olivine phenocrysts have been altered completely to iddingsite. Vugs

are filled with analcime, calcite, and clay minerals. 11-KT-02 displays glomerophyric texture with many small clusters of fine-grained clinopyroxene and magnetite.

3.1.3.2 Sample 11-KT-03A

11-KT-03A was collected from a boulder in an epiclastic unit in the Kalecik-Gorcenoren Village field area. The sample is a melanocratic medium-grained porphyritic rock. Petrographic analysis reveals a phenocryst assemblage of clinopyroxene (~45%), leucite (~40%), magnetite (~15%), and apatite with a groundmass assemblage of magnetite, clinopyroxene, and leucite. There are only rare sanidine phenocrysts in the thin section of 11-KT-03A. Clinopyroxene phenocrysts are strongly zoned with light green cores and dark green bands; the darker bands are strongly pleochroic (green-blue to green-yellow) [See Figure 3.5]. A few clinopyroxenes are twinned, and the largest is 2 mm in diameter. Clinopyroxene phenocrysts in glomerocrysts display little to weak epitaxial banding and are frequently sector zoned. Leucite phenocrysts have been completely replaced by analcime and are at most 2 mm in diameter. 11-KT-03A displays glomerophyric texture with clusters of clinopyroxene and magnetite. Vugs are filled with analcime and calcite.

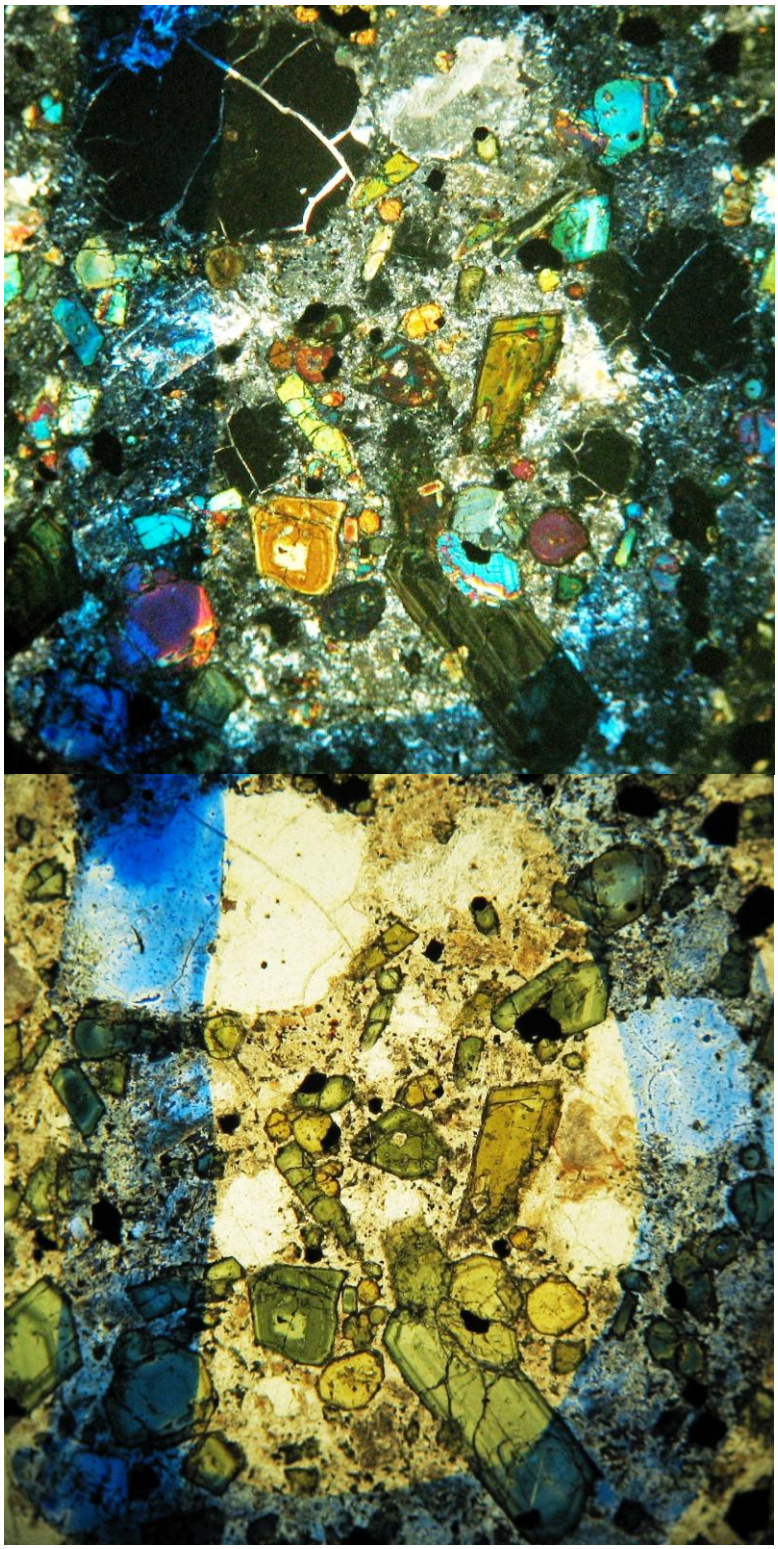

Figure 3.5) Light photomicrographs of phenocrysts from 11-KT-03A. Cross-polarized and plane-polarized light photomicrographs of complexly zoned clinopyroxenes, showing the range of pleochroic colors in the green bands. Note the large leucite phenocrysts. Field of view is 3.4 mm in diameter.

3.1.3.3 Sample 11-KT-04D

11-KT-04D was collected from a lava flow in the Kalecik-Gokcenoren Village field area. It is a melanocratic coarse to medium-grained porphyritic rock. Petrographic analysis reveals a phenocryst assemblage of clinopyroxene (~50%), biotite (~45%), magnetite (~5%), and apatite with a groundmass assemblage of magnetite, clinopyroxene, and biotite. Clinopyroxene phenocrysts display large clear cores and thick green epitaxial bands; these bands exhibit oscillatory zoning. [See Figure 3.6] The largest clinopyroxenes are 4 mm in diameter. Some clinopyroxenes include multiple magnetite crystals and others are twinned. Biotite is heavily altered however some of the original basal cleavage is preserved by the alteration minerals. Additionally the altered 'phenocrysts' have rims of oxides and rounded corners further supporting the interpretation that the original mineral was biotite. Biotite frequently includes smaller clinopyroxenes. 11-KT-04D displays glomerophyric texture with glomerocrysts of clinopyroxene and magnetite. There was a single fine-grained clinopyroxene, magnetite, and apatite enclave. Vugs have been filled with analcime, clays, and calcite.

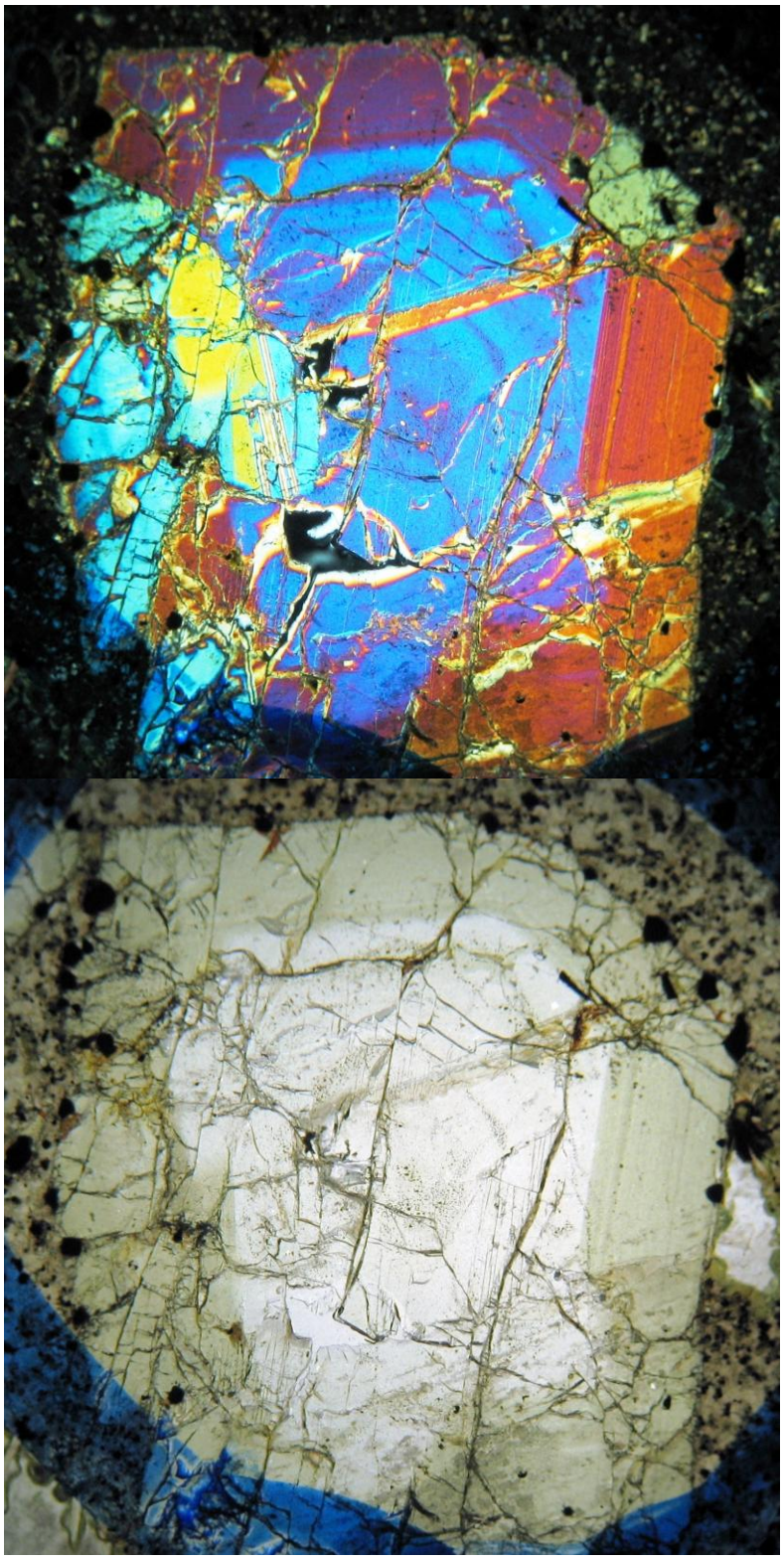

Figure 3.6) Light photomicrographs of 11-KT-04D Cpx 5. Cross-polarized and plane-polarized light photomicrographs showing the diopside clear core and green salite epitaxial band. Field of view is 3.6 mm in diameter.

3.2 Clinopyroxene Microprobe Analysis Results

Electron microprobe analyses of the clinopyroxenes of this study were conducted on a JEOL 8600 Electron Microprobe to determine chemical composition of the phenocrysts and from that determine the nature of compositional zoning. The overarching goal was to determine the petrogenetic origins and modifying petrogenetic processes that each crystal recorded. Over the course of this study the oxide concentrations of 91 clinopyroxene phenocrysts in 9 rock samples were determined. Oxides measured include SiO_2, Al_2O_3, MgO, FeO, MnO, CaO, Na_2O, TiO_2, and Cr_2O_3. These oxide abundances were then converted into cation units following Deer Howie and Zussman (DHZ, 1985). Using cation units it is possible to calculate the oxidation state of iron in each pyroxene. Iron can exist in two oxidation states in pyroxenes and because the electron microprobe cannot distinguish between the different valence states of iron it is necessary to calculate the cation proportions of Fe^{2+} and Fe^{3+} from FeO. A reliable method for accomplishing this involves normalizing the pyroxene analyses to four cations and following Morimoto et al., (1988) regarding site assignments. Upon normalizing to four cations any positive charge deficit generated by the summation of the cations must be made up by assuming that a portion of the calculated iron cations is in the +3 valence state instead of the normal +2 valence state. This method relies on very accurate microprobe analysis (Dexter Perkins, personal communication) and has no self-checking mechanism like the method of normalizing to 6 oxygen anions as outlined in DHZ (1985). The DHZ method does not account for multiple iron oxidation states and instead assumes all iron is +2. Interestingly, when the DHZ method was applied to clinopyroxenes of this study the cation totals were, for the most part, high (ranging up to 4.1). This result can be attributed to the relatively large Fe^{3+}/Fe^{2+}

values of these samples which when the DHZ method is followed results in high cation totals due to the use of an estimate of oxygen anions that is too low.

Why these magmas have such high Fe^{3+}/Fe^{2+} values is an interesting question. As will be show in the tables of this section, many of the clinopyroxenes are sub-silicic (Si cation < 1.75 in formula) creating the need for $Al^{3+}$and Fe^{3+} to fill the tetrahedral site (normally Si^{4+}.) This substitution causes a charge deficiency, which requires iron substitution in the M1 structure site as a Fe^{3+} to maintain charge neutrality. That said, the cause effect relationship between the lack of silica and the presence Fe^{3+} could be reversed. This substitution is called a type 3 coupled substitution (Morimoto et al., 1988). More importantly, the high Fe^{3+}/Fe^{2+} values indicate that these magmas were highly oxidized.

Magnesium number was originally calculated utilizing cation units and the formula $Mg\# = 100*(Mg/(Mg+Fe^{2+})$ in an effort to judge the degree of magmatic evolution. However, as noted these clinopyroxenes are sub-silicic and possibly came from highly oxidized magmas resulting in high Fe^{3+} abundances. Thus using only Fe^{2+} is problematic, because not all the iron will be included in the Mg# calculation and the magma will appear to be closer to a primitive composition than it is. [See Table 3.3 for example] A potential solution to this problem is to utilize all iron in the clinopyroxene via the formula: $Mg\#^* = 100*Mg/(Mg+Fe_{total})$ to determine degree of relative evolution. The calculated error for Mg#* is ±3.5%, representing analytical precision at 2σ.

O'Brien et al. (1988) outlined an alternative method of expressing relative magma evolution in their study of similar mafic potassic igneous rocks in the Highwood Mountains of Montana. His method utilized a ***cation index*** (DS) to discriminate clinopyroxene compositions. The DS cation index is the sum of cation species that are concentrated in

diopside relative to salite minus the sum of the cation species that are more concentrated in salite relative to diopside; therefore the formula in cation units is DS=(Si+Cr+Mg+Ca)-(Ti+Al+Fe+Mn+Na) (O'Brien et al., 1988). 'Salite' was originally defined by Poldervaart and Hess (1951) as a clinopyroxene with components: Wo = 45 to 50, En= 90 to 50, and the remainder Fs; salite was later re-classified by Morimoto et al. 1988 as 'ferrian or ferroan diopside'. The significance of the DS cation index is that it is another measure, alongside Mg#, of how evolved a given clinopyroxene composition is. Both Mg# and the DS cation index decrease as the magma becomes more evolved; a perfect diopside would produce a DS value of 4.0 while a perfect hedenbergite would produce a DS value of 2.0. In light of substitutions like Al and Na for Si and Ca cations DS values could be even lower. An advantage to this index is that it relies on several cation species as opposed to just Mg and Fe^{2+}, thus it is not as greatly affected by high Fe^{3+} compared to Mg#. The calculated error for the DS cation index is ±0.05, representing analytical precision at 2σ.

Growth bands or epitaxial bands are the planar sections of chemically distinct mantles or coatings of a phenocryst as earlier stated. These bands are typically optically and chemically distinct from other portions of the phenocryst and display sharp contacts on their inner and outer surfaces (O'Brien et al., 1988). These contacts frequently display a non-linear shape indicating that the inner (preexisting) part of the crystal was eroded prior to the deposition of the outer adjacent epitaxial band. This pattern is most easily identifiable with dissolution surfaces on the outer edges of Fe-rich bands followed by an abrupt change to Mg-rich compositions. Fe-rich bands are commonly green in plane polarized light and correspond to the bright bands on the backscatter electron images (BSE) in the following section whereas optically clear bands correspond to Mg-rich bands

that are darker on BSE. Thus bright areas in BSE reflect relatively high total Fe, low Mg#* values and low DS cation index values. Conversely, the relatively dark bands in BSE reflect relatively low total Fe, high Mg#* values and high DS cation index values.

As I discuss clinopyroxenes, I will consistently describe composition variations starting with the grain core or center and proceeding outwards towards the outer rim of the grain. Additionally I will abbreviate 'clinopyroxene' to 'Cpx' and add an identifying number when discussing individual phenocrysts. A summary of the behaviors of clinopyroxene compositions seen in the samples is provided in section 4.1.

3.2.1 Amasya Bogazkoy Region

The three samples from the Amasya Bogazkoy region (11-AMS-06, 11-KT-34B, 11-KT-36D) host populations of clinopyroxenes that display varying ranges of compositional zonation. The sample with phenocrystal biotite and groundmass biotite and feldspar (11-KT-36D) has clinopyroxene phenocrysts with minor compositional zonation compared to the sample with groundmass biotite and groundmass feldspars (11-AMS-06), which has clinopyroxene phenocrysts with moderate compositional zoning. Sample (11-KT-34B) with phenocrysts of leucite and feldspars hosts clinopyroxenes with the most extreme compositional zoning.

3.2.1.1 Sample 11-AMS-06

Eight clinopyroxene phenocrysts from this sample (a diopside olivine madupitic lamprophyre) were analyzed. All pyroxenes and epitaxial bands plot in the diopside field on the pyroxene quadrilateral as defined by Morimoto et al. (1988) [Figure 3.7]. In BSE images darker bands display higher Mg, Si, Ca, and Cr cation totals while lighter bands display higher Fe, Al, Mn, Na, and Ti cation totals. Tables presenting the electron microprobe data for select clinopyroxenes of this sample can be found in Appendix A.

Clinopyroxenes in 11-AMS-06 have a range of characteristics, with the majority displaying thick Fe-rich diopside (salite) epitaxial bands and cores intermittently punctuated by smaller Mg-rich diopside bands. The number of Mg-rich bands contained in each crystal is not consistent throughout the thin section. Two crystals (Cpx 7 and Cpx unk1) display no Mg-rich bands which is interesting considering their size; Cpx 7 has a diameter of 2200 μm and Cpx unk1 has a diameter of 1400 μm [Figure 3.8]. This lack of strong zoning is obvious on chemical variation diagrams [Figure 3.9]. Other crystals (Cpx 11 and Cpx 15) display an Fe-rich resorbed core surrounded by a Mg-rich band (which also displays dissolution features) and then an Fe-rich band [Figure 3.10]. Chemical variation diagrams show relatively high Mg#*, DS cation indices, and Ca cation totals and low Al and Ti cation totals in the Mg-rich band [Figure 3.11]. The remaining analyzed clinopyroxenes in 11-AMS-06 (Cpx 1, Cpx 8, Cpx 9, Cpx 12, and Cpx18) have two Mg-rich bands separated by Fe-rich diopside (salite) of similar composition to the resorbed Fe-rich core of the crystal [Figure 3.12]. All contacts between bands display resorption features. In some phenocrysts the Mg-rich bands are thick and well preserved (such as Cpx 9, Figure 3.12A) in other crystals the Mg-rich bands have been eroded to the point of vanishing (Cpx 1,

Figure 3.12B). Despite this complexity, these Mg-rich bands are frequently similar to one another in composition both within single grains and to Mg-rich bands in other clinopyroxenes [See Table 3.3 and Figure 3.13]. Figure 3.14 shows the range of chemical variation in clinopyroxenes analyzed in this sample; all phenocrysts share a similar more-evolved salite signature typified by Cpx 7 and to a lesser degree Cpx unk1. The greater range of compositions displayed by other clinopyroxenes (Figure 3.14) is derived from the presence of one or more Mg-rich bands.

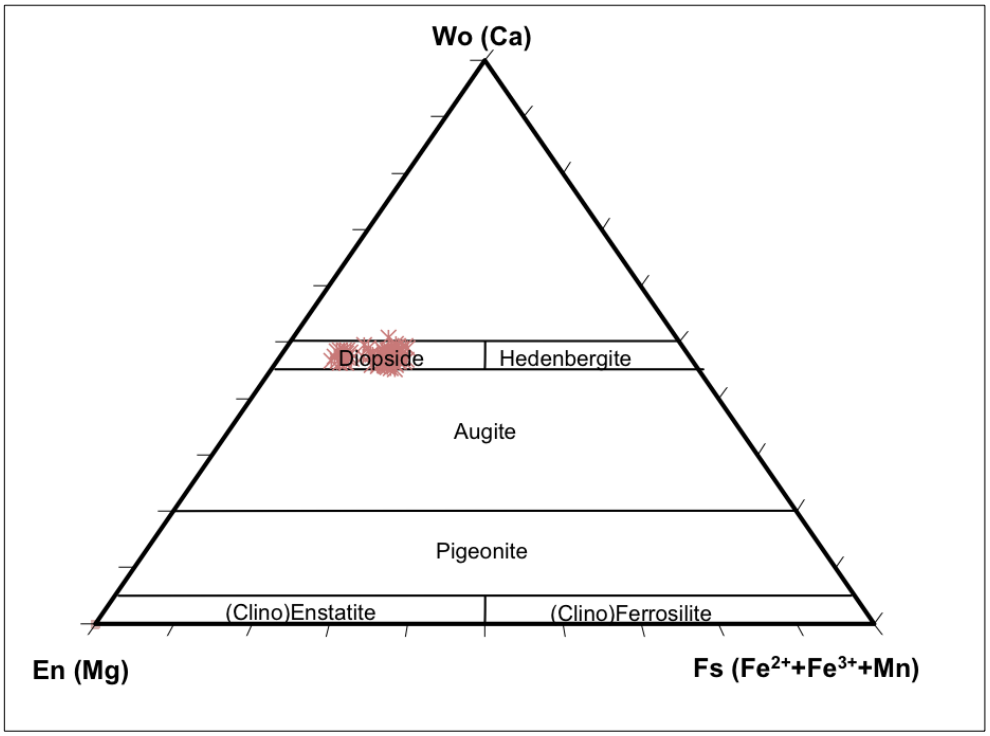

Figure 3.7) Clinopyroxene analyses obtained for 11-AMS-06 plotted in the pyroxene quadrilateral based on Morimoto et al. (1988).

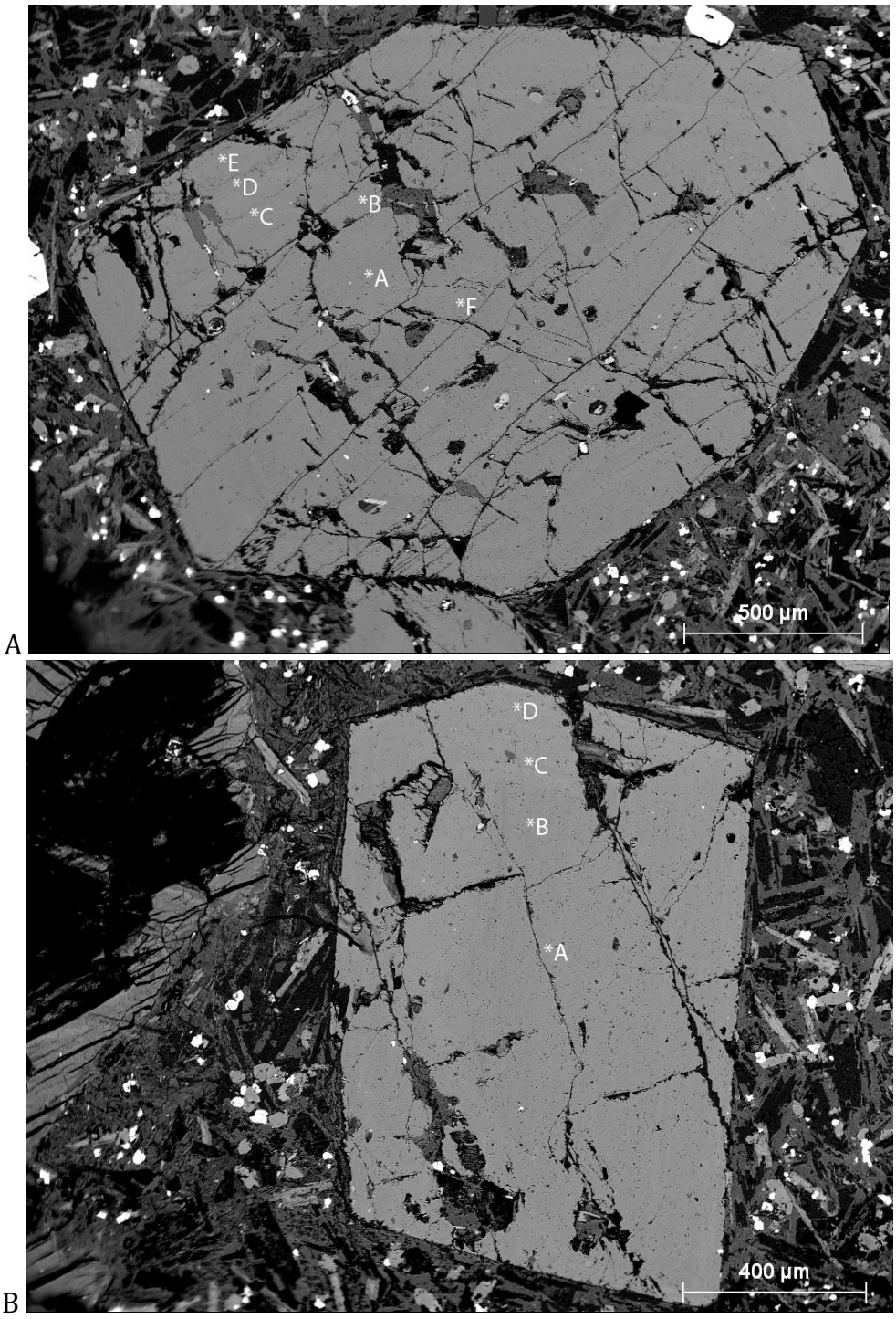

Figure 3.8) BSE images of 11-AMS-06: Cpx 7 and Cpx Unk1. Images of clinopyroxenes lacking Mg-rich bands, A) Cpx 7, B) Cpx unk1, Microprobe analysis points indicated by center of asterisk next to letters, individual analyses are presented in Appendix A.

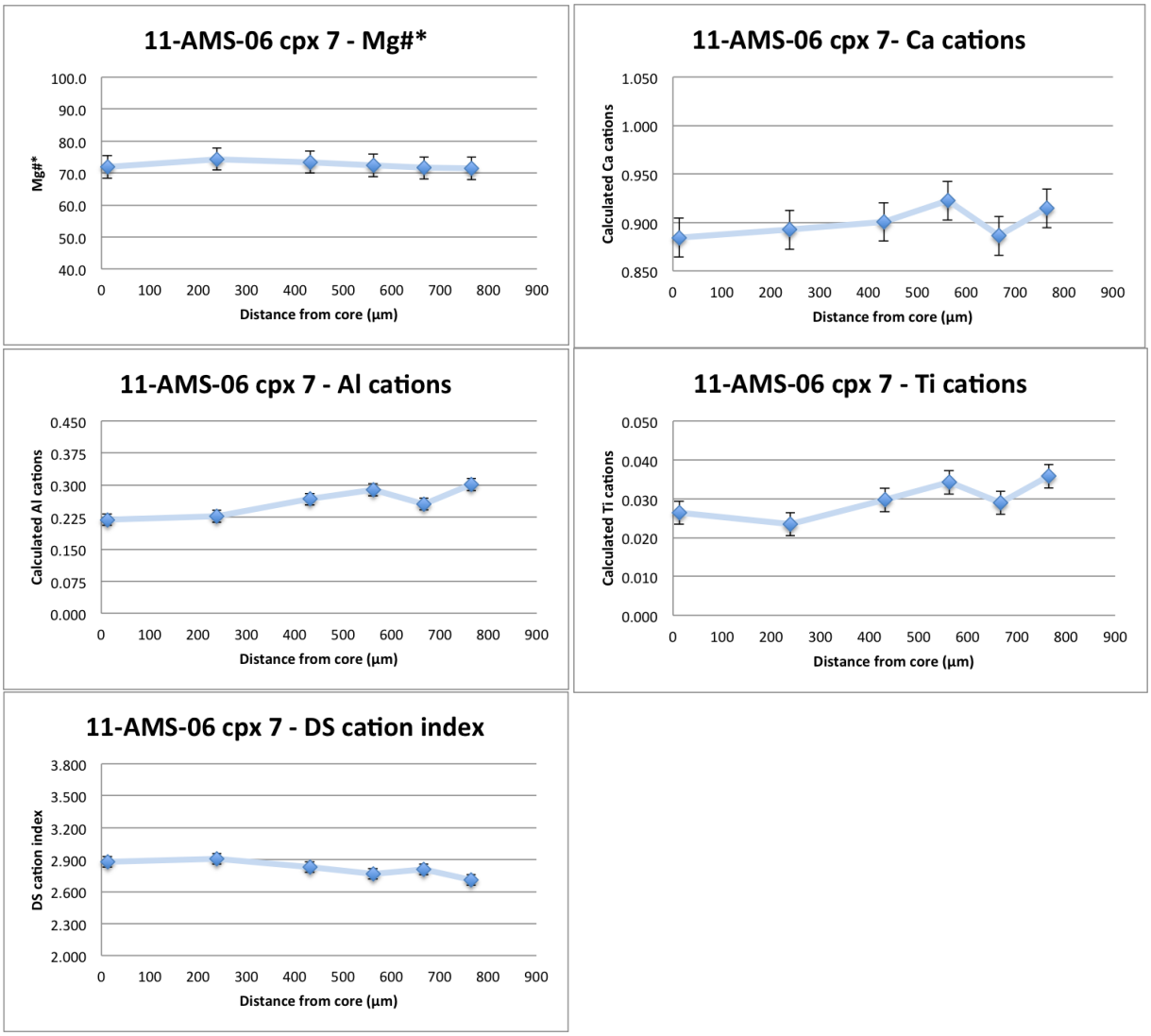

Figure 3.9) Chemical variation plots for 11-AMS-06 Cpx 7. The lack of dark bands on backscatter image in Figure 3.7 is displayed here as relatively flat lines on the Mg#* and DS cation index plots and the Ti and Al cation plots.

A

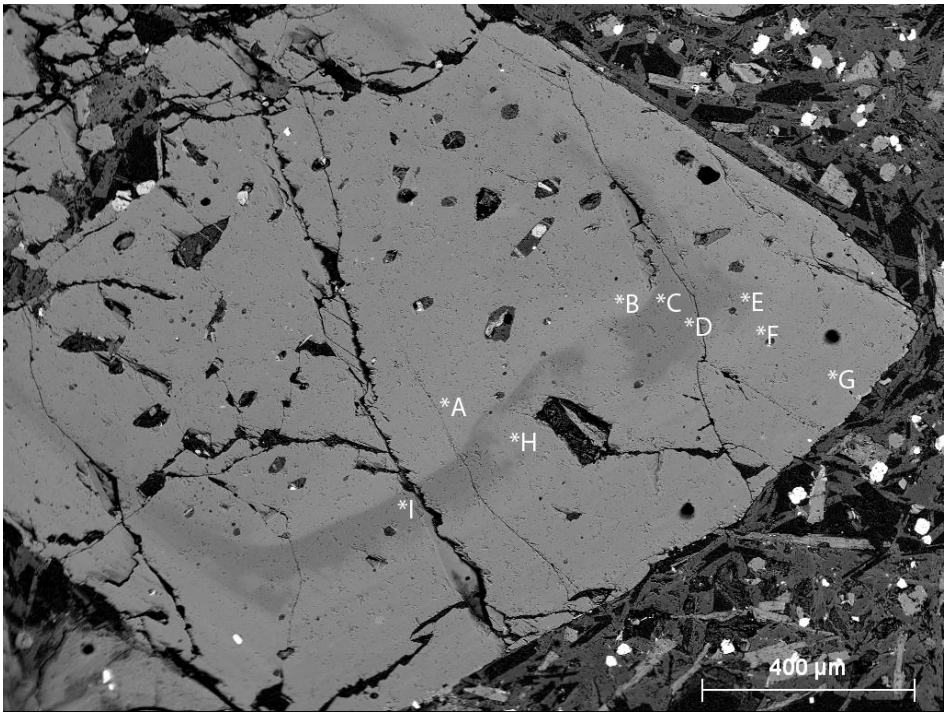

B

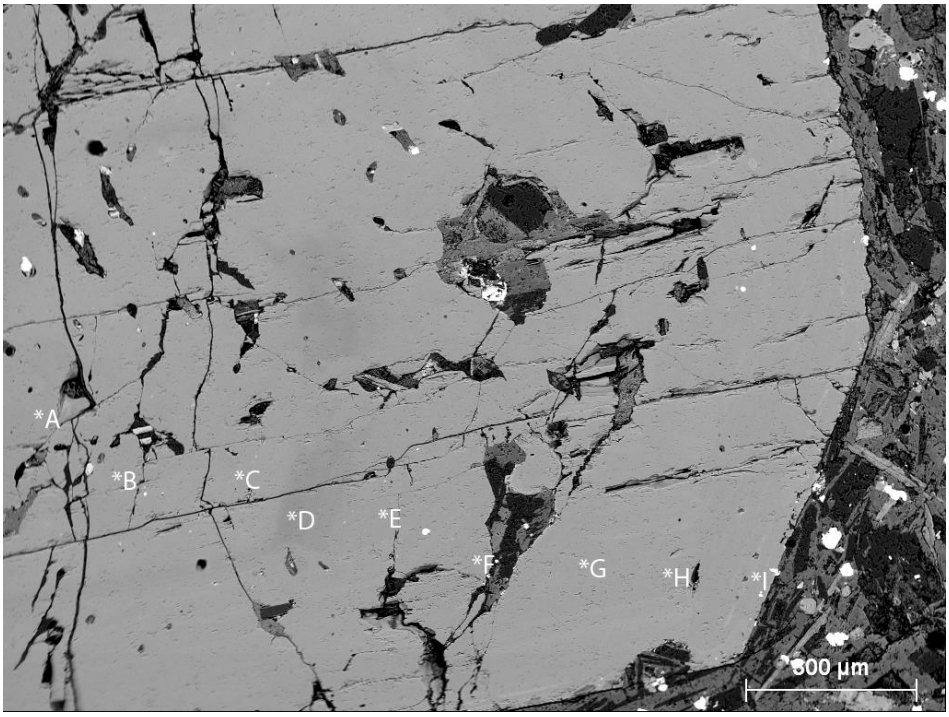

Figure 3.10) BSE images of 11-AMS-06 Cpx 11 and Cpx 15. Images of clinopyroxenes showing a single Mg-rich band, A) Cpx 11, B) Cpx 15. Microprobe analysis points indicated by center of asterisk next to letters, individual analyses are presented in Appendix A.

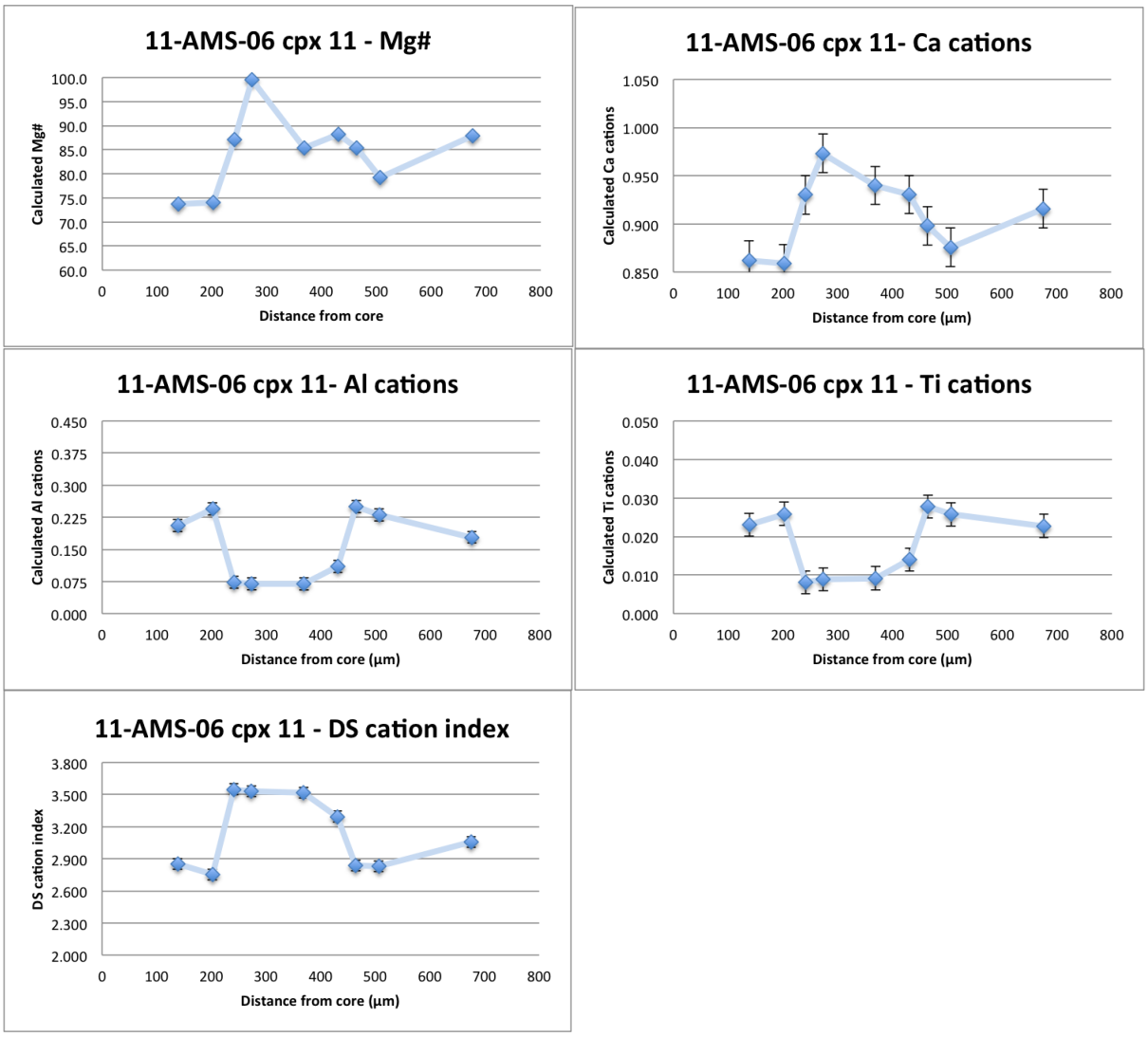

Figure 3.11) Chemical variation plots for 11-AMS-06 Cpx 11. Dark bands on backscatter image in Figure 3.4 are seen as positive plateaus on the Mg#* plot and the DS cation index plot and negative plateaus on the Ti and Al cation plots.

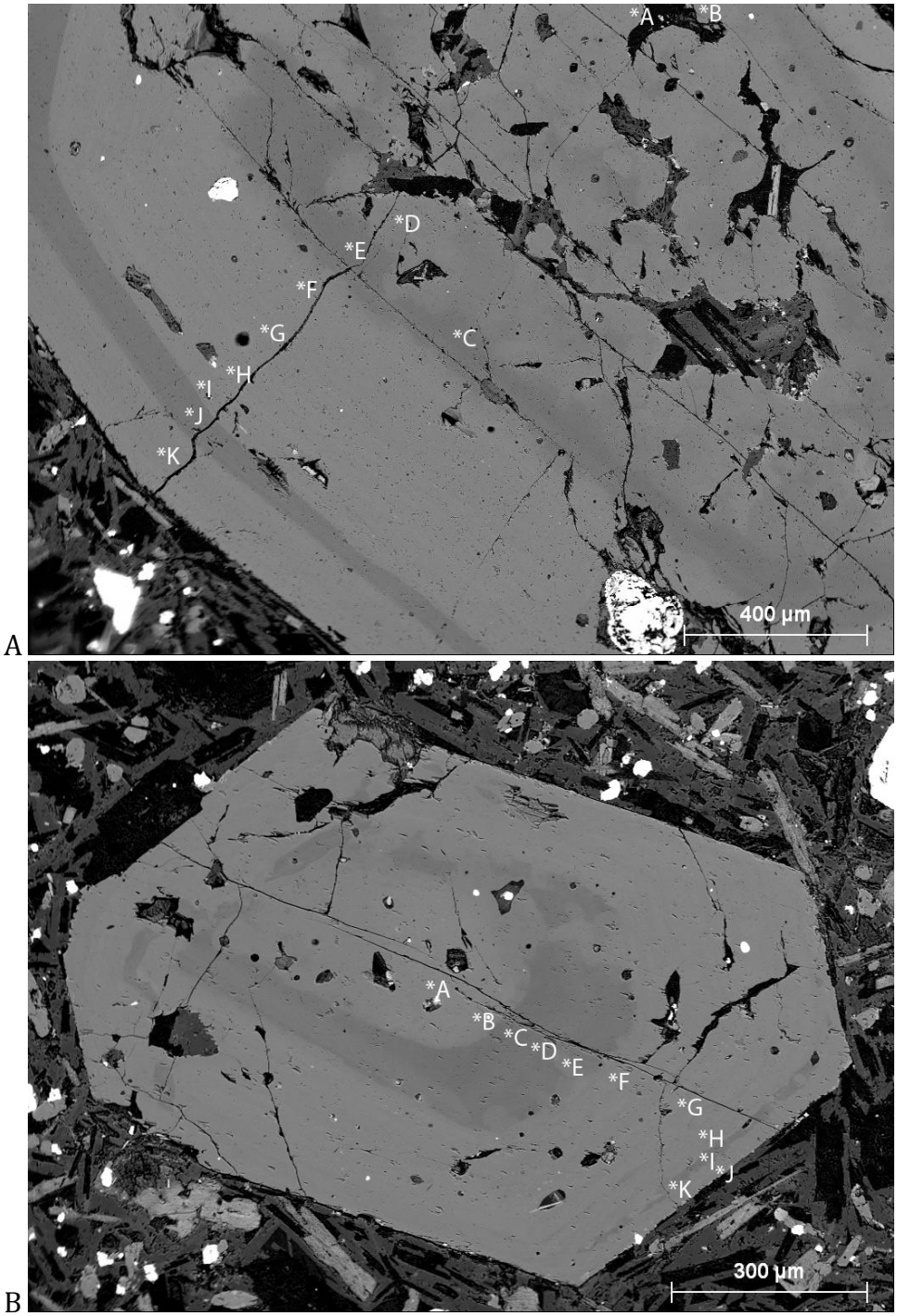

Figure 3.12) BSE images of 11-AMS-06 Cpx 9 and Cpx 1. Images of clinopyroxenes with two Mg-rich bands. A) Cpx 9, B) Cpx 1, Microprobe analysis points indicated by center of asterisk next to letters, individual analyses for Cpx 1 are presented in Table 3.3 and in Appendix A for Cpx 9.

Table 3.3) Representative clinopyroxene analysis of 11-AMS-06							
sample	11-AMS-06						
Cpx #	Cpx 1						
probe site	a	b	c	d	e	f	g
	Wt% oxide						
SiO_2	49.80	49.64	52.11	52.21	49.13	48.50	48.42
Al_2O_3	4.10	3.90	1.35	1.78	3.93	4.61	4.85
MgO	13.13	13.76	16.46	15.82	14.13	13.66	13.37
FeO	8.97	8.51	4.80	5.37	7.15	8.06	8.24
MnO	0.28	0.28	0.16	0.13	0.09	0.18	0.25
CaO	22.02	22.19	23.44	23.57	23.29	22.55	22.70
Na_2O	0.43	0.43	0.20	0.20	0.32	0.30	0.34
TiO_2	0.71	0.86	0.27	0.36	0.59	0.93	1.06
Cr_2O_3	n.d.	0.10	0.28	0.14	0.22	n.d.	n.d.
TOTAL	99.43	99.65	99.06	99.58	98.85	98.77	99.22
	Number of cations in formula						
Si	1.864	1.848	1.925	1.924	1.835	1.820	1.811
Al	0.181	0.171	0.059	0.077	0.173	0.204	0.214
Mg	0.732	0.764	0.906	0.869	0.787	0.764	0.745
Fe^{2+}	0.198	0.153	0.065	0.101	0.083	0.126	0.128
Fe^{3+}	0.083	0.112	0.083	0.065	0.140	0.127	0.130
Mn	0.009	0.009	0.005	0.004	0.003	0.006	0.008
Ca	0.883	0.885	0.927	0.931	0.932	0.906	0.910
Na	0.031	0.031	0.014	0.015	0.023	0.022	0.025
Ti	0.020	0.024	0.007	0.010	0.016	0.026	0.030
Cr	n.d.	0.003	0.008	0.004	0.006	n.d.	n.d.
TOTAL	4.000	4.000	4.000	4.000	4.000	4.000	4.000
$Mg/(Mg+Fe^{+2})*100$	78.7	83.3	93.3	89.6	90.4	85.8	85.3
$Mg/(Mg+Fe_{total})*100$	72.3	74.2	85.9	84.0	77.9	75.1	74.3
Cation Index DS	2.958	3.000	3.533	3.457	3.122	2.980	2.932
Wo	46.3	46.0	46.7	47.2	47.9	47.0	47.4
En	38.5	39.7	45.6	44.1	40.5	39.6	38.8
Fs	15.2	14.2	7.7	8.6	11.6	13.4	13.8

Table 3.3 *continued*				
sample	11-AMS-06			
Cpx #	Cpx 1			
probe site	h	i	j	k
	Wt% oxide			
SiO_2	48.69	51.34	47.09	51.44
Al_2O_3	4.63	2.10	5.82	2.13
MgO	13.56	16.29	13.00	16.21
FeO	7.74	5.17	8.18	5.39
MnO	0.14	0.11	0.28	0.19
CaO	22.66	23.09	22.96	23.42
Na_2O	0.34	0.16	0.28	0.21
TiO_2	0.93	0.41	1.23	0.41
Cr_2O_3	n.d.	0.25	n.d.	0.14
TOTAL	98.69	98.91	98.84	99.53
	Number of cations in formula			
Si	1.827	1.900	1.769	1.893
Al	0.205	0.092	0.258	0.092
Mg	0.759	0.899	0.728	0.889
Fe^{2+}	0.129	0.071	0.102	0.056
Fe^{3+}	0.113	0.089	0.155	0.110
Mn	0.004	0.003	0.009	0.006
Ca	0.911	0.916	0.924	0.923
Na	0.025	0.012	0.020	0.015
Ti	0.026	0.011	0.035	0.011
Cr	n.d.	0.007	n.d.	0.004
TOTAL	4.000	4.000	4.000	4.000
$Mg/(Mg+Fe^{+2})*100$	85.4	92.7	87.7	94.1
$Mg/(Mg+Fe_{total})*100$	75.7	84.9	73.9	84.3
Cation Index DS	2.994	3.444	2.842	3.419
Wo	47.5	46.3	48.2	46.5
En	39.6	45.4	38.0	44.8
Fs	12.9	8.3	13.9	8.6

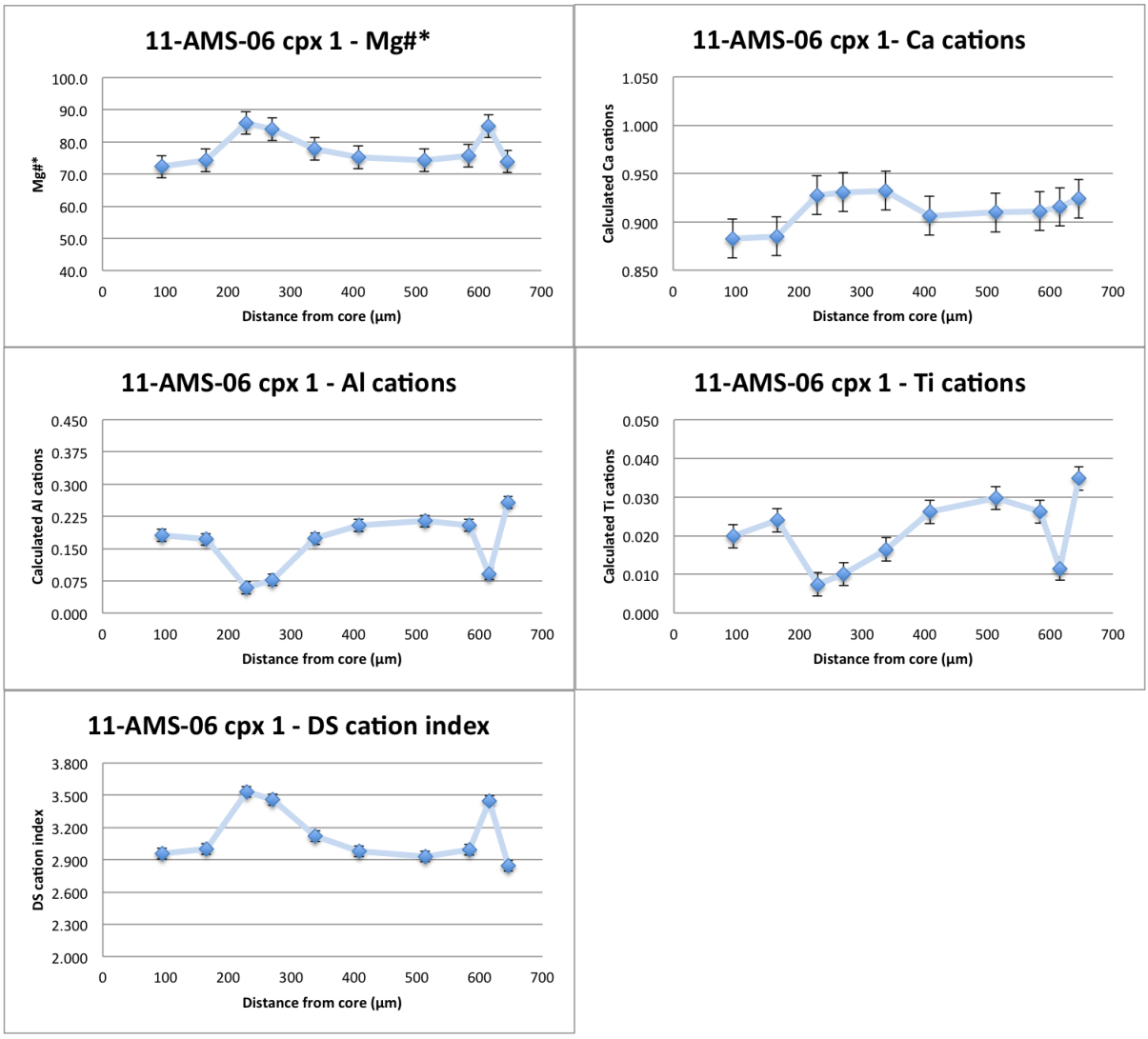

Figure 3.13) Chemical variation plots for 11-AMS-06, Cpx 1. Dark bands on backscatter image in Figure 3.12B are seen as positive spikes on both the Mg#* plot and the DS cation index plot and negative spikes on both the Ti and Al cation plots.

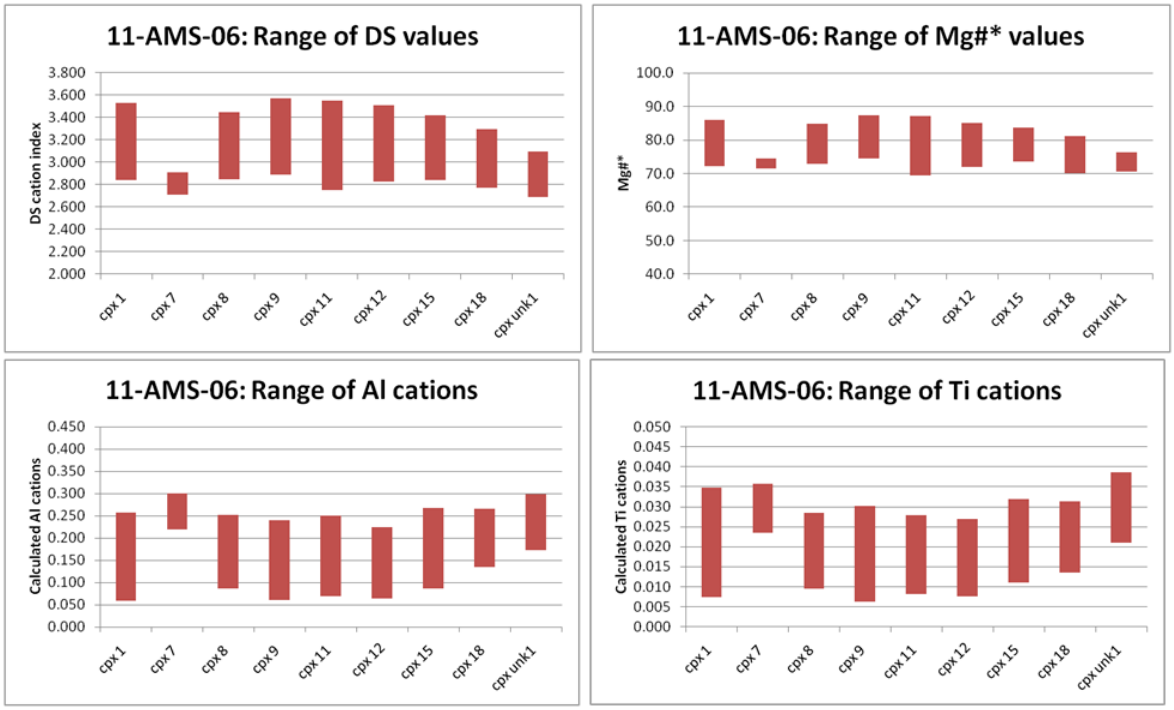

Figure 3.14) Chemical range plots of all clinopyroxene in 11-AMS-06. The ranges of various chemical variables in all clinopyroxene phenocrysts analyzed in sample 11-AMS-06. The restricted nature of the composition of Cpx 7 is unusual for this sample.

3.2.1.2 Sample 11-KT-34B

Ten clinopyroxene phenocrysts were analyzed from this sample (a tephritic leucitite). All analyses plot in the diopside field on the pyroxene quadrilateral (Morimoto et al., 1988) [Figure 3.15]. The clinopyroxenes in this sample plot in the exact same area on the pyroxene quadrilateral as the clinopyroxenes in 11-AMS-06 [Figure 3.3]; however, there are differences. The clinopyroxenes in 11-KT-34B are about half the size of their counterparts in 11-AMS-06 and the clinopyroxenes in 11-KT-34B display more Mg-rich bands. An additional difference is lack of the compositional bi-modality seen in 11-AMS-06 where epitaxial bands were either Mg-rich or Fe-rich and there were no intermediate compositions; in 11-KT-34B there is a continuum of band compositions between these two modes.

Nine out of ten clinopyroxene phenocrysts in 11-KT-34B possess a large and rounded salite core. Surrounding the grain cores there are a varying number of Mg-rich bands in each pyroxene; what follows is a sampling of this varying behavior. Cpx 1 displays a large resorbed Fe-rich core enveloped by a large Mg-rich band that becomes slightly more Fe-rich outwards. This Mg-rich band is surrounded by a large oscillatory zoned Fe-rich band with several erosion surfaces visible inside the band [See Figure 3.16 A]. An additional four pairs of Mg-rich bands and Fe-rich oscillatory-zoned bands of varying size follow this progression. Both Fe-rich and Mg-rich bands display resorption features and there is substantial chemical variation between the bands [See Figure 3.17]. Cpx 6 also displays five Mg-rich bands but with less compositional range [See Figure 3.16 B]. Cpx 11 possesses a Fe-rich oscillatory-zoned core (resorbed) surrounded by a large Mg-rich band that becomes slightly more Fe-enriched towards the outside and is truncated by a large

oscillatory-zoned Fe-rich band [See Figure 3.18]. A smaller pair of Mg-rich and Fe-rich bands follows this thick Fe-rich band, although the Mg#*-spike is less pronounced than on interior Mg-rich band [See Figure 3.19]. Resorption features are present in all bands. Finally, Cpx 15 differs from the other clinopyroxenes in 11-KT-34B because it displays a consistently Fe-rich oscillatory-zoned habit and minimal if any epitaxial banding involving Mg-rich bands [See Figure 3.20]. This lack of banding is seen in the fairly consistent and evolved Mg#* values between 75.4 and 72.2; that said, there is a markedly high concentration of Al and Ti in the very center of the phenocryst [See Figure 3.21]. This anomalous Al and Ti content is obvious when cation ranges in clinopyroxenes from 11-KT-34B are compared [See Figure 3.22].

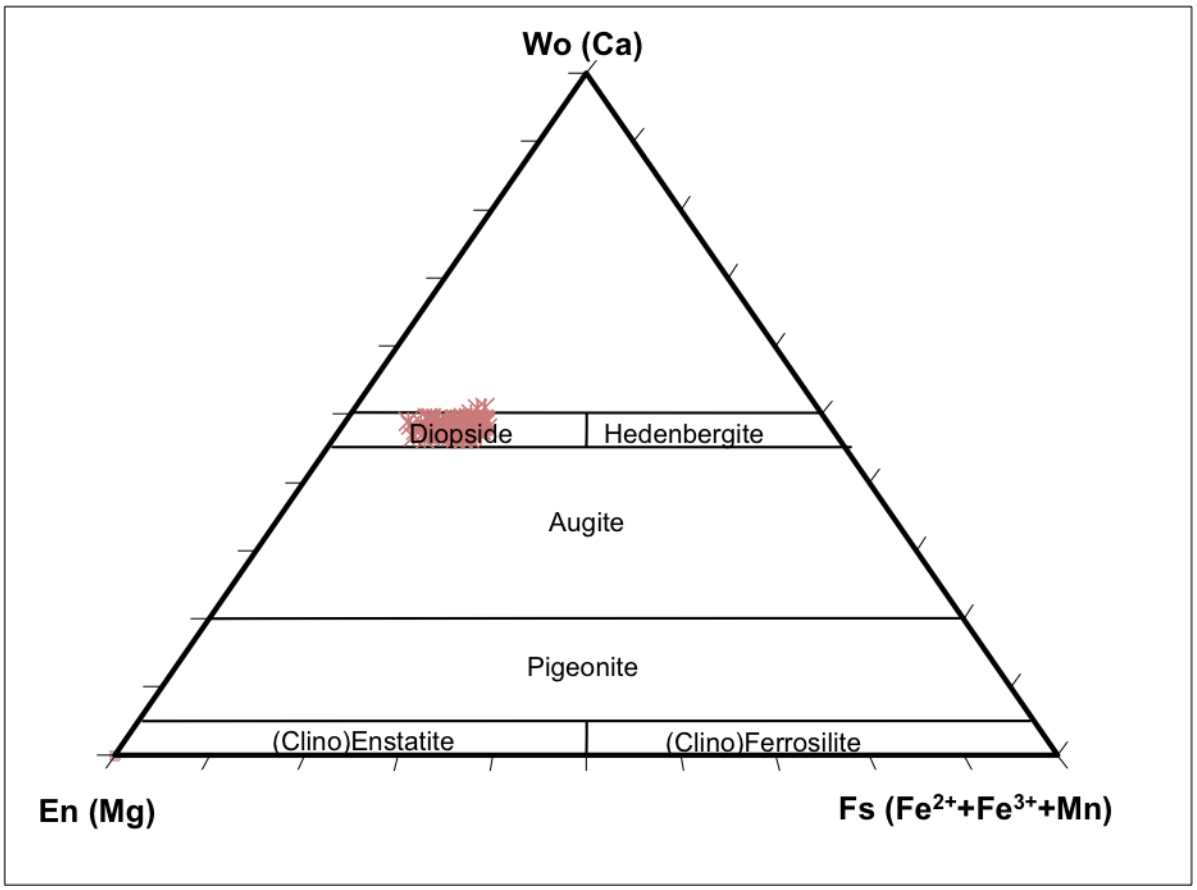

Figure 3.15) Clinopyroxene analyses obtained for 11-KT-34B plotted in the pyroxene quadrilateral based on Morimoto et al. (1988)

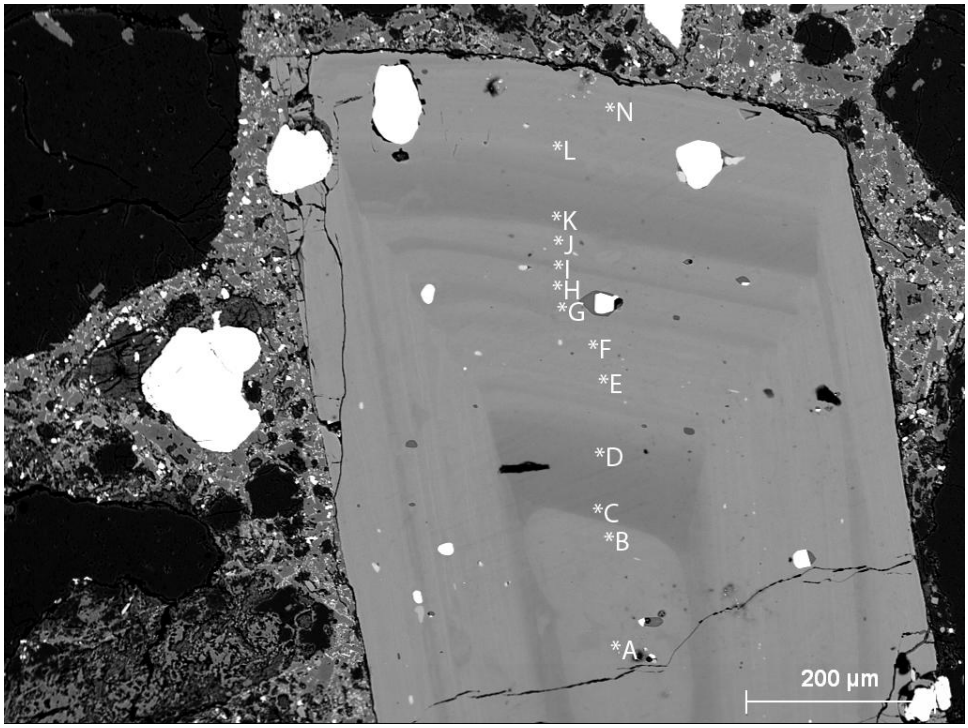

A

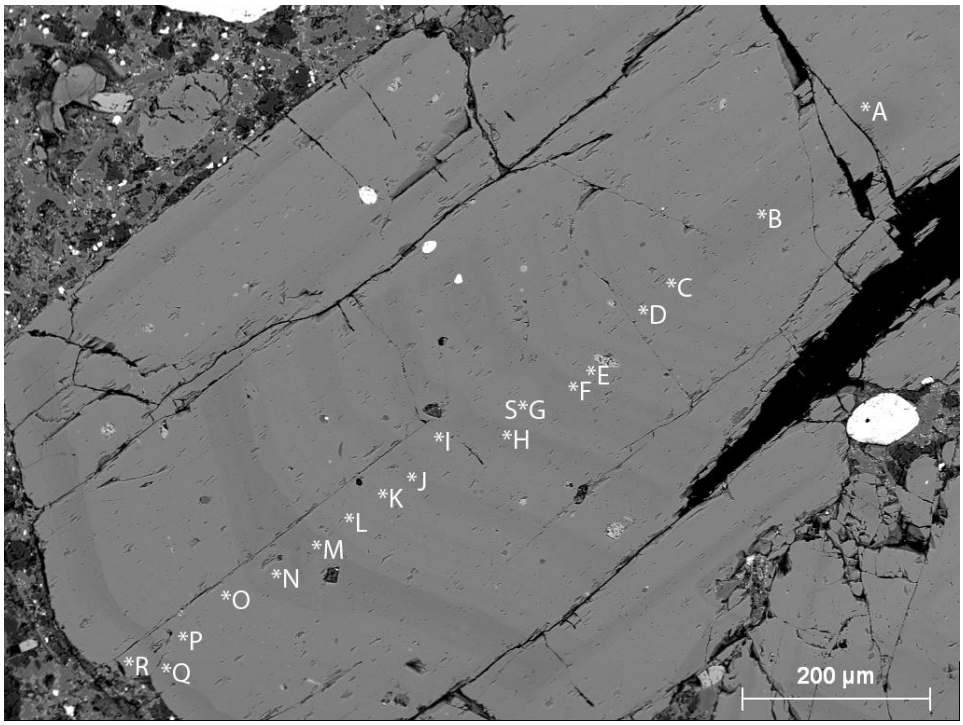

B

Figure 3.16) BSE images of in 11-KT-34B Cpx 1 and Cpx 6. Images of zoned clinopyroxenes, A) Cpx 1, B) Cpx 6, Microprobe analysis points indicated by center of asterisk next to letters, individual analyses for Cpx 1 are presented in Table 3.4 and analyses for Cpx 6 are in Appendix A.

Table 3.4) Representative of zoned clinopyroxene in 11-KT-34B							
sample	11-KT-34B						
Cpx #	Cpx 1						
probe site	a	b	c	d	e	f	g
	Wt% oxide						
SiO_2	49.06	49.99	52.37	51.31	48.53	49.03	49.62
Al_2O_3	4.63	4.71	1.57	2.35	4.54	3.92	3.38
MgO	12.51	12.46	15.82	14.80	12.71	13.27	13.84
FeO	7.93	8.30	4.14	5.53	8.39	8.15	7.01
MnO	0.19	0.19	0.07	0.16	0.24	0.32	0.16
CaO	23.07	23.05	24.17	24.22	23.33	23.25	24.08
Na_2O	0.43	0.42	0.19	0.23	0.43	0.37	0.22
TiO_2	0.85	0.96	0.33	0.49	1.00	0.81	0.60
Cr_2O_3	n.d.	0.07	0.23	n.d.	n.d.	n.d.	n.d.
TOTAL	98.67	100.14	98.91	99.09	99.15	99.10	98.91
	Number of cations in formula						
Si	1.849	1.860	1.939	1.906	1.821	1.837	1.857
Al	0.206	0.206	0.069	0.103	0.201	0.173	0.149
Mg	0.703	0.691	0.873	0.820	0.711	0.741	0.772
Fe^{2+}	0.170	0.210	0.086	0.098	0.131	0.122	0.100
Fe^{3+}	0.080	0.048	0.042	0.073	0.133	0.133	0.119
Mn	0.006	0.006	0.002	0.005	0.008	0.010	0.005
Ca	0.931	0.919	0.959	0.964	0.938	0.933	0.965
Na	0.032	0.030	0.014	0.016	0.031	0.027	0.016
Ti	0.024	0.027	0.009	0.014	0.028	0.023	0.017
Cr	0.000	0.002	0.007	0.000	0.000	0.000	0.000
TOTAL	4.000	4.000	4.000	4.000	4.000	4.000	4.000
$Mg/(Mg+Fe^{+2})*100$	80.5	76.7	91.0	89.3	84.5	85.9	88.5
$Mg/(Mg+Fe_{total})*100$	73.8	72.8	87.2	82.7	73.0	74.4	77.9
Cation Index DS	2.966	2.945	3.555	3.380	2.939	3.024	3.188
Wo	49.3	49.0	48.9	49.2	48.9	48.1	49.2
En	37.2	36.9	44.5	41.8	37.0	38.2	39.4
Fs	13.5	14.1	6.7	9.0	14.1	13.7	11.4

Table 3.4 continued						
sample	11-KT-34B					
Cpx #	Cpx 1					
probe site	h	i	j	k	l	n
	Wt% oxide					
SiO_2	48.81	50.35	47.96	50.95	48.33	50.06
Al_2O_3	4.11	2.91	5.10	2.27	3.83	3.87
MgO	12.83	14.15	12.27	14.93	12.81	12.84
FeO	8.07	6.26	8.67	5.41	8.43	7.91
MnO	0.19	0.15	0.28	0.15	0.39	0.41
CaO	25.06	24.05	23.22	24.60	23.60	23.53
Na_2O	0.42	0.27	0.56	0.19	0.42	0.40
TiO_2	0.89	0.46	0.94	0.43	0.73	0.79
Cr_2O_3	n.d.	0.13	n.d.	n.d.	n.d.	n.d.
TOTAL	100.38	98.74	99.00	98.94	98.53	99.82
	Number of cations in formula					
Si	1.807	1.883	1.803	1.894	1.825	1.866
Al	0.179	0.128	0.226	0.099	0.170	0.170
Mg	0.708	0.789	0.688	0.827	0.721	0.713
Fe^{2+}	0.063	0.099	0.116	0.067	0.097	0.165
Fe^{3+}	0.187	0.097	0.157	0.102	0.169	0.082
Mn	0.006	0.005	0.009	0.005	0.013	0.013
Ca	0.994	0.964	0.935	0.980	0.954	0.940
Na	0.030	0.020	0.041	0.014	0.030	0.029
Ti	0.025	0.013	0.027	0.012	0.021	0.022
Cr	0.000	0.004	0.000	0.000	0.000	0.000
TOTAL	4.000	4.000	4.000	4.000	4.000	4.000
$Mg/(Mg+Fe^{+2})*100$	91.8	88.8	85.6	92.6	88.2	81.3
$Mg/(Mg+Fe_{total})*100$	73.9	80.1	71.6	83.1	73.0	74.3
Cation Index DS	3.019	3.277	2.850	3.403	2.999	3.039
Wo	50.8	49.3	49.1	49.5	48.9	49.1
En	36.1	40.4	36.1	41.8	36.9	37.3
Fs	13.1	10.3	14.8	8.7	14.3	13.6

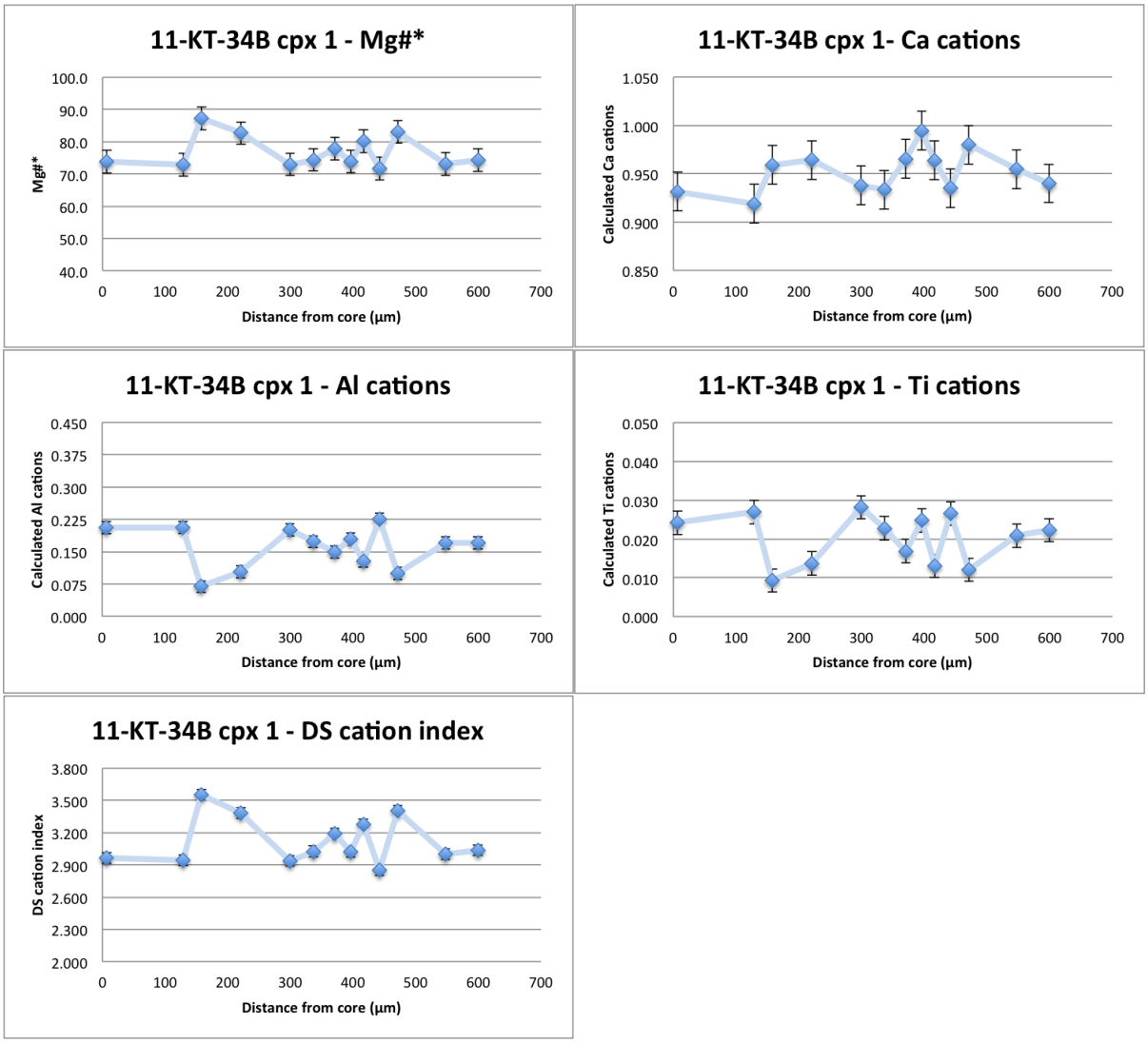

Figure 3.17) Chemical variation plots for 11-KT-34B Cpx 1. Note the large relatively homogenous Fe-rich inner core on the left of the diagrams adjacent to the pronounced positive spikes on the Mg#* and DS plots representing the large Mg-rich dark band seen in Figure 3.16 A.

A 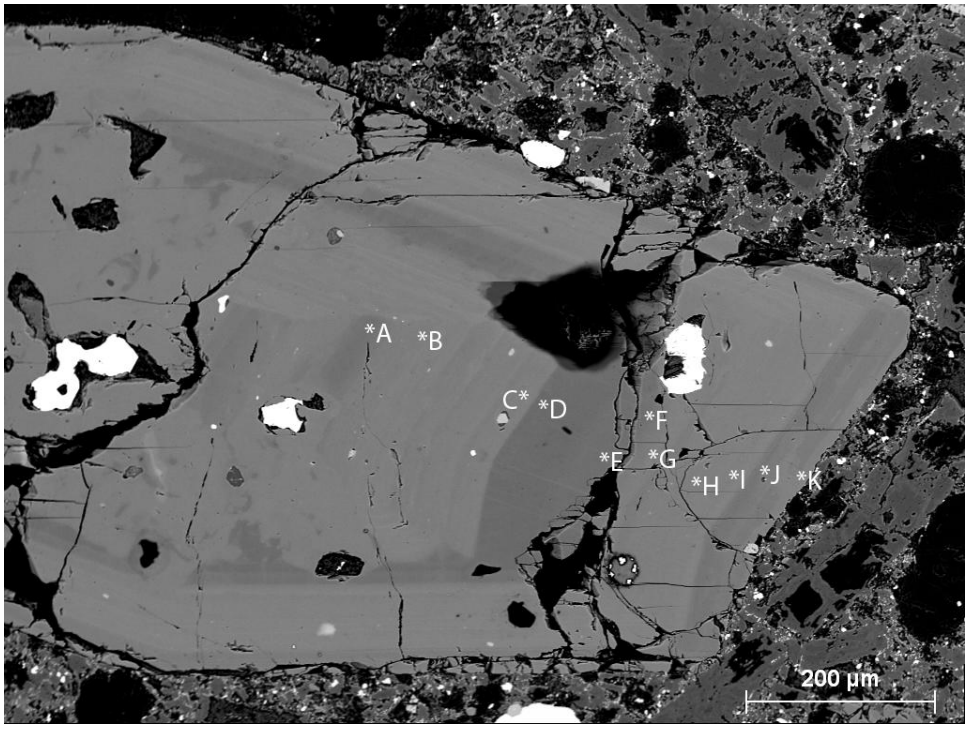

Figure 3.18) Backscatter image of 11-KT-34B Cpx 11. Microprobe analysis points indicated by center of asterisk next to letters, individual analyses are presented in Appendix A.

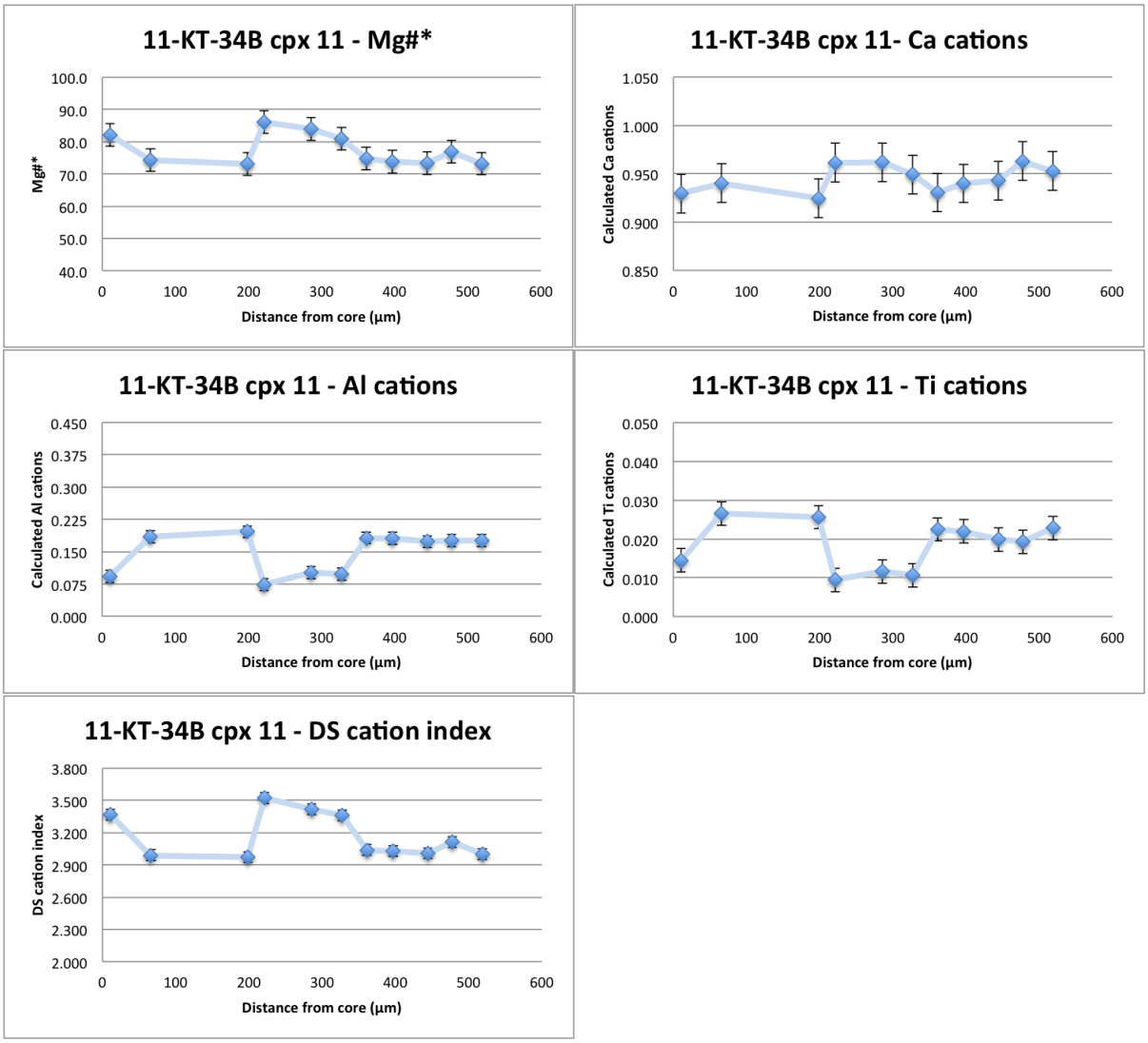

Figure 3.19) Chemical variation plots for 11-KT-34B Cpx 11. The leftmost data point of the graphs is from within a resorption cavity filled with Mg-rich material (corresponds with analysis site 'A' in Figure 3.18).

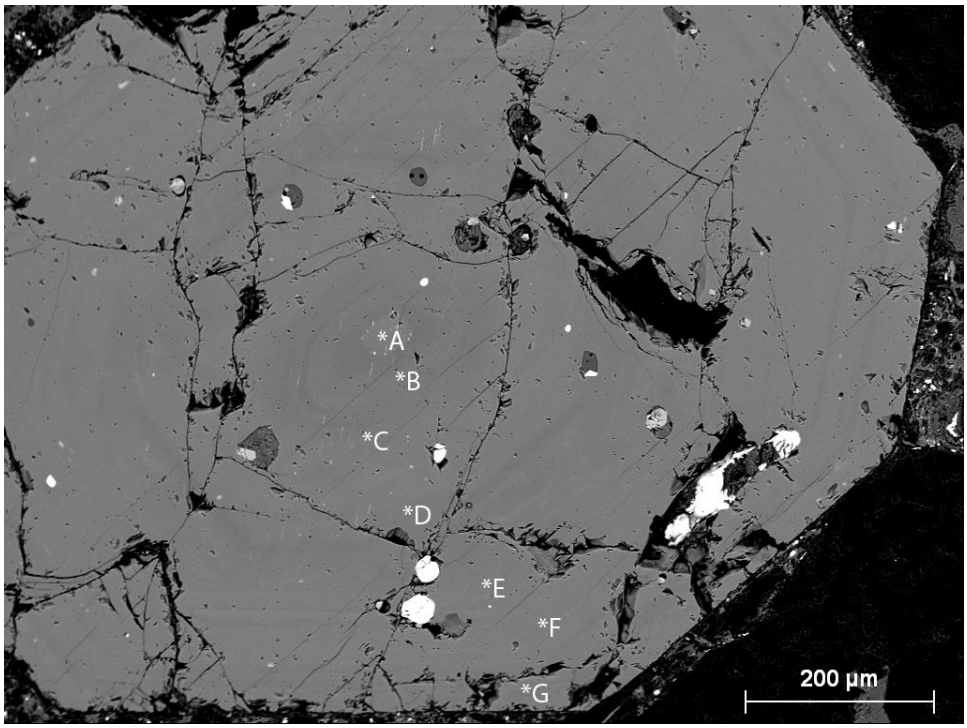

Figure 3.20) Backscatter image of 11-KT-34B Cpx 15. Microprobe analysis points indicated by center of asterisk next to letters, individual analyses are presented in Appendix A.

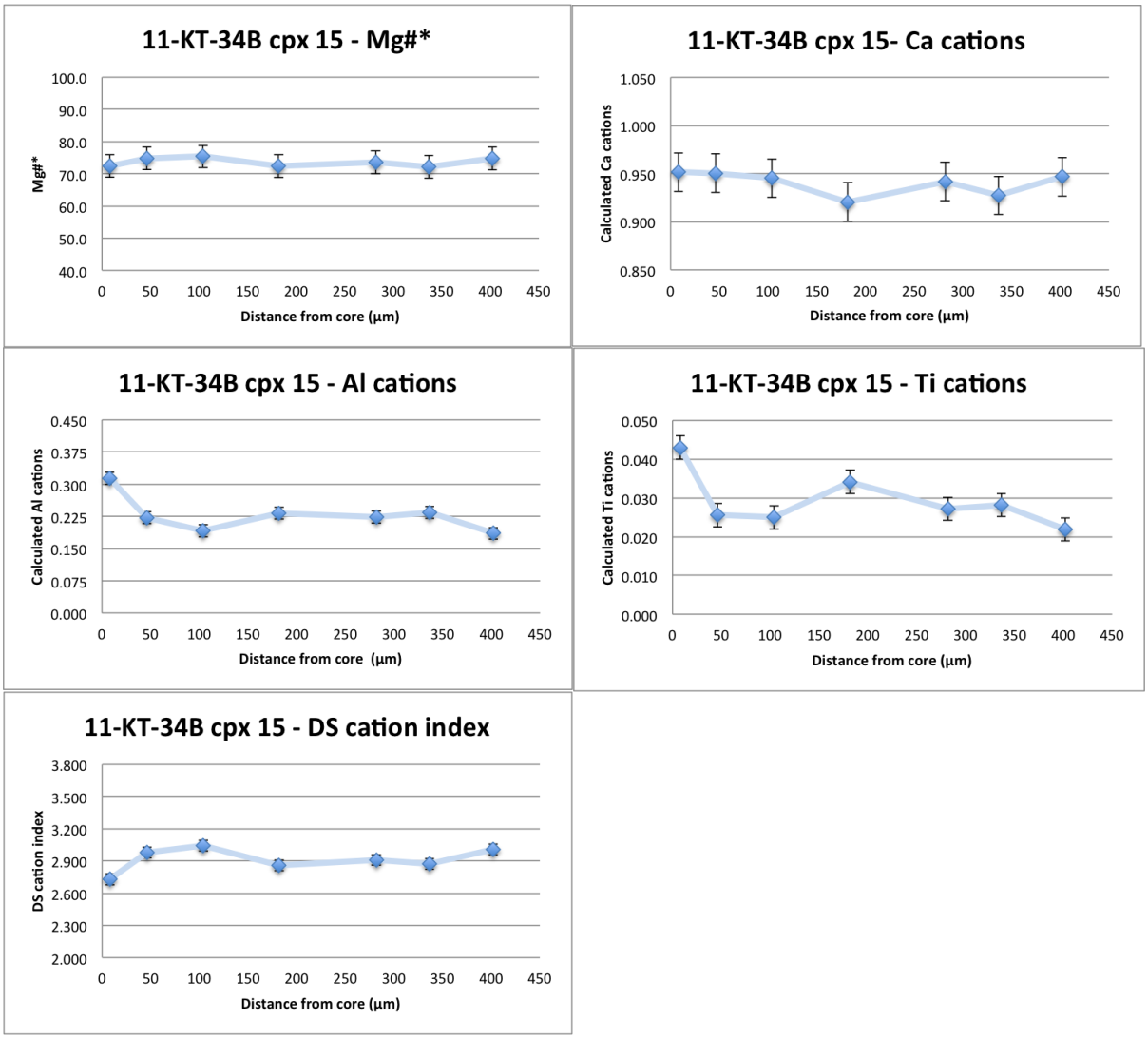

Figure 3.21) Chemical variation plots for 11-KT-34B Cpx 15. Plots show a relatively uniform composition across the phenocryst for Mg#* and Ca cation totals.

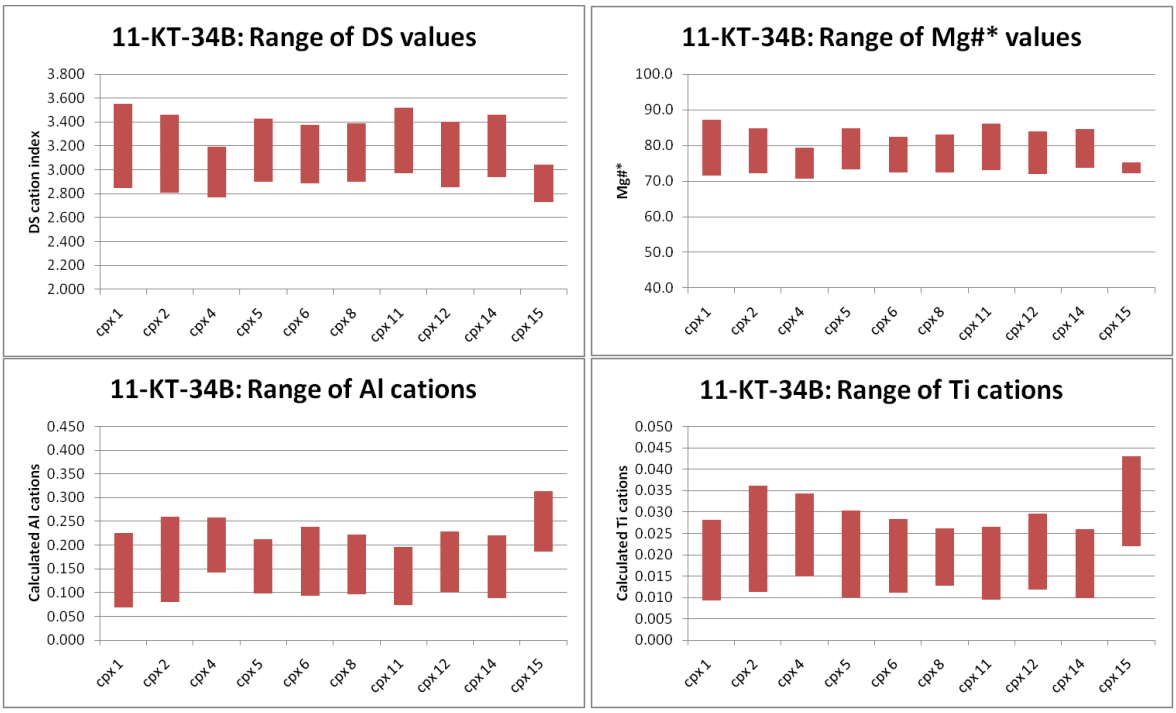

Figure 3.22) Chemical range plots of all clinopyroxene in 11-KT-34B.

3.2.1.3 Sample 11-KT-36D

Eight clinopyroxene phenocrysts from this sample (a minette) were analyzed. All pyroxenes and epitaxial bands plot in the diopside field on the pyroxene quadrilateral as defined by Morimoto et al. (1988) [See Figure 3.23]. The clinopyroxene compositions fall in the same area as the pyroxenes of 11-AMS-06 and 11-KT-34B [See Figures 3.7 and 3.15]. Clinopyroxene phenocrysts of this sample are considerably smaller than those of either 11-AMS-06 or 11-KT-34B and display less distinctive complex zoning with fewer epitaxial bands. The majority of phenocrysts have small relatively Fe-rich diopside cores that possess rounded edges [See Figure 3.24 A point A and B] that gradually grade into an outer more Mg-rich band without the presence of a sharp contact [See Figure 3.24 A point C]. The diffuse outer edge of the core is likely due to cation diffusion. These cores possess DS cation indices ranging from 3.01 to 3.23 and Mg#* values of 76.7 to 79.0. An Mg-rich band coats the aforementioned cores; within this band DS values are between 3.28 and 3.56, and Mg#* values range from 82.0 and 87.3. [See Figure 3.24A point C and Figure 3.24B point A,B,&C]. The outer edge of this Mg-rich band is also resorbed however the boundary is sharper than the interior contact [See Figure 3.24]. Outside the Mg-rich band, a Fe-rich diopside band occurs [Figure 3.24A points D to G] with lower DS cation indices between DS= 3.06 to 2.77 mirroring lower Mg#* values (70.4 to 75.2). There are no signs of resorption on the outer edge of the crystal. The compositional zonation showing a distinct core and two epitaxial bands is also visible in variation diagrams from these clinopyroxenes as two plateaus separated by a spike [Figure 3.25]. Figure 3.26 summarizes the chemical ranges and similar behaviors of the clinopyroxenes in 11-KT-36D.

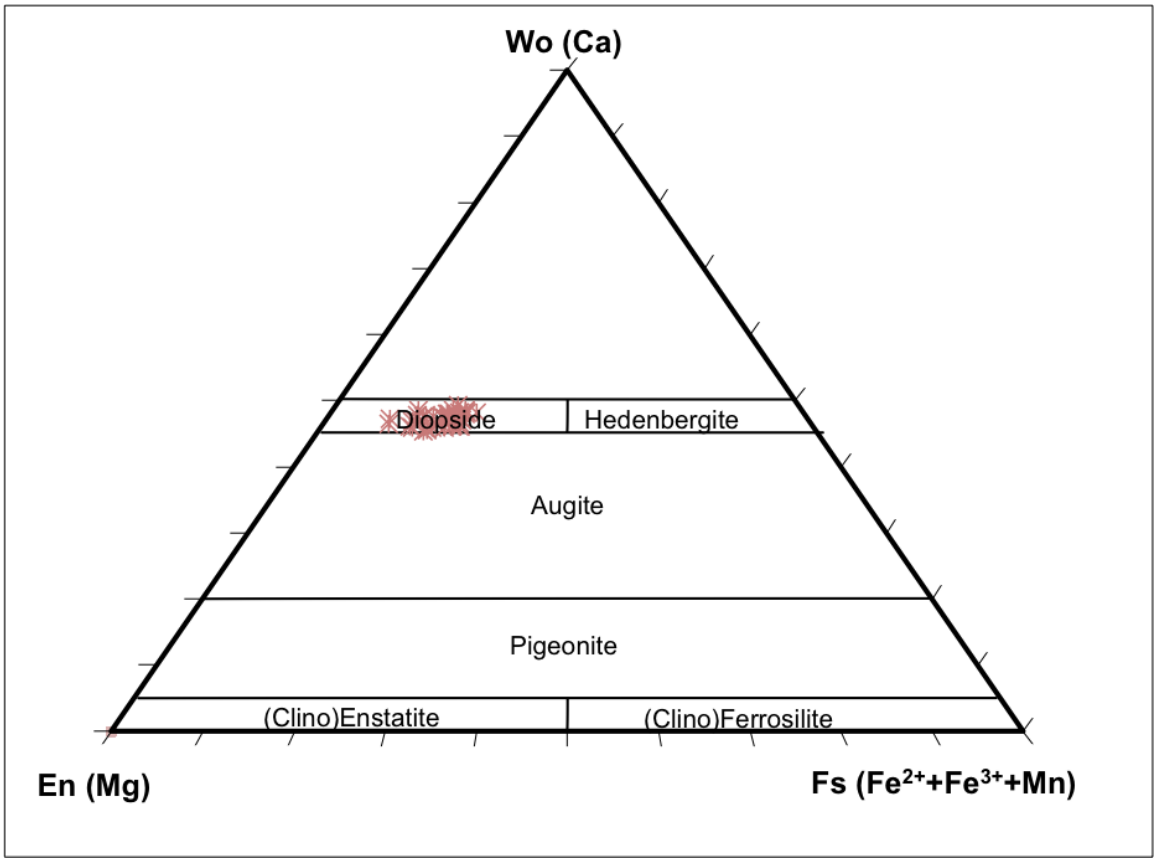

Figure 3.23) Clinopyroxene analyses obtained for 11-KT-36D plotted in the pyroxene quadrilateral based on Morimoto et al. (1988)

A 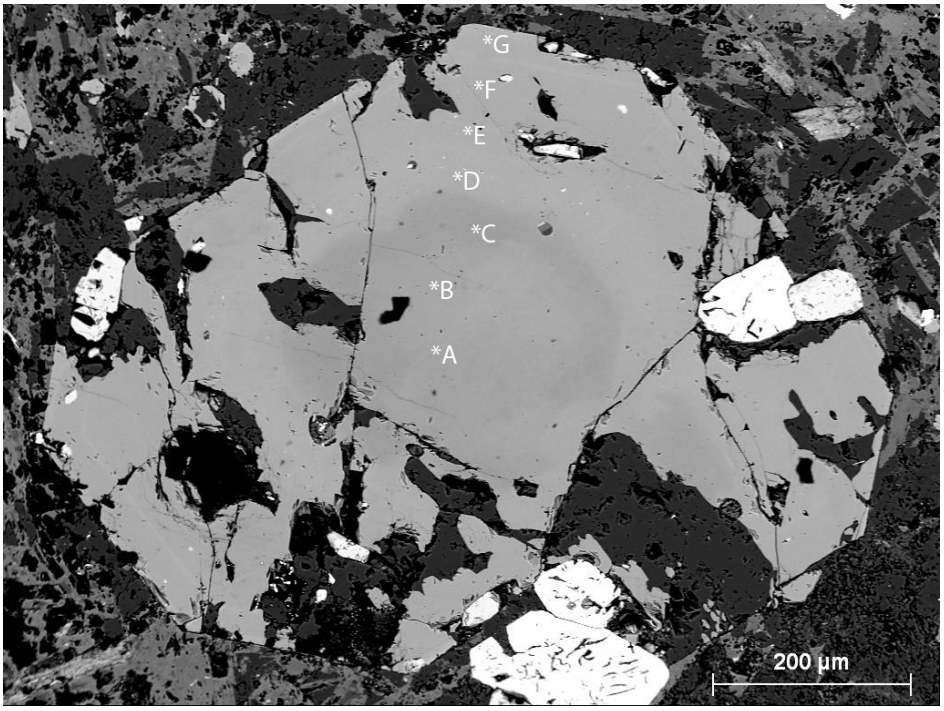

B 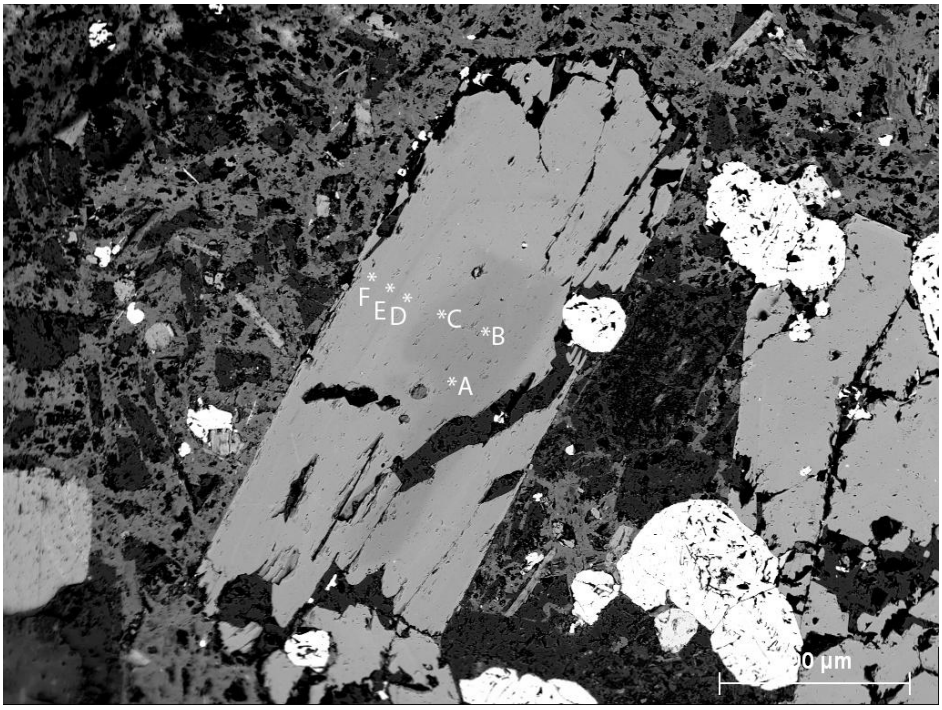

Figure 3.24) BSE image of 11-KT-36D Cpx 20 and Cpx 10. Microprobe analysis points indicated by center of asterisk next to letters, individual analyses are presented in Table 3.5.

Table 3.5) Representative clinopyroxene of 11-KT-36D							
sample	11-KT-36D						
Cpx #	Cpx 20						
probe site	a	b	c	d	e	f	g
	Wt% oxide						
SiO_2	51.15	52.20	52.22	49.19	49.75	49.40	49.84
Al_2O_3	2.73	2.95	1.74	4.34	4.09	4.15	4.17
MgO	15.19	15.37	15.69	13.25	13.75	13.58	13.53
FeO	7.21	7.05	6.25	8.74	8.09	7.76	7.95
MnO	0.29	0.29	0.16	0.34	0.37	0.23	0.24
CaO	22.64	22.47	22.74	22.33	22.49	23.17	22.90
Na_2O	0.34	0.39	0.30	0.49	0.42	0.41	0.44
TiO_2	0.44	0.51	0.36	0.73	0.77	0.62	0.67
Cr_2O_3	n.d.	n.d.	n.d.	n.d.	n.d.	n.d.	n.d.
TOTAL	99.99	101.23	99.45	99.42	99.73	99.31	99.74
	Number of cations in formula						
Si	1.885	1.899	1.930	1.837	1.849	1.842	1.851
Al	0.118	0.127	0.076	0.191	0.179	0.182	0.183
Mg	0.835	0.834	0.864	0.738	0.762	0.755	0.749
Fe^{2+}	0.111	0.139	0.127	0.144	0.140	0.113	0.139
Fe^{3+}	0.111	0.076	0.066	0.129	0.111	0.129	0.108
Mn	0.009	0.009	0.005	0.011	0.012	0.007	0.008
Ca	0.894	0.876	0.900	0.894	0.896	0.925	0.912
Na	0.024	0.028	0.022	0.035	0.030	0.029	0.032
Ti	0.012	0.014	0.010	0.020	0.021	0.017	0.019
Cr	n.d.	n.d.	n.d.	n.d.	n.d.	n.d.	n.d.
TOTAL	4.000	4.000	4.000	4.000	4.000	4.000	4.000
$Mg/(Mg+Fe^{+2})*100$	88.2	85.7	87.2	83.6	84.4	87.0	84.4
$Mg/(Mg+Fe_{total})*100$	79.0	79.5	81.7	73.0	75.2	75.7	75.2
Cation Index DS	3.228	3.217	3.389	2.938	3.012	3.044	3.024
Wo	45.6	45.3	45.9	46.7	46.6	48.0	47.6
En	42.6	43.1	44.0	38.5	39.7	39.1	39.1
Fs	11.8	11.6	10.1	14.8	13.7	12.9	13.3

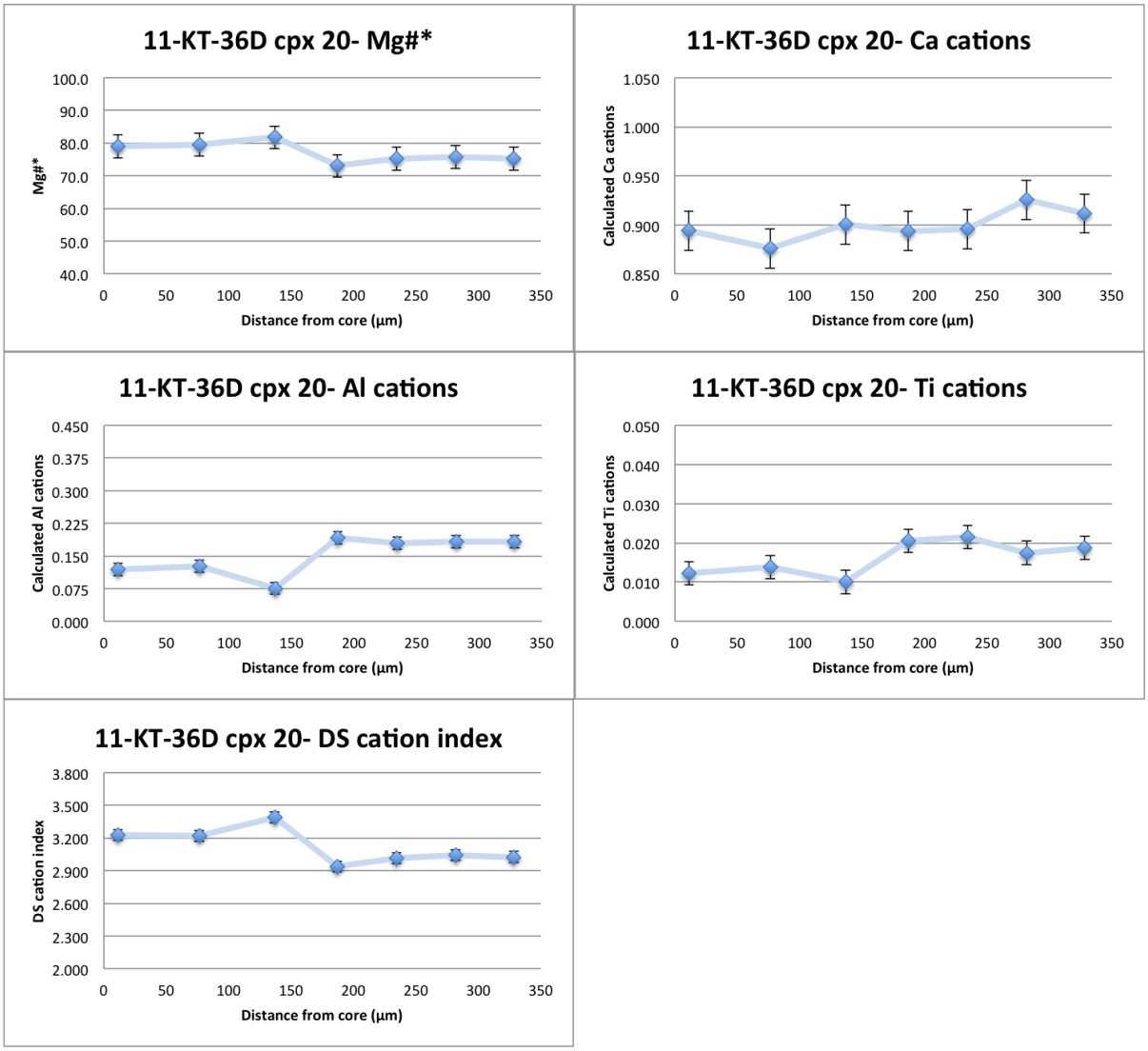

Figure 3.25) Chemical variation plots for 11-KT-36D Cpx 20. Dark bands on backscatter image in Figure 3.22A are seen as positive spikes on both the Mg#* plot and the DS cation index plot and negative spikes on both the Ti and Al cation plots.

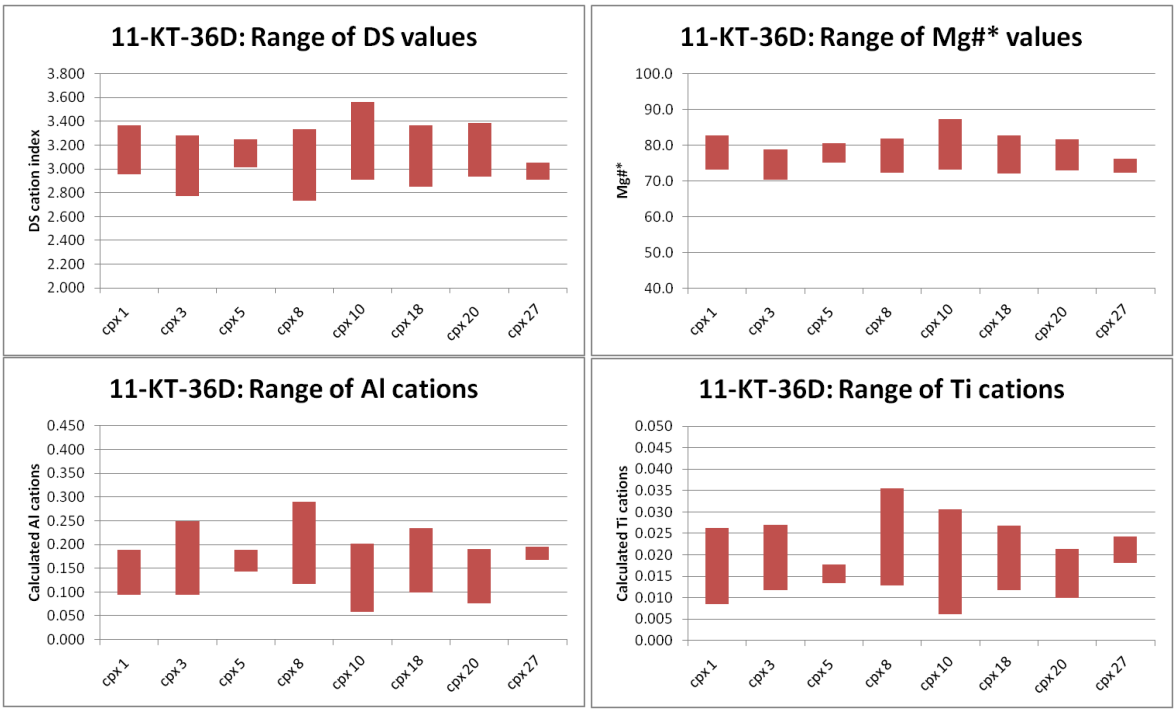

Figure 3.26) Chemical range plots of all clinopyroxene in 11-KT-36D.

3.2.2 Osmancik Region

The three samples of the Osmancik region (11-OS-12, 11-OS-33, and 11-OS-42) are all leucitites with zoned clinopyroxenes. The primary difference between these samples is the grain size. Both 11-OS-12 and 11-OS-42 are coarse grained and both contain megacrysts up to 1 cm in diameter. Clinopyroxene phenocrysts in these two samples are up to fifteen times bigger than the leucite crystals, but are typically five times as big. In contrast to this 11-OS-33 hosts clinopyroxenes that are substantially smaller, the leucite crystals are five to ten times bigger than the clinopyroxenes. Despite the noted size difference the clinopyroxenes in 11-OS-12 and 11-OS-33 both display at most four Mg-rich bands with and large compositional ranges inside each crystal while the clinopyroxenes of 11-OS-42 display at most two Mg-rich bands and less expansive compositional ranges.

3.2.2.1 Sample 11-OS-12

Twelve clinopyroxene phenocrysts from this sample (a leucitite) were selected for study and 108 microprobe analyses were performed. All pyroxenes and epitaxial bands plot in the diopside field on the pyroxene quadrilateral as defined by Morimoto et al. (1988) [Figure 3.27]. This sample possesses slightly more Mg-rich compositions compared to the samples of the Amasya Bogazkoy Region [Figures 3.23, 3.7, and 3.15]. However the clinopyroxenes of 11-OS-12 share general band features with the clinopyroxenes of the Amasya samples. By volume most of the grains are Fe-rich diopside with varying numbers of Mg-rich bands. Two phenocrysts lack Mg-rich bands, three possess only one Mg-rich band, two possess two Mg-rich bands, four crystals possess three Mg-rich bands, and one clinopyroxene hosts four Mg-rich bands. Cpx 14 possesses four Mg-rich bands, three of which are thick with resorbed internal contacts and one thin Mg-rich band [See Figure 3.28]. Chemical variation diagram for Cpx 14 show that the three thick Mg-rich bands have roughly the same composition and the thin Mg-rich band has a composition somewhere between the thick band Mg-rich diopside composition and the volumetrically dominant Fe-rich diopside of the clinopyroxene [See Figure 3.29]. Cpx 1 is interesting in that one crystal face records a single Mg-rich band (the one that was analyzed) while another records two Mg-rich bands [See Figure 3.30]. Again the phenocryst is dominated by a salite composition with elevated Al and Ti and moderate Mg#* values [See Figure 3.31]. Finally, as with Cpx 7, some phenocrysts do not display a Mg-rich band [See Figure 3.32] and display a composition similar to that of the Fe-rich bands in the other pyroxenes [See Figure 3.33]. This consistency is visible in the overlap in the chemical ranges of the pyroxenes in 11-OS-12 [See Figure 3.34].

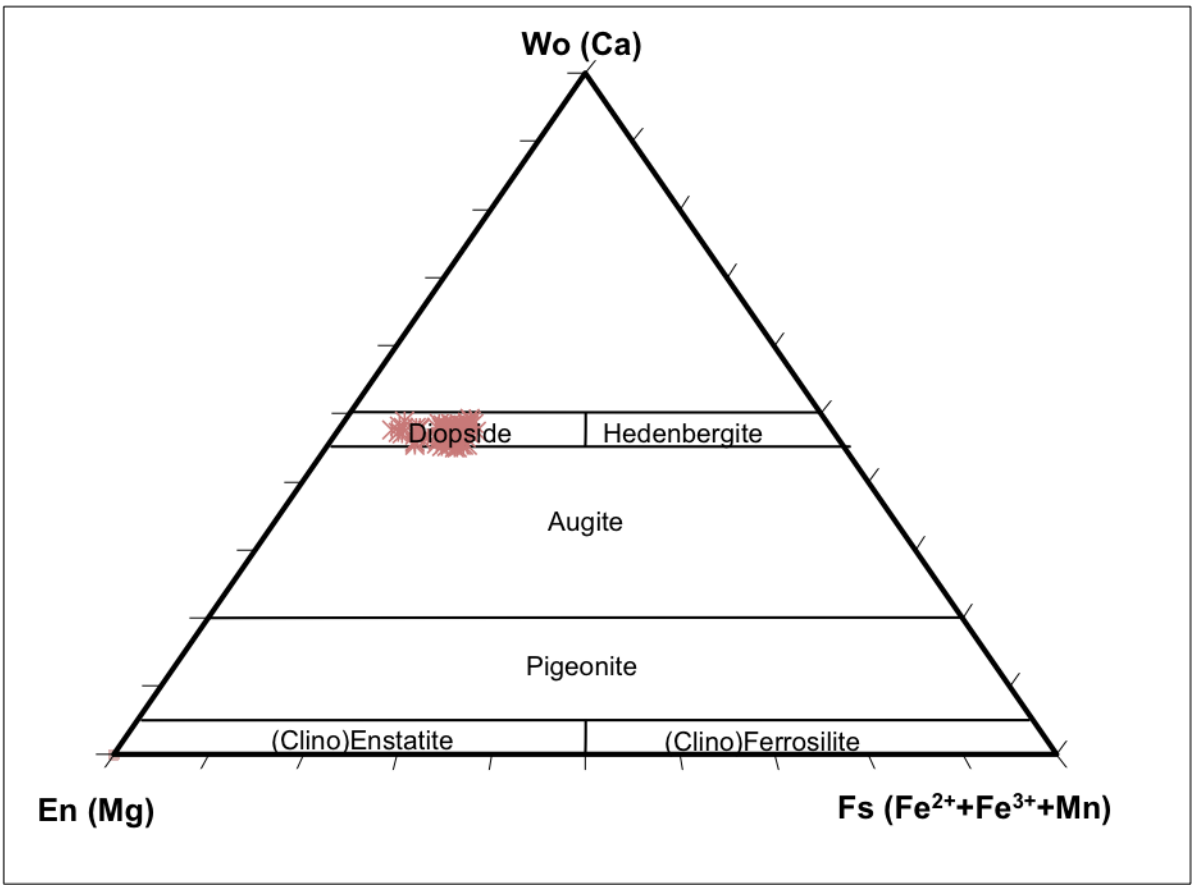

Figure 3.27) Clinopyroxene analyses obtained for 11-OS-12 plotted in the pyroxene quadrilateral based on Morimoto et al. (1988).

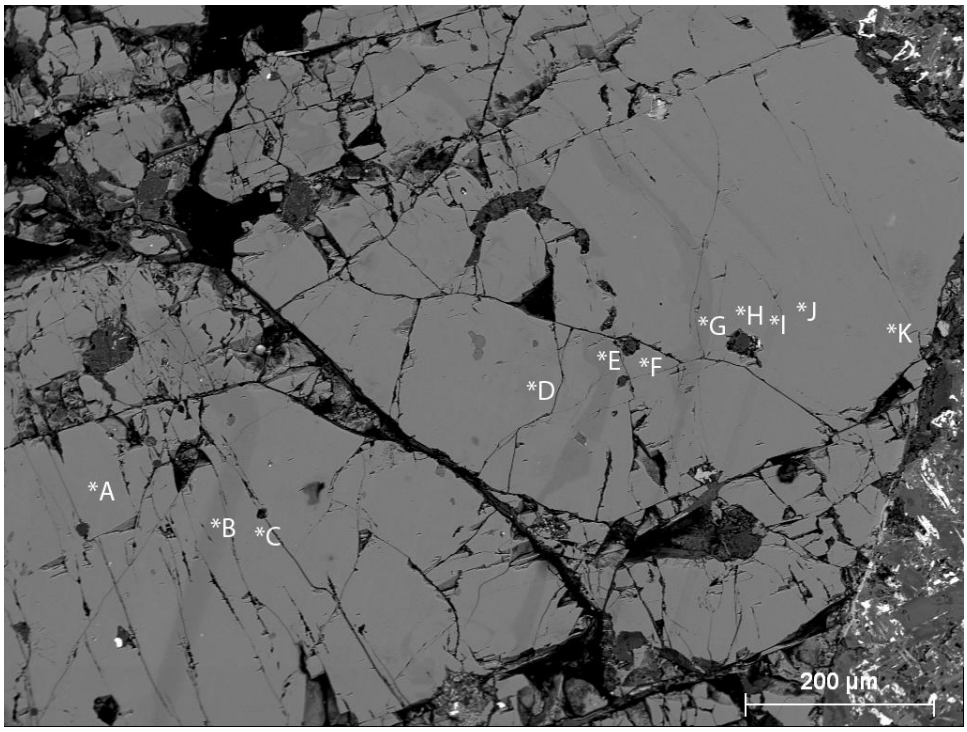

Figure 3.28) BSE image of Cpx 14 in 11- OS-12. Microprobe analysis points indicated by center of asterisk next to letters, individual analyses are presented in Table 3.6.

Table 3.6) Representative clinopyroxene of 11-OS-12							
sample	11-OS-12						
Cpx #	Cpx 14						
probe site	a	b	c	d	e	f	g
	Wt% oxide						
SiO_2	48.79	52.55	49.98	49.25	52.18	48.72	52.62
Al_2O_3	4.53	1.56	3.67	3.79	1.90	4.72	1.74
MgO	13.58	16.41	14.49	14.47	16.88	14.25	17.10
FeO	7.77	4.28	7.06	7.60	3.91	7.62	4.28
MnO	0.27	n.d.	0.18	0.11	0.13	0.17	n.d.
CaO	23.41	24.21	23.65	23.87	24.69	24.17	24.28
Na_2O	0.34	0.21	0.42	0.41	0.24	0.30	0.20
TiO_2	0.65	0.35	0.61	0.98	0.34	0.88	0.27
Cr_2O_3	n.d.	0.67	n.d.	n.d.	0.62	n.d.	0.57
TOTAL	99.35	100.25	100.06	100.49	100.91	100.83	101.07
	Number of cations in formula						
Si	1.818	1.918	1.841	1.810	1.887	1.785	1.899
Al	0.199	0.067	0.159	0.164	0.081	0.204	0.074
Mg	0.755	0.893	0.796	0.793	0.910	0.778	0.920
Fe^{2+}	0.089	0.058	0.064	0.043	0.000	0.034	0.019
Fe^{3+}	0.153	0.073	0.154	0.191	0.118	0.200	0.110
Mn	0.009	0.000	0.005	0.004	0.004	0.005	0.000
Ca	0.935	0.947	0.934	0.940	0.957	0.949	0.939
Na	0.025	0.015	0.030	0.029	0.017	0.022	0.014
Ti	0.018	0.010	0.017	0.027	0.009	0.024	0.007
Cr	0.000	0.019	0.000	0.000	0.018	0.000	0.016
TOTAL	4.000	4.000	4.000	4.000	4.000	4.000	4.000
$Mg/(Mg+Fe^{+2})*100$	89.4	93.9	92.6	94.9	100.0	95.8	98.0
$Mg/(Mg+Fe_{total})*100$	75.7	87.2	78.5	77.2	88.5	76.9	87.7
Cation Index DS	3.015	3.555	3.142	3.085	3.541	3.023	3.550
Wo	48.2	48.0	47.8	47.7	48.1	48.3	47.2
En	38.9	45.3	40.8	40.2	45.7	39.6	46.3
Fs	12.9	6.6	11.4	12.0	6.2	12.1	6.5

Table 3.6) continued				
sample	11-OS-12			
Cpx #	Cpx 14			
probe site	h	i	j	k
	Wt% oxide			
SiO_2	49.10	51.01	49.21	49.24
Al_2O_3	3.77	3.02	4.04	3.96
MgO	14.94	16.04	14.98	14.80
FeO	7.08	6.09	7.37	7.05
MnO	0.19	0.15	0.13	0.22
CaO	23.75	23.76	24.07	23.91
Na_2O	0.32	0.27	0.32	0.36
TiO_2	0.65	0.44	0.92	0.61
Cr_2O_3	n.d.	0.27	n.d.	n.d.
TOTAL	99.81	101.05	101.04	100.14
	Number of cations in formula			
Si	1.811	1.851	1.795	1.810
Al	0.164	0.129	0.174	0.171
Mg	0.822	0.868	0.815	0.811
Fe^{2+}	0.017	0.028	0.016	0.016
Fe^{3+}	0.201	0.156	0.209	0.200
Mn	0.006	0.005	0.004	0.007
Ca	0.938	0.924	0.941	0.942
Na	0.023	0.019	0.022	0.025
Ti	0.018	0.012	0.025	0.017
Cr	0.000	0.008	0.000	0.000
TOTAL	4.000	4.000	4.000	4.000
$Mg/(Mg+Fe^{+2})*100$	97.9	96.8	98.1	98.0
$Mg/(Mg+Fe_{total})*100$	79.0	82.4	78.4	78.9
Cation Index DS	3.141	3.301	3.100	3.126
Wo	47.3	46.6	47.4	47.6
En	41.4	43.8	41.1	41.0
Fs	11.3	9.6	11.5	11.3

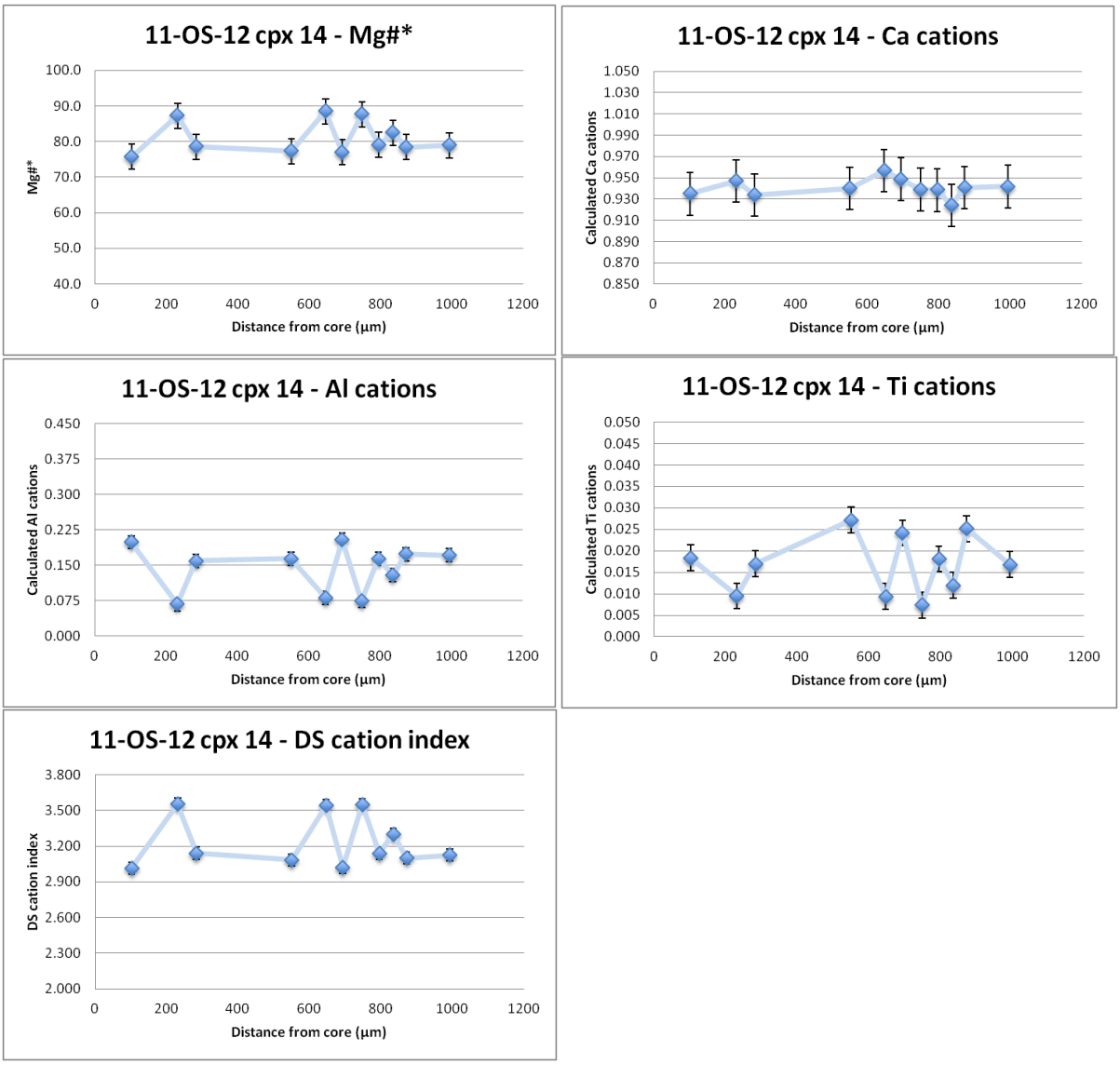

Figure 3.29) Chemical variation plots for 11-OS-12 Cpx 14. Dark bands on backscatter image in Figure 3.26 are seen as positive spikes on both the Mg#* plot and the DS cation index plot and negative spikes on both the Ti and Al cation plots.

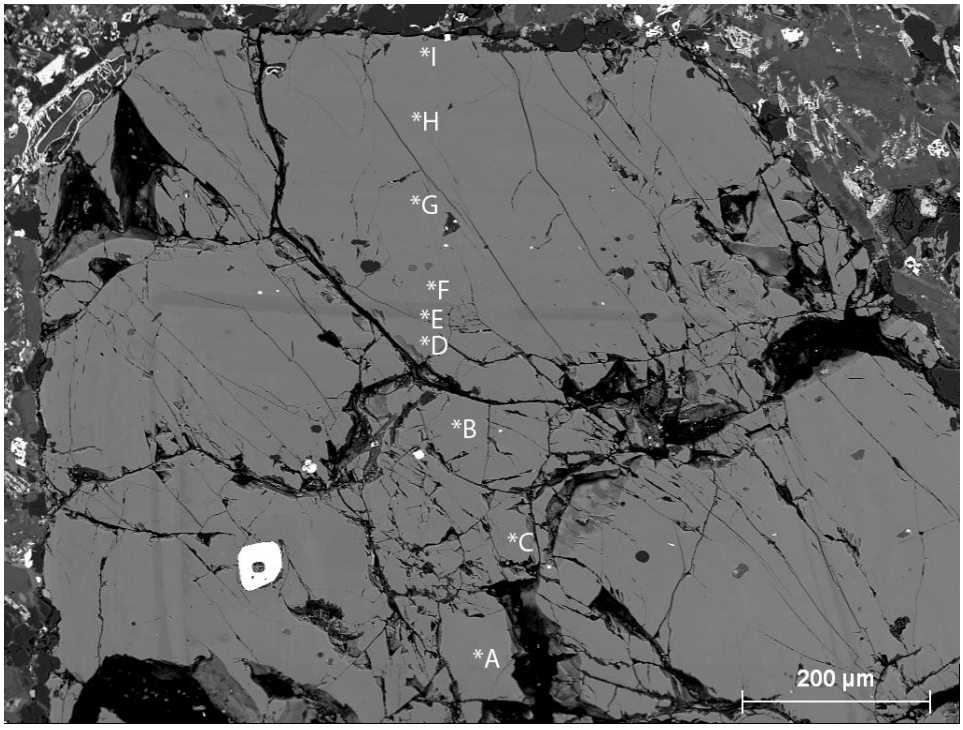

Figure 3.30) Backscatter electron image of 11-OS-12 Cpx 1. Microprobe analysis points indicated by center of asterisk next to letters, individual analyses are presented in Appendix A.

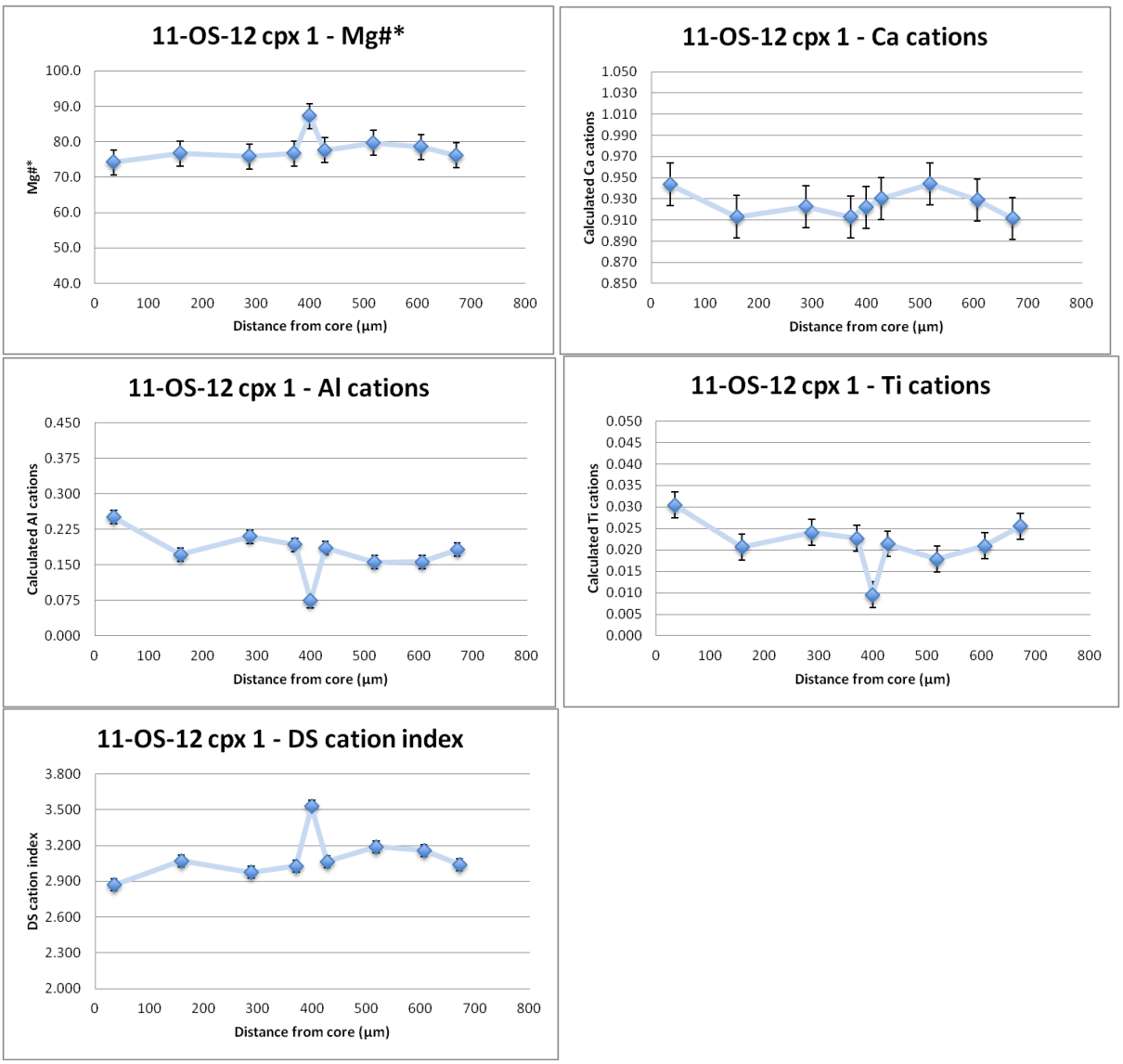

Figure 3.31) Chemical variation plots for 11-OS-12 Cpx 1. The dark band on the backscatter image in Figure 3.28 are seen as positive spikes on both the Mg#* plot and the DS cation index plot and negative spikes on both the Ti and Al cation plots.

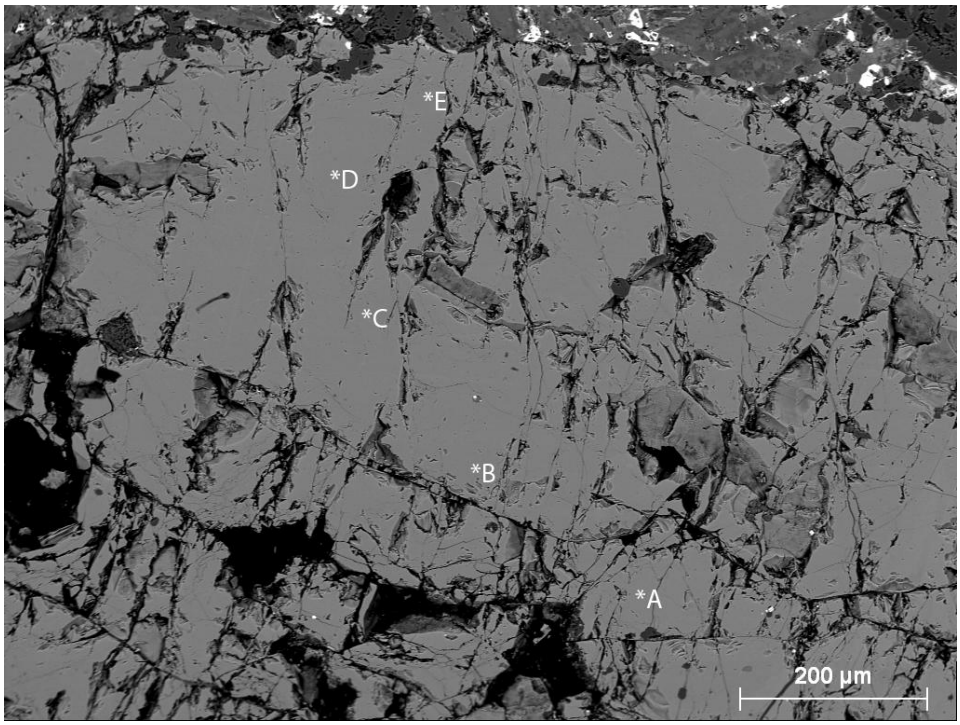

Figure 3.32) Backscatter electron image of 11-OS-12 Cpx 7. Microprobe analysis points indicated by center of asterisk next to letters, individual analyses are presented in Appendix A.

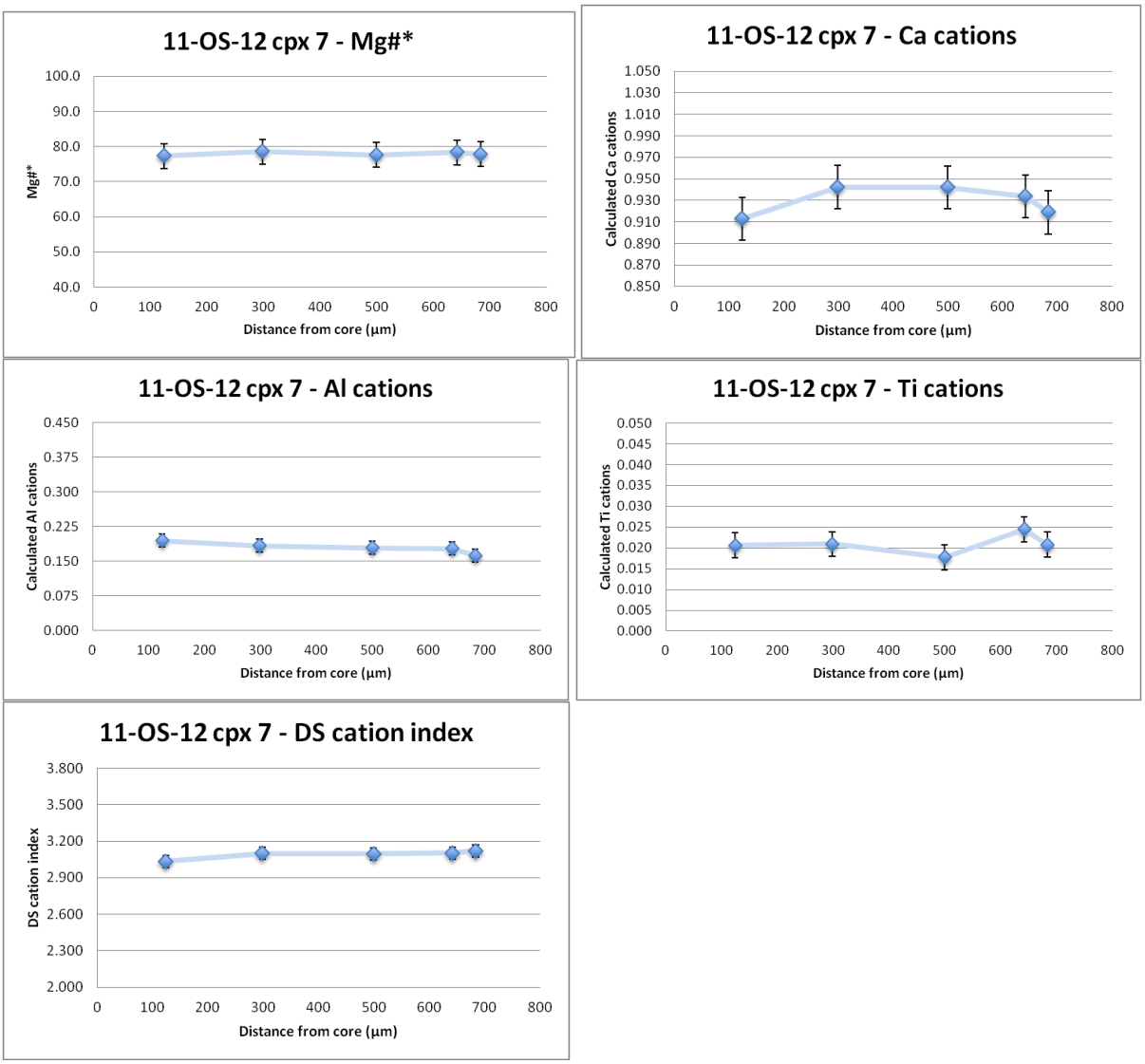

Figure 3.33) Chemical variation plots for 11-OS-12 Cpx 7. Compositions are consistent with the Fe-rich bands of the other pyroxenes.

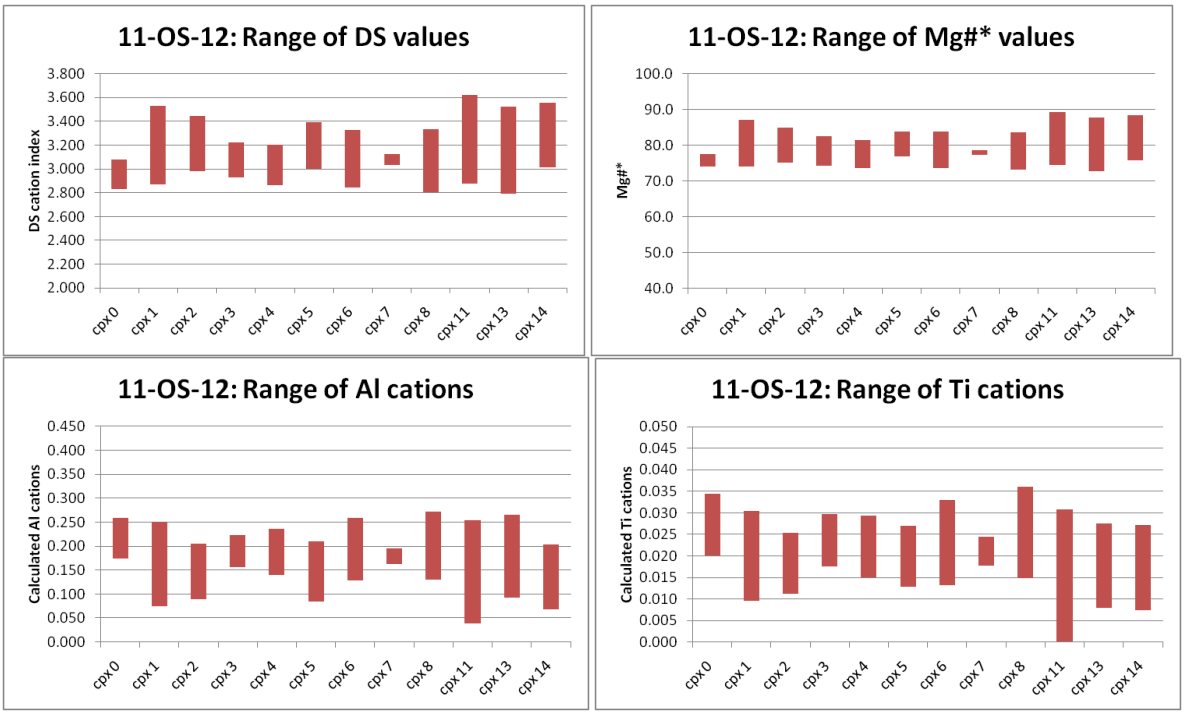

Figure 3.34) Chemical range plots of all clinopyroxene in 11-OS-12.

3.2.2.2 Sample 11-OS-33

Ten clinopyroxene phenocrysts from sample 11-OS-33 (a leucitite) were studied in detail. 127 probe sites were scanned for analysis; all but two of the bands analyzed plot within the diopside region of the pyroxene quadrilateral which plot above the clinopyroxene join indicating high wollastonite content [See Figure 3.35]. The clinopyroxenes in this sample possess the same range of compositions as those from samples collected in the Amasya Bogazkoy Region [Figures 3.23, 3.7, and 3.15] and are slightly more iron rich than the clinopyroxenes from the previously discussed leucitite 11-OS-12 from the Osmancik region [See Figure 3.27]. All of the clinopyroxenes in this sample display fluctuations in composition; however, the size of the chemical differences between the bands varies between phenocrysts. Cpx 10 records four Mg-rich bands separated by resorbed Fe-rich bands [See Figure 3.36]. These Fe-rich bands are roughly the same composition with one exception (point 'M') seen as a notable spike in the Al and Ti cation variation diagrams [See Figure 3.37]. This band is thin and bounded by two small Mg-rich bands with lower Mg#* than the other two Mg-rich bands. In contrast to Cpx 10, Cpx 7 displays less dramatic chemical zoning seen as a lack of distinct bands and only minor oscillatory zoning in BSE image [See Figure 3.38]. Values for Mg#* and Ti cations do not vary much throughout the phenocryst, however Al displays a range about 2/3rd the size of the range in Cpx 10 [See Figure 3.39]. Mg#* variation diagrams show the ranges of nearly all clinopyroxenes in the sample including the same spread Mg# (Mg#= 70 to 80); that said Cpx 1 possess two bands with Mg# less than 62.

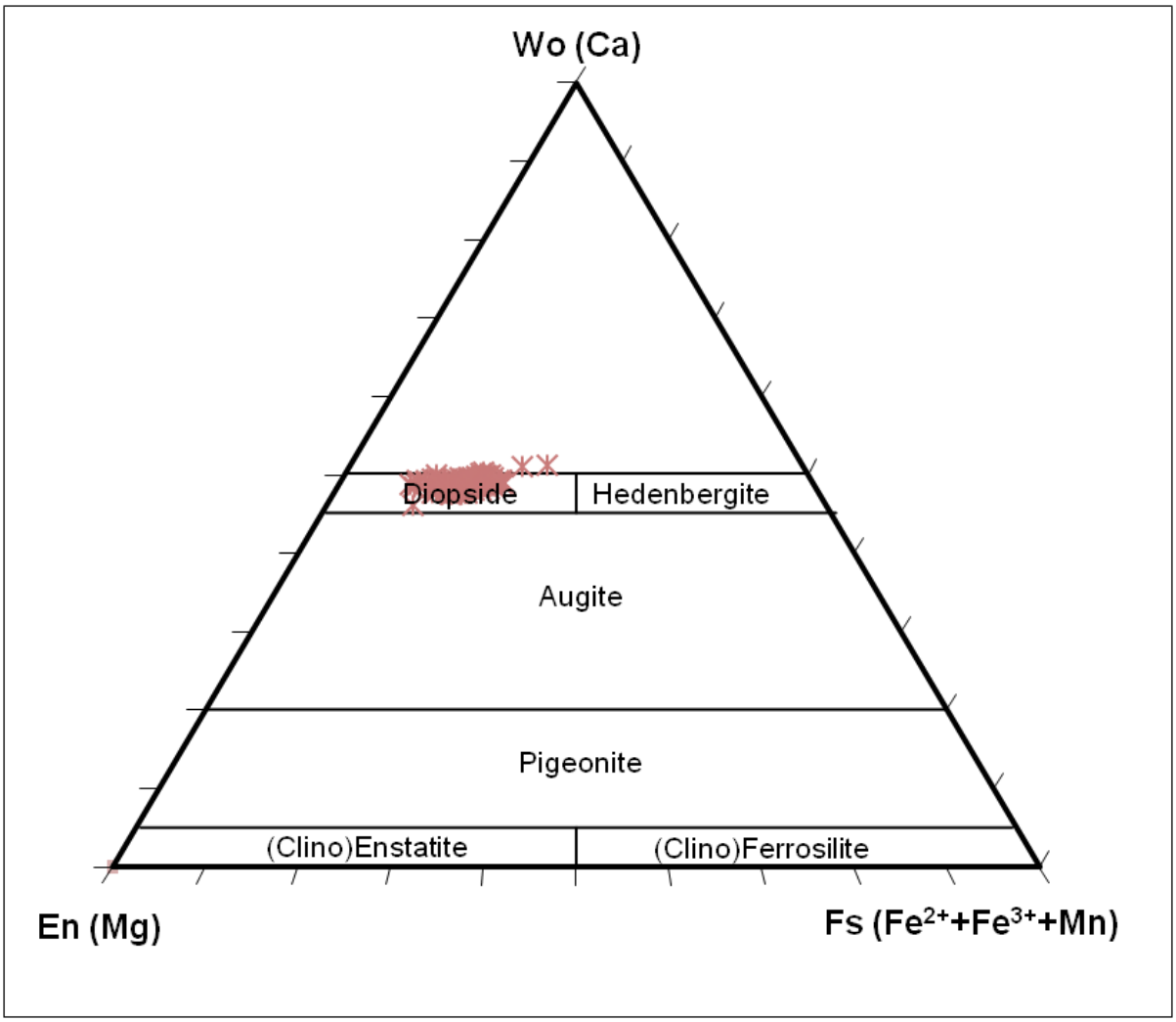

Figure 3.35) Clinopyroxene analyses obtained for 11-OS-33 plotted in the pyroxene quadrilateral based on Morimoto et al. (1988).

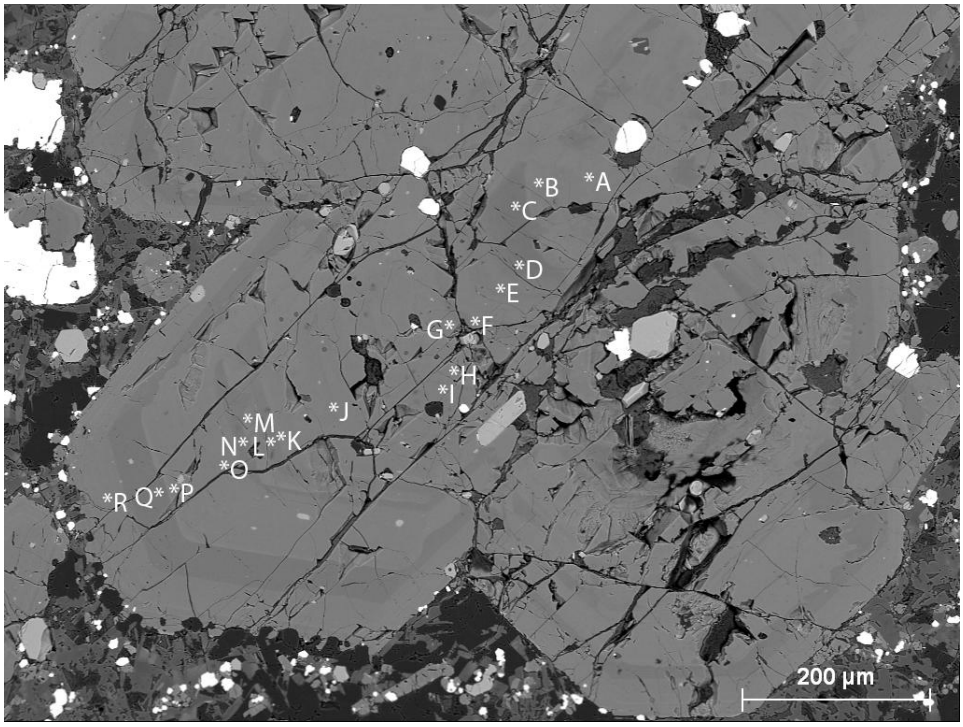

Figure 3.36) Backscatter electron image of 11-OS-33 Cpx 10. Microprobe analysis points indicated by center of asterisk next to letters, individual analyses are presented in Table 3.7.

Table 3.7) Representative clinopyroxene of 11-OS-33							
sample	11-OS-33						
Cpx #	Cpx 10						
probe site	a	b	c	d	e	f	g
	Wt% oxide						
SiO_2	48.98	49.25	53.43	52.88	51.30	51.54	49.68
Al_2O_3	4.52	4.55	1.17	1.30	2.79	2.50	3.79
MgO	12.08	12.53	15.84	15.31	13.93	14.30	12.80
FeO	8.78	8.50	4.90	5.29	7.54	6.78	8.25
MnO	0.15	0.20	0.12	0.00	0.16	0.00	0.20
CaO	23.09	23.53	24.72	24.58	23.82	24.37	23.66
Na_2O	0.74	0.63	0.21	0.24	0.50	0.34	0.49
TiO_2	0.75	0.71	0.28	0.28	0.47	0.60	0.66
Cr_2O_3	0.00	0.00	0.18	0.00	0.00	0.00	0.00
TOTAL	99.10	99.91	100.86	99.88	100.51	100.44	99.53
	Number of cations in formula						
Si	1.839	1.832	1.945	1.946	1.889	1.896	1.856
Al	0.200	0.199	0.050	0.056	0.121	0.108	0.167
Mg	0.676	0.695	0.860	0.840	0.765	0.785	0.713
Fe^{2+}	0.143	0.122	0.095	0.110	0.120	0.119	0.137
Fe^{3+}	0.133	0.142	0.054	0.053	0.112	0.090	0.120
Mn	0.005	0.006	0.004	0.000	0.005	0.000	0.006
Ca	0.929	0.938	0.964	0.969	0.940	0.961	0.947
Na	0.054	0.045	0.015	0.017	0.036	0.024	0.035
Ti	0.021	0.020	0.008	0.008	0.013	0.017	0.019
Cr	0.000	0.000	0.005	0.000	0.000	0.000	0.000
TOTAL	4.000	4.000	4.000	4.000	4.000	4.000	4.000
$Mg/(Mg+Fe^{+2})*100$	82.5	85.0	90.0	88.4	86.4	86.8	83.8
$Mg/(Mg+Fe_{total})*100$	71.0	72.4	85.2	83.8	76.7	79.0	73.5
Cation Index DS	2.889	2.930	3.548	3.512	3.186	3.284	3.031
Wo	49.3	49.3	48.8	49.2	48.4	49.2	49.2
En	35.9	36.5	43.5	42.6	39.4	40.1	37.1
Fs	14.9	14.2	7.7	8.3	12.2	10.7	13.7

Table 3.7) continued							
sample	11-OS-33						
Cpx #	Cpx 10						
probe site	h	i	j	k	l	m	n
	Wt% oxide						
SiO_2	50.06	50.67	50.46	50.15	50.56	48.10	50.57
Al_2O_3	3.53	2.93	3.34	3.63	3.02	6.26	2.88
MgO	12.96	13.67	12.98	13.23	14.09	11.40	14.38
FeO	8.78	8.14	8.59	8.71	7.81	10.35	7.40
MnO	0.22	0.33	0.28	0.24	0.09	0.23	0.29
CaO	23.77	24.00	23.69	23.82	24.32	23.06	24.41
Na_2O	0.47	0.41	0.57	0.57	0.50	0.89	0.37
TiO_2	0.75	0.54	0.75	0.87	0.52	1.11	0.55
Cr_2O_3	0.10	0.00	0.00	0.00	0.00	0.00	0.11
TOTAL	100.64	100.69	100.64	101.21	100.90	101.41	100.95
	Number of cations in formula						
Si	1.853	1.868	1.865	1.842	1.853	1.772	1.852
Al	0.154	0.127	0.145	0.157	0.130	0.272	0.124
Mg	0.715	0.751	0.715	0.724	0.770	0.626	0.785
Fe^{2+}	0.142	0.115	0.143	0.116	0.069	0.132	0.063
Fe^{3+}	0.130	0.136	0.122	0.151	0.170	0.187	0.164
Mn	0.007	0.010	0.009	0.007	0.003	0.007	0.009
Ca	0.943	0.948	0.938	0.937	0.955	0.910	0.958
Na	0.034	0.029	0.041	0.041	0.035	0.064	0.026
Ti	0.021	0.015	0.021	0.024	0.014	0.031	0.015
Cr	0.003	0.000	0.000	0.000	0.000	0.000	0.003
TOTAL	4.000	4.000	4.000	4.000	4.000	4.000	4.000
$Mg/(Mg+Fe^{+2})*100$	83.5	86.7	83.3	86.2	91.7	82.5	92.6
$Mg/(Mg+Fe_{total})*100$	72.5	75.0	72.9	73.0	76.3	66.2	77.6
Cation Index DS	3.026	3.134	3.038	3.007	3.156	2.615	3.198
Wo	48.7	48.3	48.7	48.4	48.6	48.9	48.4
En	36.9	38.3	37.1	37.4	39.1	33.6	39.7
Fs	14.4	13.3	14.2	14.2	12.3	17.5	11.9

Table 3.7) continued				
sample	11-OS-33			
Cpx #	Cpx 10			
probe site	o	p	q	r
	Wt% oxide			
SiO_2	49.50	49.04	51.30	49.27
Al_2O_3	3.59	3.94	2.09	3.82
MgO	12.76	12.53	14.57	12.99
FeO	8.39	8.44	6.38	8.44
MnO	0.29	0.14	0.26	0.34
CaO	23.76	23.77	24.79	23.91
Na_2O	0.51	0.48	0.27	0.48
TiO_2	0.81	0.85	0.52	0.86
Cr_2O_3	0.00	0.00	0.00	0.00
TOTAL	99.61	99.19	100.19	100.10
	Number of cations in formula			
Si	1.850	1.840	1.891	1.830
Al	0.158	0.174	0.091	0.167
Mg	0.710	0.701	0.800	0.720
Fe^{2+}	0.128	0.133	0.079	0.102
Fe^{3+}	0.134	0.131	0.118	0.160
Mn	0.009	0.004	0.008	0.011
Ca	0.951	0.956	0.979	0.952
Na	0.037	0.035	0.020	0.035
Ti	0.023	0.024	0.014	0.024
Cr	0.000	0.000	0.000	0.000
TOTAL	4.000	4.000	4.000	4.000
$Mg/(Mg+Fe^{+2})*100$	84.7	84.0	91.0	87.5
$Mg/(Mg+Fe_{total})*100$	73.0	72.6	80.3	73.3
Cation Index DS	3.022	2.995	3.341	3.003
Wo	49.2	49.6	49.3	49.0
En	36.8	36.4	40.3	37.0
Fs	14.0	14.0	10.3	14.0

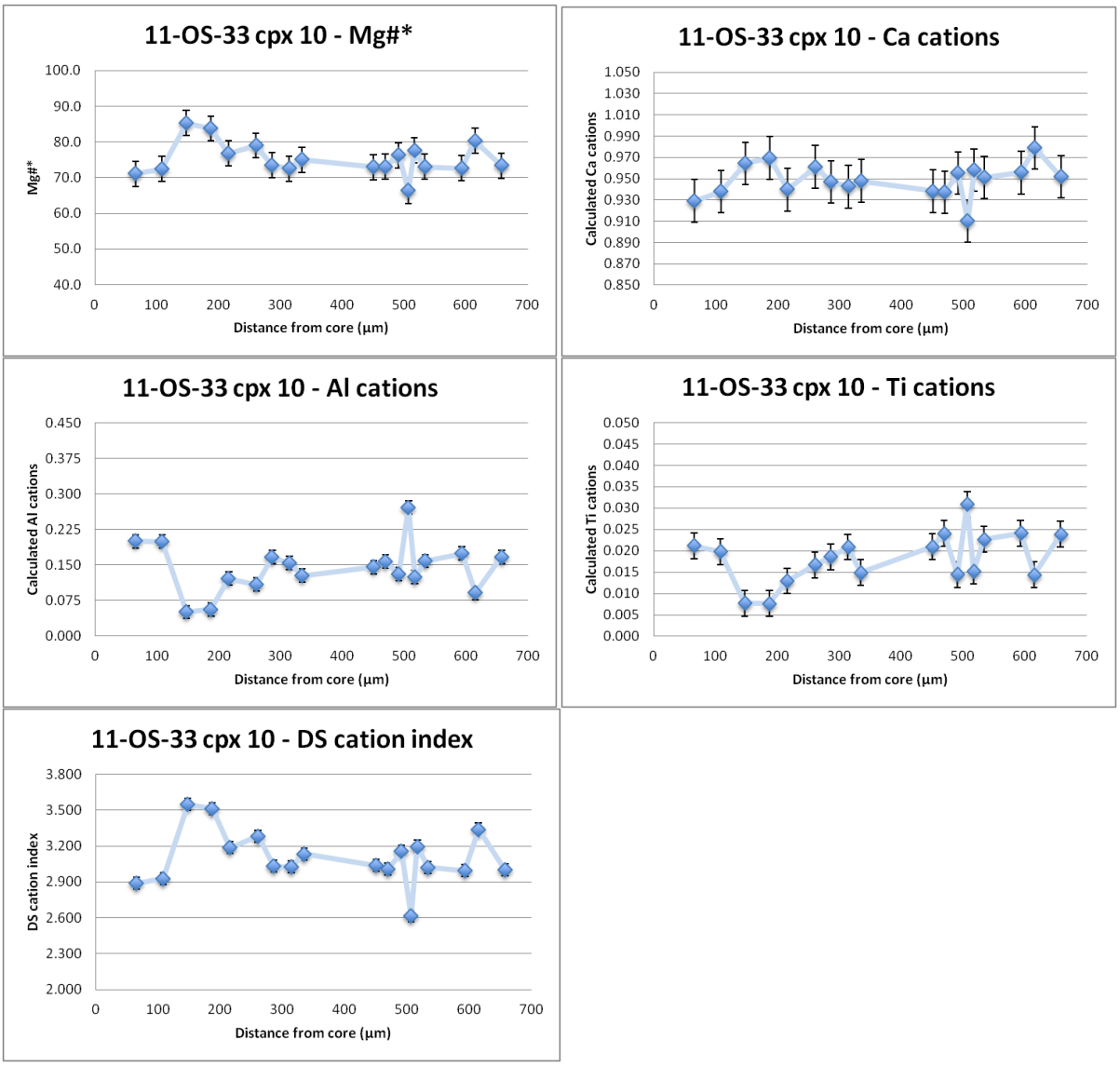

Figure 3.37) Chemical variation plots for 11-OS-33 Cpx 10. The dark band on the backscatter image in Figure 3.34 are seen as positive spikes on both the Mg#* plot and the DS cation index plot and negative spikes on both the Ti and Al cation plots.

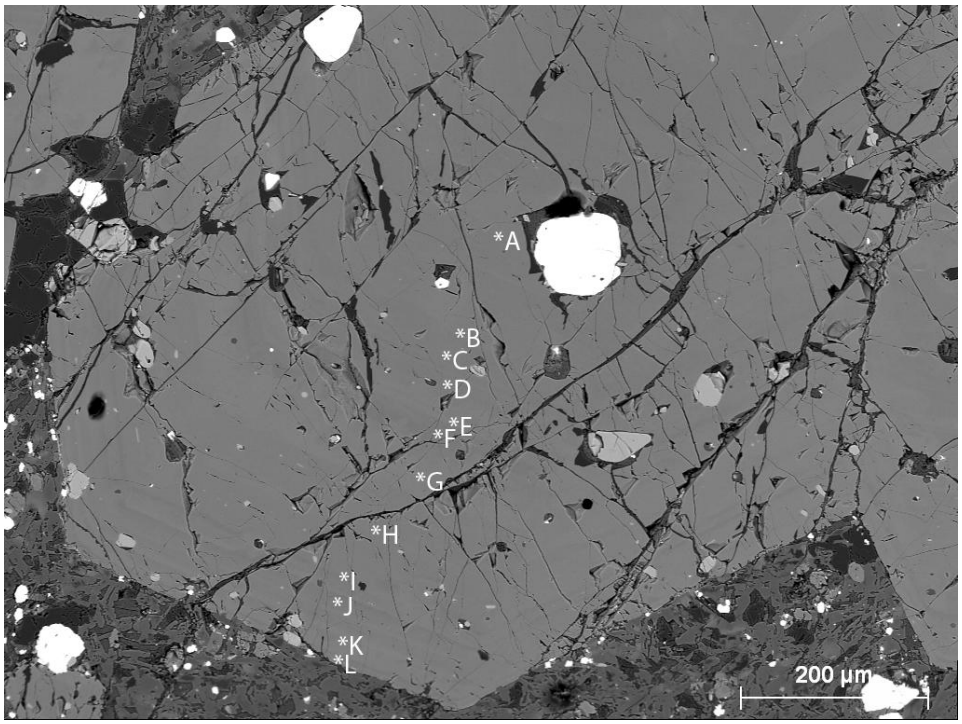

Figure 3.38) Backscatter electron image of 11-OS-33 Cpx 7. Microprobe analysis points indicated by center of asterisk next to letters, individual analyses are presented in Appendix A.

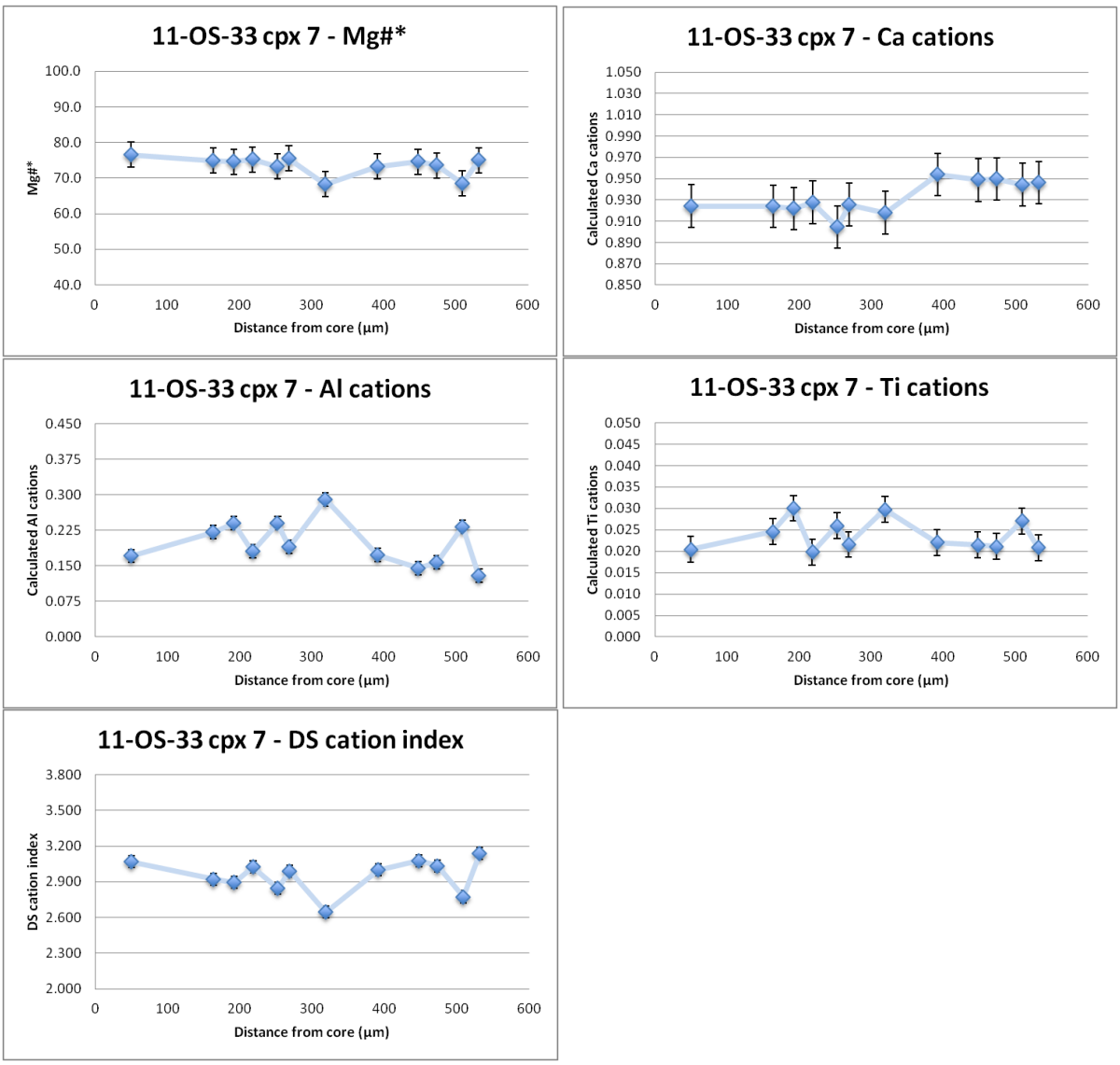

Figure 3.39) Chemical variation plots for 11-OS-33 Cpx 7.

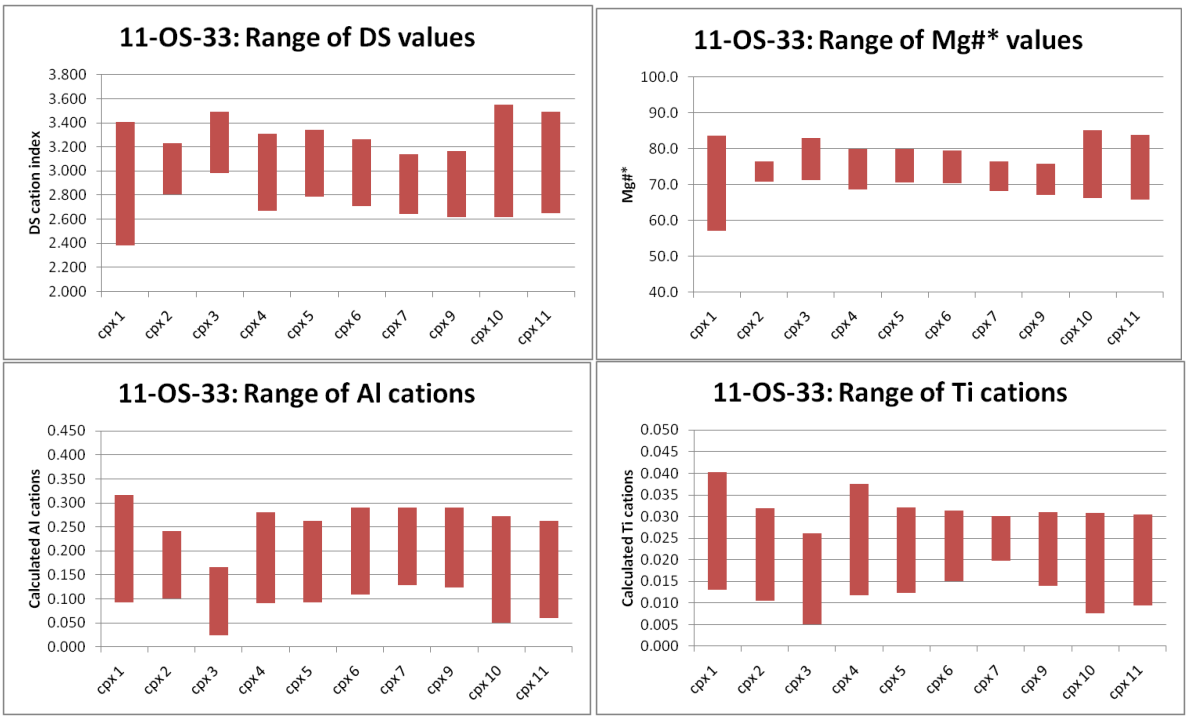

Figure 3.40) Chemical range plots of all clinopyroxene in 11-OS-33.

3.2.2.3 Sample 11-OS-42

Ten clinopyroxene phenocrysts were selected from 11-OS-42 (a leucitite) for analysis. Of the 86 epitaxial bands analyzed all but 11 plotted in the diopside region of the pyroxene quadrilateral as defined my Morimoto et al. 1988; the eleven that did not plotted just above the diopside region indicating wollastonite components above 50% [See Figure 3.41]. The majority of these bands plot within a smaller compositional range than the bands from either 11-OS-12 or 11-OS-33. Specifically they are slightly more Mg-rich than 11-OS-33, however they do not display as many Mg-rich bands as 11-OS-12. Clinopyroxenes from 11-OS-42 display less intense complex zoning in terms of both compositional differences between epitaxial bands and number of bands. The clinopyroxene with the most distinct banding is Cpx 10 which displays a resorbed Fe-rich core followed by a thick nearly homogenous Mg-rich band [See Figure 3.42]. Deposited on top of this Mg-rich band is a Fe-rich band with a composition slightly different to the core, this outer Fe-rich band is interrupted by a thin Mg-rich band [See Figure 3.43]. In contrast Cpx 5 is homogenous, despite being roughly the same size as Cpx 10, and has a composition similar to the outer Fe-rich band of Cpx 10 [See Figure 3.44 and 3.45]. Figure 3.46 shows the restricted composition of Cpx 5 compared to Cpx 10. Figure 3.46 also shows there is a gradation in the compositional ranges between these two pyroxene behaviors with four phenocrysts having very restricted ranges, four having medium sized ranges and two having large ranges.

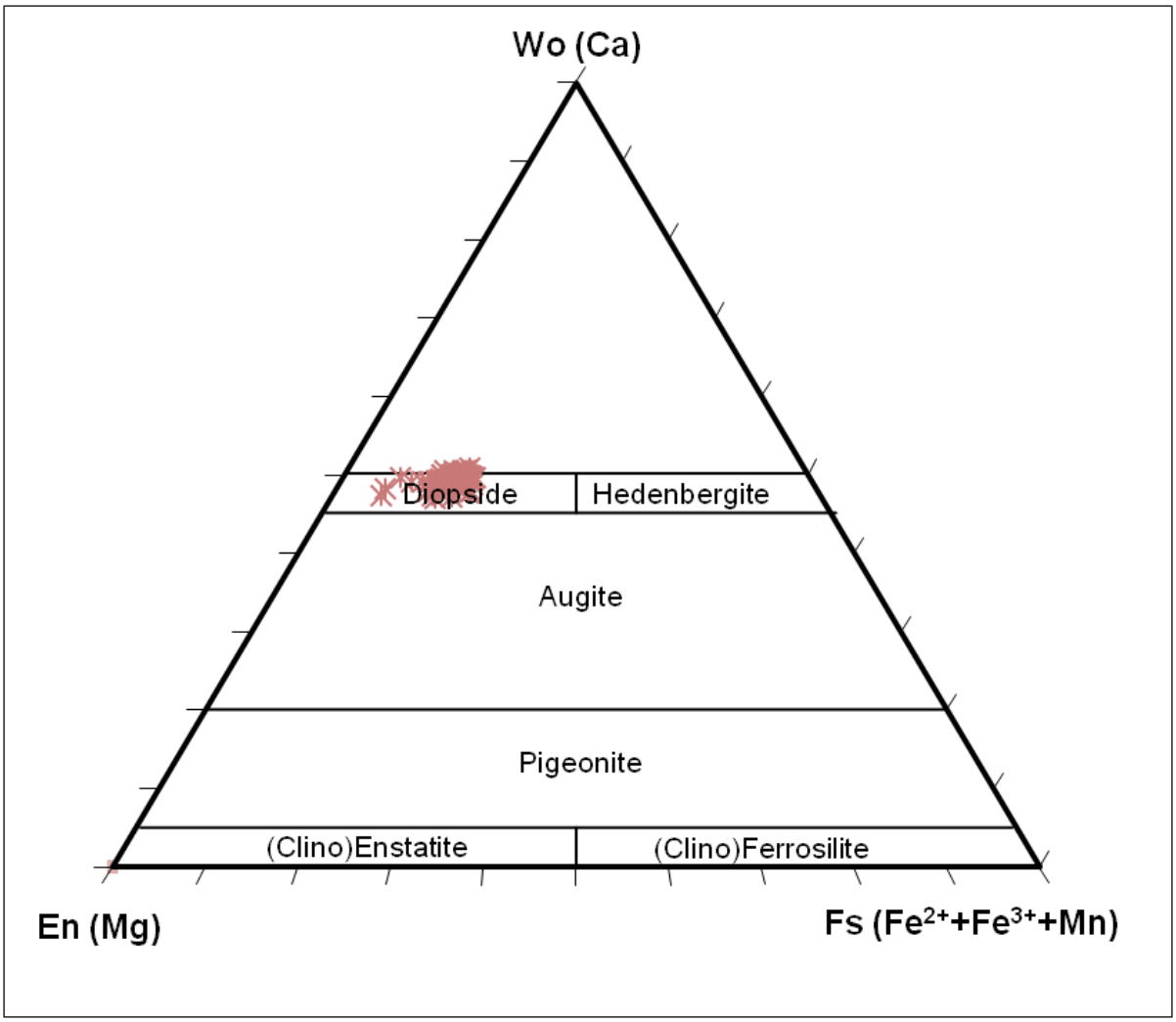

Figure 3.41) Clinopyroxene analyses obtained for 11-OS-33 plotted in the pyroxene quadrilateral based on Morimoto et al. (1988)

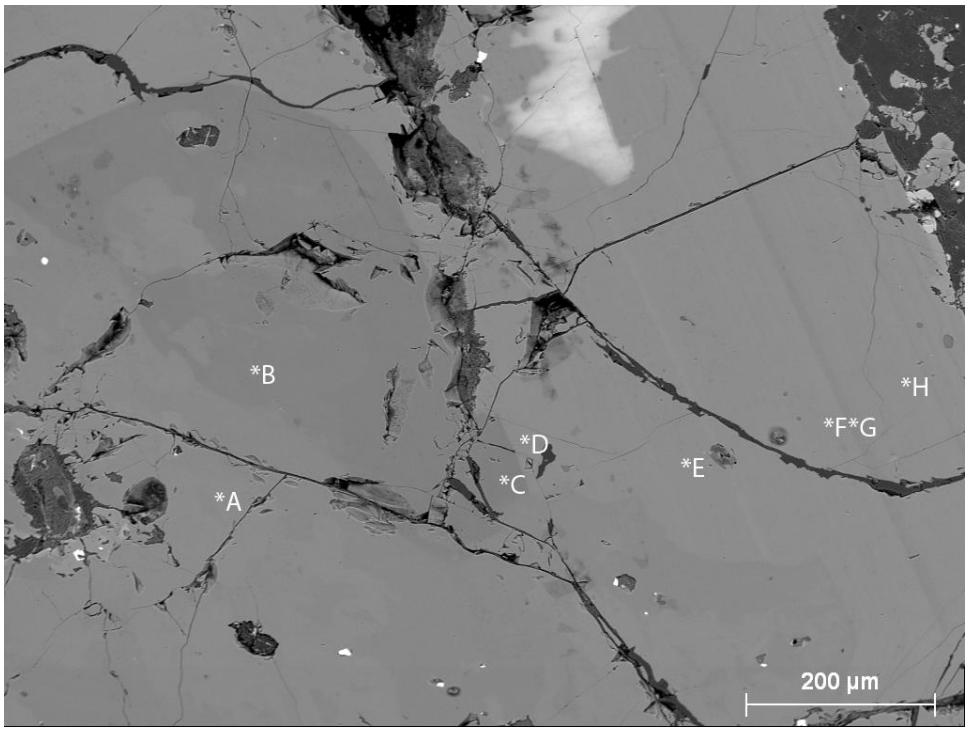

Figure 3.42) Backscatter electron image of 11-OS-42 Cpx 10. Note complex zoning in pyroxene. Microprobe analysis points indicated by center of asterisk next to letters, individual analyses are presented in Table 3.8.

Table 3.8) Representative clinopyroxene of 11-OS-42							
sample	11-OS-42						
Cpx #	Cpx 10						
probe site	a	b	c	d	e	f	g
	Wt% oxide						
SiO_2	47.53	51.85	52.38	48.30	47.88	47.71	49.35
Al_2O_3	5.95	2.18	1.63	4.78	5.10	5.07	3.81
MgO	12.35	15.60	15.91	12.72	12.57	13.12	13.77
FeO	8.40	4.97	3.98	7.60	7.76	8.04	6.42
MnO	0.27	n.d.	0.13	0.09	0.12	0.10	0.13
CaO	22.77	24.73	24.90	24.15	24.07	23.69	24.15
Na_2O	0.74	0.21	0.18	0.33	0.45	0.32	0.26
TiO_2	0.91	0.35	0.23	0.92	1.01	0.98	0.68
Cr_2O_3	n.d.	0.17	0.20	n.d.	n.d.	n.d.	0.31
TOTAL	98.92	100.07	99.54	98.89	98.97	99.02	98.88
	Number of cations in formula						
Si	1.782	1.900	1.926	1.813	1.796	1.787	1.845
Al	0.263	0.094	0.071	0.211	0.226	0.224	0.168
Mg	0.690	0.852	0.872	0.712	0.703	0.732	0.767
Fe^{2+}	0.087	0.057	0.050	0.105	0.085	0.082	0.088
Fe^{3+}	0.176	0.095	0.072	0.134	0.158	0.170	0.112
Mn	0.009	0.000	0.004	0.003	0.004	0.003	0.004
Ca	0.914	0.971	0.981	0.971	0.967	0.951	0.968
Na	0.054	0.015	0.013	0.024	0.033	0.023	0.019
Ti	0.026	0.010	0.006	0.026	0.029	0.028	0.019
Cr	0.000	0.005	0.006	0.000	0.000	0.000	0.009
TOTAL	4.000	4.000	4.000	4.000	4.000	4.000	4.000
$Mg/(Mg+Fe^{+2})*100$	88.8	93.7	94.6	87.1	89.2	89.9	89.7
$Mg/(Mg+Fe_{total})*100$	72.4	84.8	87.7	74.9	74.3	74.4	79.3
Cation Index DS	2.771	3.458	3.568	2.993	2.932	2.941	3.179
Wo	48.7	49.1	49.5	50.5	50.5	49.0	49.9
En	36.8	43.1	44.1	37.0	36.7	37.8	39.6
Fs	14.5	7.7	6.4	12.6	12.9	13.2	10.6

Table 3.8) continued	
sample	11-OS-42
Cpx #	Cpx 10
probe site	h
	Wt% oxide
SiO_2	47.43
Al_2O_3	5.47
MgO	12.50
FeO	8.15
MnO	0.08
CaO	23.62
Na_2O	0.37
TiO_2	1.05
Cr_2O_3	n.d.
TOTAL	98.68
	Number of cations in formula
Si	1.786
Al	0.243
Mg	0.702
Fe^{2+}	0.105
Fe^{3+}	0.152
Mn	0.003
Ca	0.953
Na	0.027
Ti	0.030
Cr	0.000
TOTAL	4.000
$Mg/(Mg+Fe^{+2})*100$	87.0
$Mg/(Mg+Fe_{total})*100$	73.2
Cation Index DS	2.883
Wo	49.8
En	36.7
Fs	13.5

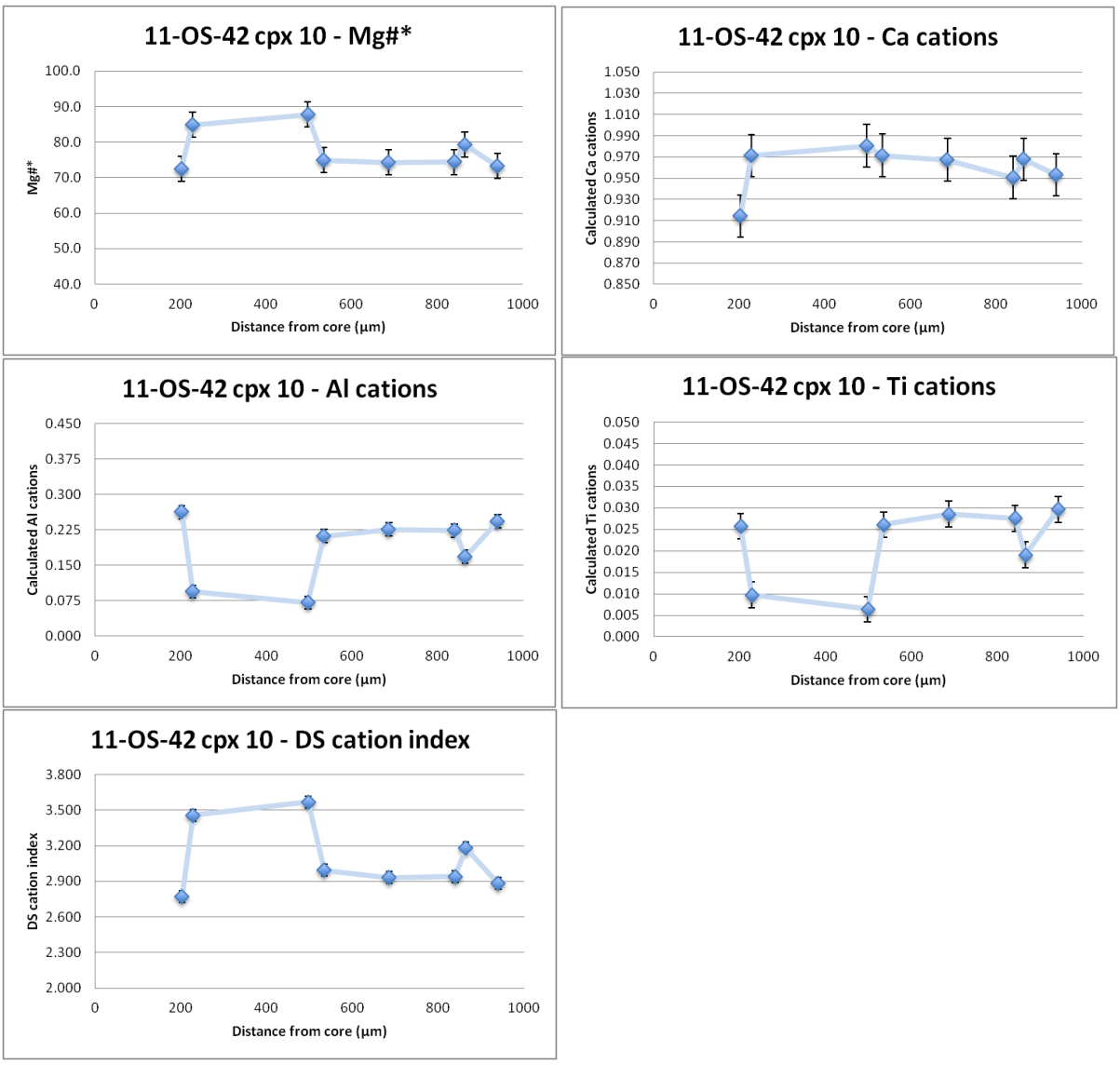

Figure 3.43) Chemical variation plots for 11-OS-42 Cpx 10. The innermost point represents a relatively resorbed Fe-rich core followed by a thick homogenous Mg-rich band which itself is coated with a thick Fe-rich band with a composition different from the core, this outer band is interrupted with a minor Mg-rich band.

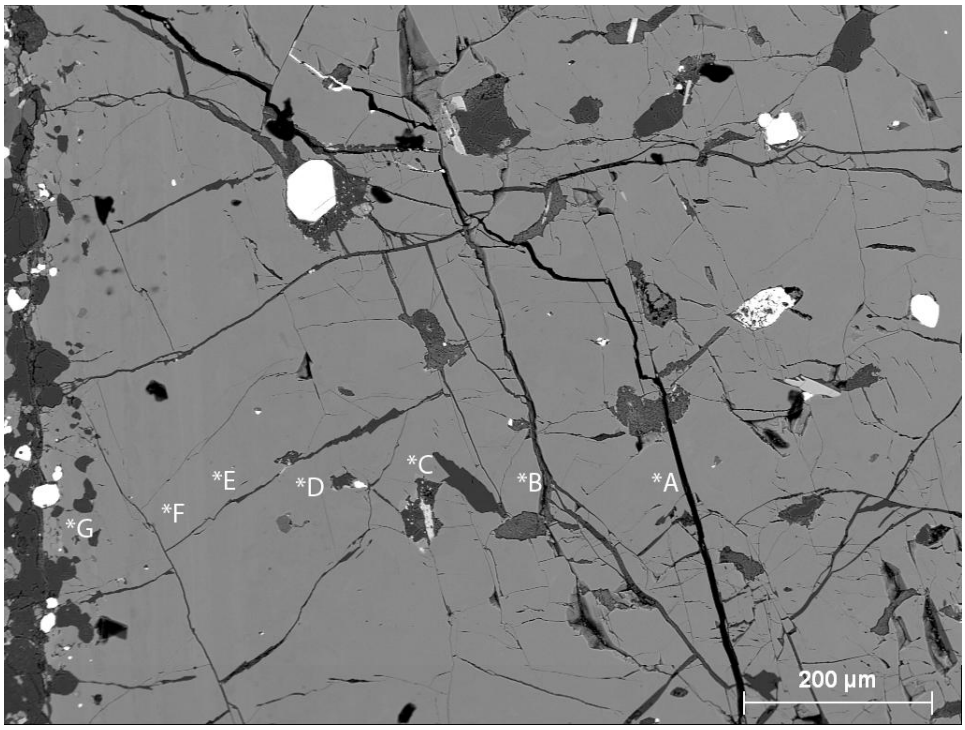

Figure 3.44) Backscatter electron image of 11-OS-42 Cpx 5. Cpx 5 displays a roughly homogenous composition from core to rim. Microprobe analysis points indicated by center of asterisk next to letters, individual analyses are presented in Appendix A.

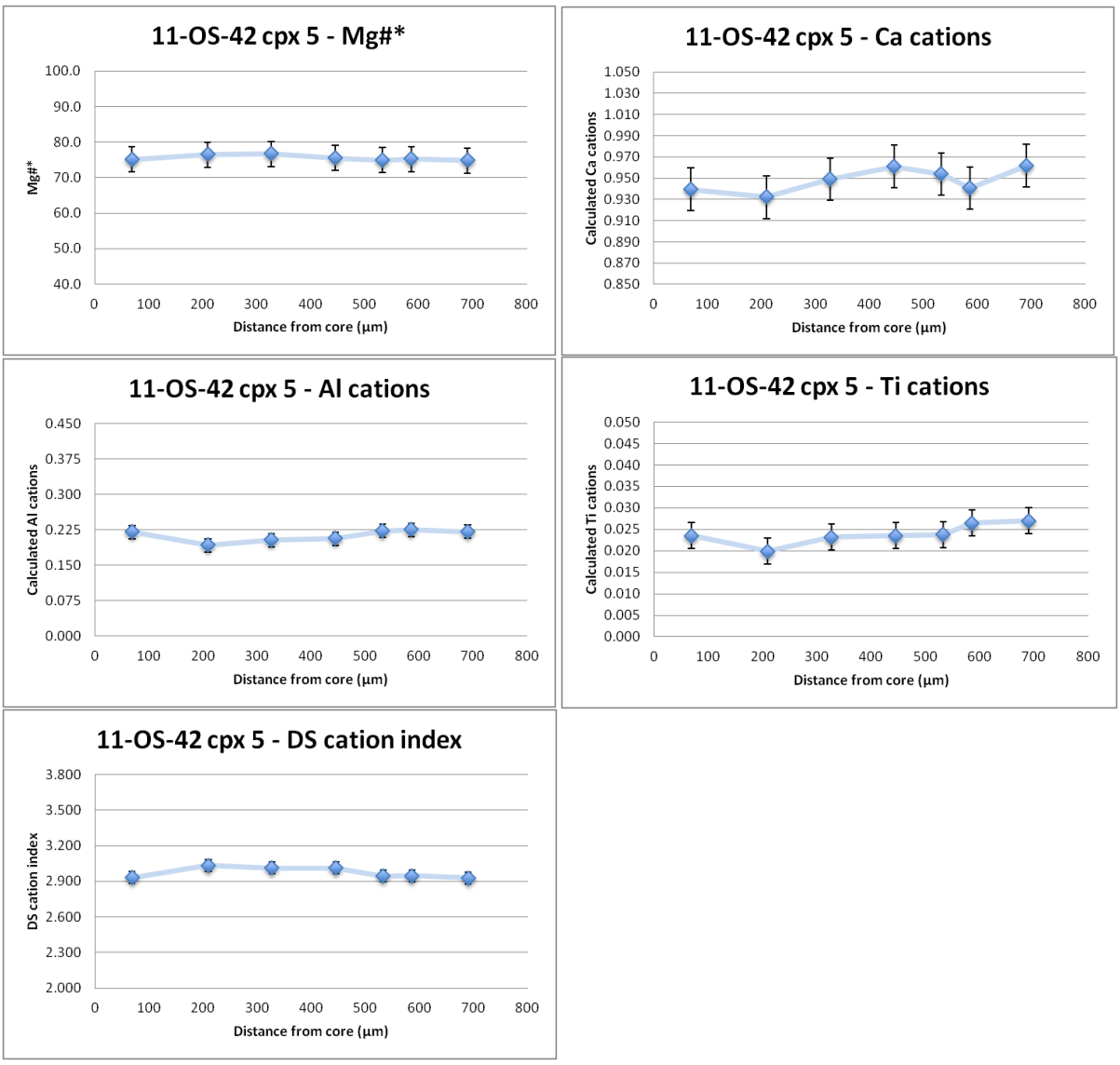

Figure 3.45) Chemical variation plots for 11-OS-42 Cpx 5. Plots show the nearly homogenous Fe-rich composition of the clinopyroxene from core to rim.

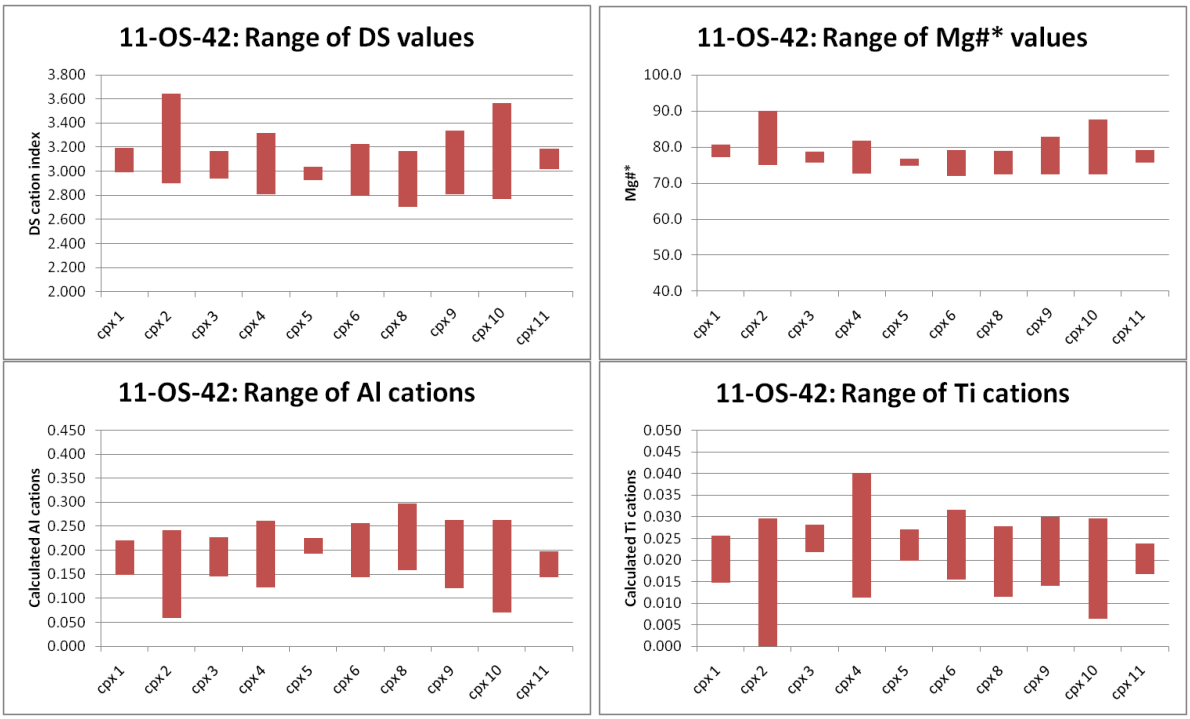

Figure 3.46) Chemical range plots of all clinopyroxene in 11-OS-42.

3.2.3 Kalecik Gökçeören Region

This region hosts a set of samples with widely different mineral assemblages and clinopyroxene behaviors. Sample 11-KT-02 possesses a phenocryst assemblage of fine grained clinopyroxene, biotite, apatite, magnetite, and olivine (now iddingsite) with feldspars and feldspathoids are restricted to groundmass. 11-KT-02 displays clinopyroxenes with weak complex zoning (only minor regressions to a more primitive composition during deposition of epitaxial bands). Sample 11-KT-04D possesses a phenocryst assemblage of coarse-grained clinopyroxene, coarse-grained biotite, and fine-grained magnetite with feldspars and feldspathoids are restricted to groundmass. In 11-KT-04D clinopyroxene phenocrysts display large homogenous Mg-rich cores with mantles of Fe-rich material that display varying numbers of intermittent Mg-rich bands (complexly zoned). Sample 11-KT-03A possesses a phenocryst assemblage of coarse-grained leucite, medium grained clinopyroxene, fine-grained apatite, and fine-grained magnetite; no feldspar present. In 11-KT-03A most clinopyroxene phenocrysts display multiple sets of thick epitaxial bands with sharp resorbed contacts between bands and large compositional differences across the divides. Additionally this sample possesses a minority of large clinopyroxenes without compositional zoning.

3.2.3.1 Sample 11-KT-02

Ten clinopyroxene phenocrysts from sample 11-KT-02 (a minette) were analyzed. All pyroxenes and epitaxial bands plot in the diopside field on the pyroxene quadrilateral as defined by Morimoto et al. (1988) [Figure 3.47]. Clinopyroxene phenocrysts of this sample are roughly the same size as those in 11-KT-03A; however, they display very weak complex zoning. Cpx 6, displays a large inner zone with substantial sieve texture voids near the outer contact filled with more Fe-rich material from the outer epitaxial band [See Figure 3.48]. The small core of the phenocryst displays material with an Mg#* of 81.7 followed by a thick coating of material with a Mg#* value of 88.7 which decreases gradually to 81.9. This inner region has a resorbed outer edge and is coated by a Fe-rich band that is normally zoned with Mg#* values from 75.3 to 69.7 [See figure 3.49]. Cpx 26 possesses a strongly asymmetrical core with weak compositional zoning, and Mg#* values range from 80.8 to 72.1 [See Figure 3.50]; however, calculated aluminum and titanium cations vary quite substantially despite the relatively minor variance in Mg#* [See Figure 3.51]. Cpx 5 displays a functionally homogenous Fe-rich material throughout the crystal despite being similar in size to Cpx 6 [See Figures 3.52 and 3.53]. The compositional range diagrams reveal the widest variance of DS value, Mg#, Al and Ti cation totals within Cpx 6, while Cpx 5 displays variances less than 1/3rd the sizes seen in Cpx 6 [See Figure 3.54].

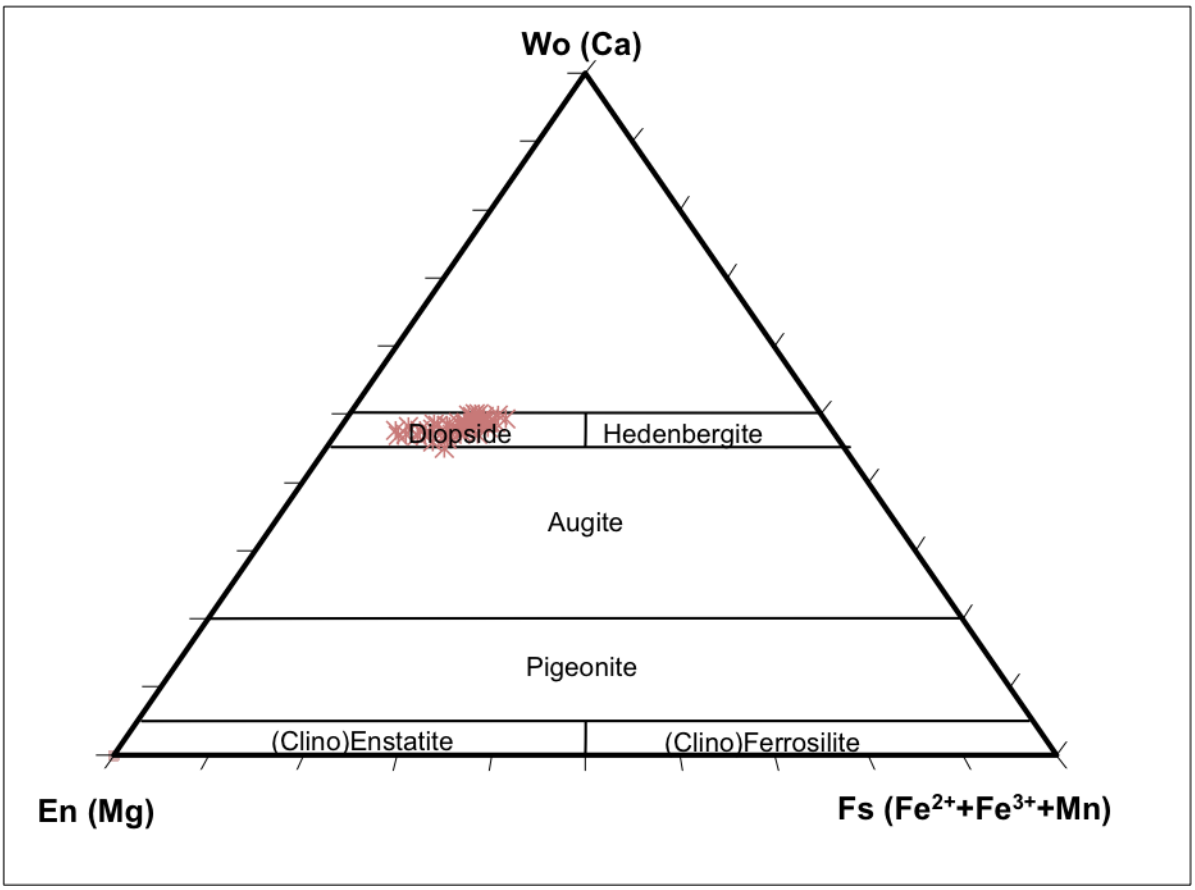

Figure 3.47) Clinopyroxene analyses obtained for 11-KT-02 plotted in the pyroxene quadrilateral based on Morimoto et al. (1988)

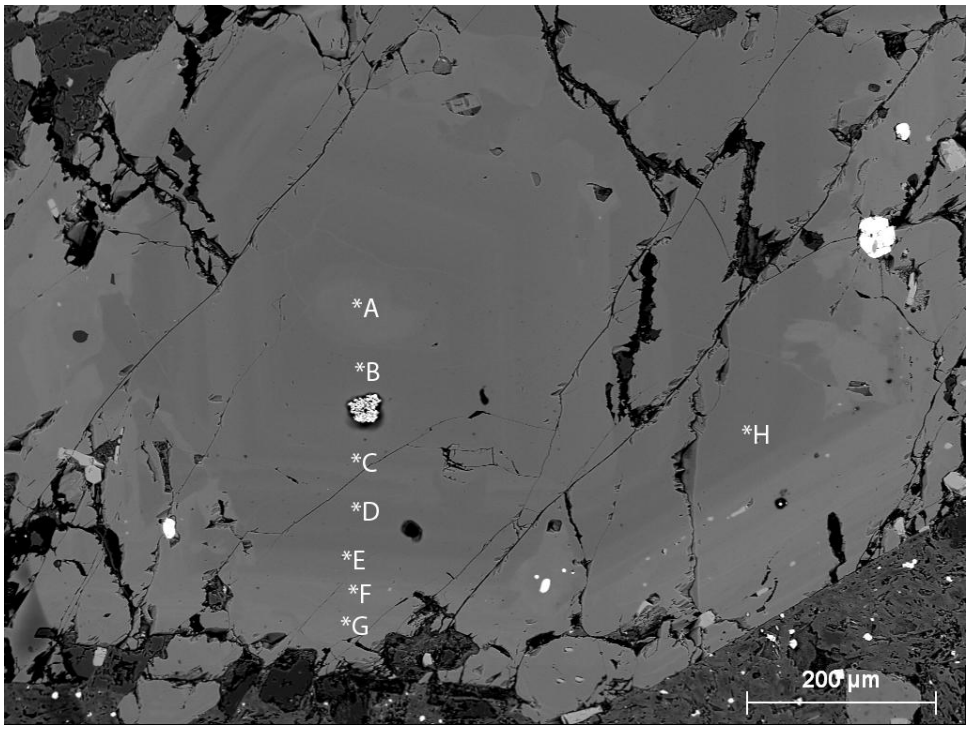

Figure 3.48) Backscatter electron image of 11-KT-02 Cpx 6. Microprobe analysis points indicated by center of asterisk next to letters, individual analyses are presented in Table 3.9

Table 3.9) Representative clinopyroxene analysis of 11-KT-02							
sample	11-KT-02						
Cpx #	Cpx 6						
probe site	a	b	c	d	e	f	g
	Wt% oxide						
SiO_2	51.93	53.33	52.17	52.78	50.47	48.28	47.16
Al_2O_3	1.37	0.97	1.47	1.24	2.43	4.57	5.33
MgO	15.56	17.33	16.76	16.39	15.31	13.10	12.36
FeO	6.21	3.93	4.86	4.47	6.01	7.66	9.59
MnO	0.21	0.10	n.d.	0.11	0.22	0.21	0.42
CaO	23.85	24.73	24.03	24.64	24.73	24.18	23.81
Na_2O	0.21	0.17	0.21	0.20	0.21	0.37	0.47
TiO_2	0.40	0.26	0.33	0.38	0.67	1.05	1.21
Cr_2O_3	n.d.	0.41	0.33	0.21	n.d.	n.d.	n.d.
TOTAL	99.73	101.23	100.16	100.41	100.07	99.42	100.34
	Number of cations in formula						
Si	1.917	1.922	1.904	1.924	1.856	1.802	1.754
Al	0.060	0.041	0.063	0.053	0.105	0.201	0.234
Mg	0.856	0.931	0.911	0.891	0.839	0.729	0.685
Fe^{2+}	0.092	0.017	0.032	0.050	0.024	0.075	0.073
Fe^{3+}	0.100	0.101	0.117	0.086	0.161	0.164	0.225
Mn	0.006	0.003	0.000	0.003	0.007	0.007	0.013
Ca	0.943	0.955	0.940	0.962	0.974	0.967	0.949
Na	0.015	0.012	0.015	0.014	0.015	0.027	0.034
Ti	0.011	0.007	0.009	0.010	0.019	0.029	0.034
Cr	0.000	0.012	0.010	0.006	0.000	0.000	0.000
TOTAL	4.000	4.000	4.000	4.000	4.000	4.000	4.000
$Mg/(Mg+Fe^{+2})*100$	90.3	98.2	96.6	94.7	97.3	90.7	90.3
$Mg/(Mg+Fe_{total})*100$	81.7	88.7	86.0	86.7	81.9	75.3	69.7
Cation Index DS	3.431	3.637	3.529	3.566	3.338	2.994	2.775
Wo	47.2	47.6	47.0	48.3	48.6	49.8	48.8
En	42.9	46.4	45.6	44.7	41.9	37.5	35.2
Fs	9.9	6.0	7.4	7.0	9.6	12.6	16.0

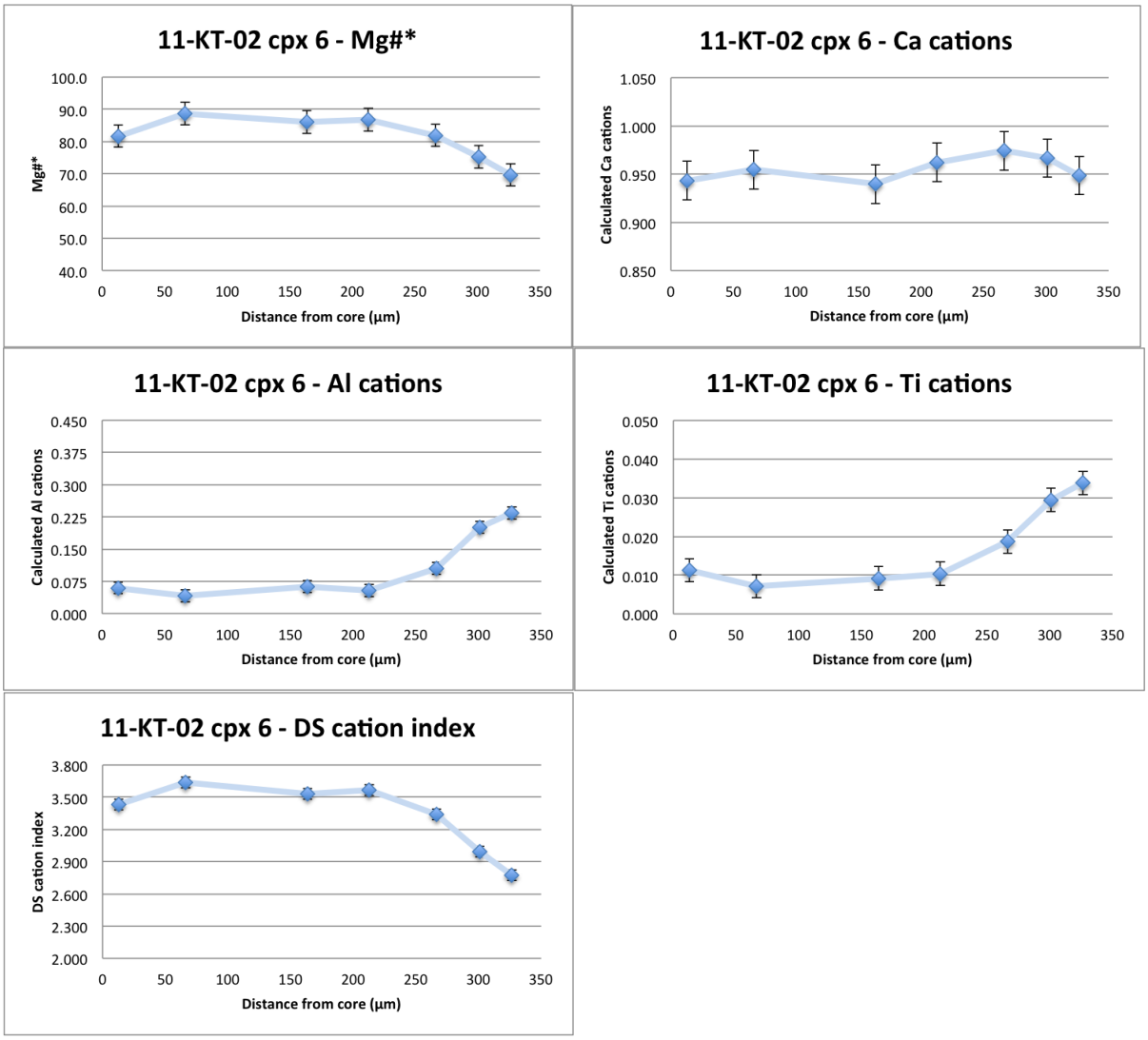

Figure 3.49) Chemical variation plots for 11-KT-02 Cpx 6

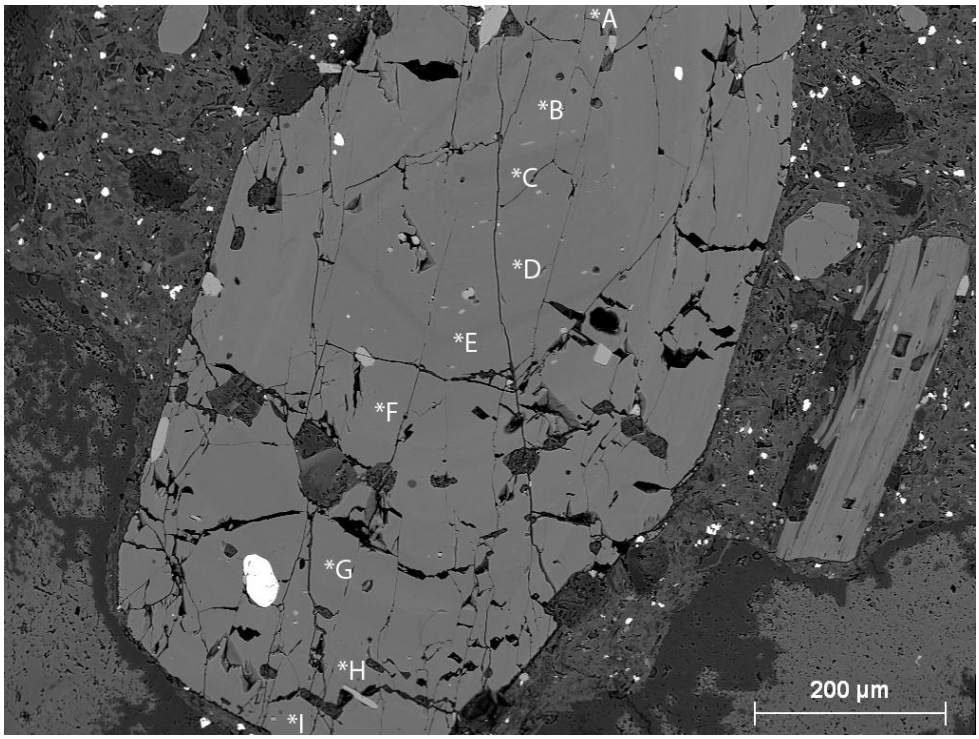

Figure 3.50) Backscatter electron image of 11-KT-02 Cpx 26. Cpx 26 shows minor complex zoning. Microprobe analysis points indicated by center of asterisk next to letters, individual analyses are presented in Appendix A.

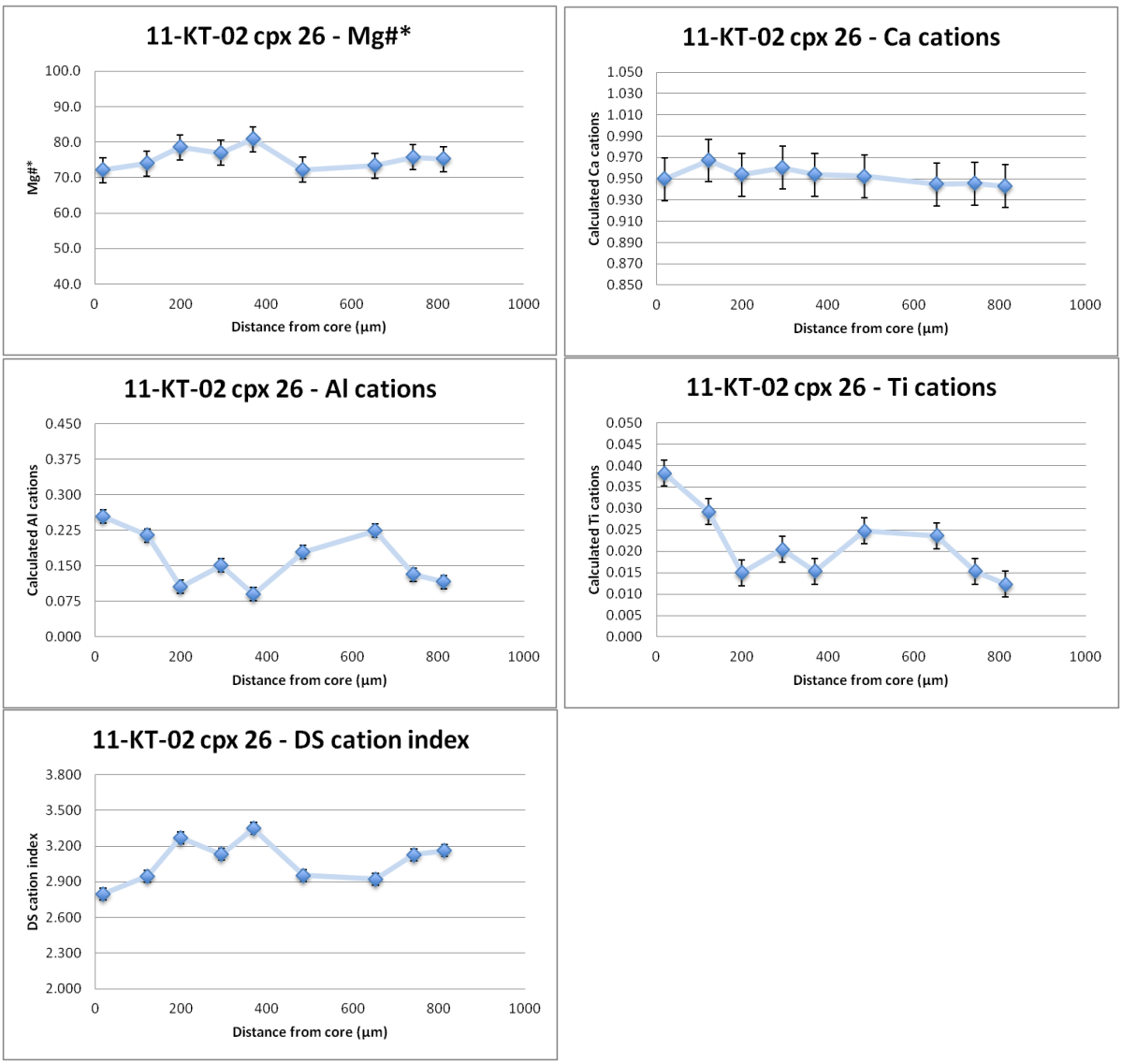

Figure 3.51) Chemical variation plots for 11-KT-02 Cpx 26. When compared to other pyroxenes in this study the Al and Ti cation totals of this sample appear to vary more than what would be expected given the small range of Mg#*.

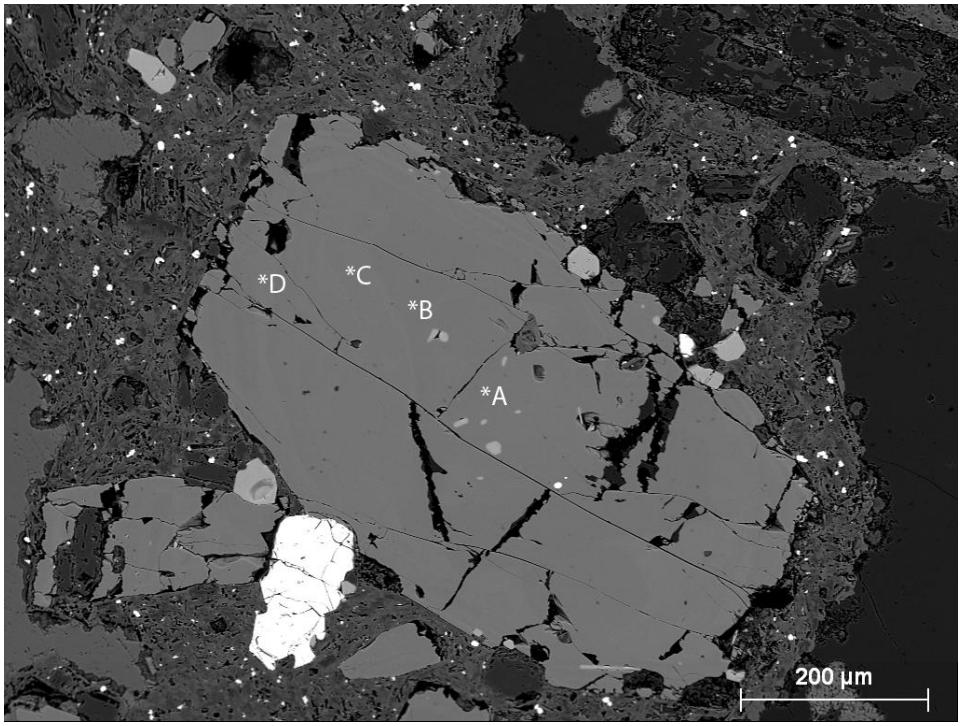

Figure 3.52) Backscatter electron image of 11-KT-02 Cpx 5. Cpx 5 is nearly compositionally homogenous. Analysis points indicated by center of asterisk next to letters, individual analyses are presented in Appendix A.

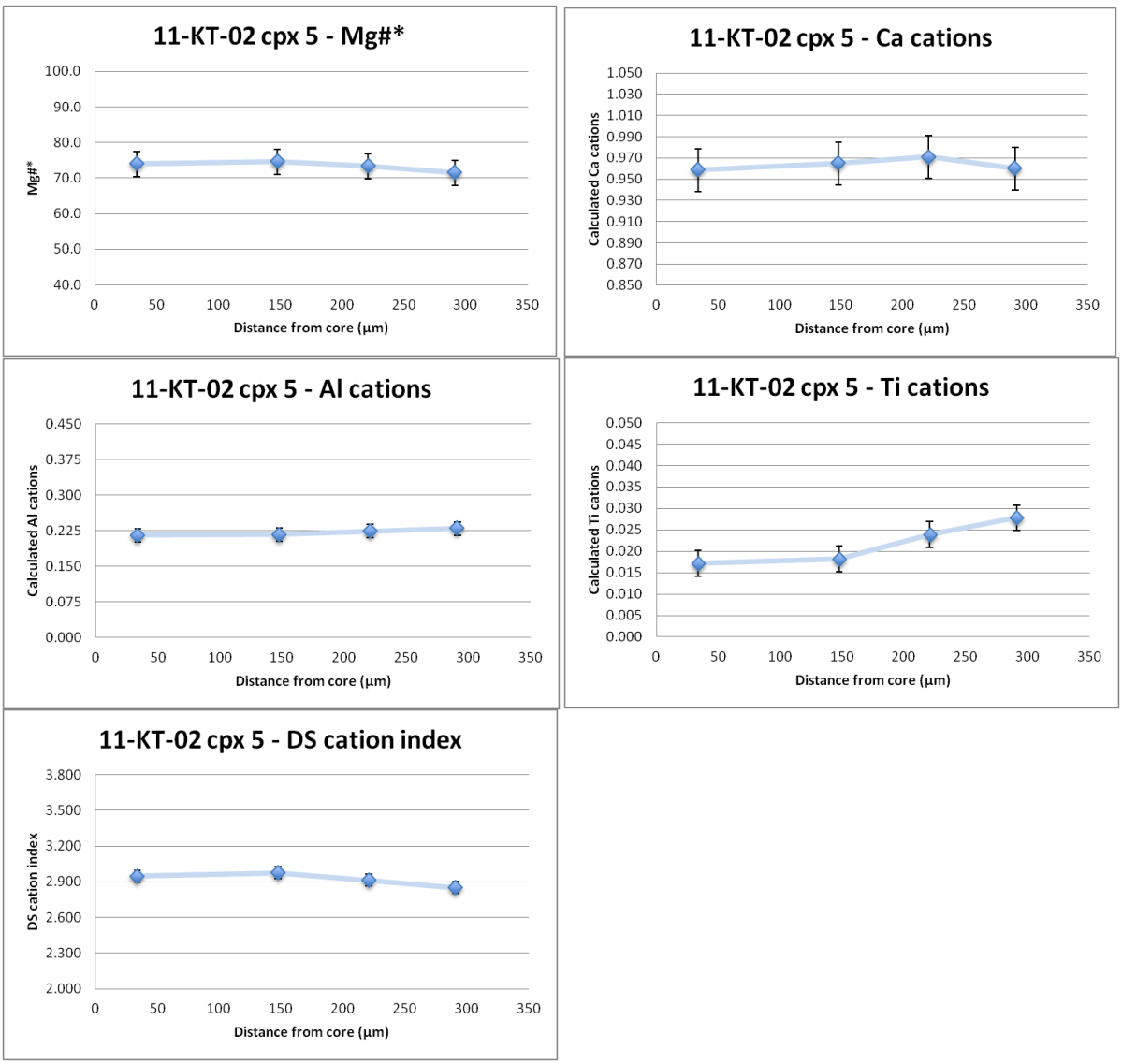

Figure 3.53) Chemical variation plots for 11-KT-02 Cpx 5. Cpx 5 is nearly compositionally homogenous.

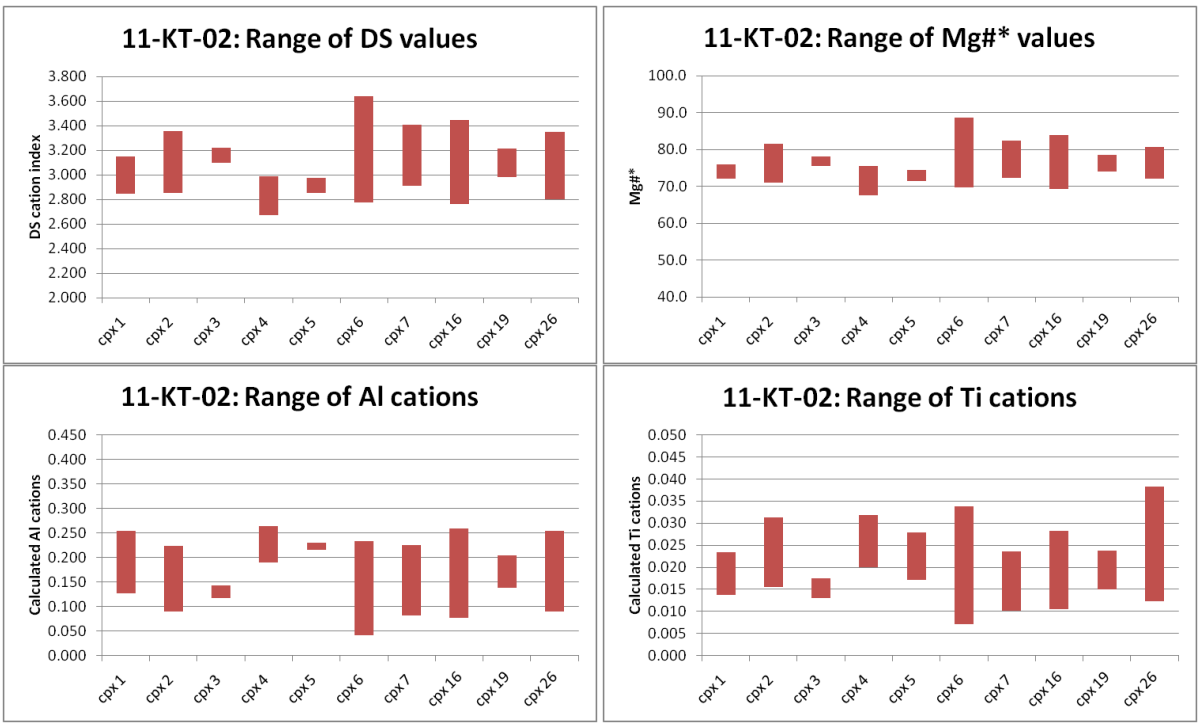

Figure 3.54) Chemical range plots of all clinopyroxene in 11-KT-02.

3.2.3.2 Sample 11-KT-03A

Eleven clinopyroxene phenocrysts from sample 11-KT-03A (a leucitite) were analyzed. In this sample 88% of the pyroxene epitaxial bands analyzed plot in the unnamed region above the diopside-hedenbergite join on the Morimoto et al. (1988) pyroxene quadrilateral, indicating that these probe locations host compositions with wollastonite components greater than 50% [Figure 3.55]. An additional feature that distinguishes this sample from others seen in this study is that 24% of points analyzed contain more atomic proportions of iron than magnesium; they would plot in the hedenbergite region if not for the high calcium – aluminum content [Figure 3.55]. Phenocrysts in this sample display very strong complex zoning, alternating Fe-rich and Mg-rich epitaxial bands separated by resorption surfaces with sharp contacts. Prime examples of this are Cpx 2 and Cpx 3, both of which display multiple reverse zoning events [See Figure 3.56]. Chemical variation diagrams show that the composition of Cpx 2, while varying substantially, alternates between a Fe-rich mode and a Mg-rich mode during the progression from the core to the rim without an overall increase in the contents of 'evolved-normative' cations (Fe, Al, Ti) [See Figure 3.57]. Chemical variation diagrams for Cpx 3 are similar in showing the bi-modal behavior however there appears to be a slight overall increase in Fe and Ti content of the clinopyroxene towards the rim [See Figure 3.58]. Save the thin outermost Fe-rich coating, Cpx 5 lacks any apparent zoning visible in BSE images and is considerably larger than phenocrysts of other families, approximately 1.5 mm across compared to 0.5 mm [Figure 3.59]. That said the core of Cpx 5 has significant variations in the concentrations of Ca, Al, and Ti despite having a homogenous Mg#* [Figure 3.60]. Figure 3.61 demonstrates behavioral differences among crystals in this sample.

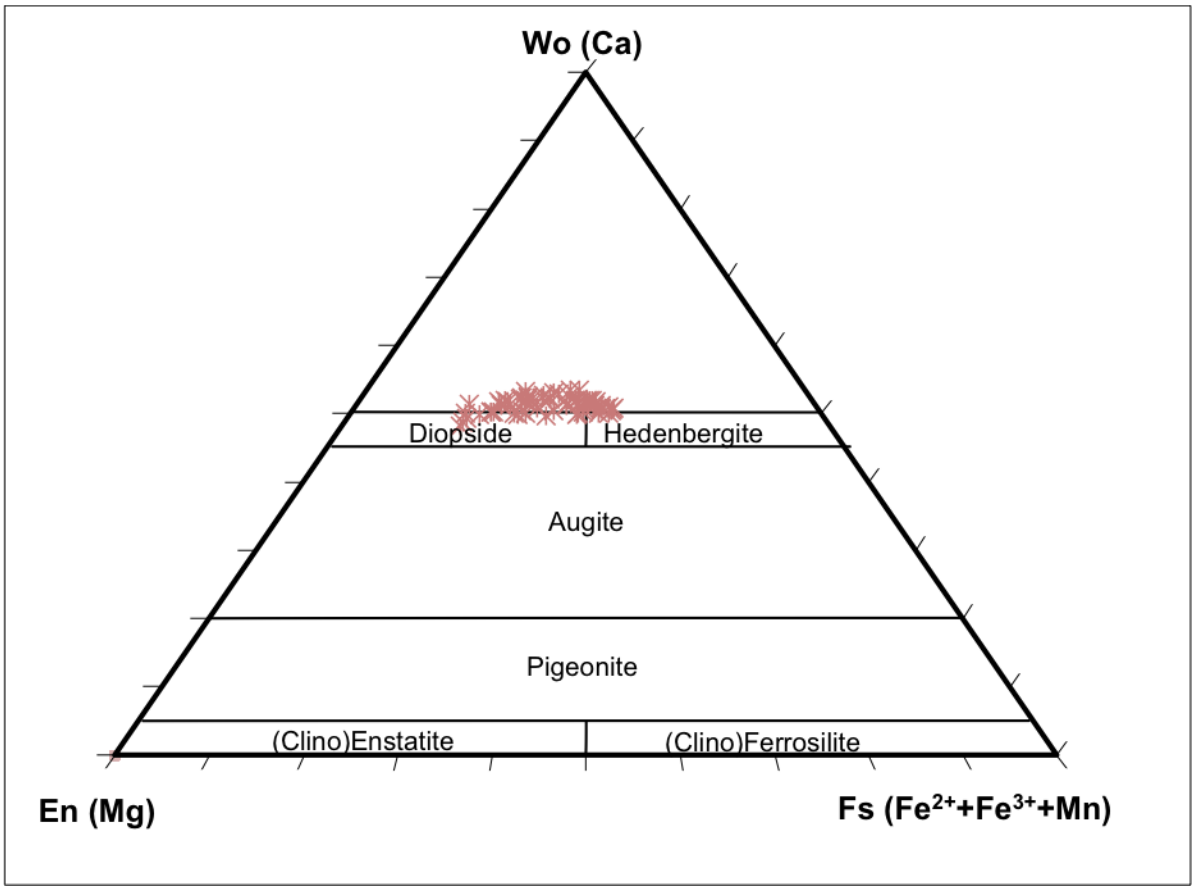

Figure 3.55) Clinopyroxene analyses obtained for 11-KT-03A plotted in the pyroxene quadrilateral based on Morimoto et al. (1988).

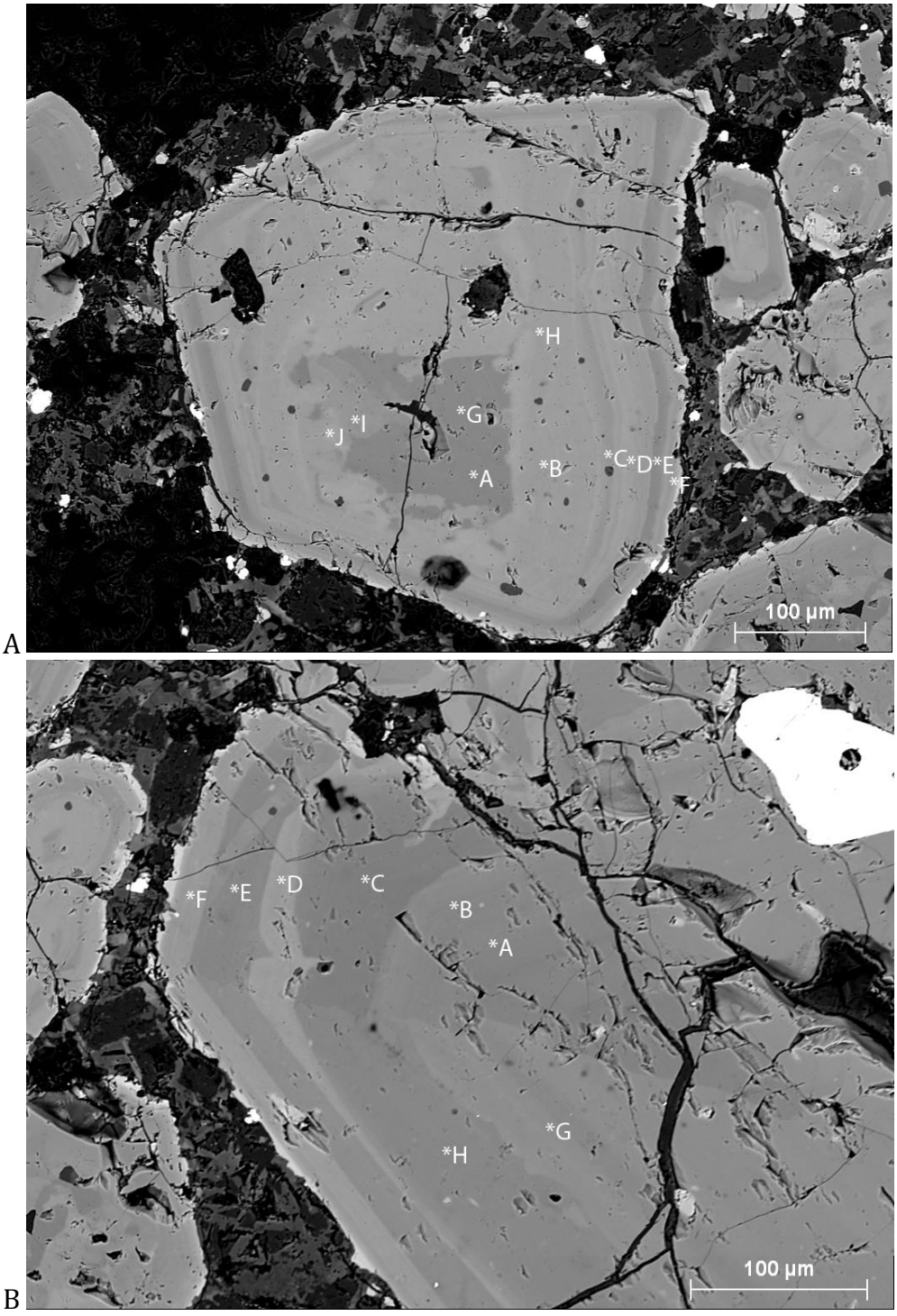

Figure 3.56) Backscatter electron images of 11-KT-03A: A) Cpx 2 and B) Cpx 3. Microprobe analysis points indicated by center of asterisk next to letters, individual analyses for Cpx 2 are presented in Table 3.10 and those for Cpx 3 are presented in Appendix A.

Table 3.10) Representative clinopyroxene analysis of 11-KT-03A							
sample	11-KT-03A						
Cpx #	Cpx 2						
probe site	a	b	c	d	e	f	g
	Wt% oxide						
SiO_2	49.58	49.02	46.59	48.89	50.58	49.24	43.75
Al_2O_3	4.43	3.63	4.75	3.81	2.42	3.31	5.93
MgO	12.16	13.01	9.73	12.23	13.69	11.13	7.78
FeO	8.93	8.55	12.35	9.34	7.54	10.88	15.26
MnO	0.19	0.26	0.71	0.15	0.27	0.78	0.59
CaO	24.37	24.79	24.09	24.64	25.28	24.58	23.99
Na_2O	0.29	0.42	0.68	0.49	0.38	0.64	0.67
TiO_2	0.70	0.59	0.84	0.60	0.41	0.48	1.42
Cr_2O_3	n.d.	n.d.	n.d.	n.d.	n.d.	n.d.	n.d.
TOTAL	100.65	100.29	99.75	100.16	100.57	101.03	99.40
	Number of cations in formula						
Si	1.840	1.817	1.768	1.821	1.865	1.834	1.688
Al	0.194	0.159	0.213	0.167	0.105	0.145	0.270
Mg	0.673	0.719	0.550	0.679	0.752	0.618	0.448
Fe^{2+}	0.169	0.061	0.139	0.099	0.062	0.132	0.170
Fe^{3+}	0.108	0.204	0.253	0.192	0.170	0.207	0.323
Mn	0.006	0.008	0.023	0.005	0.008	0.024	0.019
Ca	0.969	0.985	0.980	0.984	0.999	0.981	0.992
Na	0.021	0.030	0.050	0.036	0.027	0.046	0.050
Ti	0.020	0.017	0.024	0.017	0.011	0.013	0.041
Cr	0.000	0.000	0.000	0.000	0.000	0.000	0.000
TOTAL	4.000	4.000	4.000	4.000	4.000	4.000	4.000
$Mg/(Mg+Fe^{+2})*100$	79.9	92.2	79.9	87.2	92.4	82.4	72.5
$Mg/(Mg+Fe_{total})*100$	70.8	73.1	58.4	70.0	76.4	64.6	47.6
Cation Index DS	2.964	3.042	2.597	2.968	3.230	2.864	2.255
Wo	50.3	49.8	50.4	50.2	50.1	50.0	50.8
En	35.0	36.4	28.3	34.7	37.8	31.5	22.9
Fs	14.7	13.8	21.3	15.1	12.1	18.5	26.2

Table 3.10) continued		
sample	11-KT-03A	
Cpx #	Cpx 2	
probe site	h	i
	Wt% oxide	
SiO_2	44.17	42.29
Al_2O_3	6.47	7.81
MgO	9.04	7.62
FeO	13.09	15.19
MnO	0.40	0.36
CaO	24.35	23.91
Na_2O	0.51	0.62
TiO_2	1.06	1.40
Cr_2O_3	n.d.	n.d.
TOTAL	99.08	99.19
	Number of cations in formula	
Si	1.692	1.631
Al	0.292	0.355
Mg	0.516	0.438
Fe^{2+}	0.118	0.142
Fe^{3+}	0.302	0.348
Mn	0.013	0.012
Ca	1.000	0.988
Na	0.038	0.046
Ti	0.031	0.041
Cr	0.000	0.000
TOTAL	4.000	4.000
$Mg/(Mg+Fe^{+2})*100$	81.4	75.6
$Mg/(Mg+Fe_{total})*100$	55.2	47.2
Cation Index DS	2.415	2.114
Wo	51.3	51.3
En	26.5	22.7
Fs	22.2	26.0

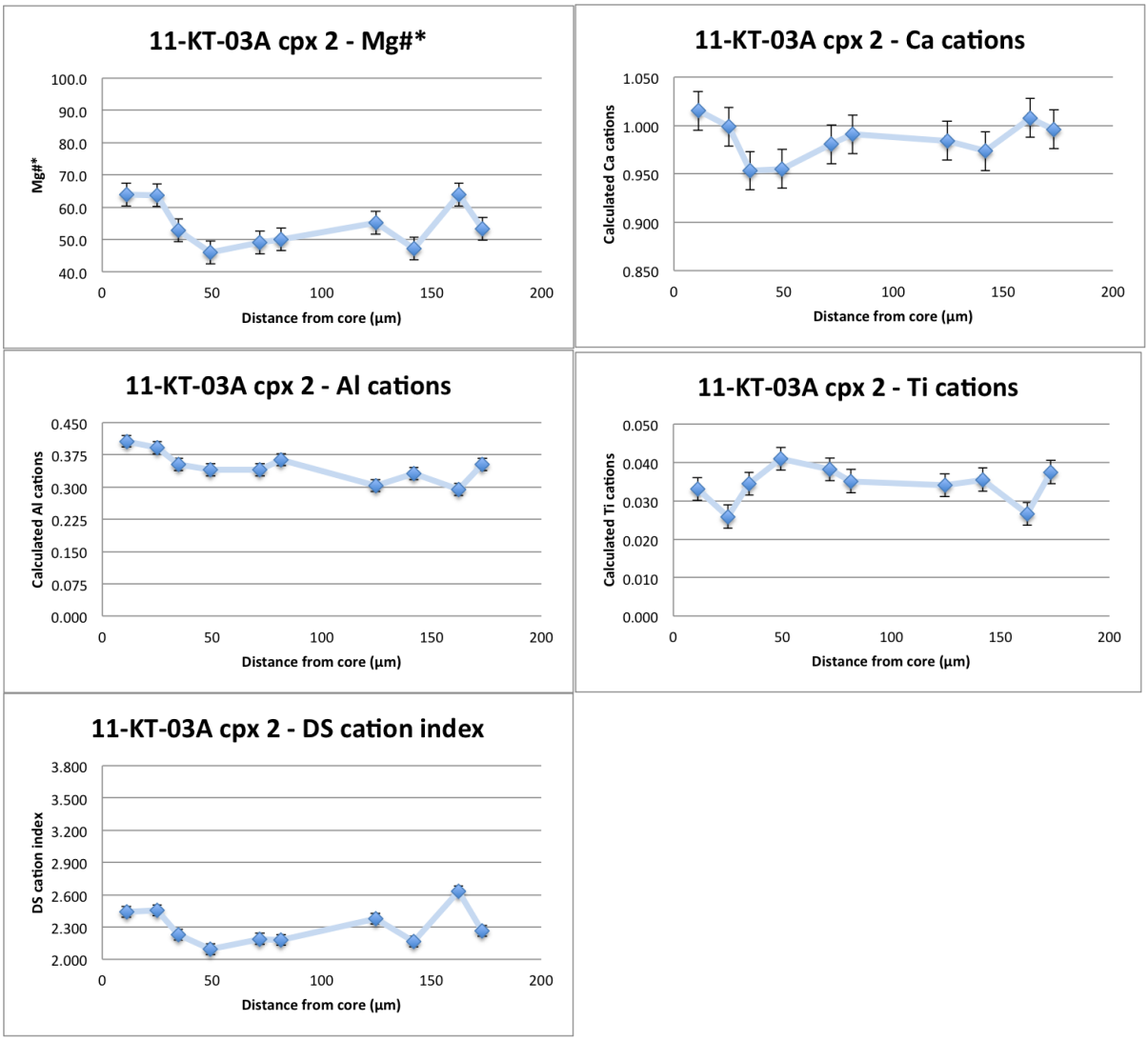

Figure 3.57) Chemical variation plots for 11-KT-03A Cpx 2.

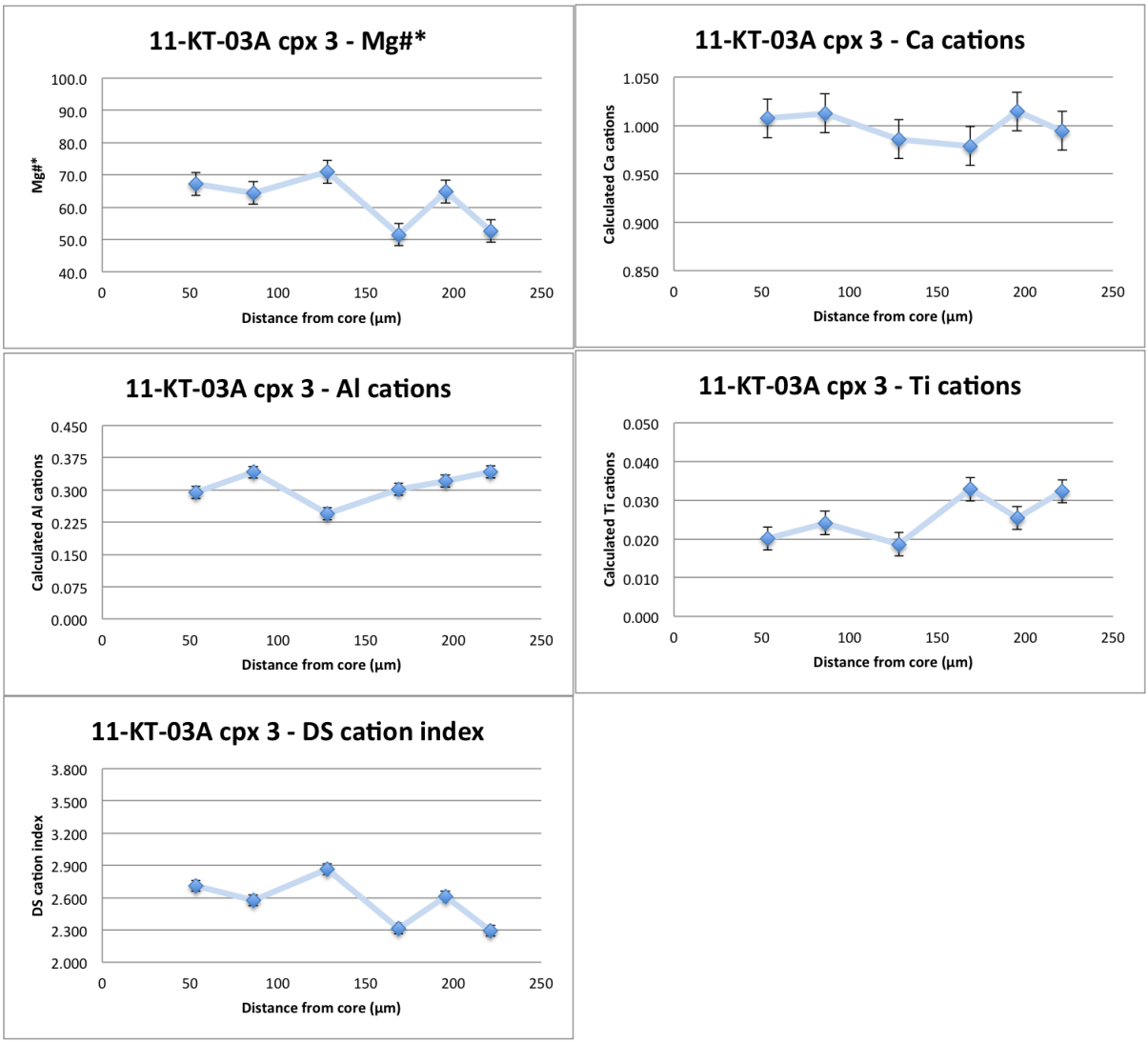

Figure 3.58) Chemical variation plots for 11-KT-03A Cpx 3.

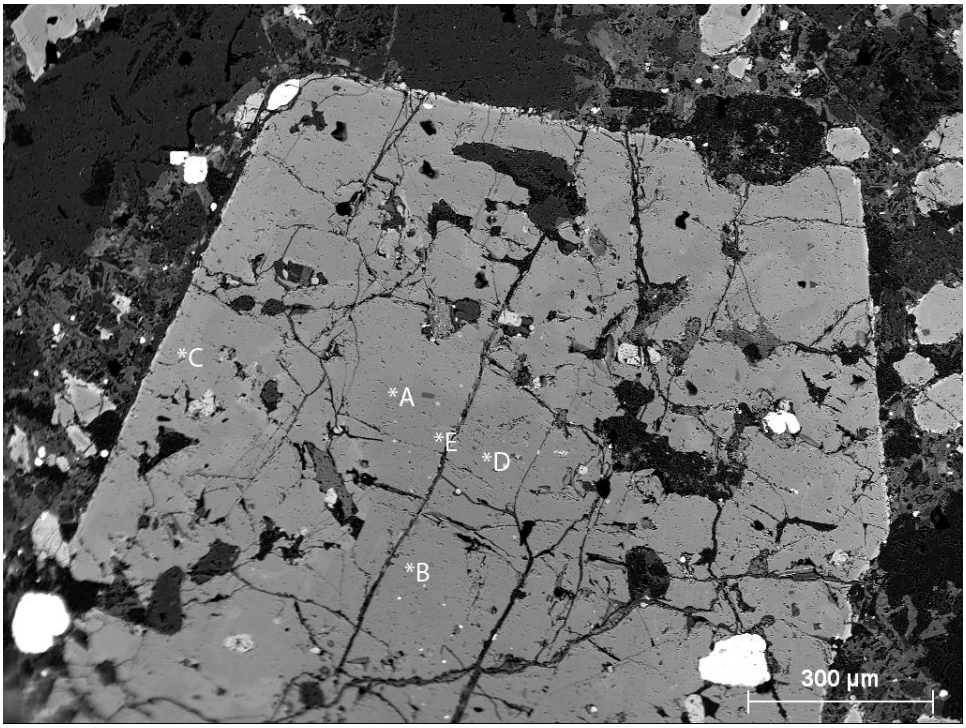

Figure 3.59) Backscatter electron image of 11-KT-03A Cpx 5. Microprobe analysis points indicated by center of asterisk next to letters, individual analyses are presented in Appendix A

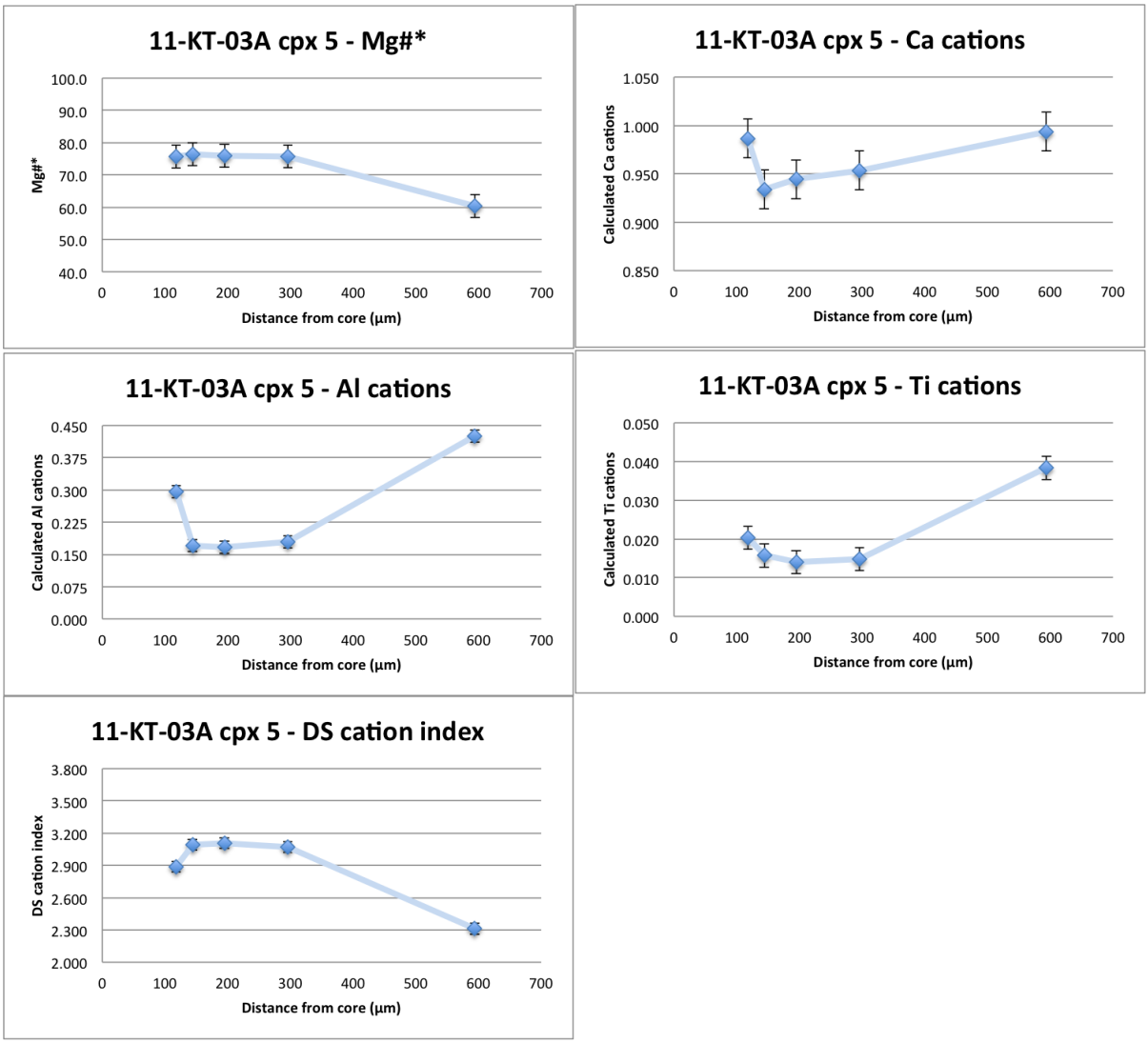

Figure 3.60) Chemical variation plots for 11-KT-03A Cpx 5. The right most data point was taken from the thin outermost Fe-rich rim of the pyroxene.

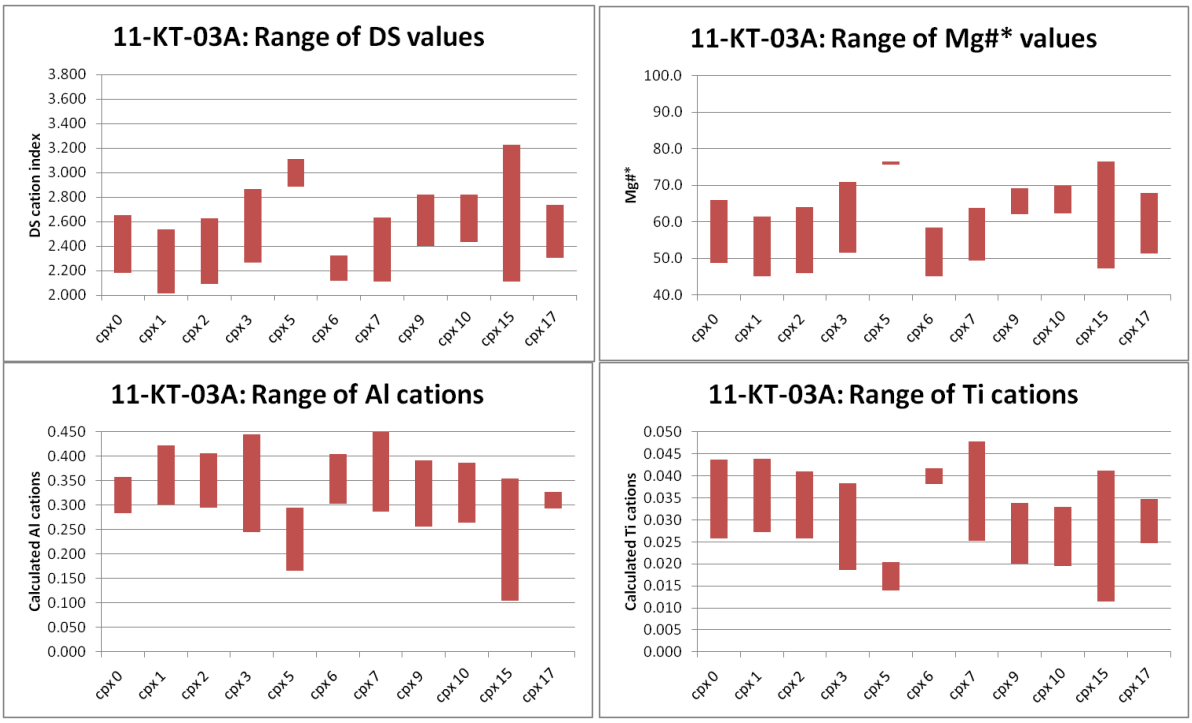

Figure 3.61) Chemical range plots of all clinopyroxene in 11-KT-03A. The outermost thin epitaxial band found on Cpx 5 and Cpx 9 was excluded from this graph as it obscured the remarkable homogeneity inside each crystal and produced the illusion of internal complex zoning.

3.2.3.3 Sample 11-KT-04D

Ten clinopyroxene phenocrysts from sample 11-KT-04D (diopside-phlogopite lamprophyre) were analyzed. Most of the epitaxial bands analyzed plot in the diopside field of pyroxene quadrilateral from Morinoto et al (1988), though 14 of the 62 analysis points possessed wollastonite components greater than 50 (albeit slightly) [Figure 3.62]. The pyroxene quadrilateral for 11-KT-04D [Figure 3.62] shows that the chemical ranges of the clinopyroxenes in this sample are considerably more primitive in nature compared to the ranges of clinopyroxenes in 11-KT-03A (a leucitite) [Figure 3.55] and are similar to the ranges of clinopyroxenes in 11-KT-02 (a minette) [Figure 3.47]. Nine out of the ten clinopyroxenes analyzed display large homogenous Mg-rich cores followed a thick set of epitaxial bands that become progressively more Fe-rich outward [Figure 3.63]. Occasional resorption features paired with small Mg-rich bands interrupt this Fe-rich set of epitaxial bands; these events are not recorded in all phenocrysts and are accompanied by changes in Al and Ti cation totals [Figure 3.64]. The phenocryst that does not have a Mg-rich core (Cpx 8) has an overall Fe-rich composition that matches the composition of the outer band found in the other clinopyroxenes. That observation in conjunction with the phenocryst's smaller size seems to indicate that it was sampled in such a way that the Mg-rich core, if it exists, was not dissected. The component range diagrams show consistent behavior of various chemical components of all clinopyroxenes in this sample, save Cpx 8 [Figure 3.65].

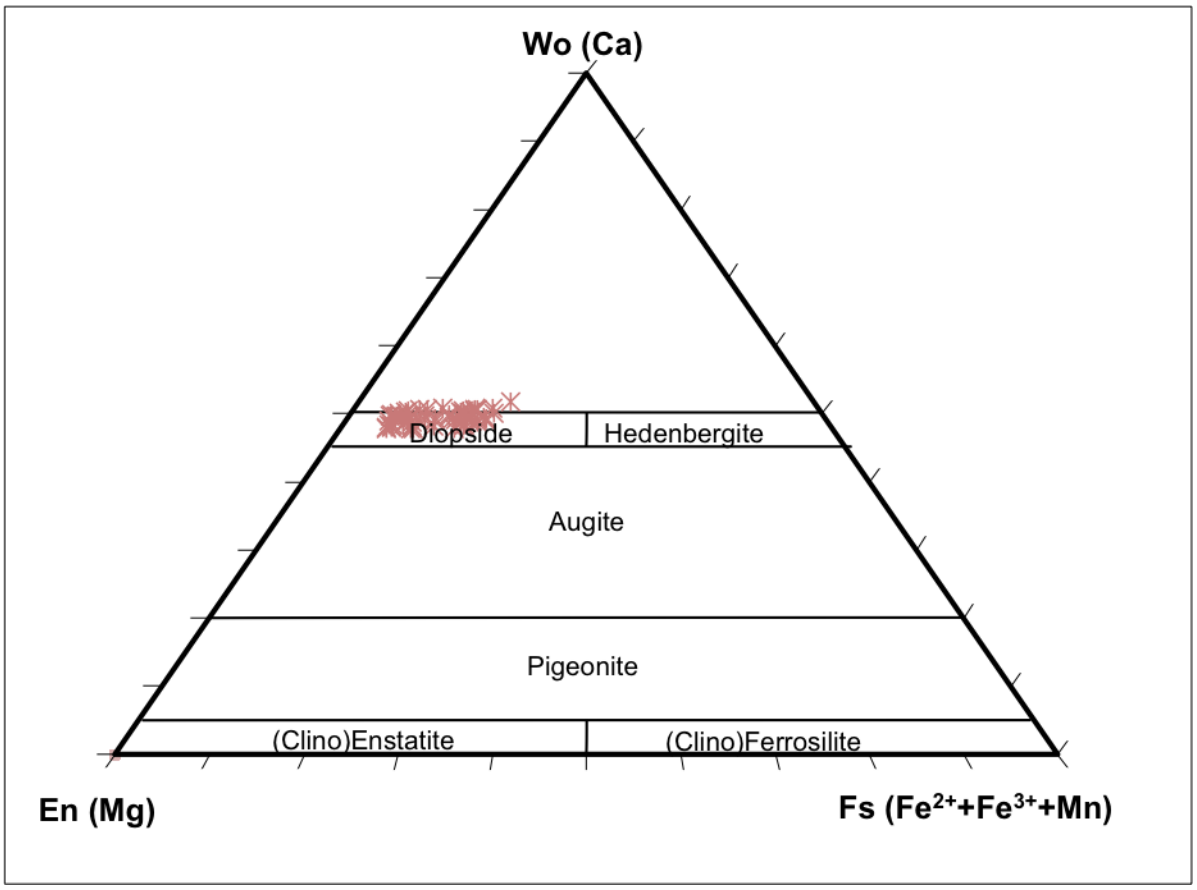

Figure 3.62) Clinopyroxene analyses obtained for 11-KT-04D plotted in the pyroxene quadrilateral based on Morimoto et al. (1988).

A)

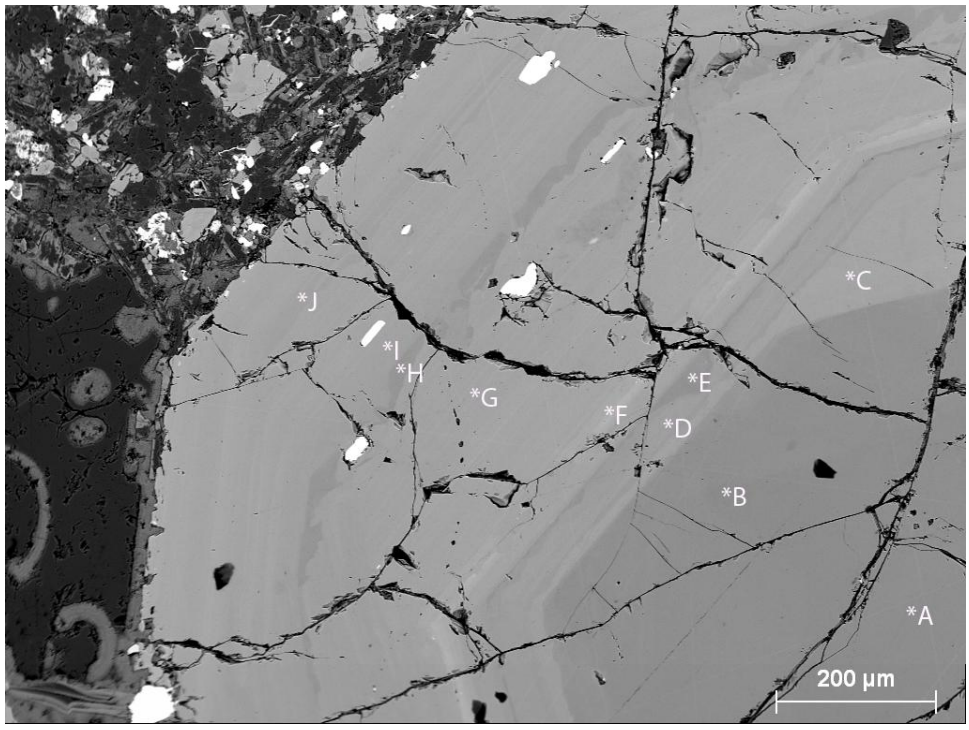

B)

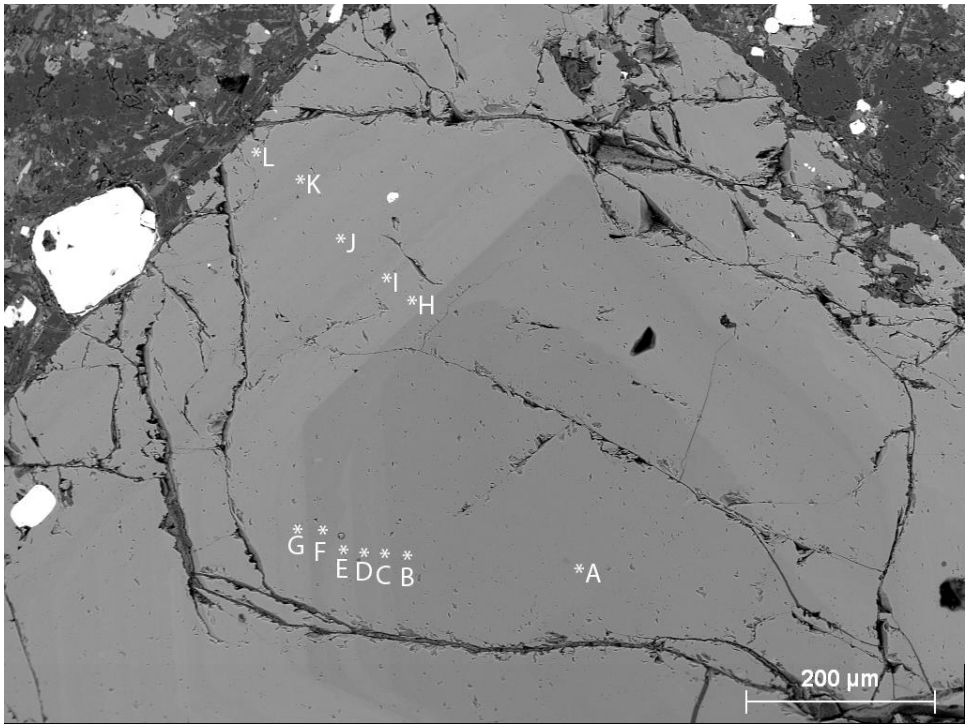

Figure 3.63) Backscatter electron images of clinopyroxenes in 11-KT-04D. A) Cpx 0, B) Cpx 3. Microprobe analysis points indicated by center of asterisk next to letters, individual analyses for Cpx 0 are presented in Table 3.11 and those for Cpx 3 are presented in Appendix A.

Table 3.11Representative clinopyroxene analysis of 11-KT-04D							
sample	11-KT-04D						
Cpx #	Cpx 0						
probe site	a	b	c	d	e	f	g
	Wt% oxide						
SiO_2	53.60	52.89	47.85	48.83	52.22	47.65	48.10
Al_2O_3	1.03	1.41	5.55	4.66	2.21	7.06	5.60
MgO	17.02	16.76	13.28	14.07	16.12	10.94	13.00
FeO	3.14	3.17	7.60	6.53	4.18	9.47	7.59
MnO	0.09	0.12	0.14	0.14	0.11	0.22	0.24
CaO	25.78	25.62	24.48	24.64	25.11	24.45	24.53
Na_2O	0.13	0.13	0.21	0.22	0.12	0.32	0.23
TiO_2	0.07	0.11	0.62	0.41	0.20	0.52	0.49
Cr_2O_3	n.d.	0.18	n.d.	n.d.	n.d.	n.d.	n.d.
TOTAL	100.87	100.39	99.73	99.50	100.27	100.63	99.78
	Number of cations in formula						
Si	1.935	1.919	1.776	1.808	1.903	1.771	1.786
Al	0.044	0.060	0.243	0.203	0.095	0.309	0.245
Mg	0.916	0.907	0.735	0.777	0.876	0.606	0.720
Fe^{2+}	0.003	0.000	0.050	0.029	0.032	0.153	0.064
Fe^{3+}	0.092	0.096	0.185	0.173	0.095	0.142	0.172
Mn	0.003	0.004	0.004	0.004	0.003	0.007	0.008
Ca	0.997	0.996	0.974	0.978	0.981	0.974	0.976
Na	0.009	0.009	0.015	0.016	0.009	0.023	0.016
Ti	0.002	0.003	0.017	0.011	0.006	0.015	0.014
Cr	n.d.	0.005	n.d.	n.d.	n.d.	n.d.	n.d.
TOTAL	4.000	4.000	4.000	4.000	4.000	4.000	4.000
$Mg/(Mg+Fe^{+2})*100$	99.7	100.0	93.6	96.4	96.5	79.9	91.9
$Mg/(Mg+Fe_{total})*100$	90.6	90.4	75.7	79.3	87.3	67.3	75.3
Cation Index DS	3.695	3.655	2.969	3.126	3.520	2.704	2.963
Wo	49.6	49.7	50.0	49.8	49.3	51.8	50.3
En	45.6	45.3	37.7	39.6	44.1	32.2	37.1
Fs	4.9	5.0	12.3	10.5	6.6	16.0	12.6

Table 3.11(*Continued*) Representative clinopyroxene analysis of 11-KT-04D			
sample	11-KT-04D		
Cpx #	Cpx 0		
probe site	h	i	j
	Wt% oxide		
SiO_2	51.17	48.21	48.52
Al_2O_3	2.74	5.16	5.01
MgO	15.38	13.62	13.27
FeO	4.98	7.81	7.10
MnO	0.20	0.19	0.15
CaO	25.07	24.60	24.64
Na_2O	0.16	0.20	0.25
TiO_2	0.28	0.54	0.47
Cr_2O_3	n.d.	n.d.	n.d.
TOTAL	99.99	100.32	99.41
	Number of cations in formula		
Si	1.877	1.778	1.805
Al	0.119	0.224	0.220
Mg	0.841	0.749	0.736
Fe^{2+}	0.030	0.037	0.060
Fe^{3+}	0.123	0.204	0.161
Mn	0.006	0.006	0.005
Ca	0.985	0.972	0.982
Na	0.011	0.014	0.018
Ti	0.008	0.015	0.013
Cr	n.d.	n.d.	n.d.
TOTAL	4.000	4.000	4.000
$Mg/(Mg+Fe^{+2})*100$	96.6	95.2	92.4
$Mg/(Mg+Fe_{total})*100$	84.6	75.7	76.9
Cation Index DS	3.407	3.000	3.047
Wo	49.6	49.4	50.5
En	42.4	38.1	37.9
Fs	8.0	12.5	11.6

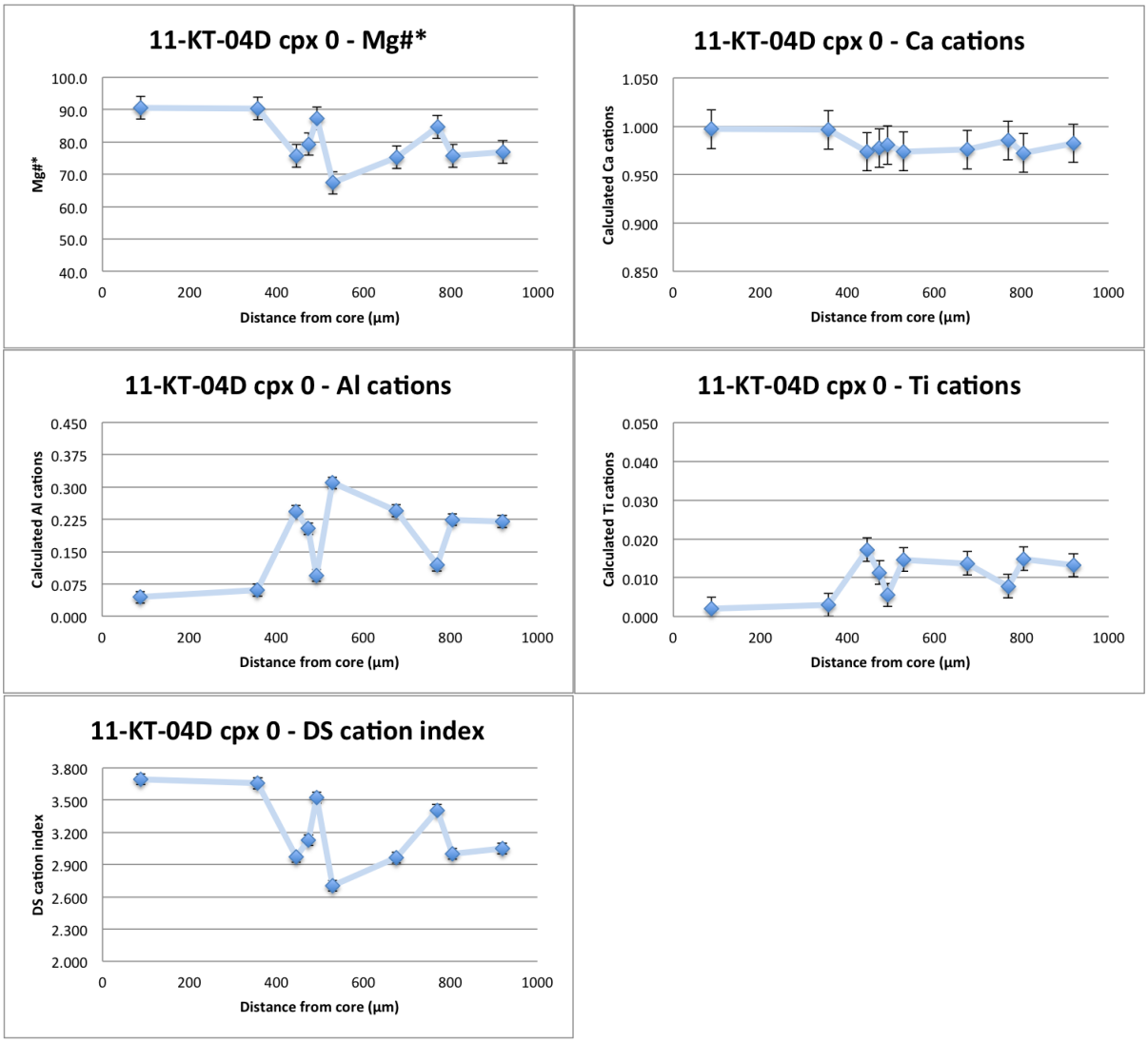

Figure 3.64) Chemical variation plots for 11-KT-04D Cpx 0.

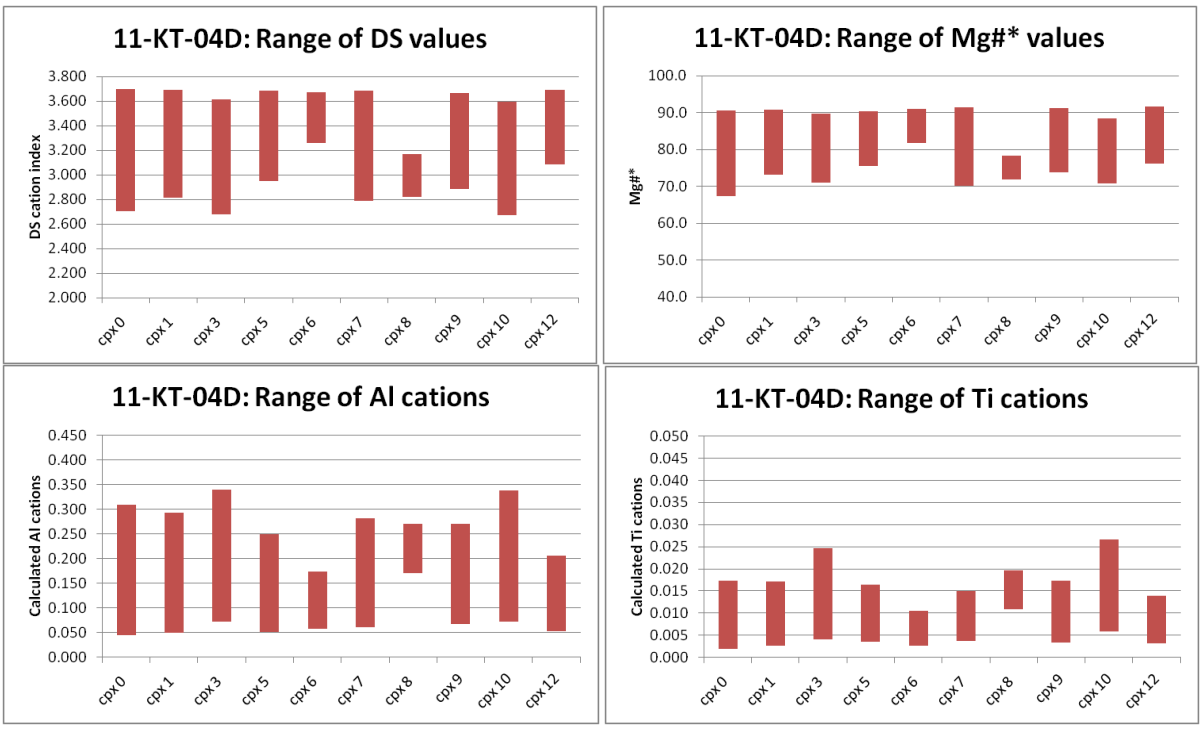

Figure 3.65) Chemical range plots of all clinopyroxene in 11-KT-04D.

4 DISCUSSION

This section will summarize the key findings of the clinopyroxene population study, discuss the results from the laboratory analysis completed in this study, present and interpret pressure and temperature calculations, and discuss the origin of green cores and epitaxial bands.

4.1 Summary of clinopyroxene compositional variations

The Pontide Arc samples can be classified into three groups based on mineralogy. On one end of the classification range, the leucitites are typified by phenocrysts of leucite, clinopyroxene, and magnetite while at the other end the minettes are typified by phenocrysts of biotite, clinopyroxene, magnetite, and apatite. Two samples fall into a class between these two endmembers, due to variations in modal phenocryst abundances or the absence of key minerals these two samples are given the generic name of lamprophyres. [See Table 4.1 for a summary.]

In general, the Pontide Arc leucitites host clinopyroxenes that display more pronounced complex zoning (have a larger number of Mg-rich bands) relative to the clinopyroxenes hosted in the minettes. The lamprophyre that has both leucite and biotite restricted to the groundmass possesses clinopyroxenes with fewer compositional bands than the leucitites and more compositional bands than the minettes. An additional difference between the leucitites and minettes is the frequency of Fe-rich cores in clinopyroxenes; clinopyroxenes from leucitites commonly possess rounded Fe-rich cores

while clinopyroxenes in minette rarely have such cores [See Table 4.1]. Despite the two group's differences, all Pontide Arc samples have clinopyroxenes with similar compositions ranging from diopside to salite, with the exception of the more Fe-rich clinopyroxenes in sample 11-KT-03A, see Figure 4.1. Despite appearing to have high Wo components, clinopyroxenes from sample 11-KT-03A rarely display calculated Ca cation totals above 1.00; however, they display Al cation totals above 0.28 so the high Wo content seen in Figure 4.1 is a result of the high calcium-Tschermak's components of these pyroxenes.

In the samples with clinopyroxenes that display complex zoning the number of Mg-rich bands contained within individual phenocrysts is not consistent between clinopyroxenes within the same sample and the bands commonly vary in size between phenocrysts. Additionally the range of chemical variation inside clinopyroxenes changes from phenocryst to phenocryst, though, the maximum difference between the largest and smallest values for Mg#* found in individual clinopyroxenes are similar across the Pontide Arc samples [See Table 4.1]. These two observations reflect that the samples that contain phenocrysts that display complex zoning also contain clinopyroxenes that are relatively homogenous and that the zoned phenocrysts of a single sample do not all have the same extent of chemical variation.

Finally there is a notable difference in clinopyroxene phenocryst sizes found in the minettes and the lamprophyres and leucitites. In the minettes the maximum clinopyroxene phenocryst size is around 1mm while in the leucitites it can range from 2mm to 3mm to 7mm, and in the lamprophyres the clinopyroxenes attain maximum diameters of 4mm.

Table 4.1) Comparison of key features clinopyroxenes from the Pontide Arc samples								
	Notable mineral	Rock Name	Cpx: Mg#* max Out of all crystals	Cpx: Mg#* min Out of all crystals	Cpx: Mg#* max range Single crystal =max-min	Max# Mg-rich bands	Cpx: Fe-rich cores	Max size of Cpx
11-KT-36D	Bt	Minette	87	70	14	1	rare	1 mm
11-KT-02	Bt	Minette	89†, 84	68	19†, 14	4†, 2	rare	1mm
11-KT-04D	Bt	Lamprophyre	92	67	23	3	absent	4mm
11-AMS-06	groundmass: Bt, Lct	Lamprophyre	87	69	18	2	common	4 mm
11-OS-12	Lct	Leucitite	89	73	15	4	common	3 mm
11-OS-33	Lct	Leucitite	85	57	27	5	common	2mm
11-OS-42	Lct	Leucitite	90	72	15	2	common	7mm††
11-KT-34B	Lct	Leucitite	87	71	16	5	common	3 mm
11-KT-03A	Lct	Leucitite	76	45	29	3	common	2mm
	all: Cpx and Mt some: Ol		†1 cored crystal		†1 cored crystal	†1 cored crystal		††megacryst

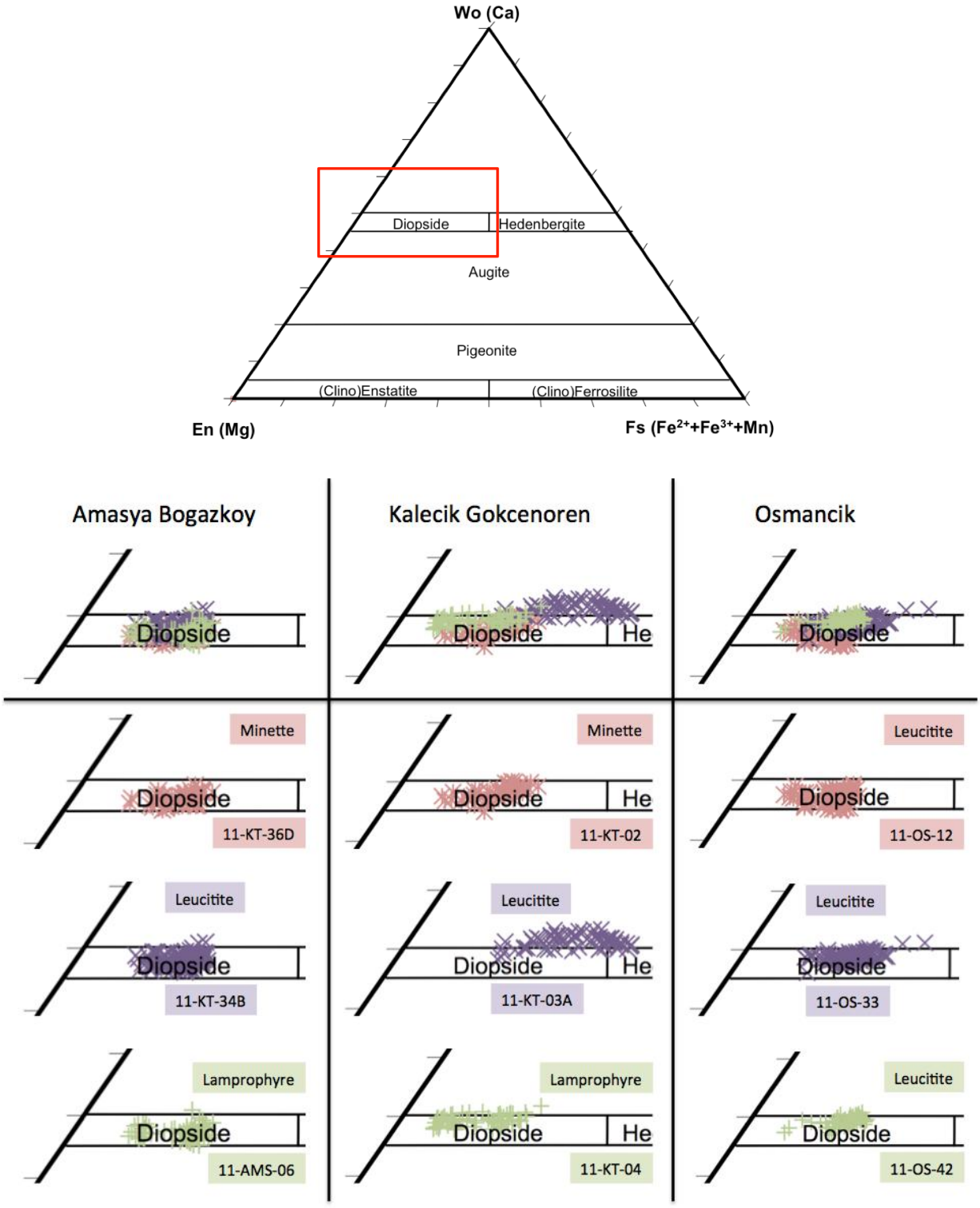

Figure 4.1) Comparison of clinopyroxenes from the nine Pontide Arc samples on the Morimoto et al (1988) clinopyroxene quadrilateral. Red box denotes area of interest.

4.2 Pressure and Temperatures Estimates

Minerals exchange elements with their host melt at varying rates depending on composition of melt and mineral, nature of the element, temperature and pressure; in the case of clinopyroxene the typical major cations that vary substantially are Mg and Fe (Putirka, 2008). It is also possible for the major cations of clinopyroxenes to be replaced by minor cations; however this can lead to charge deficiencies. In order to maintain charge balance minor cations (such as Na, Al, or Ti) commonly have to join or leave the crystal lattice in pairs (Morimoto et al., 1988). Thus, these cations can be combined to form components in a phase such as clinopyroxene that exhibits significant solid solution. Using the observed component abundances in a clinopyroxene and comparing them to the composition of the melt (which can be approximated by the whole rock composition [Putrika, 2008]) it is possible to estimate the activity of each of these components in the clinopyroxene and melt phases and from these estimates, calculate the temperature and pressure a clinopyroxene formed at following the algorithm of Putirka (2008). In a review of mineral-based thermometers and barometers of volcanic systems, Putirka (2008) demonstrated that the thermometer and barometer models for clinopyroxenes developed in Putirka (2003) possessed high precision and low systematic error in hydrous volcanic systems. Putirka (2015) provided a spreadsheet containing this model; additionally, the spreadsheet includes multiple examples of experimental clinopyroxenes-melt pairs, which formed at known pressures and temperatures. For the purposes of checking for equilibrium between melt and clinopyroxene, the spreadsheet contains algorithms for creating plots of *calculated* pyroxene composition against *observed* pyroxene composition. In these plots, each pyroxene has three calculated components: CaTs- 'Tschermak's

component', EnFs- 'enstatite ferrosilite component', and DiHd- 'diopside hedenbergite component' [Figure 4.2]. Along the line in this plot ("one-to-one line"), the calculated and observed clinopyroxene component abundances are identical. If all three calculated components match the observed pyroxene then the clinopyroxene is assumed to be in equilibrium with the melt or bulk rock composition that was used for the calculations. This implies that the calculated pressures and temperature are most likely good estimates of the conditions of clinopyroxene crystallization (Elkins-Tanton and Grove, 2003; Putirka, 2015).

I applied the clinopyroxene-liquid thermobarometer of Putirka 2003 as constructed in Putirka (2015) to the clinopyroxenes of the Pontide Arc samples. Following the recommendation of Putirka (2015) I used the whole rock composition to approximate the melt. As outlined above, clinopyroxenes from all Pontide Arc samples are strongly zoned with large compositional discrepancies between bands, and therefore some zones must be out of equilibrium with the melt as represented by the bulk rock. To mitigate this issue, I selected three compositional zones in three clinopyroxenes from each sample with bulk rock data in the hope that one of the three clinopyroxene zones would approximate an equilibrium pair with the melt (host bulk rock). The three zones selected include an Fe-rich core, a Mg-rich epitaxial band in the interior of the crystal, and an Fe-rich band near the outer edge of the phenocryst. In section 4.2.1 I discusses corrections for alteration and in sections 4.2.2 and 4.2.3 I examine the implications of the results. The calculated pressure and temperature results of individual analyses are detailed in sections 4.2.4, along with interpretation.

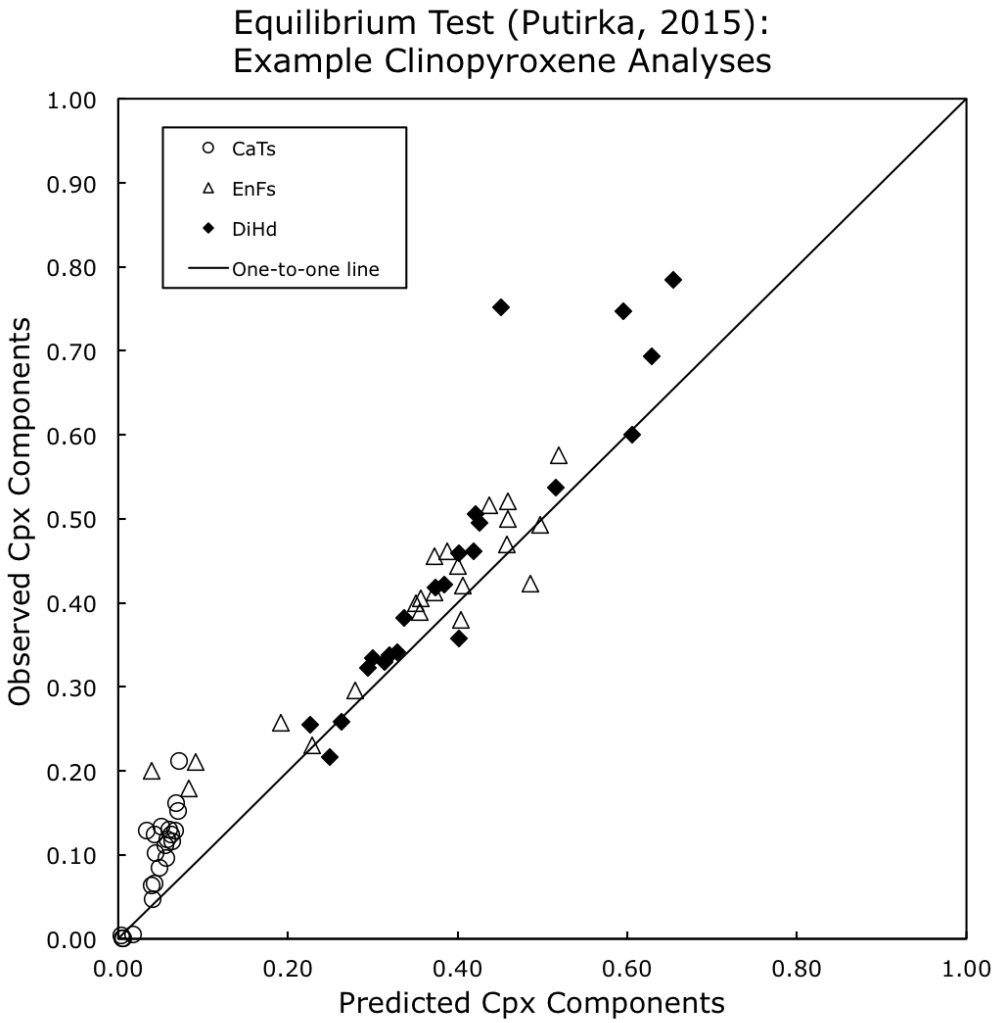

Figure 4.2) Test for equilibrium using data for experimental melt-clinopyroxene pairs complied in Putirka (2015). Each clinopyroxene has the observed CaTs, En-Fs, and Di-Hd component abundances plotted against the calculated component abundances derived from the Putirka algorithm. Equilibrium pairs should plot close to the one-to-one line, where calculated values match observed values.

4.2.1 Issue of Alteration

Gülmez and Genç (2015) determined the bulk rock compositions of five of the nine samples used in this study, and the data is provided in Table 4.2. However, before pressure and temperature calculations could be conducted an important modification was in order. As noted above these samples have been substantially altered; of particular importance is the replacement of leucite by analcime which has resulted in the removal of large amounts of K from these rocks and the addition of equivalent amounts of Na (Gülmez and Genç, 2015). The inflated Na values are important because the Putirka (2015) algorithm includes the jadeite substitution in clinopyroxene.

I corrected the K/Na ratio in the Pontide mafic potassic rocks by examining the K/Na ratios of fresh rocks of similar chemistry and mineralogy. Van Bergen et al. (1992) compared Ti/Al ratios in clinopyroxenes from the mafic potassic volcanic rocks of the East Sunda Arc to Ti/Al ratios in clinopyroxenes of other mafic potassic rocks as an indicator of petrologic similarity. Other authors have also used plots comparing the atomic formula units of Ti and Al in clinopyroxenes (and the ratios between the two) to show petrologic similarities between magmatic provinces (Perini and Conticelli, 2002; Prelevic et al., 2012; Semiz et al., 2012). Following this approach I compared TiO_2/Al_2O_3 ratios from my clinopyroxenes to published data from clinopyroxene from other mafic potassic magmatic centers where the rocks were unaltered or nearly so (five localities in total). Averaging the TiO_2/Al_2O_3 clinopyroxene ratios from all of my samples provided a value of 0.17, closely matching the value of 0.20 for the 1944 Vesuvius eruption of leucitites (Fulignati et al, 2000; Marinanelli et al., 1999). For comparison clinopyroxenes from the Leucite Hills possess TiO_2/Al_2O_3 ratios of 3.3 (Kuehner et al 1981) and clinopyroxenes in mafic potassic

rocks from the Western Mexican Volcanic Belt possess TiO_2/Al_2O_3 ratios of 0.81 (Wallace and Carmichael 1989). Mafic potassic rocks from New South Wales possess clinopyroxenes with TiO_2/Al_2O_3 ratios averaging 1.3 (Cundari and Salviula, 1989) and clinopyroxenes from the Highwood Mountains average 0.15 (O'Brien et al. 1988). The mafic potassic samples from the Highwood Mountains are altered to varying degrees. The assumption here is that the TiO_2 to Al_2O_3 ratio in clinopyroxene will reflect melt composition, specifically alumina activity. I infer that the K_2O/Na_2O ratio of a leucite-bearing mafic potassic magma that crystallizes clinopyroxene with TiO_2/Al_2O_3 ratios similar to those in the clinopyroxenes of Pontide samples is the best candidate to guide the correction of the K/Na ratio of the altered Pontide Arc samples. With that assumption in mind the leucitites from the 1944 eruption of Vesuvius possess an average K_2O/Na_2O ratio of 2.9 (Fulignati et al, 2000; Marinanelli et al., 1999), substantially higher than 0.42 average ratio of the four altered leucitites from this study. Interestingly, the leucite-free minette sample from this study possessed a K_2O/Na_2O ratio of 2.1 possibly reflecting the minor analcimization of the groundmass. However, the K_2O/Na_2O ratios of samples from other mafic potassic magmatic centers are variable (Kuehner et al 1981, Wallace and Carmichael 1989) so it is conceivable that the ratio in the minette reflects the magmatic K_2O/Na_2O ratio and thus this ratio was not adjusted in the minette. The adjusted K_2O and Na_2O values for the four leucitites are provided at the bottom of Table 4.2.

Table 4.2) Bulk rock compositions of samples with modified alkali values

Oxide wt% values of samples (Gülmez, 2015)

Sample No	11-KT-03A Leucitite	11-OS-42 Leucitite	11-OS-12 Leucitite	11-KT-34A T. Leucitite	11-KT-36D Minette
SiO_2	48.43	46.28	48.12	46.03	52.96
TiO_2	0.92	0.86	0.94	0.92	0.67
Al_2O_3	16.91	12.65	12.50	13.21	18.70
Fe_2O_3	7.76	10.26	9.55	10.14	6.17
MnO	0.13	0.17	0.17	0.19	0.13
MgO	3.47	7.55	8.31	7.02	3.43
CaO	5.07	10.39	9.97	9.33	2.20
Na_2O	7.38	4.79	3.77	3.99	3.63
K_2O	2.20	1.10	1.81	2.70	7.56
Cr_2O_3	0.00	0.02	0.04	0.01	0.00
P_2O_5	0.80	0.63	0.41	0.49	0.37
LOI	6.30	4.70	3.90	5.60	3.80
total	99.37	99.40	99.49	99.63	99.62

Modified K_2O and Na_2O wt% values of samples

Sample No	11-KT-03A Leucitite	11-OS-42 Leucitite	11-OS-12 Leucitite	11-KT-34A T. Leucitite
Na_2O	2.46	1.51	1.43	1.72
K_2O	7.12	4.38	4.15	4.97

Adjusted K_2O/Na_2O Ratio: 2.894
Value taken from leucitites from Mt. Vesuvius (Marinanelli et al., 1999)

4.2.2 Validity of Pressure and Temperatures Estimates

Most of the experimental clinopyroxene examples provided in Putirka (2015) are pigeonites (Figure 4.2) and as such are lower in Di-Hd component than the clinopyroxenes of this study, which are diopside, salite, and hedenbergite. However there were five clinopyroxenes from the experimental study of basalts and andesites by Baker and Eggler (1987) that were closer to compositions seen in the Pontide Arc samples, and these clinopyroxenes are shown in Figure 4.3. These five clinopyroxene-melt pairs equilibrated at pressures ranging from 1atm to 8 kbar under wet or dry conditions (Baker and Eggler, 1987). This set of five experimental pairs is important because 1) the clinopyroxenes are relatively calcium-rich and thus are similar to the clinopyroxenes of the Pontide samples and 2) they display deviations from the one-to-one line similar to the deviations seen in the Pontide Arc clinopyroxenes; compare Figure 4.4 (Pontide Arc samples) and Figure 4.3 (Baker and Eggler, 1987 samples).

In the graphical test for equilibrium provided by Putirka (2015) points plotting above the one-to-one line are a result of predicted cpx components being lower than what is observed. There are a few differences between the Baker and Eggler (1987) samples that plot near the one-to-one line and those that deviate from it in Figure 4.3. The three clinopyroxenes that show deviations from the one-to-one line represent experiments performed on natural rock compositions at 1 atm (#4 and #11) and 2 kbar (#704) near 1060°C (Baker and Eggler, 1987) [See Figure 4.3]. The two samples that plot on the one-to-one line were experiments that used mixtures of powdered rock and powdered augite and olivine separates, these experiments were conducted at 8 kbar near 1200°C (Baker and Eggler, 1987) [See Figure 4.3]. To ensure equilibrium could be attained in 24 hours Baker

and Eggler (1987) ran a select experiment twice, once for 480 hours and once again for 24 hours (#11 was the 480 hour duration experiment of this pair); there was no difference in phase compositions between the two experiment runs.

The conclusion to be drawn from the Baker and Eggler (1987) examples is that clinopyroxene-melt pairs that are in equilibrium can plot off the one-to-one line, implying that there is a potential problem with the algorithm. Similar deviations from the one-to-one line are seen in the Pontide Arc samples [Figure 4.4]. However, given the lack of other criteria for equilibrium I am unable to conclude that the criteria for equilibrium between clinopyroxene and bulk rock composition (as a substitute for melt) are satisfied in the case of the Pontide samples. Despite the ambiguity of the results of this assessment of equilibrium, there may be useable information in the results for the Pontide Arc samples, which I address briefly below.

The mismatch between calculated and observed Di-Hd components is present in all of the Pontide Arc clinopyroxenes considered; however the magnitude of the mismatch varies, as one might expect, according to the compositional zoned used. In the clinopyroxenes of the Pontide Arc samples, the Fe-rich cores and the Fe-rich bands plot in the same area on the equilibrium-test graph [Figure 4.4]. The Mg-rich bands also occupy a similar area with the exception that 5 of 14 analyses plot closer to the one-to-one line than any of their Fe-rich counterparts. Putirka (2015) suggested that whole rock compositions and clinopyroxene *core* compositions should approximate an equilibrium pair. However in the Pontide Arc samples the Fe-rich cores plot further away from the one-to-one line than the five Mg-rich epitaxial bands. This observation indicates the influence of an open system process that changed the magma conditions from a regime that crystalized Fe-rich material

to a regime that produced more Mg-rich material. On this basis and in the framework of the graphical test for equilibrium, the five Mg-rich bands nearest to the one-to-one line are the best candidates for useable results.

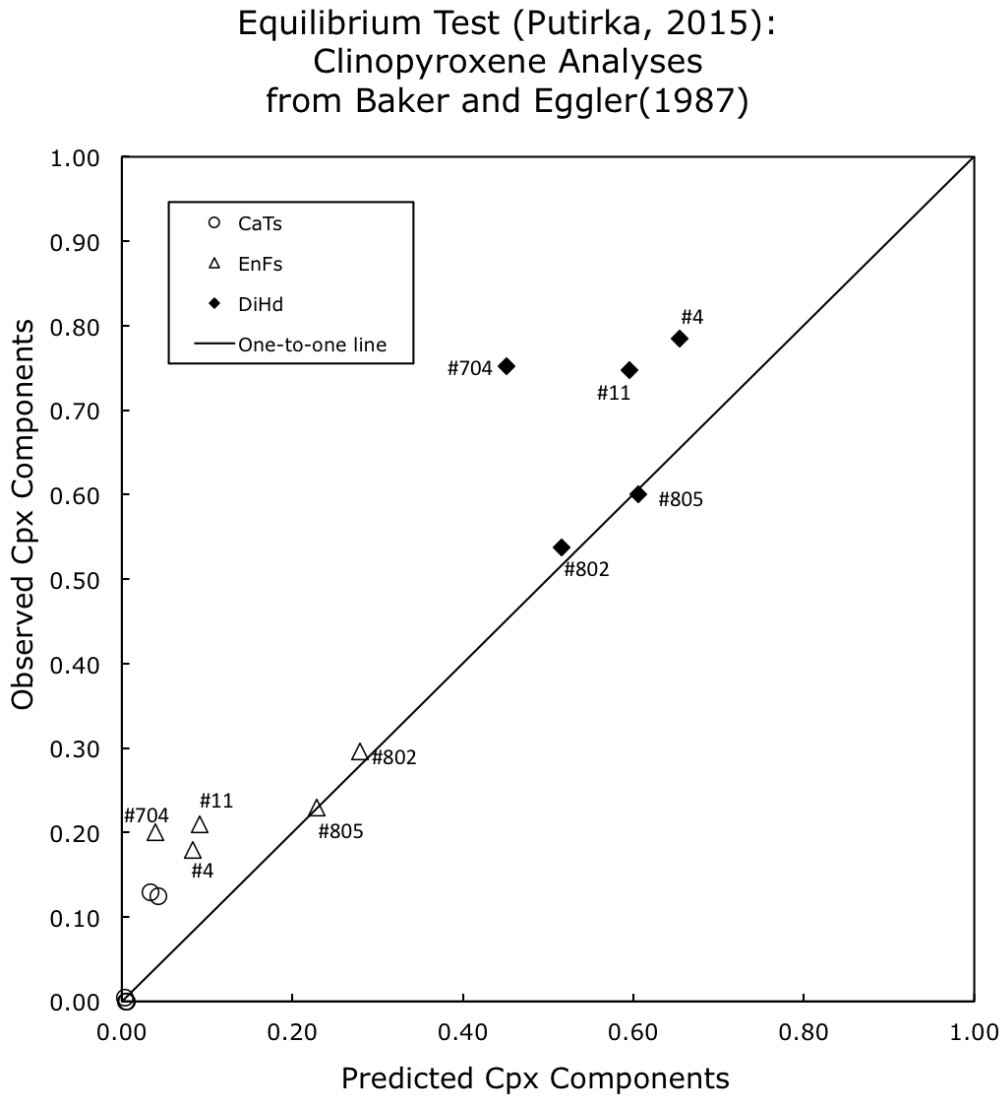

Figure 4.3) Results of the equilibrium test of Putirka (2015) for experimental clinopyroxene-melt pairs taken from Baker and Eggler (1987).

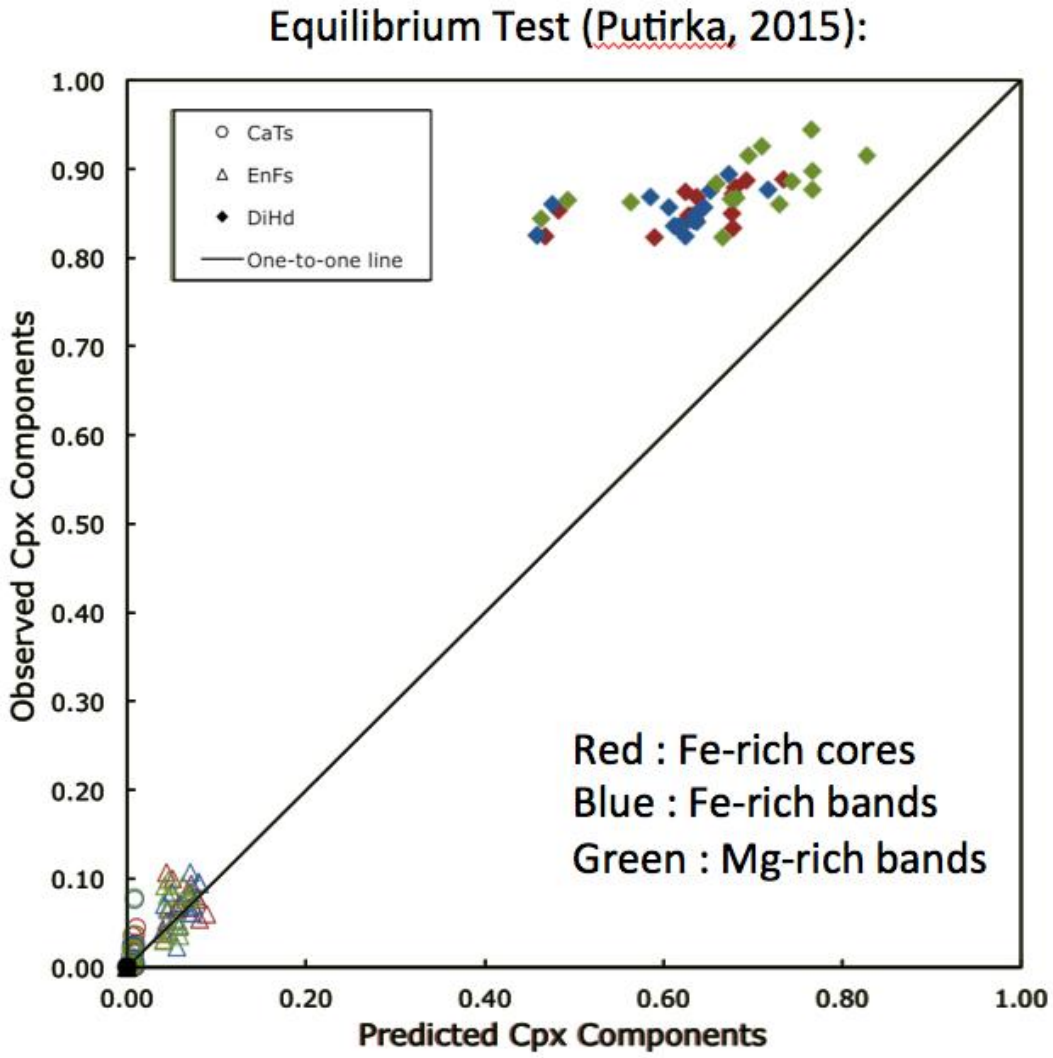

Figure 4.4) Test for equilibrium for clinopyroxene-bulk rock pairs for the samples listed in Table 4.2. Each clinopyroxene has the observed CaTs, EnFs, and DiHd component abundances plotted against the calculated component abundances. Equilibrium pairs should plot close to the one-to-one line.

4.2.3 Agreement with Melting Experiments of Mafic Potassic Magmas

An independent test to assess whether the clinopyroxene-whole rock P-T calculations are reasonable is to compare P-T estimates based on the Putirka (2003) thermobarometer to experimental studies of similar mafic potassic magmas. Calculated clinopyroxene temperatures and pressures should fall between the experimentally determined liquidi and solidi for similar igneous rocks. One approach is to assume that each clinopyroxene in a given sample has a shared history with other clinopyroxenes in that sample based on the presence of zoning features. In that case, averaging pressure-temperature estimates from three clinopyroxenes can be used to minimize errors. These averages are plotted on phase diagrams from Barton and Hamilton (1979) and Esperanca and Holloway (1986).

Barton and Hamilton (1979) subjected a mafic potassic madupite from the Leucite Hills, Wyoming to melting experiments ranging in pressure from 1 atm to 30 kbar under water-undersaturated conditions [See Figure 4.5 for experimental phase relations]. The madupite contained approximately 3 wt.% H_2O and possessed a phenocryst assemblage of small clinopyroxenes frequently surrounded by larger poikilitic crystals of phlogopite and a groundmass of diopside, leucite, potassic richterite, apatite, magnetite, and pervoskite (Barton and Hamilton, 1979). Previously, Barton and Hamilton (1978) conducted experiments on the same madupite under water-saturated conditions with lower pressures and showed that leucite is only stable at low P_{H_2O} for temperatures between the solidus and liquidus [Figure 4.6]. Additionally Esperanca and Holloway (1987) observed that potassic minettes from the Navajo volcanic field that retained their water content at low pressure would produce mineral assemblages of potassium feldspar and phlogopite, while the same

minettes that were relatively dehydrated at lower pressures would crystalize leucite at the expense of phlogopite. This suggests that the size of the stability field of leucite is negatively correlated with water content/activity as well as pressure and the size of the phlogopite stability field is positively correlated with water content. Interestingly, the madupite of Barton and Hamilton (1978, 1979) is compositionally similar to the four Pontide Arc leucitites [Compare Tables 4.2 and 4.3]. Based on this chemical similarity and the similar abundance of leucite in the Pontide Arc samples, the Barton and Hamilton (1979) water undersaturated experiments on the madupite were selected to compare the pressure and temperature results of the Putirka (2003) model for the Pontide leucitites [See Figure 4.5 for graphed results].

The absence of phenocrystic leucite and the presence of biotite phenocrysts (with clinopyroxene, magnetite, and apatite) indicate a more water rich composition for the Pontide Arc minette 11-KT-36D relative to the leucitites [See Figure 4.6]. Esperanca and Holloway (1986) conducted water-saturated melting experiments on a potassic latite with a phenocryst assemblage of phlogopite, clinopyroxene, and titanomagnetite. Chemically it is similar to the Pontide Arc minette 11-KT-36D in terms of Mg#, SiO_2 wt%, and Al_2O_3 wt% [Compare Tables 4.2 and 4.3]. Based on the similarity of the mineral assemblage and the chemical composition the Esperanca and Holloway (1986) water saturated experiments on the latite were selected to compare the pressure and temperature results of the Putirka (2003) model for the Pontide minette [See Figure 4.7 for graphed results, blue symbols].

Leucite and clinopyroxene are the dominant phenocryst phases in the Pontide Arc leucitites. Due to this observation, it is tempting to look to the low-pressure results of Barton and Hamilton (1979) [Figure 4.5] to gain perspective on the Pontide Arc samples,

because leucite is only stable at low pressures [See Figures 4.4]. However textural criteria for crystallization order in the Pontide Arc samples is ambiguous and thus crystallization of clinopyroxene and leucite was not necessarily contemporaneous. It is possible that the clinopyroxene crystalized at greater depths than the leucite. The calculated temperatures for clinopyroxene crystallization in the leucitites 11-KT-34B, 11-OS-12, and 11-OS-42 are consistent with clinopyroxene crystallization temperatures from the Barton and Hamilton (1979) madupite phase experiments under water-undersaturated conditions [Figure 4.5]. The clinopyroxenes in leucitites 11-KT-03A plot below the solidus of the water undersaturated madupite experiments, however these results can be explained by the results of Edgar et al. (1980) which showed that the liquidus of a mafic potassic ugandite was lowered by 200°C due to a change from dry to water saturated conditions at 10 kbar [Figure 4.8]. As such the clinopyroxenes of 11-KT-03A likely crystalized under conditions closer to water saturation than the clinopyroxenes of the other leucitites; the magma could then have degassed at lower pressure allowing leucite phenocrysts to form. This interpretation is further supported by the clinopyroxenes of 11-KT-03A plotting in a clinopyroxene and liquid stable field on the Esperanca and Holloway (1986) phase relation space [Figure 4.7].

The clinopyroxenes of 11-KT-36D (Pontide minette) are consistent with the crystallization conditions of Esperanca and Holloway (1986) who found that phlogopite, clinopyroxene and apatite formed together in a water-saturated latite at temperatures less than 1050°C [Figure 4.7]. The lack of leucite in 11-KT-36D (minette) can be explained by Barton and Hamilton's (1978) melting experiments [Figure 4.6] on a madupite under water-saturated conditions. Leucite is only stable at very low pressures under water-

saturated conditions [Figure 4.6] the same is true for water under-saturated conditions [Figure 4.5] (Barton and Hamilton, 1979; 1978). The absence of leucite in the minette would then indicate that the magma did not crystalize at a shallow depth.

Should the calculated pressures for the clinopyroxenes be correct for the leucitites then the leucite phenocrysts could not have formed at the same time as the clinopyroxene phenocrysts. The similarity between the compositions of the clinopyroxenes found in both the leucitites and minettes indicates that the two rock classes are genetically related; the disparity in crystal assemblage could be explained by an additional magmatic evolutionary step in the development of the leucitites: stalling in the upper crust. Under this hypothesis the minettes would not stall at a shallow level during ascent from a deep crustal magma chamber where the clinopyroxenes crystalized and would instead erupt or intrude into cold country rock directly after traveling from depth. This would prevent both the crystallization of leucite and the degassing of the magma, an event that would lead to the destabilization of the biotite, which is not stable under water-undersaturated conditions at low pressure and relatively high temperature, as shown by Barton and Hamilton (1979) [Figure 4.5]. Under this model, the magmas that become the leucitites would have crystalized leucite in a shallow magma chamber due to the decreased pressure (Barton and Hamilton, 1979; 1978). However this hypothesis by itself does not explain why minette clinopyroxenes display less zoning than leucitite clinopyroxenes.

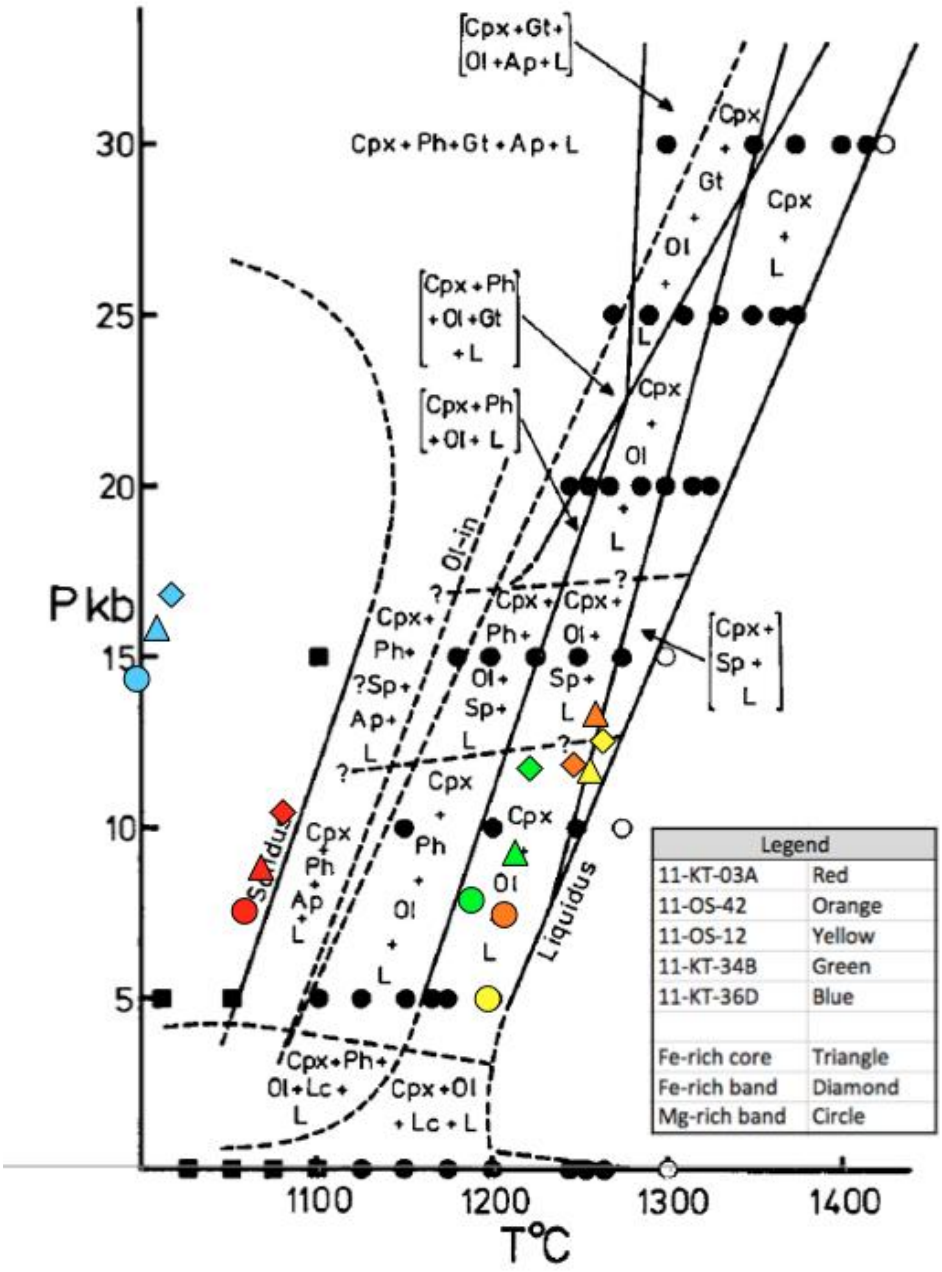

Figure 4.5) Modified figure 1 of Barton and Hamilton (1979) with Pontide Arc sample PT results plotted. Phase diagram shows results of melting experiments on a madupite (lamproite) under water-undersaturated conditions. Symbols: open circles: above liquidus; solid circles: melt + crystals; solid squares: subsolidus. Minerals Ol: olivine; Cpx: clinopyroxene; Lc: leucite; Ph: phlogopite; Sp: spinel; Gt: garnet; Ap: apatite; L: melt. Colored symbols denote calculated pressures and temperatures of Pontide Arc samples; refer to legend for further identification.

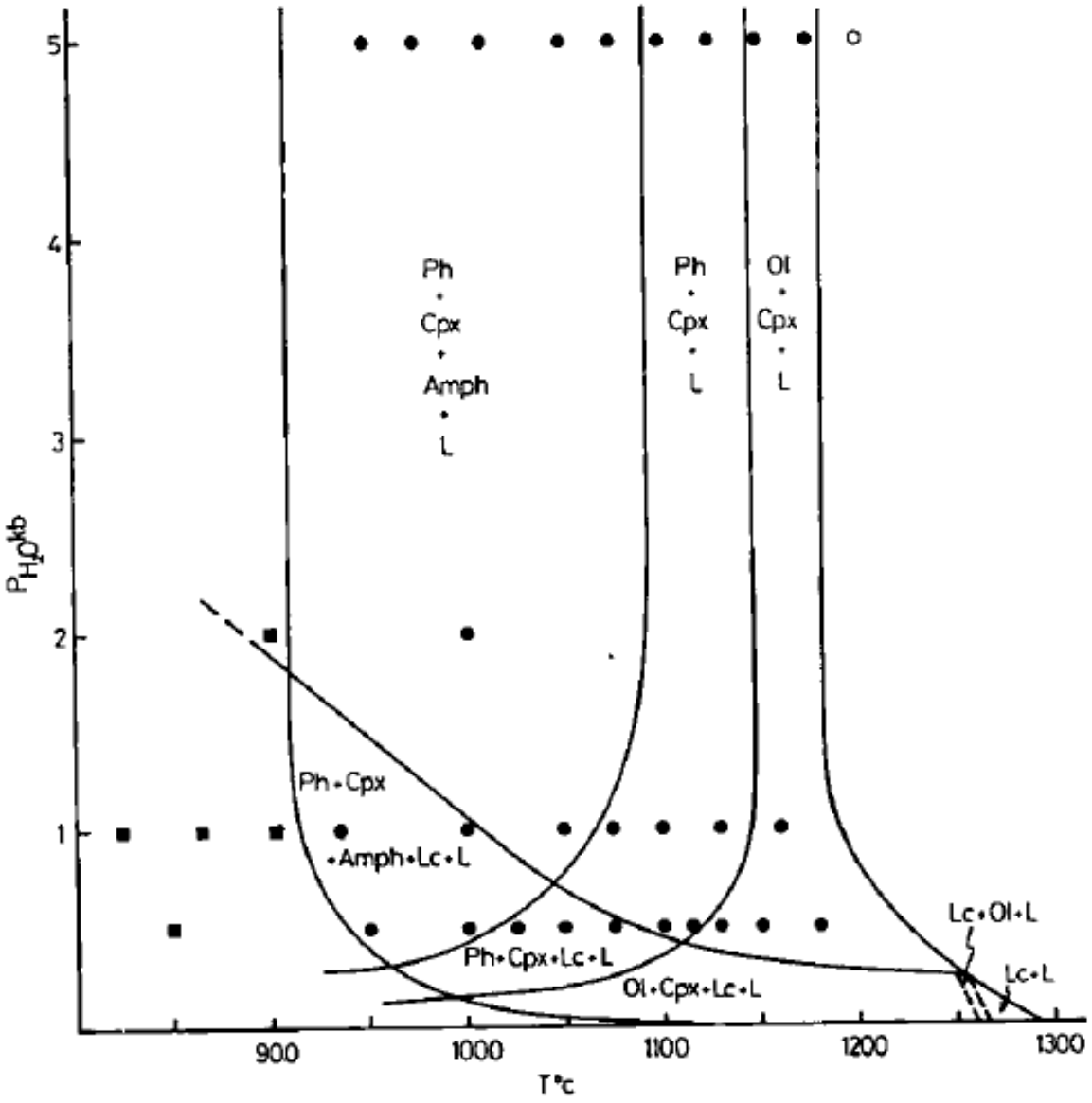

Figure 4.6) Figure 3 of Barton and Hamilton (1978). Results of melting experiments on a madupite (lamproite) under water saturated conditions. Symbols: open circles: above liquidus; solid circles: melt + crystals; solid squares: subsolidus. Minerals: Ol: olivine; Cpx: clinopyroxene; Amph: amphibole; Lc: leucite; Ph: phlogopite; San: sanidine; L: melt.

Table 4.3) Bulk compositions of referenced experimental material		
Oxide wt% values of samples		
Source	Esperanca and Holloway 1986	Barton and Hamilton 1979
sample	7596 latite	A 1805 madupite
SiO_2	59.17	43.56
TiO_2	1.02	2.31
ZrO2	-	0.27
Al_2O_3	14.33	7.85
Cr_2O_3	-	0.04
Fe_2O_3	3.75	5.57
FeO	1.72	0.85
MgO	3.55	11.03
MnO	0.04	0.15
CaO	5.58	11.89
SrO	-	0.4
BaO	-	0.66
Na_2O	2.54	0.74
K_2O	5.55	7.19
P_2O_5	0.34	1.5
H_2O	2.7	4.98
SO_3	-	0.52
total	100.29	99.51

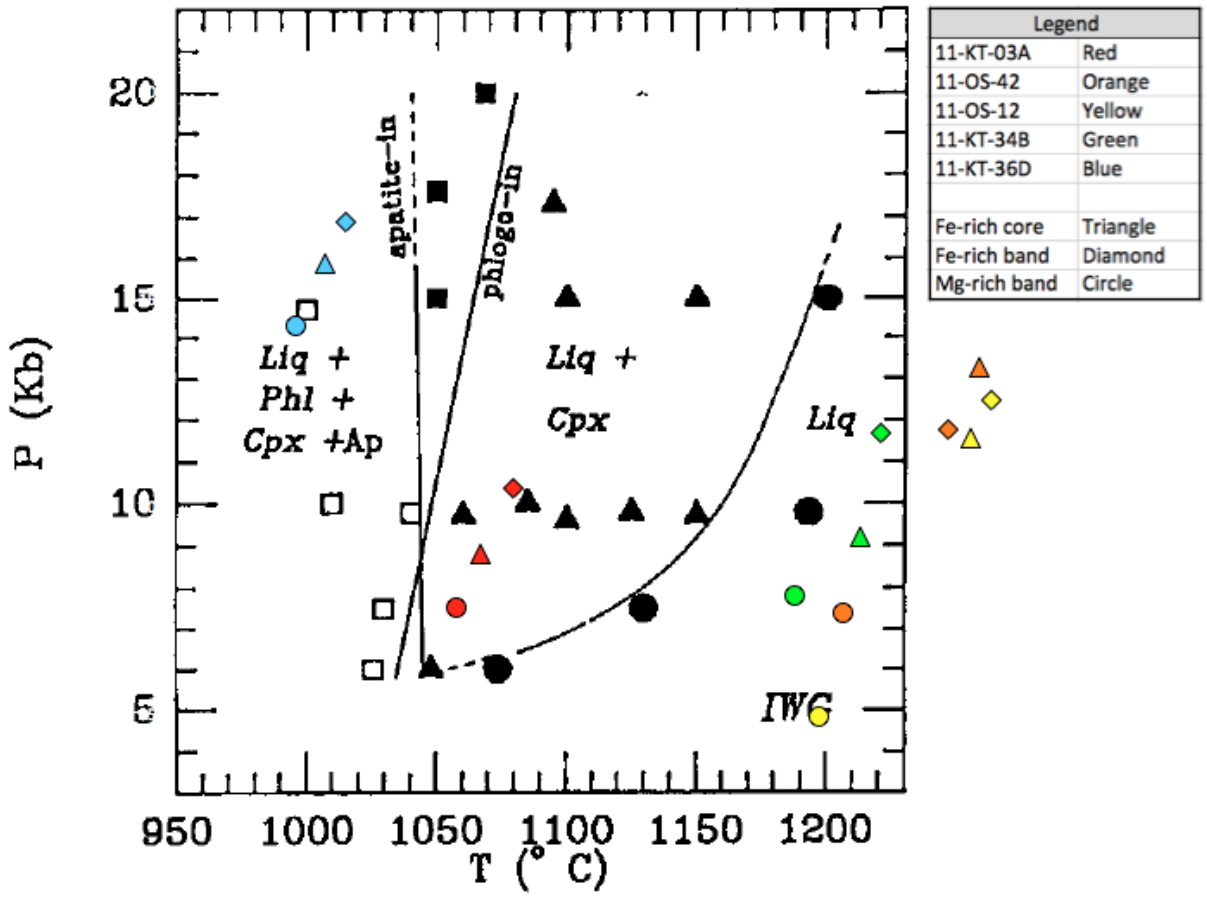

Figure 4.7) Figure 1 of Esperanca and Holloway (1986). Circles = liquid; triangles = liquid + clinopyroxene; closed squares = liquid + clinopyroxene + phlogopite; open squares = liquid + clinopyroxene +phlogopite + apatite. Colored symbols denote calculated pressures and temperatures of Pontide Arc samples; refer to legend for further identification.

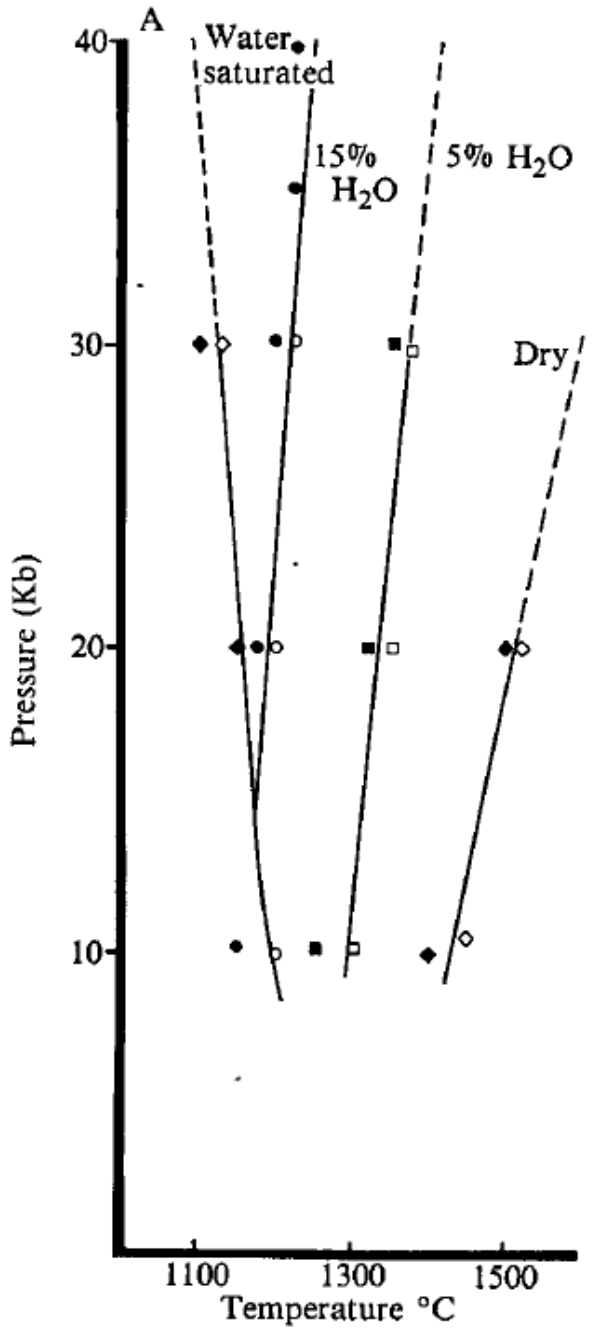

Figure 4.8) Figure 1A of Edgar et al. (1980). The liquidus position of a potassic ugandite in P-T space under varying water saturation conditions. Open symbols: above liquidus; closed symbols: below liquidus.

4.2.4 Depth and Temperature Interpretation

Using primary seismic and magnetotelluric models McGary et al. (2014) found that the forearc region near Mount Rainier in the Cascade Arc, a continental arc similar to the Cretaceous Pontide Arc, has a crustal thickness of approximately 20 km just offshore. Considering that the Pontide Arc samples occurred in marine sedimentary sequences, I assume that the crustal thickness in the Pontide forearc was also 20 km. The Pontide forearc contained carbonates grading into an ophiolitic mélange resting unconformably atop a pelitic metamorphic basement (Gülmez and Genç, 2015). Given these lithologies I assumed an average density of 2900 kg/m^3 for the crust, similar to that of diorite (http://www.edumine.com/xtoolkit/tables/sgtables.htm). A value of 3300 kg/m^3 was assumed for the peridotite mantle. Following these assumptions, depth as a function of pressure was calculated using a lithosphere column with a continental crust thickness of 20km. Calculated pressures from the Putirka (2015) algorithm for the Pontide Arc samples are given in Table 4.4. The pressure results for the Fe-rich core and outer Fe-bands of the clinopyroxenes from the leucitites indicate depths ranging between 30 km and 45 km while the Mg-rich epitaxial bands indicate depths between 17 km and 25 km. Additionally Figures 4.4 and 4.6 show that in four of the five samples the Fe-rich clinopyroxene epitaxial band purportedly formed at higher pressures than their matching Fe-rich core. These conflicting depths are inconsistent with either staging of a magma body or ascent of a magma body during clinopyroxene growth, and perhaps substantiate the results of the equilibrium test algorithm of Putirka (2015), specifically the displacement from the one-to-one line indicating disequilibrium [See Figure 4.4].

Another interesting aspect of the data plotted on Figures 4.5 and 4.7 is the linear arrays defined by the calculated pressures and temperatures. If the pressures and temperatures calculate for the phenocryst cores were at the high pressure end of the arrays with the outer Fe-rich bands at the low pressure end one interpretation would be that the calculations track magma evolution and ascent. However in four of the five samples the calculated pressures and temperatures for core growth are in the middle of the arrays.

Three leucitites (11-OS-42, 11-OS-12, and 11-KT-34B) host clinopyroxenes with calculated temperatures consistent with crystallization in a water undersaturated magma [See orange, yellow and green points on Figure 4.5]; whereas, the leucitite sample 11-KT-03A and the minette (11-KT-36D) host clinopyroxenes with calculated temperatures consistent with crystallization under water saturated conditions [See red and blue points on Figure 4.7]. Again, this may be due to varying amounts of initial water in these magmas coming from a similar source.

All the calculated temperatures for the Pontide Arc pyroxenes range from 1000°C to 1260°C [See Table 4.5]. However, the model of McGary et al (2014) shows that the forearc region above the down-going slab does not exceed 500°C at depths up to 40 km however this is the steady-state for a stable subduction zone involving the consumption of young oceanic crust. In the case of the Western Mexican Volcanic Belt, another mafic potassic volcanic province that occurred above a subduction zone, it is interpreted that significant events had to change the system to allow for the mafic potassic magma to be generated and erupted (Wallace and Carmichael, 1989). Wallace and Carmichael (1989) suggested that the mafic potassic volcanism was generated while extremely young and hot oceanic crust was being subducted and while the forearc crust was undergoing significant extension. If

the Western Mexican Volcanic Belt mafic potassic province is an appropriate analog for the Pontide Arc then the conditions in the forearc mantle would have been hotter than what the model of McGary et al (2014) shows for the Cascade subduction zone.

Table 4.4) Pressure (kbar) results from Putirka 2003 model

rock type	Sample	Fe-rich cores		Mg-rich bands		Fe-rich bands	
Leucitite	11-KT-03A	6a	8.8	6e	7.6	6f	9.6
		0a	11.0	0f	7.0	0g	10.2
		3a	6.5	3e	8.0	3d	11.5
			8.8		7.5		10.4
Leucitite	11-OS-42	2a	12.9	2d	-	2f	8.0
		4a	13.5	4d	8.8	4g	14.4
		9a	13.4	9e	6.0	9f	12.9
			13.3		7.4		11.8
Leucitite	11-OS-12	8a	12.6	8g	5.2	8k	13.2
		1a	12.5	1e	6.4	1i	12.2
		13a	9.7	13d	3.1	13e	12.0
			11.6		4.9		12.5
Leucitite	11-KT-34B	1a	10.1	1k	6.0	1n	11.5
		1b	9.9	1i	9.3	1l	10.3
		4a	9.7	4j	6.9	4k	13.5
		5a	6.9	5h	9.2	5m	11.4
			9.2		7.8		11.7
Minette	11-KT-36D	20a	15.3	20g	16.9	20c	17.1
		18p6	16.2	18p7	11.2	18p2	16.2
			-	1b	14.9	1c	17.1
			15.8		14.3		16.8
Layer position in cpx		Innermost		Intermediate		Outermost	

Number-letter combinations to the left of pressures indicate which clinopyroxene and analysis site was used for each calculation. Ex: 6a means "Cpx 6, point 'a'"
Averages are included in gray to help highlight patterns.

Table 4.5) Temperature (C) results from Putirka 2003 model

rock type	Sample	Fe-rich cores		Mg-rich bands		Fe-rich bands	
Leucitite	11-KT-03A	6a	1067	6e	1061	6f	1076
		0a	1086	0f	1053	0g	1077
		3a	1049	3e	1059	3d	1086
			1067		1058		1080
Leucitite	11-OS-42	2a	1255	2d	-	2f	1213
		4a	1257	4d	1215	4g	1268
		9a	1259	9e	1195	9f	1255
			1257		1205		1245
Leucitite	11-OS-12	8a	1262	8g	1200	8k	1269
		1a	1262	1e	1209	1i	1259
		13a	1237	13d	1180	13e	1257
			1254		1196		1262
Leucitite	11-KT-34B	1a	1233	1k	1168	1n	1218
		1b	1233	1i	1196	1l	1206
		4a	1202	4j	1183	4k	1237
		5a	1180	5h	1200	5m	1219
			1212		1187		1220
Minette	11-KT-36D	20a	1003	20g	1015	20c	1019
		18p6	1012	18p7	974	18p2	1010
			-	1b	1000	1c	1019
			1008		997		1016
Layer position in cpx		Innermost		Intermediate		Outermost	

Number-letter combinations to the left of temperatures indicate which clinopyroxene and analysis site was used for each calculation. Ex: 6a means “Cpx 6, point ‘a’”
Averages are included in gray to help highlight patterns.

4.3 The origin of clinopyroxene green cores and epitaxial bands

The clinopyroxenes of the Pontide Arc samples display two striking features that are frequently seen in the clinopyroxenes of other mafic potassic magmatic provinces: 1) green salite cores mantled by clear diopside (Barton et al., 1982; Bedard et al 1988; Zhu and Ogasawara, 2004; Semiz et al., 2012) and 2) repeated epitaxial bands of green salite punctuated by clear diopside (O'Brien et al. 1988; Cioni et al., 1998). Another feature common to mafic potassic provinces and seen in the Pontide Arc samples are clinopyroxenes with clear diopside cores and salite rims (O'Brien et al. 1988; Cioni et al., 1998). To explain the presence of green salite cores in clinopyroxenes some studies concluded that the green cores were genetically unrelated to the rest of the clinopyroxene and were crustal xenocrysts (Zhu and Ogasawara, 2004) or mantle xenocrysts (Wass, 1979). A more widely accepted hypothesis is the interpretation that the green cores were derived from either genetically distinct or more evolved magmas that were intercepted by a rising primitive magma; in this model the outer, more Mg-rich layer of the clinopyroxene was deposited on the green core by a hybridized magma (Barton et al., 1982; Bedard et al 1988; Semiz et al., 2012). Building on this idea other workers explain complex zoning, that is the presence of multiple Fe-rich bands interspersed with Mg-rich bands, by the presence of several magma chambers of varying degrees of evolution interacting and mixing with each other and new primitive batches of magma to generate the extensive zoning, sometimes mixing up to six times (O'Brien et al. 1988). A simpler model for complex zoning interprets individual Mg-rich bands interspersed in the Fe-rich bands as marking the arrival of several discreet pulses of more primitive magma in a single evolved small magma chamber in an open system (Cioni et al., 1998).

To test if any of these interpretations could help explain the green cores and complex zoning seen in the Pontide Arc samples variation diagrams comparing Al cation formula units (c.f.u.) to Ti c.f.u. as well as variation diagrams plotting Al c.f.u. against Mg#* were constructed [See Figures 4.9 and 4.10]. The near identical chemical compositions of the cores and the bands combined with the similar calculated crystallization pressures and temperatures [Tables 4.4 and 4.5] suggest that the salite cores and bands are derived from the same magma. That is to say the green salite cores of the Pontide Arc samples are not xenocrysts and outside sources of evolved magma are not needed to explain the presence of the salite epitaxial bands in the outer regions of the phenocrysts.

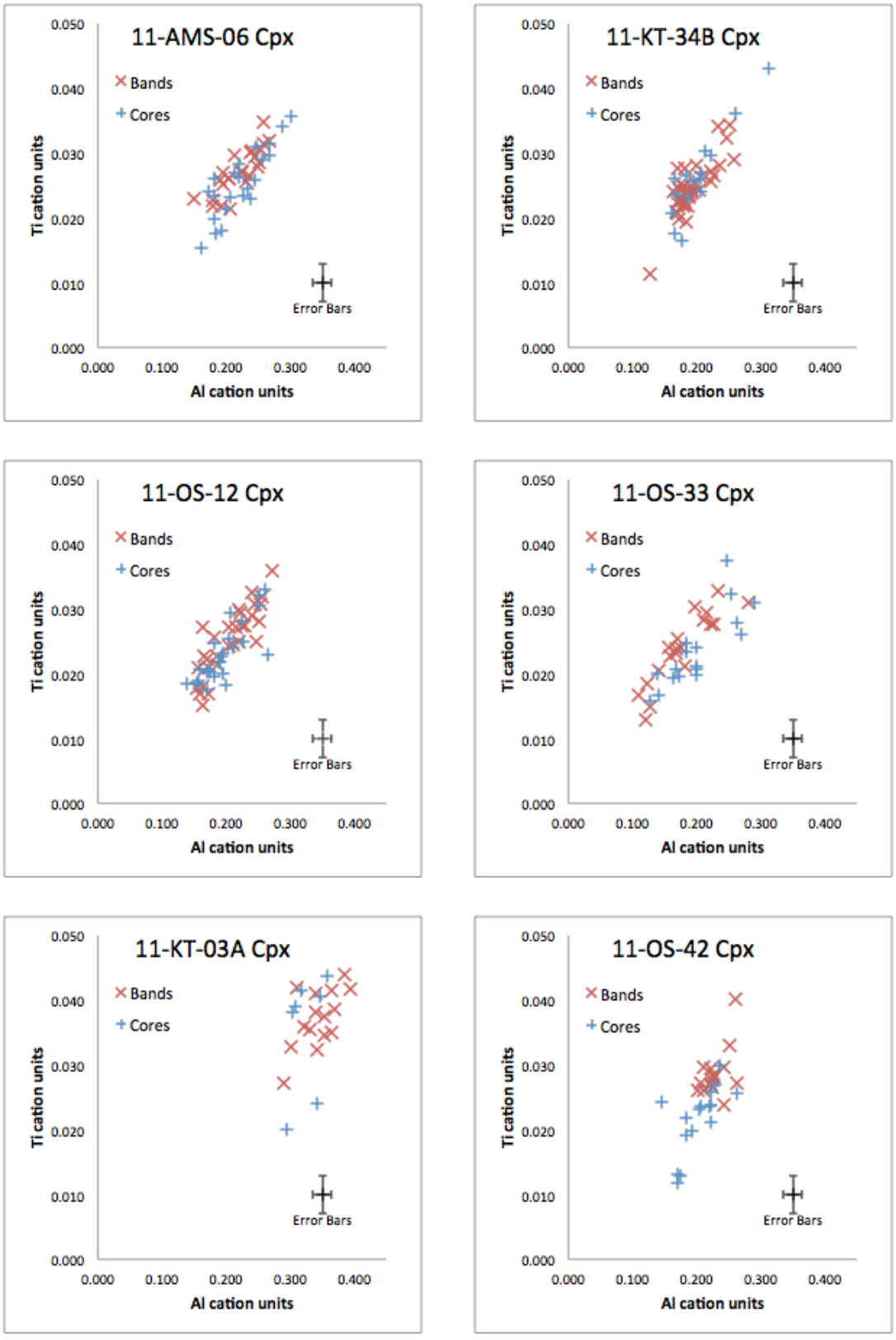

Figure 4.9) Al v Ti diagrams comparing Fe-rich cores and Fe-rich bands

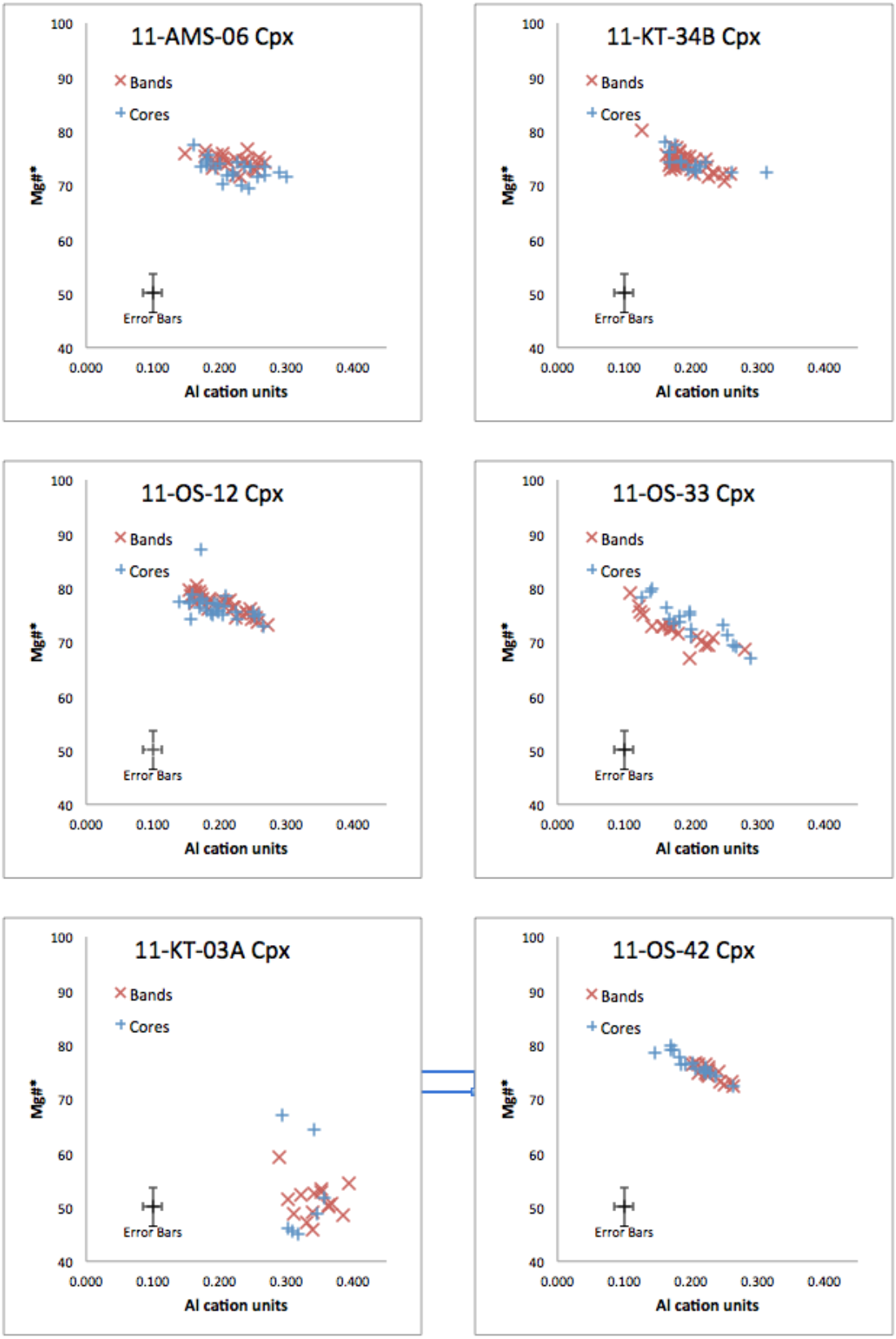

Figure 4.10) Al v Mg#* diagrams comparing Fe-rich cores and Fe-rich bands

4.3.1 Exploring water-controlled models of salite-diopside oscillation

To explain compositional zoning and the development of epitaxial bands in clinopyroxenes two hypotheses are considered. The most common explanation, as mentioned above, is magma mixing where the oscillation between the Fe-rich and Mg-rich bands represents the crystal seeing one of two magmas or varying mixtures of the two (O'Brien et al. 1988; Cioni et al., 1998). The magma-mixing hypothesis will be re-visited below. A second explanation is that the water content of the melt changes the relative activities of the oxides in the melt therefore changing the composition of the solids crystalized (Crabtree and Lange, 2011). Crabtree and Lange (2011) observed orthopyroxenes with minor complex zoning (few bands, and Mg#s that spanned a range of 10) and concluded that it was the result of variable magmatic water content changing the activities of FeO and MgO in the melt. Similar water-based mechanisms have been suggested to explain oscillatory zoning in hornblende phenocrysts at Unzen Volcano (Sato et al., 2005). Studying clinopyroxenes in the Roman Province, Holm (1982) suggested that a transition from high to low water content in leucitites could cause clinopyroxene compositions to shift from salite early in the clinopyroxene crystallization history to diopside towards the end.

Water, the primary volatile in convergent margin magmas, induces dramatic changes in the liquidus and solidus temperature of magmas and changes the rates of mineral growth (Armienti et al., 2012). In addition to this, water content in the melt correlates positively with both the amount of aluminum in the clinopyroxene tetrahedral site and the total iron found in the pyroxene (causing a decrease in Mg#), probably reflecting increased Fe^{3+} (Dolfi and Trigila, 1983). This effect can be expressed

quantitatively, for example in laboratory experiments using a 1971 phonolitic tephrite from Mount Etna Dolfi and Trigila's (1983) found that clinopyroxenes generated at 2 kbar possessed Mg# = 88 in a run with 0.1 wt% H_2O while the same rock with 2.8 wt% H_2O produced clinopyroxenes with Mg# = 71. Taking the average of these values it can be expected that in phonolitic tephrites and similar magmas an increase in water content of the magma by 1 wt% could depress the Mg# of the crystalized clinopyroxenes by about 6. For the same experiments aluminum in the clinopyroxene tetrahedral site increased from 0.10 cations at 0.1 wt% H_2O to 0.34 at 2.8 wt% H_2O, while aluminum in the octahedral site stayed nearly constant (Dolfi and Trigila, 1983). A coupled substitution of the diopside and hedenbergite components in the pyroxene structure for the esseneite component ($CaFe^{3+}AlSiO_6$) could explain this behavior (Holm, 1982; Morimoto et al., 1988).

The green salite cores and bands are characterized by relatively low Mg#* and relatively high tetrahedral Al relative to the more Mg-rich bands. If the presence of these cores and epitaxial bands are controlled by increasing water content in the melt then it would explain the correlation of the high Al content with lower Mg#*s in salite bands and cores (Figure 4.10). Additionally, the higher Mg#* (clear diopside) epitaxial bands would have been generated in melts with lower water contents. An additional implication of this hypothesis is that to produce cycling between salite and diopside compositions the water content of the magma would be cycling as well.

Armienti et al. (2012) presented a geohydrometer to estimate the water content of a magma using pyroxene composition and temperature-pressure estimates based on the Putirka et al. (2003) thermobarometer. This geohydrometer was able to correctly estimate the amount of CO_2 and H_2O in melt inclusions from Etnean magmas. The equation is

constructed in a generic form to be applicable across different magma compositions. The model of Armienti et al. (2012) was derived from trachybasalts and hawaiite, and I assumed they are a good approximation for the Pontide Arc samples given the compositional similarities. Results of this model applied to the Pontide Arc clinopyroxenes are given in Table 4.6.

Table 4.6 presents three important observations: 1) calculations for Mg-rich bands result in ***higher*** melt-water contents than the Fe-rich bands and cores, that is, the relative water contents are inconsistent with the idea that the low Mg# and high Al of the salite bands are due to higher water contents, 2) that the predicted water content of the leucitites' melts (save 11-KT-03A) and predicted water content of the minette's melt are nearly the same when they were crystalizing the clinopyroxenes, and 3) 11-KT-03A, the sample hosting clinopyroxenes with the highest hedenbergite components and highest Al cation totals, displays the lowest predicted water content- again an inconsistent result because this melt should have the highest water content if high water content is responsible for low Mg# and high Al of the clinopyroxene. Assuming that these water estimates are correct and that the generalization from Dolfi and Trigila (1983) of how melt-water content affects clinopyroxene Mg# is also correct then an additional inference is that the change in melt-water content from the Mg-rich band to the Fe-rich band can only account for a change in Mg# of 2.5. However, it is common to see Mg# fluctuations ranging from 5 to 11 times this amount in the complexly zoned clinopyroxenes of the Pontide Arc samples [See Table 4.1].

An important aspect to the hypothesis that water content controlled development of the salite and Mg-rich epitaxial bands is the ability of alkali-rich primitive magmas to hold

water. Moore et al. (1995) created an algorithm that predicts water contents for basanitic magmas. At 1200 °C such a magma would have the capacity to hold 4 wt% H_2O at 2 kbar, with higher pressures increasing this capacity even further [See Figure 4.11]. The clinopyroxenes of the Pontide Arc samples all record crystallization pressures of 4.9 to 16.8 kbar and the Armienti et al. (2012) model indicates water contents at or below 3.4 wt% [See Table 4.3 and 4.6]. Significant water degassing begins at approximately 4 kbar during magma ascent (Armienti et al., 2012). Therefore these high pressures indicated by the clinopyroxenes remove the possibility that cyclical degassing and water recharge (mechanisms of water recharge include magma mixing or volatile migration from depth (Streck, 2008)) triggered the cyclical clinopyroxene compositional banding. However, Armienti et al. (2012) noted that with non-ideal mixtures of H_2O and CO_2 modeling showed that minor magma water loss to the vapor phase occurs during the earliest stages of ascent and that the amount of water in the vapor phase grows at the same rate as the amount of water in the melt, which increases due to crystallization. All of these observations indicate that the hypothesis of water controlling the creation of these salite bands and cores (at least as the sole volatile) is incorrect. Additionally, the existence of complex zoning in clinopyroxenes from anhydrous lunar basalts (seen in trace elements) further discredits the water-content-zoning-control hypothesis (Elardo and Shearer, 2014).

Table 4.6) Results of Armienti et al. (2012)- Equation 1 Wt.% H2O in magma based on Cpx composition and Putrika 2003				
Rock	Sample	Fe-rich core	Mg-rich band	Fe-rich band
leucitite	11-KT-03A	1.6	1.9	1.8
leucitite	11-OS-42	3.1	3.4	2.5
leucitite	11-OS-12	2.7	3.4	2.5
leucitite	11-KT-34B	3.3	3.3	2.9
minette	11-KT-36D	3.3	3.4	3.2
	Average	2.8	3.1	2.6
	Position	innermost	intermediate	outermost
Standard errors ~ +/- 0.5 wt.% for Armienti et al. (2012)				

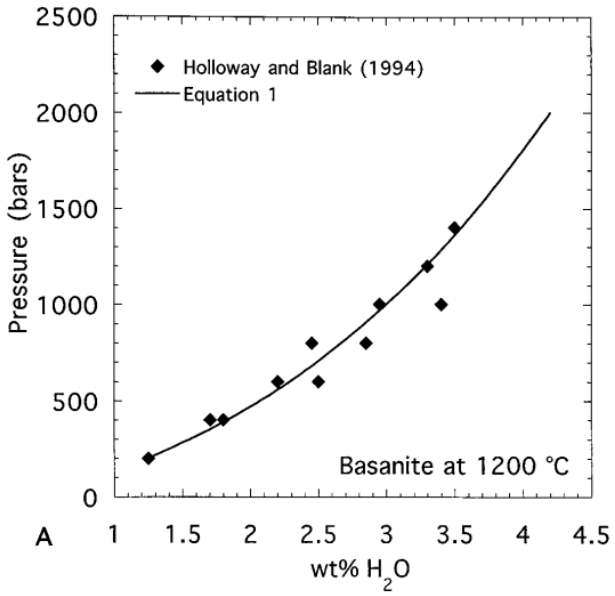

Figure 4.11) Calculated solubility of water for a basanite at 1200 °C and varying pressures. Figure 3a (Moore et al., 1995)

4.3.2 Exploring magma mixing models

Unlike with the varying water content model, invoking magma mixing as an explanation for the development of complex zoning can account for the size of the compositional jumps between the epitaxial bands. There is a variety of magma mixing models; the first two models presented below (O'Brien et al., 1988 and Cioni et al., 1998) would maintain that a single mixing event would generate a single band while the third model (Bergantz et al., 2015) shows that multiple bands can grow around a clinopyroxene during a single mafic magma injection. All three models have characteristics that may help to explain the zoning in the Pontide Arc clinopyroxenes.

4.3.2.1 Past magma mixing models

In the view of O'Brien et al. (1988) the extensive complex zoning in clinopyroxenes from the Highwood Mountains magmatic province and the diversity of that province's magmas requires the existence of a large number small discrete transient magma-filled reservoirs. These near surface magma bodies would have fairly evolved compositions and could explain the salite epitaxial bands and cores found within clinopyroxenes while Mg-rich diopside bands represent the injection of new mafic magma from depth (O'Brien et al. 1988). The sudden jumps in composition and the dissolution surfaces that separate individual bands would be due to temperature or chemical instabilities following a mixing event. In addition to invoking magma mixing of more primitive magma to explain the sudden composition jumps to diopside bands, O'Brien et al. (1988) maintains that sudden jumps to salite compositions are also results of magma mixing, only the mixing is with other evolved magmas near the surface. In this model each band represents a separate

mixing event and the envisioned small magma batches are influenced by up to and rarely over six mixing events.

Cioni et al. (1998) presents a simpler model for the development of complex zoning. Based on their work on samples from Vesuvius they envision a small relatively evolved magma chamber in the upper crust that is periodically injected with more primitive material. Phenocrysts with green salite cores and diopside rims initially grew from the evolved cooler melt of the Vesuvian magma chamber and were later incorporated into the hot plume of a newly arrived mafic magma batch prior to an eruption (Cioni et al., 1998). While clinopyroxenes with diopside cores initially grew out of the ascending and depressurizing mafic magma and were incorporated into the evolved melt of the Vesuvian magma chamber during mixing at which time the green salite epitaxial bands were deposited. Cioni et al. (1998) also found that the chemical zoning contained within an individual clinopyroxene, specifically how iron- or magnesium-rich the band was, could be correlated with both the composition of melt inclusions contained within that band and the temperature of homogenization of each melt inclusion. This emphasizes that the zoning seen in these clinopyroxenes was due to extrinsic mechanisms, specifically, magma mixing processes causing variations in temperature and melt composition with diopsidic zones marking the input of hot mafic magma (Cioni et al., 1998).

Cioni et al. (1998) observed that Vesuvius primarily generated clinopyroxenes with strong epitaxial banding during open conduit conditions characterized by small but frequent eruptions. Conversely Vesuvius did not generate near as many complexly zoned clinopyroxenes during closed conduit conditions characterized by large but infrequent eruptions. Based on a mathematical model Cioni et al. (1998) hypothesized that for

complexly zoned clinopyroxenes to develop the magma chambers involved had to be relatively small (~10^7 to 10^8 m^3) in order for the newly arriving mafic magma batch to cause abrupt thermal and compositional perturbations and be recorded as a discrete epitaxial band. The model also indicated that the smaller the chamber was the larger the perturbations would be, barring consistent mafic injections (Cioni et al., 1998). Considering the large compositional jumps seen between the epitaxial bands of the clinopyroxenes in the Pontide Arc samples I suggest that the magma chambers that generated these mafic potassic rocks were small.

4.3.2.2 The Bergantz et al. (2015) magma mixing simulation

Magmas exist as a semi-solid crystal mush batches for much of their lifetimes, slowly cooling under a crystal rich regime with the crystals interlocking to form a structure similar to a sponge (Bergantz et al., 2015). These periods of static slow cooling are punctuated by periods of magma mixing sometimes leading to an eruption. This behavior has been documented at ocean island igneous systems and large igneous provinces, in convergent margin igneous systems, as well as mid-ocean ridge igneous systems (Bergantz et al., 2015). These mixing events are typically recorded by the presence of populations of complexly zoned crystals, and time-transgressive crystal fabrics in plutons. Bergantz et al. (2015) simulated an open-system crystal-rich mush magma chamber during a primitive magma injection event; the simulation takes into account both granular interactions and fluid flow. In the 2D model the starting state is a crystal mush pile of randomly arranged grains supported by crystal-crystal contact (Bergantz et al., 2015). When new crystal-free magma is intruded into the system from below at a sufficient velocity, the mush pile

initially deforms viscoplastically, reorienting the stress field leading to the formation of two fractures 60° from horizontal in the static mush pile. Bergantz et al (2015) refers to this zone of viscoplastic failure as the "mixing bowl" (Bergantz et al 2015) [See Figure 4.12]. The volume of crystals inside this mixing bowl become unlocked and are caught in convective currents near the center and base of the bowl as new magma is vigorously injected into the system (Bergantz et al 2015) [See Figure 4.13a]. Inside the mixing bowl the melt of the newly arrived magma and the melt of the chamber's mush layer mix in varying proportions, dominated primarily by higher percentages of the new melt. This process results in phenocrysts floating in the melt of the mixing bowl to encounter melts of widely varying compositions that change as time progresses (Bergantz et al 2015) [See Figure 4.13b]. The Bergantz et al. (2015) simulation ignores the effects of temperature; as such the mixing is purely a result of the speed of injection into the chamber. The significance of coloring the mush pile with two colors (black and white in Figure 4.12) is to highlight that crystals with different ages and different evolutionary histories are brought together as a result of the convection of the mixing melt (Bergantz et al 2015). In relation to the Pontide arc this could explain why there is such variation in the zoning patterns of the crystals in my samples even over a span of a couple of centimeters.

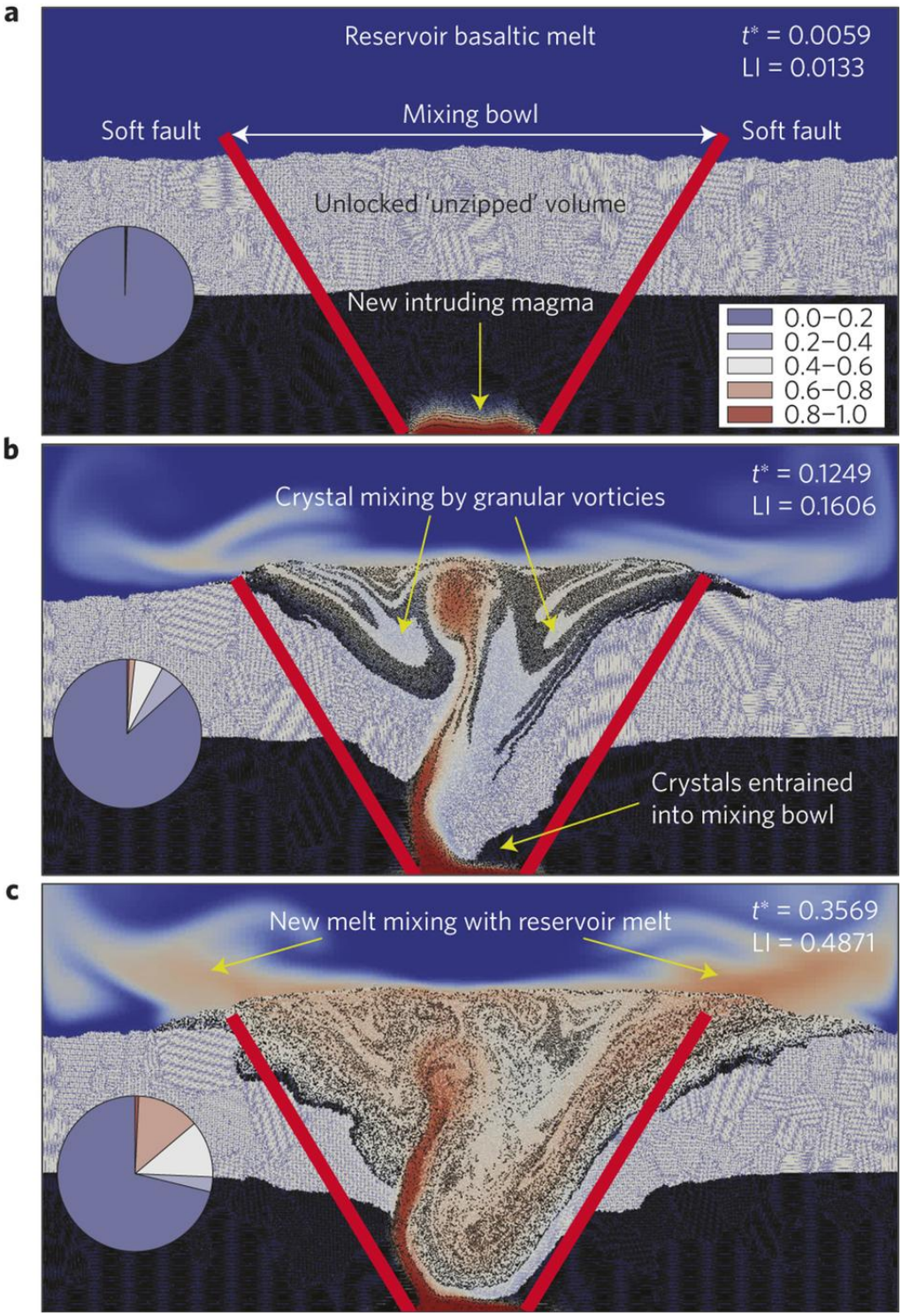

Figure 4.12) Three progressive snapshots of the Bergantz et al. (2016) simulation. This is a simulation of a primitive magma injection into a crystal mush layer of a magma chamber. Blue indicates melt sourced from the magma-chamber, red indicates melt sourced from the injected magma, and white represents a 50/50 mixture. The white and black coloring of the particle layers is to help visualize crystal mixing (Bergantz et al., 2015, Figure 1)

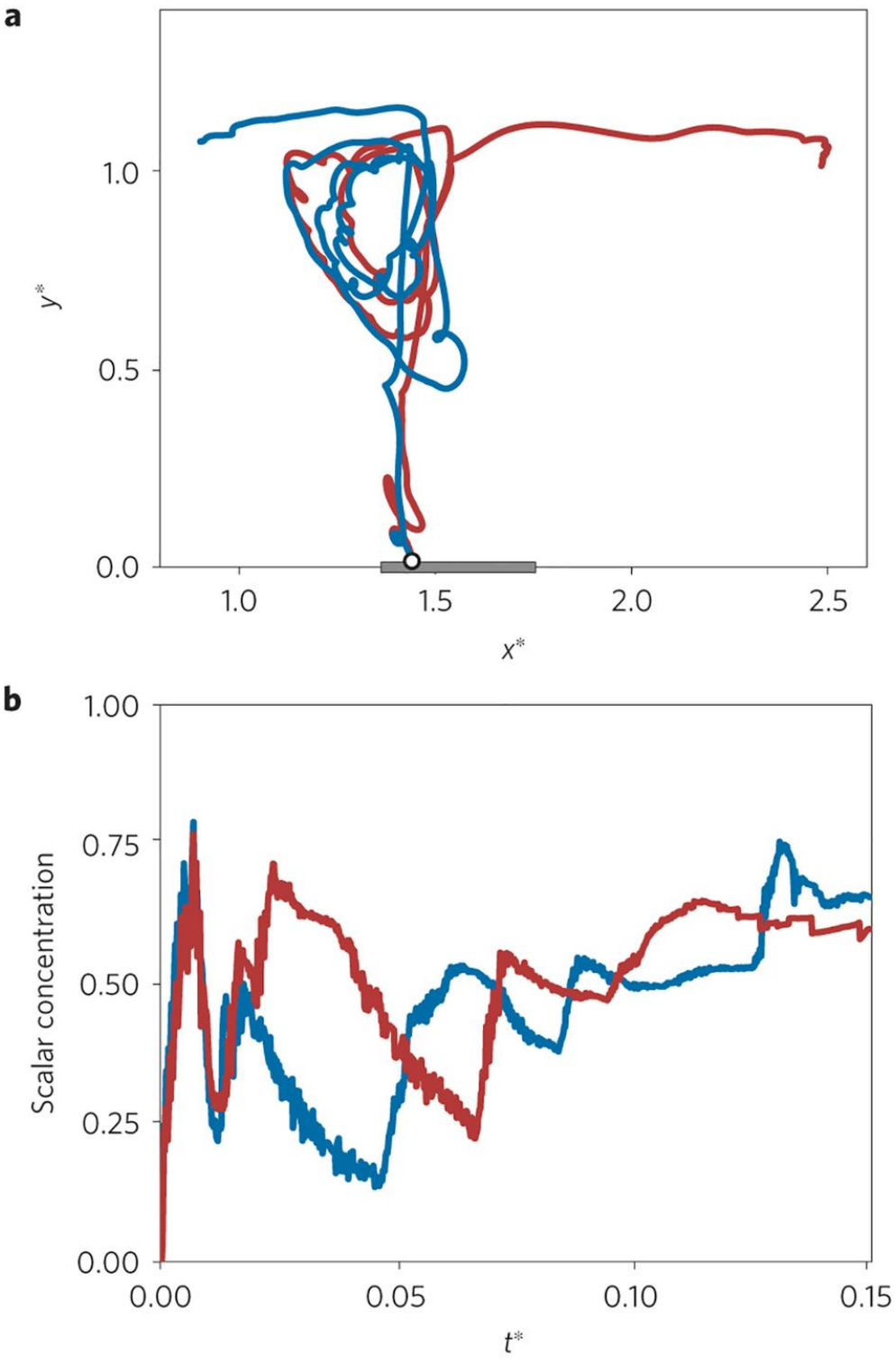

Figure 4.13) (a) The physical paths of and (b) the varying melt composition seen by two crystals during the mixing simulation. Time and positions measurement are nondimensional, and scalar concentration is on a scale of 0 (magma chamber melt) to 1 (intruding magma melt) (Bergantz et al., 2015, Figure 2)

4.3.2.3 Comparing observations and the Bergantz et al. (2015) model

Figure 4.13b shows the varying melt compositions that two crystals from the Bergantz et al (2015) simulation are in contact with as a function of nondimensional time. The scalar concentration on the y-axis ranges from a value of '0' (representing the pure magma chamber melt signature) to a value of '1' (representing the pure recharge melt signature). Presumably clinopyroxenes that experience evolving melt conditions as outlined in the simulation would record such conditions as a series of bands with varying composition deposited as the crystal grew resulting in complex zoning (Bergantz et al 2015). Figure 4.14 shows representative Mg#* profiles of complexly zoned clinopyroxenes from three Pontide Arc samples. Working within the framework of the Bergantz et al. (2015) model a potential history of a single clinopyroxene can be constructed. For instance, the clinopyroxene in Figure 4.14a could have initially grown in a melt that produced material of Mg#*=72, producing the Fe-rich core (points a and b). Following this the crystal was caught in the turbulent flow of the injection of a more primitive magma resulting in both the partial thermal dissolution and rounding of the core and the deposition of a higher Mg#* epitaxial band on top of the preexisting crystal (points c and d). The following Fe-rich epitaxial band resulted from the clinopyroxene being 'thrown' into the more Fe-rich melt as the rising current of injected melt moved away from the injection mouth, resulting in a rapid change back to Fe-rich material [Compare profiles of Figures 4.13b and 4.14a]. This Fe-rich epitaxial band (points e to j) is different from the core in that it displays saw-tooth oscillatory zoning (discussed below). The sizes of later Mg-rich and Fe-rich fluctuations and dissolution surfaces are due to the crystal becoming re-entrained in mixing bowl convection currents of varying compositions caused by continued magma injection.

a

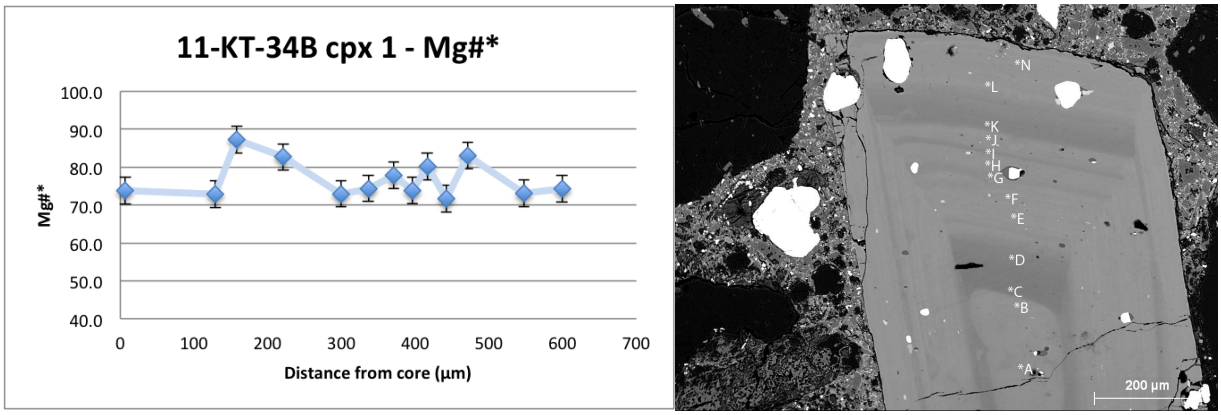

b

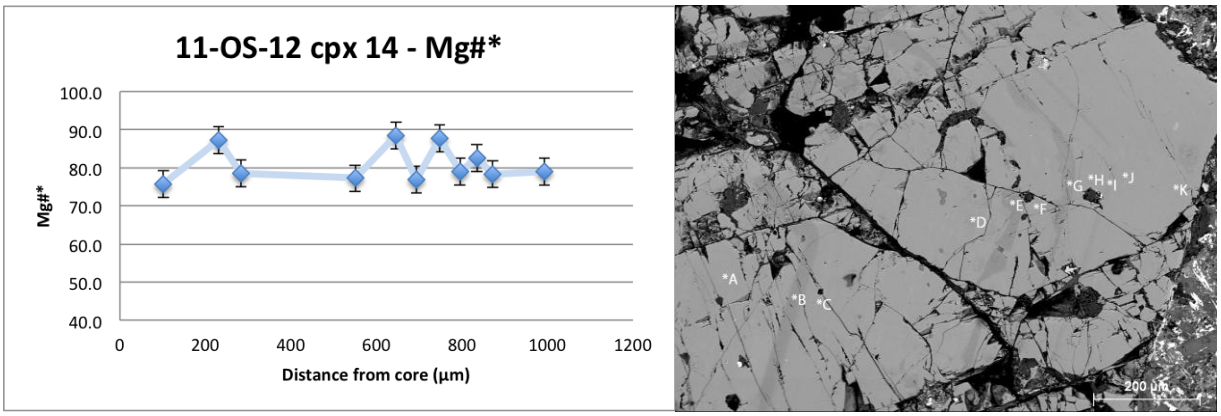

c

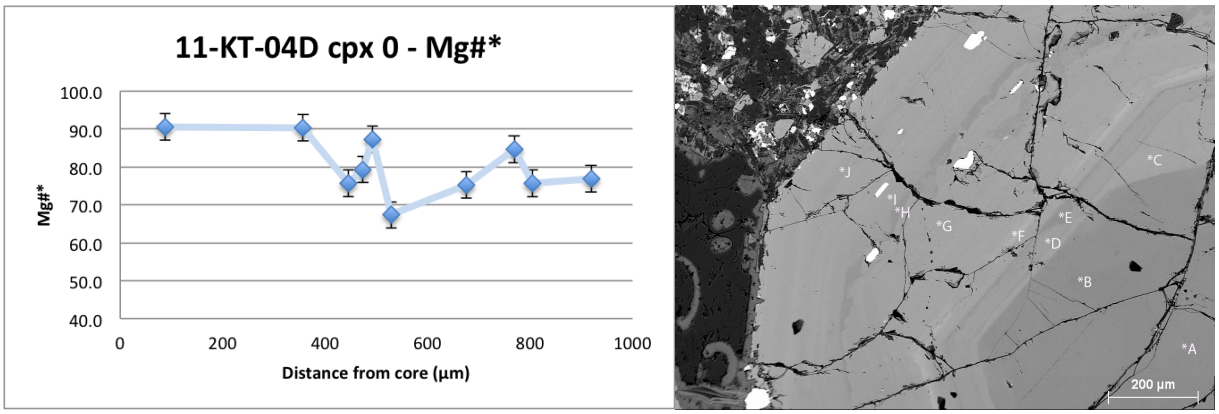

Figure 4.14) Three transects displaying Mg#* across complexly zoned clinopyroxenes. A) and B) show clinopyroxenes with iron rich cores while C) shows a clinopyroxene with a magnesium rich core. Compare pattern with Figure 4.13b.

Under this model the same mechanism that generates the rounded character of the green Fe-rich core also generates the alternating Mg-rich and Fe-rich bands and the associated dissolution features. Additionally the source melt for the Fe-rich salite cores and the source melt for the Fe-rich salite bands are the same. This model could also explain why zoning patterns are not ubiquitous across individual magmas: the paths single crystals take through the chamber are chaotic and so no single set of epitaxial bands can define an entire magma batch. Some phenocrysts would interact with the mixing bowl extensively and display three or more Mg-rich bands- representing three or more instances where it became entrained in a current of more primitive melt (such as with Figure 4.14b). Other phenocrysts may only become entrained once and record a single Mg-rich band [See Results Section; Figure 3.10 and others]. And still others may not interact with the mixing bowl at all and instead display a homogenous Fe-rich composition throughout [See Results Section; Figure 3.8 and others]. This explains the multitude of complex zoning patterns seen in the Pontide Arc samples, detailed in the Results section. Expanding on this clinopyroxenes with Mg-rich cores (such as the one in Figure 4.14c) would have initially crystalized from the rising primitive magma (as opposed to the magma chamber). This primitive composition clinopyroxene core would then have more Fe-rich material encase it upon being ejected from the current of primitive melt into the more evolved melt of the chamber during convection in the mixing bowl. Subsequent dissolution surfaces and Mg-rich bands result from the crystal being temporarily entrained in more mafic currents in the mixing bowl. The Bergantz et al. (2015) model could also explain why the chemical ranges within individual clinopyroxenes are not the same size across all clinopyroxenes from the same magmas, different crystal see different melt histories as such not all the

crystals within a magma will record the same minimum and maximum values for considered components [See Figure 3.14, 3.34, and others in the Results Section].

In the introduction the distinction was made between complex zoning and saw-tooth oscillatory zoning. Both are marked by dissolution surfaces and compositional discontinuities however in complex zoning the size of the jumps are much larger and much less frequent. The interpretation given by other workers is that saw-tooth zoning is due to convection in a magma chamber with a thermal gradient under closed system conditions (Ginibre et al., 2002), while complex zoning is due to open system processes (Streck, 2008). The Bergantz et al (2015) model could bridge this gap and have both zoning type form in response to magma injection. The hypothesis of vigorous magma chamber convection brought on by magma injection is not new; for instance the Couch et al. (2001) model despite being a closed system maintains a basalt layer at the bottom of the chamber providing heat that caused the convection and resulting complex zoning. Other models that predicted convection due to magma injection allow for mass exchange. Elardo and Shearer (2014) explained complex zoning (seen in trace elements) in clinopyroxenes in lunar basalt by invoking vigorous convection in a magma chamber due to a large thermal gradient driven by hot magma injection from below with potential chemical mixing. If the saw-tooth oscillatory zoning is a product of convection in the Bergantz et al. (2015) 'mixing bowl' that would explain why the clinopyroxene in Figure 4.14a has a homogenous core (it grew from a Fe-rich melt that was not convecting) while the Fe-rich epitaxial bands are saw-toothed zoned (they grew under turbulent conditions in which melts of differing composition were mixed together). Dissolution surfaces would be caused by either thermal or compositional perturbations. The second large Mg-rich band (point K in the back-scattered image)

appears to have a bit of saw tooth zoning towards the outer edge, which is consistent with turbulent mixing of a more primitive melt current.

The relative sizes of epitaxial bands may indicate characteristics of the magma mixing scenarios that formed them. The relatively larger size of the Fe-rich epitaxial bands compared to the Mg-rich bands indicates either faster growth under more evolved melt conditions or the dominance of the more-evolved magma chamber melt over the melt of the primitive magma in the mixing bowl [Figure 4.14 a, b, and c (excluding the core)]. Examining the clinopyroxene in Figures 4.14a and 4.14b shows a clear size difference between the Mg-rich bands, this could be explained by a difference in the strength of the mixing events or the size of the mafic magma batch being injected that led to the eruptions of both samples.

There is a discrepancy between the theoretical composition-time profiles of the phenocrysts in the Bergantz et al. (2015) simulation [Figure 4.13b] and the composition-distance profiles of the clinopyroxenes of the Pontide Arc [Figure 4.14]. In the Bergantz et al. (2015) simulation the profile of the melt composition gradually moves towards the composition of the melt of the injected magma; this is seen as an overall positive slope on Figure 4.13b. If the simulated crystals are taken as clinopyroxenes and the newly-arrived injected magma is more mafic than the melt of the chamber then this would be recorded as increasing average Mg# moving away from the core of the clinopyroxene. The Pontide Arc clinopyroxenes typically do not show this and instead show relatively flat average trends with a range of Mg#* restricted between two values, indicating a steady state. Two possible explanations for the discrepancy are examined.

The first explanation is that Pontide Arc evolved magma chambers that were intruded were large compared to the volume of the intruding primitive magma batch and the Pontide chamber melt acted as a compositional buffer preventing clinopyroxene composition migration. Given that the Bergantz et al. (2016) magma chamber is only eight times wider than the dike intercepting the simulated chamber this is a plausible explanation (Bergantz et al., 2015, Supplementary Information). If extreme size differences magmas were the case then the majority of the clinopyroxenes produced in the Pontide Arc magma chambers would be homogenous Fe-rich salite and only a few phenocrysts near the mixing bowl would display complex zoning. The majority of clinopyroxenes in the Pontide Arc samples are complexly zoned. This inconsistency could result from the simple fact that the 'unlocked' mobile crystals in the mixing bowl (the crystals that become complexly zoned) are the most likely to be erupted while crystals still locked in the crystal mush layer (un-zoned or weakly zoned crystals) stay in the magma chamber (Bergantz et al., 2015). In this case then the first explanation involving a large chamber buffering the melt composition would work. Related to size is how mass flux was handled in the Bergantz et al. (2015) simulation: the top boundary of the magma chamber was open allowing for fluid to flow out of the chamber as new material flowed in from the bottom; this could explain the evolution of melt signatures. The second explanation is that this discrepancy between patterns is a product of the Bergantz et al. (2015) simulation not taking into account the effects of phase crystallization on melt composition. The number of particles (147,040) and the size of the particles (4 mm) were held constant during the simulation, as were the viscosity and density of the melt (Bergantz et al. 2015, Supplementary Information). Additionally it could be both explanations contributing to the discrepancy.

4.3.3 Further evidence for magma mixing

The oscillation from one epitaxial band with a salite composition to another band with diopside composition without the overall migration by the system to more Fe- rich compositions [Figure 4.14 a, b, and c] may itself be hinting at magma mixing. In studying plagioclase zoning in the 2004 dacite from Mount St. Helens Streck et al. (2008) noted three profiles in the Anorthite (An) contents across individual phenocrysts [See Figure 4.15]. Profile A shows an overall decrease in An content from the plagioclase core (on the right of the graph) to the rim (on the left of the graph); this pattern is expected of a magma chamber crystalizing under closed-system conditions with crystals experiencing varying temperatures (Streck et al., 2008). Profile B shows an idealized plagioclase phenocryst with An content varying between two An values, a pattern most easily explained by periodic injections of more primitive magma into the system that buffer what should be a decreasing Ca/Na ratio due to continued crystallization (Streck et al., 2008). Profile C shows a plagioclase with overall An content increasing towards the rim requiring the addition of great amounts of calcium rich (more primitive) magma to the system and is strong evidence for an open system (Streck et al., 2008). Most of the clinopyroxenes of the Pontide Arc samples display composition trends similar to Profile B of Streck et al. (2008), implying an open system.

Another interesting feature of the data that is easily explained by an open system magma recharge model is the Cr contents of the bands within the clinopyroxenes of the Pontide Arc. Considering only the tables presented in the results section, there are 22 instances where Cr was detected at a clinopyroxene analysis site, with 20 of those occurring in Mg-rich bands. That said the reported levels of chrome are barely above the

detection limit, as such it is possible these detections are due to instrument noise. However, if these detection events were purely random then only ~50% should occur on Mg-rich bands not 91% (for the most part there was one Mg-rich band analyzed for each Fe-rich band). According to Streck et al. (2002) Mg-rich bands grow during periods where the clinopyroxenes are in contact with more primitive magma compositions during recharge events. The Bergantz et al. (2015) model is consistent with the higher incidence of Cr detection in Mg-rich bands as in even slightly more evolved magmas phases like chromite and clinopyroxene will have consumed significant amounts of the chrome in the melt even after a small amount of fractionation (Streck et al., 2002). The positive correlation between Cr content and Mg#* in clinopyroxenes provides additional evidence that Mg-rich epitaxial bands grew in more mafic magmas and magma mixing most easily explains the Fe-rich bands separating the Mg-rich bands (Streck, 2008). This observation also lends credit to the interpretation that new magma was being mixed into an open system as opposed to a closed self-mixing scenario where a crystal is visiting various parts of the magma chamber at different temperatures (a model that could not explain Cr content fluctuations). Such models have been proposed by Couch et al. (2001) to explain compositional zoning.

Trace elements can provide additional chemical evidence on the cause of the complex zoning (Streck, 2008). Gülmez et al (2016) determined the Rare Earth Element (REE) abundances of the Mg-rich cores and Fe-rich rims of several Pontide Arc clinopyroxenes [See Figure 4.16]. The Fe-rich zones displayed significantly higher concentrations of REEs compared to the Mg-rich zones; however, the shapes of the chondrite-normalized REE patterns from both zones in the same crystal are similar despite

this concentration difference. This pattern is common to all clinopyroxenes from all mafic potassic rocks of the Pontide Arc (Gülmez et al., 2016). REE concentration in more evolved Fe-rich melts would be expected to be higher than in Mg-rich melts; consequently the REE also support the Bergantz-style mixing model outlined above providing the magma in the intruded chamber is a magma further progressed on the liquid line of descent of the primitive magma intruding the chamber.

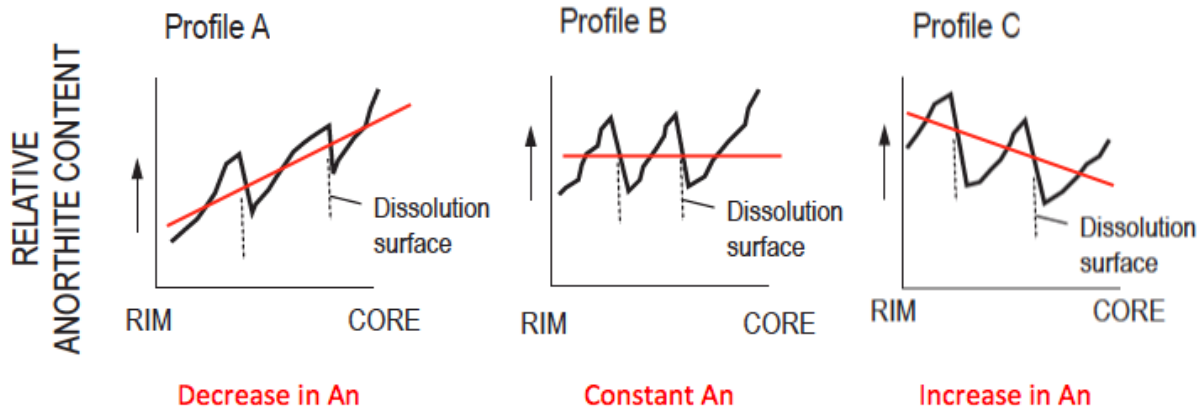

Figure 4.15) Theoretical An profiles of zoned plagioclase. Note: core is on right- this is opposite to my Pontide Cpx profiles. Figure modified after Figure 11 of Streck et al. (2008)

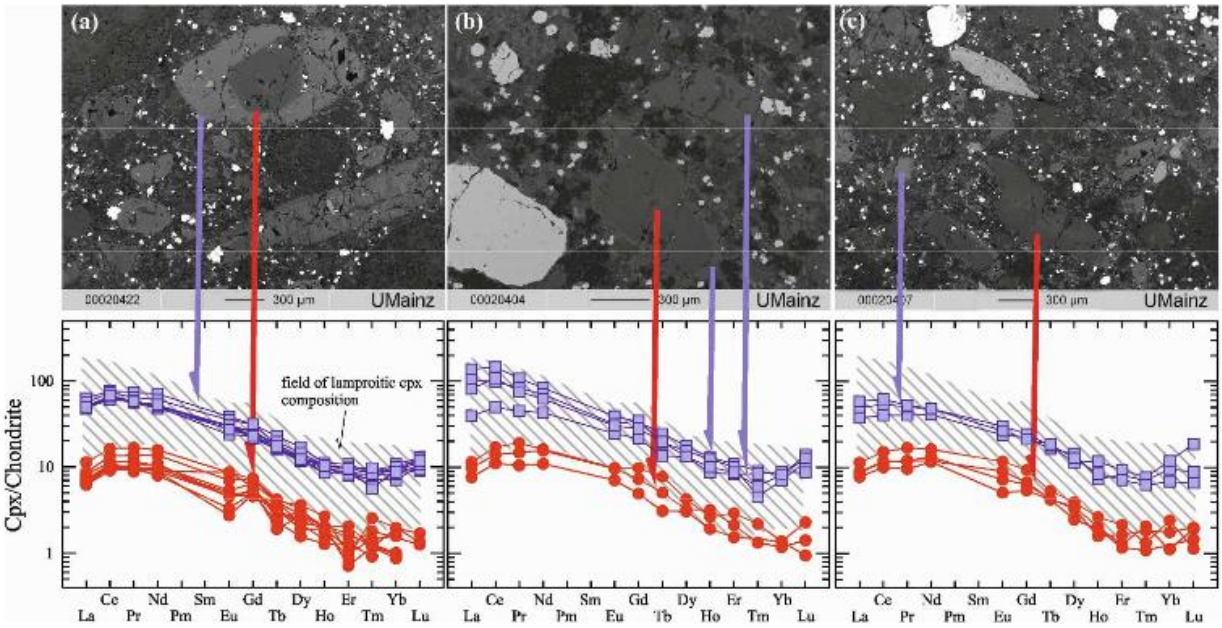

Figure 4.16) Rare Earth Element diagrams of analyses performed on Mg-rich cores and Fe-rich rims of clinopyroxenes from the Pontide Arc samples (Figure 5 of Gülmez et al. (2016))

5 CONCLUSIONS

The purpose of this study was to examine the textural and chemical zonation patterns in clinopyroxenes from Late Cretaceous mafic potassic igneous rocks from the forearc region of Pontide magmatic arc (present day north-central Turkey) to discern insights into the evolutionary histories of these magmas.

The clinopyroxenes of leucitites of the Pontide Arc have more epitaxial bands and more commonly possess green cores compared to clinopyroxenes found in minettes. However the clinopyroxenes of both rock types span the same compositional range (diopside to salite). The number of Mg-rich bands found in complexly zoned clinopyroxenes is not consistent across samples nor are the ranges of chemical constituents of said clinopyroxenes ubiquitous to all phenocrysts inside a sample. The Fe-rich bands and cores plot off of the one-to-one line from Putirka (2015) indicating a lack of equilibrium between the clinopyroxene and the melt and hint at the influence of open system processes. The same is true of the Mg-rich bands but to a lesser degree and they may represent more accurate pressure and temperature results. The leucite (when present) and clinopyroxene seem to have crystalized at different pressures, as leucite is not stable at the pressures recorded by the clinopyroxene, which implicate stalling at the base of the forearc crust. When the calculated pressures and temperatures of the Pontide Arc samples are compared to the melting experiments of other mafic potassic rocks the results indicate that some samples crystalized under water saturated conditions while other samples crystalized under water-undersaturated conditions.

In light of the near identical compositional signatures of the green salite cores and green salite epitaxial bands and the higher incidence of detectable chrome in Mg-rich bands I interpret that 1) the green salite bands and green salite cores are deposits grown from the same resident magma, 2) the Mg-rich epitaxial bands are caused by the arrival of a new, more primitive magma, and 3) the repeated fluctuations between Fe-rich bands and Mg-rich bands are caused by the turbulent and convective flow resulting from that new magma being injected into and mixing with the more evolved melt of a magma chamber as modeled in Bergantz et al. (2015). Under the Bergantz et al. (2015) model a single magma-mixing event can induce the formation of multiple Mg-rich epitaxial bands simplifying the single chamber model proposed by Cioni et al. (1998). The variable number of Mg-rich bands and the variable ranges of chemical components across clinopyroxenes from a single sample are also explained by the convective mixing model proposed by Bergantz et al. (2015). Additionally, the convective currents in the Bergantz et al. (2015) mixing bowl can potentially cause saw-tooth oscillatory zoning inside the larger epitaxial bands. The lack of a system-wide evolution towards more Fe-rich clinopyroxene compositions indicates open system conditions in which magma recharge buffers the melt's Fe/Mg ratio. REE chemical analysis by Gülmez et al. (2016) indicates that the evolved salite-producing melts are derived from more primitive diopside-producing melts. Additionally the REE data of Gülmez et al. (2016) and the size of the changes in Mg#* between epitaxial bands indicate that changing water content of the magma is insufficient to causes the compositional changes seen in the clinopyroxenes of the Pontide Arc magmas. Additionally calculated magma water contents during clinopyroxene formation show a correlation opposite of what is expected under a water-controlled clinopyroxene composition model. Further

discrediting this water-controlled model is the observation that the pressures recorded by the clinopyroxenes indicate that water should not have been degassing in appreciable amounts, preventing the zoning mechanism. These results indicate the importance of magma mixing in the evolution of the Pontide Arc magmatic products.

6 WORKS CITED

Armienti, P., Perinelli, C., & Putirka, K. D., 2012, A new model to estimate deep-level magma ascent rates, with applications to Mt. Etna (Sicily, Italy): Journal of Petrology, v. 54, v. 4, p. 795-813

Armstrong, J.T., 1988, Quantitative analysis of silicate and oxide materials: comparison of Monte Carlo, ZAF, and phi-rho-z procedures. Microbeam Analysis, 239-246.

Baker, D. R., & Eggler, D. H., 1987, Compositions of anhydrous and hydrous melts coexisting with plagioclase, augite, and olivine or low-Ca pyroxene from 1 atm to 8 kbar; application to the Aleutian volcanic center of Atka: American Mineralogist, v. 72, i.1-2, p. 12-28.

Barton, M., Hamilton, D. L., 1978, Water-saturated melting relations to 5 kilobars of three Leucite Hills lavas: Contributions to Mineralogy and Petrology, v. 66, i. 1, p. 41-49.

Barton, M., & Hamilton, D. L., 1979, The melting relationships of a madupite from the Leucite Hills, Wyoming, to 30 kb: Contributions to Mineralogy and Petrology, v. 69, i. 2, p. 133-142.

Barton, M., Varekamp, J. C., & Van Bergen, M. J., 1982, Complex zoning of clinopyroxenes in the lavas of Vulsini, Latium, Italy: evidence for magma mixing: Journal of Volcanology and Geothermal Research, v. 14, i. 3, p. 361-388.

Bédard, J. H., Francis, D. M., & Ludden, J., 1988, Petrology and pyroxene chemistry of Monteregian dykes: the origin of concentric zoning and green cores in

clinopyroxenes from alkali basalts and lamprophyres: Canadian Journal of Earth Sciences, v. 25, i.12, p. 2041-2058.

Bergantz, G. W., Schleicher, J. M., & Burgisser, A., 2015, Open-system dynamics and mixing in magma mushes: Nature Geoscience, v. 8, n. 10, p. 793-796.

Cioni, R., Marianelli, P., & Santacroce, R., 1998, Thermal and compositional evolution of the shallow magma chambers of Vesuvius: evidence from pyroxene phenocrysts and melt inclusions: Journal of Geophysical Research: Solid Earth, v. 103, i. B8, p. 18277-18294.

Couch, S., Sparks, R. S. J., & Carroll, M. R., 2001, Mineral disequilibrium in lavas explained by convective self-mixing in open magma chambers: Nature, v. 411, p. 1037-1039.

Crabtree, S. M., & Lange, R. A., 2011, Complex phenocryst textures and zoning patterns in andesites and dacites: Evidence of degassing-induced rapid crystallization?: Journal of Petrology, v. 52, n. 1, p. 3-38.

Cundari, A., & Salviulo, G., 1989, Ti solubility in diopsidic pyroxene from a suite of New South Wales leucitites (Australia): Lithos, v. 22, i. 3, p. 191-198.

Deer, W. A., Howie, R., A., and Zussman, J., 1985, An Introduction to the rock forming minerals, Essex, England, Longman Group Limited, Appendix 1.

Dolfi, D., and Trigila, R., 1983, Clinopyroxene solid solutions and water in magmas: results in the system phnolititc tephrite- H_2O: Mineralogical Magazine, v.47, pp. 347-351.

Edgar, A. D., Condliffe, E., Barnett, R. L., & Shirran, R. J., 1980, An experimental study of an olivine ugandite magma and mechanisms for the formation of its K-enriched derivatives: Journal of Petrology, v. 21, i. 3, p. 475-497.

Elardo, S. M., & Shearer, C. K., 2014, Magma chamber dynamics recorded by oscillatory zoning in pyroxene and olivine phenocrysts in basaltic lunar meteorite Northwest Africa 032: American Mineralogist, v. 99, v. 2-3, p. 355-368.

Elkins-Tanton, L. T., & Grove, T. L., 2003, Evidence for deep melting of hydrous metasomatized mantle: Pliocene high‐potassium magmas from the Sierra Nevadas: Journal of Geophysical Research: Solid Earth, v. 108, i. B7.

Esperança, S. and Holloway, J. R., 1986, The origin of the high-K latites from Camp Creek, Arizona: constraints from experiments with variable fO2 and aH2O: Contributions to Mineralogy and Petrology, v. 93, i. 4, p. 504-512.

Esperança, S. and Holloway, J. R., 1987, On the origin of some mica-lamprophyres: experimental evidence from a mafic minette: Contributions to Mineralogy and Petrology, v. 95, i. 2, p. 207-216.

Fulignati, P., Marianelli, P., & Sbrana, A., 2000, Glass-bearing felsic nodules from the crystallizing sidewalls of the 1944 Vesuvius magma chamber: Mineralogical Magazine, v. 64, i. 3, p. 481-496.

Ginibre, C., Kronz, A., & WoÈrner, G. (2002). High-resolution quantitative imaging of plagioclase composition using accumulated backscattered electron images: new constraints on oscillatory zoning: Contributions to Mineralogy and Petrology, 142(4), 436-448.

Gülmez, F., Genç, C., Tüysüz, O., Karacik, Z., Roden, M., Billor, Z., Hames, W., 2013, Geochemistry and petrogenesis of the late Cretaceous potassic-alkaline volcanic rocks from the Amasya Region (northern Turkey): Geophysical Research Abstracts, v. 15, EGU2013-9833

Gülmez, F., & Genç, S. C., 2015, Differentiation processes in Late Cretaceous ultrapotassic volcanics around Amasya: Bulletin of the Mineral Research and Exploration, v.151, p. 149-168.

Gulmez, F., Genc, S. C., Prelvie, D., Tuysuz, O., Zekiye, K., Roden, M. F., Billor, Z., 2016, Ultrapotassic volcanism from the waning stage of the Neotethyan subduction: a key study from the Izmir Ankara Erzincan Suture Belt, central northern Turkey: Journal of Petrology, submitted, in press.

Holm, P. M., 1982, Mineral chemistry of perpotassic lavas of the Vulsinian district, the Roman Province, Italy: Mineralogical Magazine, v. 46, p. 379-386.

Kuehner, S. M., Edgar, A. D., & Arima, M.,1981, Petrogenesis of the ultrapotassic rocks from the Leucite Hills, Wyoming: American Mineralogist, v. 66, i. 7-8, p. 663-677.

Marianelli, P., Métrich, N., & Sbrana, A., 1999, Shallow and deep reservoirs involved in magma supply of the 1944 eruption of Vesuvius: Bulletin of Volcanology, v. 61, i. 1-2, p. 48-63.

McGary, R. S., Evans, R. L., Wannamaker, P. E., Elsenbeck, J., & Rondenay, S., 2014, Pathway from subducting slab to surface for melt and fluids beneath Mount Rainier: Nature, v. 511, p. 338-340.

Moore, G., Vennemann, T., & Carmichael, I. S. E., 1995, Solubility of water in magmas to 2 kbar: Geology, v. 23, n. 12, p. 1099-1102.

Morimoto, N., 1988, Nomenclature of pyroxenes: American Mineralogist, v. 73, pp 1123-1133.

O'Brein, H.E., Irving, A.J., McCallum, I.S., 1988, Complex zoning and resorption of phenocrysts in mixed potassix mafic magmas of the Highwood Mountains, Montana: American Mineralogist, v.73, pp. 1007-1024.

Okay, A., I., 2015, Geology of Turkey Maps and Diagrams: http://web.itu.edu.tr/~okay/AralOkayMapsAndDiagrams.htm

Peccerillo, A., 2005, Plio-quaternary volcanism in Italy (Vol. 365). Springer-Verlag Berlin Heidelberg.

Perini, G., & Conticelli, S., 2002, Crystallization conditions of leucite-bearing magmas and their implications on the magmatological evolution of ultrapotassic magmas: the Vico Volcano, Central Italy: Mineralogy and Petrology, v. 74, i. 2-4, p. 253-276.

Poldervaart, A., & Hess, H. H., 1951, Pyroxenes in the crystallization of basaltic magma. The Journal of Geology, v. 59, n. 5 p. 472-489.

Prelević, D., Akal, C., Foley, S. F., Romer, R. L., Stracke, A., & Van Den Bogaard, P. , 2012, Ultrapotassic mafic rocks as geochemical proxies for post-collisional dynamics of orogenic lithospheric mantle: the case of southwestern Anatolia, Turkey: Journal of Petrology, v. 53, i. 5, p. 1019-1055.

Putirka, K., Ryerson, F. J., & Mikaelian, H., 2003, New igneous thermobarometers for mafic and evolved lava compositions, based on clinopyroxene+ liquid equilibria: American Mineralogist, v. 88, p. 1542-1554.

Putirka, K. D., 2008, Thermometers and Barometers for Volcanic Systems: Reviews in Mineralogy and Geochemistry, v. 69, p. 61-120.

Putirka, K. D., 2015, http://www.fresnostate.edu/csm/ees/faculty-staff/putirka.html.

Sato, H., Holtz, F., Behrens, H., Botcharnikov, R., & Nakada, S., 2005, Experimental petrology of the 1991–1995 Unzen dacite, Japan. Part II: Cl/OH partitioning between hornblende and melt and its implications for the origin of oscillatory zoning of hornblende phenocrysts: Journal of Petrology, v. 46, n. 2, p. 339-354.

Semiz, B., Çoban, H., Roden, M. F., Özpınar, Y., Flower, M. F., & McGregor, H., 2012, Mineral composition in cognate inclusions in Late Miocene–Early Pliocene potassic lamprophyres with affinities to lamproites from the Denizli region, Western Anatolia, Turkey: Implications for uppermost mantle processes in a back-arc setting: Lithos, v. 134, p. 253-272.

Streck, M. J., Dungan, M. A., Malavassi, E., Reagan, M. K., & Bussy, F., 2002, The role of basalt replenishment in the generation of basaltic andesites of the ongoing activity at Arenal volcano, Costa Rica: evidence from clinopyroxene and spinel: Bulletin of Volcanology, v. 64, n.5 , p. 316-327.

Streck, M.J., 2008, Mineral Textures and Zoning as Evidence for Open System Processes: Reviews in Mineralogy and Geochemistry, v. 69, pp.592-622.

Streck, M. J., Broderick, C. A., Thornber, C. R., Clynne, M. A., & Pallister, J. S., 2008, Plagioclase populations and zoning in Dacite of the 2004–2005 Mount St. Helens Eruption: constraints for magma origin and dynamics: U.S. Geological Survey Professional Paper 1750.

Van Bergen, M.J., Vroon, P.Z., Varekamp, J.C., Poorter, R.P.E., 1992, The origin of the potassic rock suite from Batu Tara volcano (East Sunda Arc, Indonesia): Lithos v. 28, p. 261–282.

Wallace, P., and Carmichael, I. S., 1989, Minette lavas and associated leucitites from the Western Front of the Mexican Volcanic Belt: petrology, chemistry, and origin: Contributions to Mineralogy and Petrology, v.103, i. 4, p. 470-492.

Wass, S. Y., 1973, The origin and petrogenetic significance of hour-glass zoning in titaniferous clinopyroxenes: Mineralogical Magazine, v. 39, n. 302, p. 133-144.

Wass, S. Y., 1979, Multiple origins of clinopyroxenes in alkali basaltic rocks: Lithos, v. 12, n.2, p. 115-132.

Winter, J. D., 2010, *Principles of igneous and metamorphic petrology*, New York: Prentice Hall, p. 38-39.

Yilmaz, Y., Tüysüz, O., Yigitbas, E., Genç, C., S., Sengor A., 1997, Geology and tectonic evolution of the Pontides: ed. Robinson A.G., Regional and petroleum geology of the Black Sea and surrounding region: AAPG Memoir 68, p. 183-226.

Zhu, Y., & Ogasawara, Y., 2004, Clinopyroxene phenocrysts (with green salite cores) in trachybasalts: implications for two magma chambers under the Kokchetav UHP massif, North Kazakhstan: Journal of Asian Earth Sciences, v. 22, i. 5, p. 517-527.

APPENDIX A

sample	11-AMS-06					
Cpx #	Cpx 7					
probe site	a	b	c	d	e	f
	Wt% oxide					
SiO2	48.82	49.20	47.34	48.81	46.50	50.25
Al2O3	5.18	6.18	6.51	5.77	6.77	5.02
MgO	13.48	13.02	12.21	12.17	12.21	12.58
FeO	8.27	8.40	8.33	8.61	8.69	8.76
MnO	0.27	0.19	0.15	0.18	0.19	0.36
CaO	22.41	22.93	22.92	21.99	22.64	22.29
Na2O	0.42	0.34	0.37	0.48	0.40	0.46
TiO2	0.84	1.08	1.21	1.02	1.26	0.95
Cr2O3	n.d.	n.d.	n.d.	n.d.	n.d.	n.d.
TOTAL	99.69	101.33	99.02	99.03	98.65	100.65
	Number of cations in formula					
Si	1.814	1.804	1.778	1.835	1.754	1.861
Al	0.227	0.267	0.288	0.256	0.301	0.219
Mg	0.747	0.712	0.684	0.682	0.686	0.694
Fe^{2+}	0.130	0.167	0.149	0.221	0.124	0.231
Fe^{3+}	0.127	0.090	0.113	0.050	0.150	0.040
Mn	0.008	0.006	0.005	0.006	0.006	0.011
Ca	0.892	0.901	0.922	0.886	0.915	0.884
Na	0.030	0.024	0.027	0.035	0.029	0.033
Ti	0.023	0.030	0.034	0.029	0.036	0.026
Cr	0.000	0.000	0.000	0.000	0.000	0.000
TOTAL	4.000	4.000	4.000	4.000	4.000	4.000
$Mg/(Mg+Fe^{+2})*100$	85.2	81.0	82.1	75.6	84.7	75.0
$Mg/(Mg+Fe_{total})*100$	74.4	73.4	72.3	71.6	71.5	71.9
Cation Index DS	2.907	2.832	2.769	2.807	2.709	2.878
Wo	46.8	48.0	49.3	48.0	48.6	47.5
En	39.2	37.9	36.5	37.0	36.5	37.3
Fs	13.9	14.0	14.2	15.0	14.9	15.2

APPENDIX A							
sample	11-AMS-06						
Cpx #	Cpx unk1					Cpx 11	
probe site	a	b	c	d		a	b
	Wt% oxide						
SiO2	48.72	49.44	49.21	46.55		50.00	49.23
Al2O3	4.72	3.88	5.60	6.75		4.66	5.53
MgO	13.09	13.37	12.42	11.87		12.39	11.99
FeO	7.88	7.37	8.13	8.80		9.39	9.38
MnO	0.19	0.20	0.21	0.21		0.31	0.26
CaO	23.12	23.28	23.05	22.95		21.50	21.36
Na2O	0.39	0.28	0.38	0.45		0.58	0.69
TiO2	0.74	0.78	1.08	1.36		0.82	0.92
Cr2O3	n.d.	n.d.	n.d.	n.d.		n.d.	n.d.
TOTAL	98.83	98.60	100.07	98.94		99.65	99.37
	Number of cations in formula						
Si	1.828	1.860	1.830	1.753		1.872	1.847
Al	0.209	0.172	0.246	0.299		0.205	0.245
Mg	0.732	0.749	0.689	0.666		0.692	0.671
Fe^{2+}	0.126	0.147	0.192	0.127		0.247	0.235
Fe^{3+}	0.122	0.085	0.061	0.150		0.047	0.059
Mn	0.006	0.006	0.006	0.007		0.010	0.008
Ca	0.929	0.938	0.919	0.926		0.862	0.859
Na	0.028	0.020	0.027	0.033		0.042	0.050
Ti	0.021	0.022	0.030	0.039		0.023	0.026
Cr	0.000	0.000	0.000	0.000		0.000	0.000
TOTAL	4.000	4.000	4.000	4.000		4.000	4.000
$Mg/(Mg+Fe^{+2})*100$	85.4	83.6	78.2	84.0		73.7	74.1
$Mg/(Mg+Fe_{total})*100$	74.8	76.4	73.1	70.6		70.2	69.5
Cation Index DS	2.978	3.094	2.875	2.691		2.851	2.753
Wo	48.5	48.7	49.2	49.3		46.4	46.9
En	38.2	38.9	36.9	35.5		37.2	36.6
Fs	13.2	12.4	13.9	15.1		16.4	16.5

APPENDIX A							
sample	11-AMS-06						
Cpx #	Cpx 11						
probe site	c	d	e	f	g	h	i
	Wt% oxide						
SiO2	53.91	53.62	50.65	49.25	48.81	47.76	52.28
Al2O3	1.71	1.60	2.50	5.27	4.03	5.65	1.63
MgO	15.87	15.45	14.73	12.86	13.93	13.02	16.46
FeO	4.17	4.73	6.46	9.16	7.66	8.46	4.51
MnO	0.12	0.06	0.22	0.37	0.25	0.28	0.19
CaO	23.80	23.92	23.21	22.04	22.76	22.34	25.08
Na2O	0.19	0.22	0.27	0.47	0.31	0.42	0.21
TiO2	0.29	0.33	0.50	0.92	0.81	0.99	0.33
Cr2O3	0.52	0.26	n.d.	n.d.	n.d.	n.d.	0.33
TOTAL	100.59	100.18	98.55	100.35	98.55	98.91	101.03
	Number of cations in formula						
Si	1.966	1.967	1.895	1.827	1.833	1.792	1.893
Al	0.073	0.069	0.110	0.230	0.178	0.250	0.070
Mg	0.863	0.845	0.821	0.711	0.780	0.728	0.889
Fe^{2+}	0.127	0.145	0.110	0.186	0.107	0.124	0.004
Fe^{3+}	0.000	0.000	0.092	0.098	0.133	0.141	0.132
Mn	0.004	0.002	0.007	0.012	0.008	0.009	0.006
Ca	0.930	0.940	0.930	0.876	0.916	0.898	0.973
Na	0.014	0.016	0.020	0.034	0.023	0.030	0.015
Ti	0.008	0.009	0.014	0.026	0.023	0.028	0.009
Cr	0.015	0.007	0.000	0.000	0.000	0.000	0.009
TOTAL	4.000	4.000	4.000	4.000	4.000	4.000	4.000
$Mg/(Mg+Fe^{+2})*100$	87.2	85.3	88.2	79.3	87.9	85.4	99.6
$Mg/(Mg+Fe_{total})*100$	87.2	85.3	80.3	71.4	76.4	73.3	86.7
Cation Index DS	3.548	3.518	3.294	2.828	3.056	2.836	3.528
Wo	48.3	48.7	47.4	46.5	47.1	47.3	48.6
En	44.9	43.7	41.9	37.8	40.1	38.3	44.3
Fs	6.8	7.6	10.7	15.7	12.8	14.4	7.1

APPENDIX A							
sample	11-AMS-06						
Cpx #	Cpx 15						
probe site	a	b	c	d	e	f	g
	Wt% oxide						
SiO2	50.19	49.56	49.76	52.27	49.27	47.37	47.84
Al2O3	5.41	4.16	4.18	2.03	4.41	5.87	5.52
MgO	12.75	14.02	13.90	16.40	13.14	13.35	13.19
FeO	8.20	8.43	8.88	5.70	8.26	7.87	8.10
MnO	0.14	0.32	0.25	0.13	0.21	0.20	0.20
CaO	22.11	22.46	22.21	23.67	22.57	22.69	22.52
Na2O	0.44	0.42	0.46	0.23	0.41	0.38	0.38
TiO2	0.82	0.84	0.94	0.40	0.89	1.11	1.04
Cr2O3	n.d.	n.d.	n.d.	n.d.	n.d.	n.d.	n.d.
TOTAL	100.06	100.22	100.58	100.83	99.16	98.83	98.78
	Number of cations in formula						
Si	1.864	1.832	1.836	1.899	1.846	1.774	1.795
Al	0.237	0.181	0.182	0.087	0.195	0.259	0.244
Mg	0.706	0.773	0.765	0.888	0.734	0.745	0.738
Fe^{2+}	0.233	0.122	0.146	0.064	0.165	0.088	0.120
Fe^{3+}	0.021	0.139	0.128	0.109	0.093	0.158	0.134
Mn	0.004	0.010	0.008	0.004	0.007	0.006	0.006
Ca	0.880	0.890	0.878	0.921	0.906	0.910	0.905
Na	0.032	0.030	0.033	0.016	0.030	0.028	0.028
Ti	0.023	0.023	0.026	0.011	0.025	0.031	0.029
Cr	0.000	0.000	0.000	0.000	0.000	0.000	0.000
TOTAL	4.000	4.000	4.000	4.000	4.000	4.000	4.000
$Mg/(Mg+Fe^{+2})*100$	75.2	86.4	83.9	93.3	81.6	89.4	86.0
$Mg/(Mg+Fe_{total})*100$	73.5	74.8	73.6	83.7	73.9	75.2	74.4
Cation Index DS	2.899	2.988	2.956	3.418	2.970	2.859	2.877
Wo	47.7	46.0	45.6	46.4	47.5	47.7	47.6
En	38.3	40.0	39.7	44.7	38.5	39.1	38.8
Fs	14.0	14.0	14.7	8.9	13.9	13.2	13.7

APPENDIX A							
sample	11-AMS-06						
Cpx #	Cpx 15			Cpx 9			
probe site	h	i		a	b	c	d
	Wt% oxide						
SiO_2	47.53	49.81		49.18	51.49	52.41	49.25
Al_2O_3	6.07	3.37		4.16	1.78	1.40	3.65
MgO	13.11	13.47		14.17	15.56	17.11	14.59
FeO	8.09	7.59		8.10	5.40	4.44	7.52
MnO	0.17	0.38		0.17	0.11	0.07	0.19
CaO	22.94	23.30		22.10	24.09	23.96	22.44
Na_2O	0.33	0.24		0.42	0.25	0.16	0.39
TiO_2	1.14	0.81		0.63	0.31	0.23	0.55
Cr_2O_3	n.d.	0.08		n.d.	n.d.	0.25	0.08
TOTAL	99.38	99.04		98.93	98.99	100.03	98.67
	Number of cations in formula						
Si	1.773	1.869		1.837	1.909	1.911	1.840
Al	0.267	0.149		0.183	0.078	0.060	0.161
Mg	0.729	0.753		0.789	0.860	0.930	0.813
Fe^{2+}	0.106	0.155		0.115	0.062	0.026	0.081
Fe^{3+}	0.147	0.083		0.138	0.105	0.110	0.154
Mn	0.005	0.012		0.006	0.003	0.002	0.006
Ca	0.917	0.937		0.885	0.956	0.936	0.899
Na	0.024	0.017		0.030	0.018	0.012	0.028
Ti	0.032	0.023		0.018	0.009	0.006	0.015
Cr	0.000	0.002		0.000	0.000	0.007	0.002
TOTAL	4.000	4.000		4.000	4.000	4.000	4.000
$Mg/(Mg+Fe^{+2})*100$	87.4	82.9		87.3	93.3	97.3	90.9
$Mg/(Mg+Fe_{total})*100$	74.3	76.0		75.7	83.7	87.3	77.6
Cation Index DS	2.839	3.122		3.021	3.450	3.569	3.109
Wo	48.2	48.3		45.8	48.1	46.7	46.0
En	38.3	38.8		40.8	43.3	46.4	41.6
Fs	13.5	12.9		13.4	8.6	6.9	12.3

APPENDIX A						
sample	11-AMS-06					
Cpx #	Cpx 9					
probe site	e	f	g	i	j	k
	Wt% oxide					
SiO_2	51.30	47.15	47.42	47.31	49.66	47.23
Al_2O_3	2.07	5.07	5.37	5.38	3.54	5.50
MgO	16.68	13.94	13.82	13.44	15.64	14.17
FeO	4.36	8.34	8.46	8.18	5.08	7.69
MnO	0.13	0.26	0.25	0.20	0.11	0.17
CaO	24.08	22.51	22.80	23.05	23.83	23.30
Na_2O	0.22	0.44	0.32	0.32	0.32	0.23
TiO_2	0.33	0.96	0.94	1.07	0.64	1.08
Cr_2O_3	0.29	n.d.	0.10	n.d.	0.33	0.09
TOTAL	99.46	98.68	99.49	98.97	99.15	99.46
	Number of cations in formula					
Si	1.882	1.766	1.765	1.771	1.833	1.754
Al	0.089	0.224	0.235	0.238	0.154	0.241
Mg	0.912	0.778	0.767	0.750	0.860	0.785
Fe^{2+}	0.000	0.038	0.061	0.073	0.000	0.034
Fe^{3+}	0.134	0.223	0.202	0.183	0.157	0.205
Mn	0.004	0.008	0.008	0.006	0.003	0.005
Ca	0.946	0.903	0.909	0.925	0.942	0.927
Na	0.016	0.032	0.023	0.024	0.023	0.016
Ti	0.009	0.027	0.026	0.030	0.018	0.030
Cr	0.008	0.000	0.003	0.000	0.010	0.003
TOTAL	4.000	4.000	4.000	4.000	4.000	4.000
$Mg/(Mg+Fe^{+2})*100$	100.0	95.3	92.6	91.1	100.0	95.8
$Mg/(Mg+Fe_{total})*100$	87.2	74.9	74.4	74.5	84.6	76.7
Cation Index DS	3.496	2.895	2.887	2.892	3.289	2.937
Wo	47.4	46.3	46.7	47.7	48.0	47.4
En	45.7	39.9	39.4	38.7	43.8	40.1
Fs	6.9	13.8	13.9	13.6	8.2	12.5

APPENDIX A							
sample	11-KT-34B						
Cpx #	Cpx 6						
probe site	a	b	c	d	e	f	g
	Wt% oxide						
SiO_2	50.74	50.93	47.93	48.50	48.58	49.33	48.78
Al_2O_3	2.15	4.24	5.45	4.08	4.06	3.79	3.65
MgO	16.09	14.04	13.65	14.30	13.68	14.59	14.07
FeO	6.16	7.74	8.23	7.80	8.21	7.14	8.32
MnO	0.12	0.10	0.18	0.23	0.16	0.26	0.28
CaO	23.62	23.10	23.14	22.76	22.67	23.26	22.60
Na_2O	0.19	0.26	0.36	0.40	0.37	0.29	0.42
TiO_2	0.40	0.64	1.02	0.84	0.90	0.55	0.70
Cr_2O_3	n.d.	0.13	n.d.	n.d.	n.d.	n.d.	n.d.
TOTAL	99.46	101.19	99.95	98.90	98.63	99.22	98.81
	Number of cations in formula						
Si	1.871	1.865	1.776	1.811	1.826	1.833	1.827
Al	0.093	0.183	0.238	0.180	0.180	0.166	0.161
Mg	0.885	0.766	0.754	0.796	0.766	0.808	0.785
Fe^{2+}	0.033	0.170	0.075	0.064	0.113	0.064	0.085
Fe^{3+}	0.157	0.067	0.180	0.180	0.145	0.158	0.176
Mn	0.004	0.003	0.006	0.007	0.005	0.008	0.009
Ca	0.933	0.906	0.919	0.911	0.913	0.926	0.907
Na	0.014	0.018	0.026	0.029	0.027	0.021	0.030
Ti	0.011	0.018	0.028	0.024	0.025	0.015	0.020
Cr	0.000	0.004	0.000	0.000	0.000	0.000	0.000
TOTAL	4.000	4.000	4.000	4.000	4.000	4.000	4.000
$Mg/(Mg+Fe^{+2})*100$	96.4	81.8	90.9	92.6	87.2	92.7	90.3
$Mg/(Mg+Fe_{total})*100$	82.3	76.4	74.7	76.6	74.8	78.5	75.1
Cation Index DS	3.377	3.081	2.896	3.035	3.009	3.135	3.039
Wo	46.4	47.4	47.5	46.5	47.0	47.1	46.2
En	44.0	40.1	39.0	40.7	39.4	41.2	40.0
Fs	9.6	12.6	13.5	12.8	13.6	11.7	13.7

APPENDIX A							
sample	11-KT-34B						
Cpx #	Cpx 6						
probe site	h	i	j	k	l	m	n
	Wt% oxide						
SiO_2	52.42	49.30	51.00	50.02	48.13	50.08	49.35
Al_2O_3	3.13	4.12	3.76	4.82	4.81	2.83	4.28
MgO	14.58	13.76	13.91	13.16	12.84	15.34	13.81
FeO	6.44	7.87	7.08	8.74	8.68	6.38	7.34
MnO	0.15	0.22	0.16	0.29	0.31	0.15	0.23
CaO	23.23	22.67	23.68	23.05	22.87	24.32	23.32
Na_2O	0.22	0.47	0.26	0.44	0.49	0.17	0.30
TiO_2	0.56	0.56	0.63	0.84	0.88	0.42	0.63
Cr_2O_3	n.d.	n.d.	n.d.	n.d.	n.d.	n.d.	0.10
TOTAL	100.74	99.47	100.47	101.37	99.01	99.68	99.35
	Number of cations in formula						
Si	1.922	1.831	1.879	1.834	1.806	1.847	1.838
Al	0.135	0.181	0.163	0.208	0.213	0.123	0.188
Mg	0.797	0.762	0.764	0.720	0.718	0.843	0.766
Fe^{2+}	0.191	0.061	0.156	0.160	0.112	0.026	0.108
Fe^{3+}	0.006	0.183	0.062	0.108	0.160	0.171	0.121
Mn	0.005	0.007	0.005	0.009	0.010	0.005	0.007
Ca	0.913	0.902	0.935	0.906	0.920	0.961	0.930
Na	0.016	0.034	0.019	0.032	0.036	0.012	0.022
Ti	0.015	0.016	0.017	0.023	0.025	0.012	0.018
Cr	0.000	0.000	0.000	0.000	0.000	0.000	0.003
TOTAL	4.000	3.976	4.000	4.000	4.000	4.000	4.000
$Mg/(Mg+Fe^{+2})*100$	80.7	92.6	83.1	81.8	86.5	97.1	87.6
$Mg/(Mg+Fe_{total})*100$	80.1	75.7	77.8	72.9	72.5	81.1	77.0
Cation Index DS	3.262	3.014	3.155	2.920	2.889	3.304	3.074
Wo	47.7	47.1	48.6	47.6	47.9	47.9	48.1
En	41.7	39.8	39.7	37.8	37.4	42.0	39.7
Fs	10.6	13.1	11.6	14.6	14.7	10.0	12.2

APPENDIX A					
sample	11-KT-34B				
Cpx #	Cpx 6				
probe site	o	p	q	r	s
	Wt% oxide				
SiO_2	48.92	50.72	49.78	47.84	48.61
Al_2O_3	4.00	4.00	3.25	4.70	4.58
MgO	13.48	13.27	14.95	13.15	13.11
FeO	8.08	8.45	6.57	8.62	8.80
MnO	0.24	0.24	0.16	0.27	0.38
CaO	23.46	23.45	24.01	23.06	23.19
Na_2O	0.36	0.37	0.22	0.39	0.39
TiO_2	0.71	0.77	0.53	0.95	0.90
Cr_2O_3	0.09	0.07	0.09	n.d.	n.d.
TOTAL	99.34	101.35	99.54	98.98	99.96
	Number of cations in formula				
Si	1.827	1.862	1.841	1.795	1.808
Al	0.176	0.173	0.142	0.208	0.201
Mg	0.751	0.726	0.824	0.736	0.727
Fe^{2+}	0.097	0.175	0.044	0.094	0.113
Fe^{3+}	0.155	0.085	0.159	0.176	0.160
Mn	0.007	0.008	0.005	0.009	0.012
Ca	0.938	0.922	0.952	0.927	0.925
Na	0.026	0.026	0.016	0.028	0.028
Ti	0.020	0.021	0.015	0.027	0.025
Cr	0.003	0.002	0.003	0.000	0.000
TOTAL	4.000	4.000	4.000	4.000	4.000
$Mg/(Mg+Fe^{+2})*100$	88.5	80.6	94.9	88.6	86.5
$Mg/(Mg+Fe_{total})*100$	74.8	73.7	80.2	73.1	72.6
Cation Index DS	3.036	3.025	3.239	2.916	2.920
Wo	48.2	48.2	48.0	47.7	47.7
En	38.5	37.9	41.5	37.9	37.5
Fs	13.3	13.9	10.5	14.4	14.8

APPENDIX A							
sample	11-KT-34B						
Cpx #	Cpx 11						
probe site	a	b	c	d	e	f	g
	Wt% oxide						
SiO_2	51.33	48.52	49.92	51.73	52.41	52.81	50.35
Al_2O_3	2.11	4.17	4.45	1.69	2.34	2.27	4.14
MgO	15.41	13.11	12.51	16.05	14.97	14.71	12.86
FeO	5.98	8.07	8.23	4.61	5.12	6.17	7.72
MnO	0.15	0.24	0.25	n.d.	0.19	0.13	0.31
CaO	23.40	23.38	23.09	24.28	24.47	24.27	23.32
Na_2O	0.27	0.46	0.37	0.20	0.22	0.26	0.36
TiO_2	0.52	0.94	0.91	0.34	0.42	0.39	0.80
Cr_2O_3	n.d.	n.d.	n.d.	0.14	0.19	0.15	n.d.
TOTAL	99.19	98.89	99.73	99.04	100.33	101.16	99.87
	Number of cations in formula						
Si	1.902	1.821	1.865	1.911	1.923	1.927	1.875
Al	0.092	0.184	0.196	0.074	0.101	0.098	0.182
Mg	0.851	0.734	0.697	0.884	0.819	0.800	0.714
Fe^{2+}	0.092	0.099	0.208	0.047	0.117	0.148	0.192
Fe^{3+}	0.094	0.154	0.049	0.095	0.040	0.041	0.049
Mn	0.005	0.008	0.008	0.000	0.006	0.004	0.010
Ca	0.929	0.940	0.925	0.961	0.962	0.949	0.931
Na	0.020	0.034	0.027	0.014	0.015	0.018	0.026
Ti	0.015	0.027	0.026	0.009	0.012	0.011	0.022
Cr	0.000	0.000	0.000	0.004	0.006	0.004	0.000
TOTAL	4.000	4.000	4.000	4.000	4.000	4.000	4.000
$Mg/(Mg+Fe^{+2})*100$	90.3	88.1	77.0	94.9	87.5	84.4	78.8
$Mg/(Mg+Fe_{total})*100$	82.1	74.3	73.0	86.1	83.9	81.0	74.8
Cation Index DS	3.366	2.989	2.973	3.521	3.418	3.362	3.039
Wo	47.1	48.6	49.0	48.4	49.5	48.9	49.1
En	43.2	37.9	36.9	44.5	42.1	41.2	37.7
Fs	9.7	13.5	14.1	7.2	8.4	9.9	13.2

APPENDIX A				
sample	11-KT-34B			
Cpx #	Cpx 11			
probe site	h	i	j	k
	Wt% oxide			
SiO_2	50.45	48.79	49.19	48.71
Al_2O_3	4.14	3.91	3.98	3.97
MgO	12.93	12.97	13.61	12.80
FeO	8.21	8.40	7.27	8.35
MnO	0.26	0.23	0.10	0.39
CaO	23.76	23.39	24.07	23.66
Na_2O	0.30	0.42	0.25	0.38
TiO_2	0.79	0.70	0.69	0.81
Cr_2O_3	n.d.	n.d.	n.d.	n.d.
TOTAL	100.84	98.81	99.17	99.07
	Number of cations in formula			
Si	1.863	1.835	1.836	1.830
Al	0.180	0.173	0.175	0.176
Mg	0.712	0.727	0.758	0.717
Fe^{2+}	0.182	0.116	0.095	0.116
Fe^{3+}	0.071	0.148	0.132	0.146
Mn	0.008	0.007	0.003	0.012
Ca	0.940	0.943	0.963	0.953
Na	0.021	0.031	0.018	0.027
Ti	0.022	0.020	0.019	0.023
Cr	0.000	0.000	0.000	0.000
TOTAL	4.000	4.000	4.000	4.000
$Mg/(Mg+Fe^{+2})*100$	79.6	86.2	88.8	86.1
$Mg/(Mg+Fe_{total})*100$	73.8	73.4	76.9	73.2
Cation Index DS	3.030	3.010	3.114	2.998
Wo	49.1	48.6	49.4	49.0
En	37.2	37.5	38.8	36.9
Fs	13.7	14.0	11.8	14.1

APPENDIX A							
sample	11-KT-34B						
Cpx #	Cpx 15						
probe site	a	b	c	d	e	f	g
	Wt% oxide						
SiO_2	47.69	49.29	49.96	48.86	47.95	49.33	48.54
Al_2O_3	7.22	5.08	4.38	5.33	5.05	5.37	4.24
MgO	11.96	12.79	13.03	12.58	12.86	12.33	13.59
FeO	8.11	7.67	7.60	8.58	8.27	8.49	8.18
MnO	0.20	0.14	0.17	0.22	0.31	0.22	0.26
CaO	24.12	23.88	23.81	23.16	23.46	23.35	23.78
Na_2O	0.33	0.28	0.32	0.43	0.35	0.43	0.38
TiO_2	1.55	0.91	0.90	1.22	0.97	1.01	0.78
Cr_2O_3	n.d.	n.d.	0.12	n.d.	n.d.	n.d.	n.d.
TOTAL	101.19	100.04	100.28	100.39	99.22	100.53	99.76
	Number of cations in formula						
Si	1.756	1.831	1.851	1.813	1.796	1.828	1.803
Al	0.313	0.222	0.191	0.233	0.223	0.235	0.186
Mg	0.657	0.708	0.720	0.696	0.718	0.681	0.753
Fe^{2+}	0.137	0.153	0.160	0.162	0.103	0.179	0.063
Fe^{3+}	0.113	0.085	0.076	0.105	0.156	0.084	0.192
Mn	0.006	0.004	0.005	0.007	0.010	0.007	0.008
Ca	0.951	0.950	0.945	0.920	0.942	0.927	0.947
Na	0.024	0.020	0.023	0.031	0.025	0.031	0.027
Ti	0.043	0.026	0.025	0.034	0.027	0.028	0.022
Cr	0.000	0.000	0.004	0.000	0.000	0.000	0.000
TOTAL	4.000	4.000	4.000	4.000	4.000	4.000	4.000
$Mg/(Mg+Fe^{+2})*100$	82.8	82.2	81.8	81.2	87.5	79.2	92.3
$Mg/(Mg+Fe_{total})*100$	72.4	74.8	75.4	72.3	73.5	72.2	74.7
Cation Index DS	2.728	2.979	3.040	2.857	2.911	2.873	3.005
Wo	51.0	50.0	49.6	48.7	48.8	49.4	48.2
En	35.2	37.3	37.8	36.8	37.2	36.3	38.4
Fs	13.7	12.8	12.6	14.5	13.9	14.4	13.4

APPENDIX A							
sample	11-OS-12						
Cpx #	Cpx 1						
probe site	a	b	c	d	e	f	g
	Wt% oxide						
SiO_2	47.54	49.07	49.54	48.89	53.12	48.90	50.00
Al_2O_3	5.74	4.80	3.94	4.42	1.73	4.24	3.56
MgO	13.16	13.48	14.25	14.42	16.70	14.14	14.46
FeO	8.18	7.64	7.74	7.82	4.37	7.28	6.60
MnO	0.12	0.33	0.09	n.d.	0.14	0.14	0.16
CaO	23.74	23.22	23.02	23.05	23.73	23.35	23.79
Na_2O	0.36	0.44	0.40	0.40	0.21	0.41	0.31
TiO_2	1.09	0.86	0.74	0.82	0.35	0.76	0.64
Cr_2O_3	n.d.	n.d.	0.10	n.d.	0.51	n.d.	n.d.
TOTAL	99.93	99.84	99.82	99.82	100.85	99.22	99.51
	Number of cations in formula						
Si	1.764	1.819	1.834	1.807	1.926	1.819	1.852
Al	0.251	0.210	0.172	0.192	0.074	0.186	0.155
Mg	0.728	0.745	0.786	0.795	0.903	0.784	0.798
Fe^{2+}	0.067	0.102	0.095	0.065	0.077	0.063	0.077
Fe^{3+}	0.187	0.135	0.145	0.177	0.055	0.164	0.127
Mn	0.004	0.010	0.003	0.000	0.004	0.004	0.005
Ca	0.944	0.923	0.913	0.913	0.922	0.930	0.944
Na	0.026	0.032	0.029	0.029	0.015	0.029	0.023
Ti	0.030	0.024	0.021	0.023	0.010	0.021	0.018
Cr	0.000	0.000	0.003	0.000	0.015	0.000	0.000
TOTAL	4.000	4.000	4.000	4.000	4.000	4.000	4.000
$Mg/(Mg+Fe^{+2})*100$	91.6	88.0	89.2	92.5	92.1	92.6	91.2
$Mg/(Mg+Fe_{total})*100$	74.1	75.9	76.6	76.7	87.2	77.6	79.6
Cation Index DS	2.870	2.974	3.072	3.029	3.530	3.065	3.190
Wo	48.9	48.2	47.0	46.8	47.0	47.8	48.4
En	37.7	38.9	40.5	40.8	46.0	40.3	40.9
Fs	13.4	12.9	12.5	12.4	7.0	11.9	10.7

APPENDIX A							
sample	11-OS-12						
Cpx #	Cpx 1		Cpx 7				
probe site	h	i	a	b	c	d	e
	Wt% oxide						
SiO_2	50.15	48.94	48.96	48.65	49.14	49.48	49.81
Al_2O_3	3.57	4.14	4.45	4.20	4.09	4.09	3.73
MgO	14.36	13.98	14.15	14.49	14.05	14.34	14.61
FeO	6.99	7.81	7.41	7.06	7.23	7.07	7.41
MnO	0.18	0.13	0.14	0.21	0.16	0.15	0.14
CaO	23.40	22.76	22.93	23.70	23.65	23.63	23.24
Na_2O	0.30	0.34	0.45	0.28	0.35	0.33	0.32
TiO_2	0.75	0.91	0.74	0.75	0.63	0.88	0.75
Cr_2O_3	n.d.	n.d.	n.d.	n.d.	n.d.	0.16	n.d.
TOTAL	99.71	99.01	99.24	99.34	99.30	100.12	100.01
	Number of cations in formula						
Si	1.857	1.829	1.820	1.805	1.827	1.825	1.838
Al	0.156	0.182	0.195	0.184	0.179	0.178	0.162
Mg	0.793	0.779	0.784	0.802	0.779	0.788	0.804
Fe^{2+}	0.108	0.112	0.073	0.035	0.068	0.076	0.086
Fe^{3+}	0.109	0.132	0.157	0.184	0.157	0.142	0.142
Mn	0.006	0.004	0.005	0.007	0.005	0.005	0.004
Ca	0.929	0.911	0.913	0.942	0.942	0.934	0.919
Na	0.022	0.024	0.033	0.020	0.025	0.023	0.023
Ti	0.021	0.026	0.021	0.021	0.018	0.024	0.021
Cr	0.000	0.000	0.000	0.000	0.000	0.005	0.000
TOTAL	4.000	4.000	4.000	4.000	4.000	4.000	4.000
$Mg/(Mg+Fe^{+2})*100$	88.0	87.4	91.5	95.8	92.0	91.2	90.3
$Mg/(Mg+Fe_{total})*100$	78.6	76.1	77.3	78.5	77.6	78.3	77.8
Cation Index DS	3.159	3.039	3.034	3.099	3.096	3.104	3.122
Wo	47.8	47.0	47.3	47.8	48.3	48.0	47.0
En	40.8	40.2	40.6	40.7	39.9	40.5	41.1
Fs	11.4	12.8	12.2	11.5	11.8	11.5	11.9

APPENDIX A							
sample	11-OS-33						
Cpx #	Cpx 7						
probe site	a	b	c	d	e	f	g
	Wt% oxide						
SiO_2	49.73	48.68	48.67	50.29	48.50	48.81	46.57
Al_2O_3	3.93	5.11	5.52	4.16	5.51	4.33	6.56
MgO	14.13	13.58	13.25	13.36	13.09	13.61	11.65
FeO	7.73	8.13	8.04	7.86	8.52	7.87	9.65
MnO	0.26	0.20	0.23	0.31	0.32	0.30	0.30
CaO	23.40	23.42	23.32	23.52	22.81	23.24	22.78
Na_2O	0.40	0.50	0.38	0.50	0.53	0.55	0.60
TiO_2	0.74	0.89	1.08	0.72	0.93	0.77	1.05
Cr_2O_3	0.00	0.00	0.00	0.00	0.00	0.00	0.00
TOTAL	100.32	100.50	100.51	100.71	100.21	99.48	99.15
	Number of cations in formula						
Si	1.833	1.792	1.796	1.851	1.795	1.815	1.752
Al	0.171	0.222	0.240	0.180	0.240	0.190	0.291
Mg	0.776	0.745	0.729	0.733	0.722	0.754	0.653
Fe^{2+}	0.088	0.070	0.113	0.129	0.108	0.068	0.113
Fe^{3+}	0.151	0.180	0.135	0.113	0.156	0.177	0.191
Mn	0.008	0.006	0.007	0.010	0.010	0.009	0.009
Ca	0.924	0.924	0.922	0.928	0.904	0.926	0.918
Na	0.029	0.036	0.027	0.036	0.038	0.040	0.044
Ti	0.020	0.025	0.030	0.020	0.026	0.022	0.030
Cr	0.000	0.000	0.000	0.000	0.000	0.000	0.000
TOTAL	4.000	4.000	4.000	4.000	4.000	4.000	4.000
$Mg/(Mg+Fe^{+2})*100$	89.9	91.4	86.6	85.0	87.0	91.8	85.3
$Mg/(Mg+Fe_{total})*100$	76.5	74.9	74.6	75.2	73.2	75.5	68.3
Cation Index DS	3.067	2.923	2.894	3.025	2.844	2.990	2.645
Wo	47.5	48.0	48.4	48.5	47.6	47.9	48.7
En	39.9	38.7	38.2	38.3	38.0	39.0	34.7
Fs	12.7	13.3	13.4	13.2	14.4	13.1	16.6

APPENDIX A					
sample	11-OS-33				
Cpx #	Cpx 7				
probe site	h	i	j	k	l
	Wt% oxide				
SiO_2	48.89	49.73	49.28	47.91	50.42
Al_2O_3	3.91	3.31	3.58	5.28	2.94
MgO	12.86	13.18	13.18	11.64	13.39
FeO	8.39	8.02	8.44	9.57	7.98
MnO	0.31	0.28	0.19	0.30	0.32
CaO	23.80	23.73	23.79	23.54	23.78
Na_2O	0.46	0.49	0.49	0.60	0.34
TiO_2	0.78	0.77	0.75	0.96	0.75
Cr_2O_3	0.00	0.00	0.00	0.00	0.27
TOTAL	99.40	99.51	99.72	99.79	100.18
	Number of cations in formula				
Si	1.829	1.856	1.835	1.794	1.873
Al	0.173	0.145	0.157	0.233	0.129
Mg	0.717	0.734	0.732	0.649	0.742
Fe^{2+}	0.103	0.116	0.098	0.130	0.147
Fe^{3+}	0.159	0.135	0.165	0.169	0.101
Mn	0.010	0.009	0.006	0.010	0.010
Ca	0.954	0.949	0.950	0.944	0.946
Na	0.034	0.035	0.036	0.043	0.025
Ti	0.022	0.021	0.021	0.027	0.021
Cr	0.000	0.000	0.000	0.000	0.008
TOTAL	4.000	4.000	4.000	4.000	4.000
$Mg/(Mg+Fe^{+2})*100$	87.4	86.4	88.2	83.3	83.5
$Mg/(Mg+Fe_{total})*100$	73.2	74.5	73.6	68.4	75.0
Cation Index DS	2.999	3.077	3.034	2.775	3.136
Wo	49.1	48.9	48.7	49.6	48.6
En	36.9	37.8	37.5	34.1	38.1
Fs	14.0	13.4	13.8	16.2	13.2

APPENDIX A							
sample	11-OS-42						
Cpx #	Cpx 5						
probe site	a	b	c	d	e	f	g
	Wt% oxide						
SiO_2	48.70	50.02	49.06	48.51	48.62	48.29	47.72
Al_2O_3	5.10	4.42	4.71	4.66	5.13	5.11	5.09
MgO	13.47	13.29	13.98	12.83	13.25	13.06	13.39
FeO	7.96	7.30	7.57	7.40	7.90	7.69	8.05
MnO	n.d.	0.13	0.11	0.13	0.19	0.25	0.09
CaO	23.87	23.56	24.20	23.83	24.16	23.49	24.28
Na_2O	0.64	0.58	0.44	0.36	0.45	0.37	0.50
TiO_2	0.85	0.72	0.84	0.83	0.86	0.94	0.97
Cr_2O_3	n.d.	0.26	n.d.	n.d.	n.d.	n.d.	n.d.
TOTAL	100.59	100.27	100.91	98.55	100.55	99.21	100.10
	Number of cations in formula						
Si	1.789	1.847	1.796	1.826	1.791	1.805	1.764
Al	0.221	0.192	0.203	0.207	0.223	0.225	0.222
Mg	0.737	0.731	0.762	0.720	0.727	0.728	0.738
Fe^{2+}	0.044	0.117	0.041	0.113	0.065	0.102	0.017
Fe^{3+}	0.201	0.108	0.191	0.120	0.179	0.138	0.232
Mn	0.000	0.004	0.003	0.004	0.006	0.008	0.003
Ca	0.939	0.932	0.949	0.961	0.954	0.941	0.962
Na	0.046	0.041	0.031	0.026	0.032	0.027	0.036
Ti	0.024	0.020	0.023	0.024	0.024	0.027	0.027
Cr	0.000	0.007	0.000	0.000	0.000	0.000	0.000
TOTAL	4.000	4.000	4.000	4.000	4.000	4.000	4.000
$Mg/(Mg+Fe^{+2})*100$	94.4	86.2	94.9	86.5	91.8	87.7	97.8
$Mg/(Mg+Fe_{total})*100$	75.1	76.4	76.7	75.5	74.9	75.2	74.8
Cation Index DS	2.931	3.034	3.014	3.014	2.945	2.947	2.927
Wo	48.9	49.2	48.7	50.1	49.4	49.1	49.3
En	38.4	38.6	39.2	37.5	37.7	38.0	37.8
Fs	12.7	12.1	12.1	12.4	12.9	13.0	12.9

APPENDIX A							
sample	11-KT-02						
Cpx #	Cpx 26						
probe site	a	b	c	d	e	f	g
	Wt% oxide						
SiO_2	46.79	48.01	51.39	49.58	51.37	49.05	48.11
Al_2O_3	5.72	4.85	2.45	3.46	2.05	4.08	5.10
MgO	12.24	12.66	14.57	13.91	14.79	12.62	12.99
FeO	8.45	7.94	7.11	7.42	6.26	8.68	8.42
MnO	0.34	0.23	n.d.	0.27	0.18	0.40	0.16
CaO	23.53	24.08	24.26	24.19	24.02	23.89	23.64
Na_2O	0.43	0.37	0.36	0.35	0.30	0.52	0.32
TiO_2	1.35	1.04	0.54	0.73	0.55	0.88	0.84
Cr_2O_3	n.d.	n.d.	n.d.	n.d.	n.d.	n.d.	n.d.
TOTAL	98.85	99.17	100.67	99.91	99.53	100.13	99.59
	Number of cations in formula						
Si	1.762	1.800	1.885	1.837	1.903	1.824	1.794
Al	0.254	0.214	0.106	0.151	0.090	0.179	0.224
Mg	0.687	0.707	0.797	0.768	0.817	0.700	0.722
Fe^{2+}	0.090	0.094	0.099	0.071	0.099	0.110	0.100
Fe^{3+}	0.176	0.154	0.119	0.159	0.095	0.160	0.163
Mn	0.011	0.007	0.000	0.008	0.006	0.013	0.005
Ca	0.950	0.967	0.954	0.960	0.954	0.952	0.945
Na	0.031	0.027	0.025	0.025	0.022	0.037	0.023
Ti	0.038	0.029	0.015	0.020	0.015	0.025	0.024
Cr	0.000	0.000	0.000	0.000	0.000	0.000	0.000
TOTAL	4.000	4.000	4.000	4.000	4.000	4.000	4.000
$Mg/(Mg+Fe^{+2})*100$	88.4	88.2	88.9	91.6	89.2	86.4	87.9
$Mg/(Mg+Fe_{total})*100$	72.1	74.0	78.5	77.0	80.8	72.2	73.3
Cation Index DS	2.799	2.948	3.271	3.131	3.347	2.953	2.922
Wo	49.6	50.1	48.4	48.8	48.4	49.2	48.8
En	35.9	36.6	40.5	39.1	41.5	36.2	37.3
Fs	14.5	13.3	11.1	12.1	10.1	14.6	13.8

APPENDIX A							
sample	11-KT-02						
Cpx #	Cpx 26			Cpx 5			
probe site	h	i		a	b	c	d
	Wt% oxide						
SiO_2	50.39	50.69		48.19	48.44	47.92	47.15
Al_2O_3	3.02	2.65		4.94	4.95	5.11	5.22
MgO	13.69	13.72		13.15	13.01	12.71	12.57
FeO	7.81	8.07		8.27	7.91	8.24	8.95
MnO	0.47	0.41		0.34	0.23	0.28	0.40
CaO	23.86	23.73		24.12	24.20	24.38	23.94
Na_2O	0.47	0.38		0.38	0.32	0.42	0.33
TiO_2	0.55	0.44		0.61	0.65	0.85	0.99
Cr_2O_3	n.d.	n.d.		n.d.	n.d.	n.d.	n.d.
TOTAL	100.25	100.10		99.99	99.71	99.91	99.54
	Number of cations in formula						
Si	1.863	1.880		1.787	1.802	1.781	1.764
Al	0.131	0.116		0.216	0.217	0.224	0.230
Mg	0.755	0.759		0.727	0.721	0.704	0.701
Fe^{2+}	0.096	0.123		0.054	0.081	0.060	0.071
Fe^{3+}	0.145	0.127		0.202	0.166	0.196	0.210
Mn	0.015	0.013		0.011	0.007	0.009	0.013
Ca	0.945	0.943		0.958	0.965	0.971	0.960
Na	0.034	0.027		0.027	0.023	0.030	0.024
Ti	0.015	0.012		0.017	0.018	0.024	0.028
Cr	0.000	0.000		0.000	0.000	0.000	0.000
TOTAL	4.000	4.000		4.000	4.000	4.000	4.000
$Mg/(Mg+Fe^{+2})*100$	88.7	86.0		93.1	90.0	92.1	90.8
$Mg/(Mg+Fe_{total})*100$	75.8	75.2		73.9	74.6	73.3	71.4
Cation Index DS	3.127	3.163		2.946	2.976	2.913	2.851
Wo	48.3	48.0		49.1	49.7	50.0	49.1
En	38.6	38.6		37.2	37.2	36.3	35.9
Fs	13.1	13.4		13.7	13.1	13.7	15.0

APPENDIX A							
sample	11-KT-03A						
Cpx #	Cpx 3						
probe site	a	b	c	d	e	f	g
	Wt% oxide						
SiO_2	46.42	44.78	47.59	44.70	45.12	44.12	42.19
Al_2O_3	6.76	7.71	5.62	6.74	7.26	7.67	10.05
MgO	11.50	10.60	12.50	8.47	10.72	8.41	9.63
FeO	10.04	10.42	9.14	14.22	10.38	13.48	11.50
MnO	0.23	n.d.	0.27	0.44	0.15	0.41	0.17
CaO	25.47	25.17	24.90	24.03	25.27	24.51	25.11
Na_2O	0.21	0.28	0.19	0.57	0.28	0.53	0.26
TiO_2	0.73	0.85	0.67	1.15	0.90	1.14	1.36
Cr_2O_3	n.d.	n.d.	n.d.	n.d.	n.d.	0.22	n.d.
TOTAL	101.35	99.82	100.89	100.33	100.08	100.50	100.26
	Number of cations in formula						
Si	1.713	1.681	1.758	1.699	1.691	1.671	1.583
Al	0.294	0.341	0.245	0.302	0.320	0.342	0.444
Mg	0.633	0.593	0.688	0.480	0.599	0.475	0.539
Fe^{2+}	0.056	0.059	0.067	0.175	0.058	0.142	0.030
Fe^{3+}	0.254	0.268	0.215	0.277	0.267	0.285	0.331
Mn	0.007	0.000	0.008	0.014	0.005	0.013	0.005
Ca	1.007	1.012	0.986	0.979	1.015	0.994	1.010
Na	0.015	0.020	0.014	0.042	0.020	0.039	0.019
Ti	0.020	0.024	0.019	0.033	0.025	0.032	0.038
Cr	0.000	0.000	0.000	0.000	0.000	0.007	0.000
TOTAL	4.000	4.000	4.000	4.000	4.000	4.000	4.000
$Mg/(Mg+Fe^{+2})*100$	91.8	91.0	91.1	73.3	91.2	76.9	94.7
$Mg/(Mg+Fe_{total})*100$	67.1	64.5	70.9	51.5	64.8	52.7	59.9
Cation Index DS	2.708	2.574	2.864	2.314	2.608	2.293	2.264
Wo	51.5	52.4	50.2	50.8	52.2	52.1	52.7
En	32.3	30.7	35.0	24.9	30.8	24.9	28.1
Fs	16.2	16.9	14.8	24.2	17.0	23.0	19.1

APPENDIX A							
sample	11-KT-03A						
Cpx #	Cpx 3		Cpx 5				
probe site	h		a	b	c	d	e
	Wt% oxide						
SiO_2	43.11		49.95	47.26	42.98	50.24	50.08
Al_2O_3	9.10		4.11	6.76	9.57	3.94	3.80
MgO	10.49		13.33	12.80	9.64	13.90	13.54
FeO	10.91		7.59	7.35	11.32	7.65	7.66
MnO	0.13		0.27	n.d.	0.23	0.29	0.20
CaO	25.48		24.07	24.85	24.60	23.69	23.72
Na_2O	0.21		0.39	0.17	0.23	0.34	0.29
TiO_2	1.18		0.53	0.73	1.35	0.57	0.50
Cr_2O_3	n.d.		n.d.	n.d.	n.d.	n.d.	n.d.
TOTAL	100.61		100.25	99.93	99.93	100.62	99.79
	Number of cations in formula						
Si	1.607		1.847	1.751	1.620	1.849	1.860
Al	0.400		0.179	0.295	0.425	0.171	0.166
Mg	0.583		0.735	0.707	0.542	0.762	0.750
Fe^{2+}	0.005		0.109	0.054	0.082	0.110	0.132
Fe^{3+}	0.335		0.126	0.174	0.275	0.125	0.106
Mn	0.004		0.009	0.000	0.007	0.009	0.006
Ca	1.018		0.954	0.987	0.993	0.934	0.944
Na	0.015		0.028	0.012	0.017	0.024	0.021
Ti	0.033		0.015	0.020	0.038	0.016	0.014
Cr	0.000		0.000	0.000	0.000	0.000	0.000
TOTAL	4.000		4.000	4.000	4.000	4.000	4.000
$Mg/(Mg+Fe^{+2})*100$	99.2		87.1	92.9	86.9	87.3	85.1
$Mg/(Mg+Fe_{total})*100$	63.2		75.8	75.6	60.3	76.4	75.9
Cation Index DS	2.415		3.070	2.889	2.310	3.089	3.109
Wo	52.3		49.4	51.3	52.3	48.1	48.7
En	30.0		38.0	36.8	28.5	39.3	38.7
Fs	17.7		12.6	11.9	19.2	12.6	12.6

APPENDIX A							
sample	11-KT-04D						
Cpx #	Cpx 3						
probe site	a	b	c	d	e	f	g
	Wt% oxide						
SiO_2	52.33	52.69	52.14	51.87	49.94	51.43	48.94
Al_2O_3	1.65	2.18	2.47	2.66	3.87	2.64	4.87
MgO	17.05	16.26	16.09	16.17	14.96	16.30	14.29
FeO	3.51	3.92	4.74	4.56	5.99	4.68	7.34
MnO	n.d.	0.13	0.19	0.18	0.08	0.11	0.27
CaO	24.36	24.21	24.11	24.35	23.81	24.17	23.71
Na_2O	0.12	0.15	0.11	0.12	0.16	0.21	0.10
TiO_2	0.20	0.15	0.23	0.27	0.35	0.18	0.54
Cr_2O_3	0.12	n.d.	n.d.	n.d.	n.d.	n.d.	0.12
TOTAL	99.34	99.68	100.09	100.17	99.17	99.73	100.18
	Number of cations in formula						
Si	1.917	1.930	1.907	1.893	1.850	1.882	1.805
Al	0.071	0.094	0.107	0.115	0.169	0.114	0.212
Mg	0.931	0.888	0.877	0.880	0.826	0.889	0.786
Fe^{2+}	0.018	0.071	0.069	0.046	0.063	0.017	0.075
Fe^{3+}	0.089	0.049	0.076	0.093	0.123	0.126	0.151
Mn	0.000	0.004	0.006	0.005	0.003	0.003	0.009
Ca	0.956	0.950	0.945	0.952	0.945	0.948	0.937
Na	0.008	0.011	0.008	0.008	0.011	0.015	0.007
Ti	0.005	0.004	0.006	0.007	0.010	0.005	0.015
Cr	0.004	0.000	0.000	0.000	0.000	0.000	0.004
TOTAL	4.000	4.000	4.000	4.000	4.000	4.000	4.000
$Mg/(Mg+Fe^{+2})*100$	98.1	92.6	92.7	95.0	93.0	98.1	91.2
$Mg/(Mg+Fe_{total})*100$	89.6	88.1	85.8	86.3	81.7	86.1	77.6
Cation Index DS	3.615	3.535	3.457	3.450	3.243	3.439	3.062
Wo	47.9	48.4	47.9	48.2	48.2	47.8	47.9
En	46.7	45.3	44.5	44.5	42.2	44.8	40.1
Fs	5.4	6.3	7.6	7.3	9.6	7.4	12.0

APPENDIX A					
sample	11-KT-04D				
Cpx #	Cpx 3				
probe site	h	i	j	k	l
	Wt% oxide				
SiO_2	47.34	46.77	45.64	46.90	45.45
Al_2O_3	5.63	6.94	7.07	5.81	7.68
MgO	13.70	12.80	12.44	13.73	12.43
FeO	7.97	8.32	9.00	7.99	8.82
MnO	0.09	0.20	0.10	0.10	0.13
CaO	23.76	23.63	23.70	23.65	23.52
Na_2O	0.19	0.19	0.23	0.20	0.22
TiO_2	0.76	0.78	0.68	0.68	0.87
Cr_2O_3	n.d.	n.d.	0.14	n.d.	n.d.
TOTAL	99.44	99.63	99.00	99.04	99.12
	Number of cations in formula				
Si	1.761	1.741	1.713	1.750	1.702
Al	0.247	0.305	0.313	0.255	0.339
Mg	0.760	0.711	0.696	0.764	0.694
Fe^{2+}	0.045	0.076	0.047	0.028	0.053
Fe^{3+}	0.203	0.183	0.236	0.221	0.223
Mn	0.003	0.006	0.003	0.003	0.004
Ca	0.947	0.942	0.953	0.945	0.944
Na	0.014	0.014	0.017	0.014	0.016
Ti	0.021	0.022	0.019	0.019	0.025
Cr	0.000	0.000	0.004	0.000	0.000
TOTAL	4.000	4.000	4.000	4.000	4.000
$Mg/(Mg+Fe^{+2})*100$	94.4	90.3	93.7	96.4	92.9
$Mg/(Mg+Fe_{total})*100$	75.4	73.3	71.1	75.4	71.5
Cation Index DS	2.934	2.789	2.732	2.918	2.681
Wo	48.4	49.1	49.3	48.2	49.2
En	38.8	37.0	36.0	38.9	36.2
Fs	12.8	13.8	14.8	12.9	14.6